

# FAULT TOLERANT OPERATIONS OF INDUCTION MOTOR-DRIVE SYSTEMS

by

Chia-Chou Yeh, B.S., M.S.

A Dissertation submitted to the Faculty of the  
Graduate School, Marquette University,  
in Partial Fulfillment of  
the Requirements for  
the Degree of

DOCTOR OF PHILOSOPHY

Milwaukee, Wisconsin

May, 2008

# Preface

## **FAULT TOLERANT OPERATIONS OF INDUCTION MOTOR-DRIVE SYSTEMS**

Chia-Chou Yeh

Under the Supervision of Professor Nabeel A. O. Demerdash at

Marquette University

This dissertation presents fault-tolerant / “limp-home” strategies of ac motor soft starters and adjustable-speed drives (ASDs) when experiencing a power switch open-circuit or short-circuit fault. The present low-cost fault mitigation solutions can be retrofitted into the existing off-the-shelf soft starters and ASDs to enhance their reliability and fault tolerant capability, with only minimum hardware modifications. The conceived fault-tolerant soft starters are capable of operating in a two-phase mode in the event of a thyristor/SCR open-circuit or short-circuit switch-fault in any one of the phases using a novel resilient closed-loop control scheme. The performance resulting from using the conceived soft starter fault-tolerant control has demonstrated reduced starting motor torque pulsations and reduced inrush current magnitudes. Small-signal model representation of the motor-soft starter controller system is also developed here in order to design the closed-loop regulators of the control system at a desired bandwidth to render a good dynamic and fast transient response. In addition, the transient motor performance under these types of faults is investigated using analytical closed-form solutions, the results of which are in good agreement with both the detailed simulation and experimental test results of the actual hardware.

As for ASDs, a low-cost fault mitigation strategy, based on a quasi-cycloconverter-based topology and control, for low-speed applications such as “self-healing/limp-home” needs for vehicles and propulsion systems is developed. The present approach offers the potential of mitigating both transistor open-circuit and short-circuit switch faults, as well as other drive-related faults such as faults occurring in the rectifier bridge or dc-link capacitor. Furthermore,

some of the drawbacks associated with previously known fault mitigation techniques such as the need for accessibility to a motor neutral, the need for larger size dc-link capacitors, or higher dc-bus voltage, are overcome here using the present approach. Due to its unique control algorithm, torque pulsations are introduced as a result of the non-sinusoidal current waveforms. Meanwhile, application considerations and opportunities for practical use of the conceived design are also investigated here in this work. The results of this research suggest that the conceived approach is best suited for partial motor-loading operating condition, which is normally the case for many practical industrial applications where the motors are usually oversized. The reason for choosing to operate under such conditions is the resulting reduced torque pulsations that the motor will experience when supplied by the conceived topology at light-load conditions. In addition, the negative impact of inverter switch fault on motor performance is also analyzed in this work using the averaged switching function modeling concept. Simulation and experimental work have been performed to demonstrate the efficacy and validity of the conceived fault-tolerant solutions for induction motor fault mitigation applications.

# Acknowledgement

First of all, I wish to express my sincere and deepest gratitude to my advisor, Professor Nabeel A. O. Demerdash, for his encouragement, time, and expert technical guidance throughout the completion of this work. Without his open-mindedness and patient guidance, this dissertation would not come to exist. His endless hours of advice and help in my research work are very much appreciated and will always be remembered. Our discussions involve not only technical matters, but also life in general. In fact, he serves as a father figure to me. It is my extreme privilege to have him as my advisor as well as my dear friend. His famous quote: “No question is a stupid question” will always be buried in my mind.

I would also like to extend my deepest gratitude to my other dissertation committee members, namely Prof. Ronald H. Brown and Prof. Edwin E. Yaz of Marquette University, Dr. Thomas W. Nehl of Delphi Automotive Research, and Dr. Russel J. Kerkman of Allen Bradley-Rockwell Automation, for their precious time, support, and useful suggestions/insights.

I am also very grateful to my internship employer, Eaton Corporation, when I was with them for the majority part of my Ph.D. studies, for the technical experience, skills and knowledge that I gained which enabled the completion of this work. Furthermore, I wish to thank my co-workers, Madhav D. Manjrekar, Ian T. Wallace, Vijay Bhavaraju, Jun Kikuchi, and Edward F. Buck for all the helpful discussions in various projects.

In addition, I wish to acknowledge the financial support from the US National Science Foundation under Grant ECS-0322974 and the Rev. John P. Raynor Fellowship. I also wish to thank the Marquette University EECE department, professors, and support staff, especially Jean M. Weiss, for providing the environment that made this research work possible.

The support of the Eaton Corporation, Allen Bradley-Rockwell Automation, and A. O. Smith Corporation, in providing the test motors, drives, and other electronic equipment, is gratefully acknowledged. The experimental portion of this research work would not be possible without their support and generosity.

I also wish to extend special thanks to my dearest friends, Ahmed Sayed-Ahmed, Behrooz Mirafzal, Gennadi Y. Sizov, and Anushree Kadaba for their support, useful insights, and fruitful discussions throughout my graduate studies at Marquette University. The time when we all spent together in the lab is something I will never forget. I will definitely miss the moment and fun in our weekly “Tuesday Pizza”.

Most importantly, I would like to thank a special person, my lovely wife Huili, for her infinite patience, kindness, and endless love throughout this period. Her continued support and belief in me in things I wish to accomplish in my life will always be remembered. Her strong character has kept me motivated in the completion of this work. She definitely plays a major role in my life. Finally, I owe my deepest appreciation and special thanks to my family for their love, support, and encouragement throughout my life and education. This dissertation would not be possible without them.

There are many other people who have helped me in some ways in my research work. Although I cannot mention each one of their names, I never forget their kindness. Once again, I would like to express my greatest gratitude to all these people. Thank you all, it is good knowing you.

Chia-Chou Yeh  
May 2008

# Contents

<b>List of Figures .....</b>	<b>X</b>
------------------------------	----------

<b>List of Tables .....</b>	<b>xvii</b>
-----------------------------	-------------

<b>1 Introduction .....</b>	<b>1</b>
-----------------------------	----------

1.1 Motivation behind This Work .....	1
1.2 Literature Search Surveying Preceding Work .....	6
1.3 Objectives and Contributions .....	16
1.4 Dissertation Organizations .....	18
1.5 Summary .....	19

<b>2 Transient Analysis of Induction Motor-Soft Starter .....</b>	<b>20</b>
---	-----------

2.1 Introduction .....	20
2.2 Soft Starters .....	21
2.2.1 Topology .....	21
2.2.2 Principles of Operations .....	22
2.3 Closed-Form Derivation.....	25
2.3.1 Closed-Form Expressions of Motor Phase Voltages.....	25
2.3.2 Closed-Form Expressions of Motor Phase Currents .....	34
2.4 Analysis of Failure Modes and Effects .....	38
2.4.1 Short-Circuit SCR Fault .....	39
2.4.2 Open-Circuit SCR Fault .....	44
2.5 Summary .....	46

<b>3 Fault Tolerant Soft Starter.....</b>	<b>48</b>
---	-----------

3.1 Introduction .....	48
3.2 Principles of Fault Tolerant Operations .....	49
3.2.1 Modified Topology .....	50
3.2.2 A Resilient Closed-Loop Two-Phase Control Scheme .....	52
3.3 Small-Signal Modeling of Motor-Soft Starter Controller .....	56
3.3.1 Transfer Function of Controller .....	59
3.3.2 Transfer Function of Induction Motor.....	59

---

3.3.3	Nonlinear Representation of Soft Starter .....	62
3.3.4	Small-Signal Model Representation of Overall System.....	65
3.4	Design Procedures of Soft Starter PI Controllers.....	66
3.4.1	Voltage Control Loop.....	66
3.4.2	Current Control Loop .....	68
3.5	Summary .....	71
<b>4</b>	<b>Circuit Simulations of Fault Tolerant Soft Starter.....</b>	<b>74</b>
4.1	Introduction .....	74
4.2	Circuit Simulation Model.....	75
4.3	Verifications between Closed-Form Analytical and Simulation Results .....	79
4.3.1	Healthy Condition .....	79
4.3.2	Short-Circuit SCR Switch Fault Condition .....	84
4.4	Motor Performance under Fault Tolerant Operations .....	85
4.5	Summary .....	90
<b>5</b>	<b>Hardware Experiments of Fault Tolerant Soft Starter.....</b>	<b>95</b>
5.1	Introduction .....	95
5.2	Hardware Prototype.....	96
5.3	Experimental Results.....	101
5.3.1	Comparisons with Simulation and Analytical Results .....	101
5.3.2	Motor Performance under Fault Tolerant Operations .....	110
5.4	Summary .....	113
<b>6</b>	<b>Analysis of Failure Mode and Effect of Inverter Switch Faults on Motor Performance.....</b>	<b>121</b>
6.1	Introduction .....	121
6.2	Averaged Switching Function Model.....	122
6.2.1	Motor Phase Voltage Representations .....	124
6.2.2	Averaged Switching Function Formulations.....	125
6.3	Analysis of Failure Modes and Effects .....	130
6.3.1	Short-Circuit Switch Fault .....	131
6.3.1.1	Circuit Simulation Model.....	133
6.3.1.2	Analytical and Simulation Results .....	136
6.3.2	Open-Circuit Switch Fault .....	144
6.3.2.1	Simulation Results .....	148

6.4	Summary .....	160
<b>7</b>	<b>A Quasi-Cycloconverter-Based Topology and Control for Inverter Fault Mitigation.....</b>	<b>162</b>
7.1	Introduction .....	162
7.2	Present Fault Mitigation Topology and Control.....	167
7.2.1	Operating Principle of Present Topology.....	167
7.2.2	Discrete-Frequency Control Algorithm.....	172
7.3	Summary .....	179
<b>8</b>	<b>Simulation and Experimental Results of Inverter-Motor Fault Tolerant Operation .....</b>	<b>181</b>
8.1	Introduction .....	181
8.2	Simulation Performance.....	182
8.2.1	Circuit Simulation Model.....	182
8.2.2	Simulation Results.....	186
8.2.2.1	The No-Load Case .....	186
8.2.2.2	Limp-Home Operation of the Conceived Topology under Inverter Fault Case.....	187
8.2.2.3	Starting Performance of the Conceived Topology .....	198
8.3	Experimental Validations.....	204
8.3.1	The No-Load Case .....	207
8.3.2	Limp-Home Operation of the Conceived Topology under Inverter Fault Case .....	207
8.3.3	Starting Performance of the Conceived Topology .....	222
8.4	Application Considerations and Opportunities .....	224
8.5	Summary .....	229
<b>9</b>	<b>Conclusions, Contributions, and Suggested Future Work.....</b>	<b>230</b>
9.1	Summary and Conclusions.....	230
9.2	Contributions of this Work.....	237
9.3	Future Investigations .....	238
	<b>Bibliography.....</b>	<b>240</b>
<b>Appendix A</b>	<b>Designs and Specifications of Hardware Prototype .....</b>	<b>250</b>
A.1	Introduction .....	250
A.2	System Descriptions.....	250

A.2.1	Motor Design Specifications and Datasheets .....	255
A.2.2	Soft Starter and Quasi-Cycloconverter Designs.....	259
A.2.3	PWM Drive .....	262
A.2.4	DSP Controller Board .....	262
A.2.5	Signal Conditioning Circuits .....	265
A.2.6	Data Acquisition System .....	268

# List of Figures

Figure 1.1: Types of inverter switch failure modes under investigation.....	5
Figure 1.2: Categorization of various “limp-home” strategies for three-phase ac motor-drives. ...	7
Figure 1.3: Fault-tolerant inverter topology by Liu et al. [49] and Elch-Heb et al. [50]. ....	8
Figure 1.4: Fault-tolerant inverter topology by Van Der Broeck et al. [52] and Ribeiro et al. [44]. .....	11
Figure 1.5: First fault-tolerant inverter topology by Bolognani et al. [40]. ....	13
Figure 1.6: Second fault-tolerant inverter topology by Bolognani et al. [40]. ....	14
Figure 2.1: Conventional three-phase soft starter topology. ....	23
Figure 2.2: Definitions of firing angles. ....	23
Figure 2.3: Voltage ramp profiles. ....	25
Figure 2.4: (a) 3-phase conduction mode. (b) 2-phase conduction mode. ....	26
Figure 2.5: Healthy transient current space-vector plot during soft starting. ....	30
Figure 2.6: Healthy transient three-phase currents during soft starting. ....	30
Figure 2.7: T-equivalent circuit model ( $h$ is the harmonic order). ....	33
Figure 2.8: Analytical solution of healthy three-phase line-to-neutral motor voltage waveforms at operating conditions of $\phi = 60^\circ$ and $\alpha = 90^\circ$ . ....	33
Figure 2.9: Analytical solution of healthy three-phase current waveforms at transient conditions of $\phi = 60^\circ$ , $\alpha = 90^\circ$ , and motor speed of 200-r/min. ....	37
Figure 2.10: Failure modes in soft starter circuit. (a) Short-circuit fault. (b) Open-circuit fault. ....	39
Figure 2.11: Transient current space-vector plot during soft starting under a short-circuit SCR fault. ....	40
Figure 2.12: Three-phase line-to-neutral motor voltage waveforms from analytical solution under a short-circuit SCR fault. ....	42
Figure 2.13: Analytical solution of three-phase current waveforms at transient conditions of $\phi = 60^\circ$ , $\alpha = 90^\circ$ , and motor speed of 400-r/min under a short-circuit SCR fault. ....	43
Figure 3.1: Industrial type three-phase soft starter topology. ....	51
Figure 3.2: Modified version of soft starter with fault tolerance/isolation capabilities. ....	51
Figure 3.3: Post-fault soft starter configuration. ....	52
Figure 3.4: Present closed-loop two-phase control for fault tolerant soft starter. ....	54
Figure 3.5: Reference voltage ramp profile. ....	54
Figure 3.6: Simplified control system representation of motor-soft starter controller. ....	58

Figure 3.7: Voltage control loop.....	58
Figure 3.8: Current control loop.....	58
Figure 3.9: Transfer function of per-phase induction motor model.....	62
Figure 3.10: A plot of motor phase voltage (rms) versus $\alpha_V$ using Equation (3.14). ....	65
Figure 3.11: Bode plot of voltage control feedback loop system. (a) Open-loop transfer function. (b) Closed-loop transfer function.....	69
Figure 3.12: Bode plot of current control feedback loop system. (a) Open-loop transfer function. (b) Closed-loop transfer function.....	72
Figure 4.1: Schematic of motor-soft starter power structure in Matlab-Simulink [91]. ....	76
Figure 4.2: Block diagram of soft starter controller in Matlab-Simulink [91].....	78
Figure 4.3: Healthy three-phase line-to-neutral motor voltage waveforms at operating conditions of $\phi = 60^\circ$ and $\alpha = 90^\circ$ . (a) Analytical. (b) Simulation. ....	81
Figure 4.4: Healthy three-phase current waveforms at transient conditions of $\phi = 60^\circ$ , $\alpha = 90^\circ$ , and motor speed of 200-r/min. (a) Analytical. (b) Simulation. ....	82
Figure 4.5: RMS values of healthy three-phase stator currents from analytical solution and dynamic simulation. ....	84
Figure 4.6: Three-phase line-to-neutral motor voltage waveforms at operating conditions of $\phi = 60^\circ$ and $\alpha = 90^\circ$ under a short-circuit SCR fault. (a) Analytical. (b) Simulation.....	86
Figure 4.7: Three-phase current waveforms at transient conditions of $\phi = 60^\circ$ , $\alpha = 90^\circ$ , and motor speed of 400-r/min under a short-circuit SCR fault. (a) Analytical. (b) Simulation.....	87
Figure 4.8: RMS values of three-phase stator currents from analytical solution and dynamic simulation under a short-circuit SCR fault.....	89
Figure 4.9: Simulation results of three-phase current waveforms. (a) 3-phase open-loop control. (b) 2-phase open-loop control. (c) Proposed 2-phase closed-loop control.....	92
Figure 4.10: Simulation results of current space-vector plots. (a) 3-phase open-loop control. (b) 2-phase open-loop control. (c) Proposed 2-phase closed-loop control. ....	93
Figure 4.11: Simulation results of motor developed torque. (a) 3-phase open-loop control. (b) 2-phase open-loop control. (c) Proposed 2-phase closed-loop control. ....	94
Figure 5.1: Schematic of experimental setup of induction motor-soft starter system.....	98
Figure 5.2: Test rigs. (a) Soft starter. (b) Induction motor and dynamometer. ....	99
Figure 5.3: Healthy three-phase line-to-neutral motor voltage waveforms. (a) Test. (b) Simulation. (c) Analytical.....	104
Figure 5.4: Healthy three-phase current waveforms. (a) Test. (b) Simulation. (c) Analytical. ....	105
Figure 5.5: Three-phase line-to-neutral motor voltage waveforms under a short-circuit SCR fault. (a) Test. (b) Simulation. (c) Analytical. ....	107
Figure 5.6: Three-phase current waveforms under a short-circuit SCR fault. (a) Test. (b) Simulation. (c) Analytical.....	108

Figure 5.7: Test results obtained under direct-line-starting. (a) Three-phase motor currents. (b) Motor developed torque.....	114
Figure 5.8: Three-phase motor currents obtained under 3-Phase Open-Loop Control. (a) Test. (b) Simulation. ....	115
Figure 5.9: Motor developed torque obtained under 3-Phase Open-Loop Control. (a) Test. (b) Simulation. ....	116
Figure 5.10: Three-phase motor currents obtained under 2-Phase Open-Loop Control. (a) Test. (b) Simulation. ....	117
Figure 5.11: Motor developed torque obtained under 2-Phase Open-Loop Control. (a) Test. (b) Simulation. ....	118
Figure 5.12: Three-phase motor currents obtained under 2-Phase Closed-Loop Control. (a) Test. (b) Simulation. ....	119
Figure 5.13: Motor developed torque obtained under 2-Phase Closed-Loop Control. (a) Test. (b) Simulation. ....	120
Figure 6.1: Types of inverter switch failure modes under investigation.....	123
Figure 6.2: Inverter circuit.....	123
Figure 6.3: PWM switching function, $H_l$ , of switch, $S_l$ , of inverter leg- $a$ .....	127
Figure 6.4: Switching function expressed over a switching period of switch, $S_l$ . ....	127
Figure 6.5: Schematic of induction motor-drive power structure in Matlab-Simulink [91]. ....	134
Figure 6.6: Three-phase motor phase voltages during short-circuit switch fault condition. (a) Analytical. (b) Simulation.....	138
Figure 6.7: FFT spectra of simulated three-phase motor phase voltages during short-circuit switch fault condition. (a) Phase- $a$ . (b) Phase- $b$ . (c) Phase- $c$ . ....	139
Figure 6.8: Simulation results of three-phase motor currents during pre- and post-fault short- circuit switch fault conditions (fault occurs at $t = 1.3 \text{ sec}$ ). ....	140
Figure 6.9: FFT spectra of simulated three-phase motor currents during short-circuit switch fault condition. (a) Phase- $a$ . (b) Phase- $b$ . (c) Phase- $c$ .....	141
Figure 6.10: Simulation results of motor speed during short-circuit switch fault condition (fault occurs at $t = 1.3 \text{ sec}$ ). (a) Time-domain profile during pre- and post-fault. (b) FFT spectrum during post-fault. ....	142
Figure 6.11: Simulation results of motor developed torque during short-circuit switch fault condition (fault occurs at $t = 1.3 \text{ sec}$ ). (a) Time-domain profile during pre- and post-fault. (b) FFT spectrum during post-fault.....	143
Figure 6.12: Inverter circuit topology with an open-circuit fault at switch $S_l$ . ....	145
Figure 6.13: Simulation waveforms of motor quantities during pre- and post-fault conditions (open-circuit switch fault occurred at switch $S_l$ at $t = 1.3 \text{ sec}$ ). ....	147
Figure 6.14: Simulation results of three-phase motor currents during pre- and post-fault open- circuit switch fault conditions. (a) Healthy. (b) Post-Fault. ....	154
Figure 6.15: FFT spectra of simulated three-phase motor currents during open-circuit switch fault condition. (a) Healthy case in all phases. (b) Faulty case of $i_a$ . (c) Faulty case of $i_b$ . (d) Faulty case of $i_c$ .....	155

Figure 6.16: Simulation results of dc link voltage during open-circuit switch fault condition (fault occurs at $t = 1.3 \text{ sec}$ ). (a) Time-domain profile during pre- and post-fault. (b) FFT spectrum during post-fault. (c) Close-up view of FFT spectrum of Figure (b).....	156
Figure 6.17: Simulation results of motor developed torque during open-circuit switch fault condition (fault occurs at $t = 1.3 \text{ sec}$ ). (a) Time-domain profile during pre- and post-fault. (b) FFT spectrum during pre-fault. (c) FFT spectrum during post-fault. .....	157
Figure 6.18: Simulation results of motor speed during pre- and post-fault open-circuit switch fault conditions (fault occurs at $t = 1.3 \text{ sec}$ ).....	158
Figure 6.19: The origination of torque pulsations at a frequency, $\omega_{syn}$ . (a) Interactions between dc flux/field and positive-seq. 1 <sup>st</sup> harmonic. (b) Interactions between dc flux/field and negative-seq. 1 <sup>st</sup> harmonic. (c) Interactions between positive-seq. 1 <sup>st</sup> , 2 <sup>nd</sup> , and 3 <sup>rd</sup> harmonics. ....	158
Figure 6.20: Simulation results of current space-vector locus .....	159
Figure 7.1: SCR voltage-controlled topology.....	163
Figure 7.2: Different types of existing fault tolerant inverter topologies. ....	163
Figure 7.3: Present topology based on quasi-cycloconverter configuration.....	166
Figure 7.4: Present topology for inverter fault mitigation. ....	168
Figure 7.5: Example current patterns using discrete-frequency control for adjustable-speed mode operation for a supply mains frequency, $f_s = 60\text{Hz}$ .....	170
Figure 7.6: Graphical illustrations on the sequence order of input supply mains to achieve output waveforms with different frequency. (a) 15-Hz output. (b) 30-Hz output. ....	174
Figure 7.7: Firing sequence of the SCRs of phase- <i>a</i> . (a) 30-Hz operation. (b) 15-Hz operation. (c) 12-Hz operation. ....	175
Figure 7.8: Block diagram of proposed control scheme for variable-speed operation. ....	176
Figure 7.9: Control logic of phase-delayed pulse generator for each phase. ....	178
Figure 7.10: Graphical illustration of the control logic to achieve 15-Hz operation. ....	179
Figure 8.1: Schematic of induction motor-drive power structure with “limp-home” capability in Matlab-Simulink [91]. ....	183
Figure 8.2: Block diagram of discrete-frequency control algorithm in Matlab-Simulink [91]...	185
Figure 8.3: Simulation, 30-Hz operation. ....	188
Figure 8.4: Simulation, 15-Hz operation. ....	188
Figure 8.5: Simulation, 12-Hz operation. ....	189
Figure 8.6: Simulation, 8.57-Hz operation. ....	189
Figure 8.7: Simulation, 7.5-Hz operation. ....	190
Figure 8.8: Simulation, 6-Hz operation. ....	190
Figure 8.9: Simulation results of motor performance at 60-Hz operation during pre- and post-fault conditions. (a) Three-phase currents. (b) Developed torque. (c) Motor speed. .....	191

Figure 8.10: Simulation results of motor performance at 30-Hz operation during pre- and post-fault conditions at full-load. (a) Three-phase currents. (b) Steady-state “limp-home” post-fault current. (c) Developed torque. (d) Motor speed. ....	195
Figure 8.11: Simulation results of motor performance at 15-Hz operation during pre- and post-fault conditions at full-load. (a) Three-phase currents. (b) Steady-state “limp-home” post-fault current. (c) Developed torque. (d) Motor speed. ....	197
Figure 8.12: Simulation results of soft-starting performance of present topology for 15-Hz operation at full-load (8.169 Nm) condition. (a) Motor phase current. (b) Torque. (c) Speed. ....	200
Figure 8.13: Simulation results of soft-starting performance of present topology for 15-Hz operation at half-load (4.084 Nm) condition. (a) Motor phase current. (b) Torque. (c) Speed. ....	201
Figure 8.14: Simulation results of soft-starting performance of present topology for 12-Hz operation at full-load (8.169 Nm) condition. (a) Motor phase current. (b) Torque. (c) Speed. ....	202
Figure 8.15: Simulation results of soft-starting performance of present topology for 12-Hz operation at half-load (4.084 Nm) condition. (a) Motor phase current. (b) Torque. (c) Speed. ....	203
Figure 8.16: Schematic and specifications of induction motor-drive test setup system. ....	205
Figure 8.17: Test rigs. (a) PWM drive and quasi-cycloconverter power topology. (b) Induction motor and dynamometer. ....	206
Figure 8.18: Experimental results, 30-Hz operation. ....	208
Figure 8.19: Experimental results, 15-Hz operation. ....	208
Figure 8.20: Experimental results, 12-Hz operation. ....	208
Figure 8.21: Experimental results, 8.57-Hz operation. ....	209
Figure 8.22: Experimental results, 7.5-Hz operation. ....	209
Figure 8.23: Experimental results, 6-Hz operation. ....	209
Figure 8.24: Measured three-phase motor current waveforms at 15-Hz output frequency, 25% load condition under an inverter open-circuit switch fault at $S_I$ . ....	210
Figure 8.25: Experimental results of current space-vector locus at 15-Hz, 25% load condition. ....	211
Figure 8.26: “Limp-home” motor performance of measured phase currents at 15-Hz, 25% load condition in the event of an inverter open-circuit switch fault at $S_I$ . ....	212
Figure 8.27: Experimental results of post-fault limp-home motor performance for 15-Hz operation at full-load condition. (a) Motor phase current. (b) Motor phase voltage. (c) Motor developed torque. ....	214
Figure 8.28: Experimental results of post-fault limp-home motor performance for 15-Hz operation at half-load condition. (a) Motor phase current. (b) Motor phase voltage. (c) Motor developed torque. ....	215
Figure 8.29: Steady-state “zoom” form of the simulation results of Figure 8.12 for 15-Hz operation at full-load (8.169 Nm) condition. (a) Motor phase current. (b) Torque. ....	216

Figure 8.30: Steady-state “zoom” form of the simulation results of Figure 8.13 for 15-Hz operation at half-load (4.084 Nm) condition. (a) Motor phase current. (b) Torque. ....	217
Figure 8.31: Experimental results of post-fault limp-home motor performance for 12-Hz operation at full-load condition. (a) Motor phase current. (b) Motor phase voltage. (c) Motor developed torque.....	218
Figure 8.32: Experimental results of post-fault limp-home motor performance for 12-Hz operation at half-load condition. (a) Motor phase current. (b) Motor phase voltage. (c) Motor developed torque.....	219
Figure 8.33: Steady-state “zoom” form of the simulation results of Figure 8.14 for 12-Hz operation at full-load (8.169 Nm) condition. (a) Motor phase current. (b) Torque. ....	220
Figure 8.34: Steady-state “zoom” form of the simulation results of Figure 8.15 for 12-Hz operation at half-load (4.084 Nm) condition. (a) Motor phase current. (b) Torque. ....	221
Figure 8.35: Experimental results of soft-starting performance of present topology for 15-Hz operation at 25% load (~ 2 Nm) condition. (a) Motor phase current. (b) Motor developed torque. ....	223
Figure 8.36: Simulation results of torque-ripple percentage of full-load torque at different load levels. ....	225
Figure 8.37: Torque-ripple percentage of full-load torque versus load torque at different output motor frequencies. (a) 30-Hz operation. (b) 15-Hz operation. (c) 12-Hz operation. ....	227
Figure 8.38: RMS value of motor phase currents versus load torque at different output motor frequencies. (a) 30-Hz operation. (b) 15-Hz operation. (c) 12-Hz operation.....	228
Figure A.1: Photos of the overall system. (a) Power electronic circuit. (b) Motor-load system. ....	252
Figure A.2: Schematic and specifications of induction motor-soft starter test setup system.....	253
Figure A.3: Schematic and specifications of induction motor-drive test setup system. ....	254
Figure A.4: Datasheets of 2-hp induction motor. (a) Performance data. (b) Performance curves. ....	258
Figure A.5: Three-phase SCR bridge. (a) Digital photo. (b) A drawing of the SCR bridge with terminal labels. (c) Circuit diagram with wiring labels.....	260
Figure A.6: Gate drive of the SCR bridge. (a) Digital Photo. (b) Circuit diagram.....	261
Figure A.7: Digital photo of the RC snubber circuits ( $R = 57\Omega$ and $C = 112\text{pF}$ ). ....	261
Figure A.8: Photos of the PWM drive. (a) Drive and precharge device. (b) Closed-up view. .	263
Figure A.9: Gate drive of the inverter bridge. (a) A drawing of the gate drive. (b) Primary side connection diagram. (c) Secondary side connection diagram. ....	263
Figure A.10: Opto-coupler. (a) Block diagram. (b) Circuit diagram ( $\text{GND}_{5\text{V}}$ is tied to $\text{GND}_{15\text{V}}$ ). ....	264
Figure A.11: DSP controller board. ....	264

- 
- Figure A.12: Signal conditioning board #1. (a) Digital photo. (b) Voltage circuit. (c) 1.5Volt dc-offset circuit. (d) A/D calibration circuit. (e) Speed circuit..... 266
- Figure A.13: Signal conditioning board #2. (a) Digital photo. (b) Voltage circuit. (c) Current circuit. (d) 1.5Volt dc-offset circuit..... 268

# List of Tables

Table 1.1: Percentage of component failures in ASD [34].	3
Table 1.2: Percentage of component failures in switch-mode power supply [35], [85].	3
Table 2.1: Harmonic contents of healthy three-phase motor phase voltages obtained from analytical solution.	34
Table 2.2: Harmonic contents of healthy three-phase motor currents obtained from analytical solution.	37
Table 2.3: Analytical solution of RMS values of healthy three-phase stator currents during the soft starting transient period.	38
Table 2.4: Harmonic contents of three-phase motor phase voltages obtained from analytical solution under a short-circuit SCR fault.	42
Table 2.5: Harmonic contents of three-phase motor currents obtained from analytical solution under a short-circuit SCR fault.	43
Table 2.6: Analytical solution of RMS values of three-phase stator currents under a short-circuit SCR fault during the soft starting transient period.	44
Table 4.1: Design properties of 2-hp induction motor.	77
Table 4.2: Utility grid input parameters.	77
Table 4.3: Harmonic contents of healthy three-phase motor phase voltages – Analytical and Simulation.	83
Table 4.4: Harmonic contents of healthy three-phase motor currents – Analytical and Simulation.	83
Table 4.5: Harmonic contents of three-phase motor phase voltages under a short-circuit SCR fault – Analytical and Simulation.	88
Table 4.6: Harmonic contents of three-phase motor currents under a short-circuit SCR fault – Analytical and Simulation.	88
Table 5.1: Specifications of hardware prototype.	100
Table 5.2: Harmonic contents of healthy three-phase motor phase voltages – Test, Simulation, and Analytical.	106
Table 5.3: Harmonic contents of healthy three-phase motor currents – Test, Simulation, and Analytical.	106
Table 5.4: Harmonic contents of three-phase motor phase voltages under a short-circuit SCR fault – Test, Simulation, and Analytical.	109
Table 5.5: Harmonic contents of three-phase motor currents under a short-circuit SCR fault – Test, Simulation, and Analytical.	109
Table 6.1: Simulation conditions of induction motor-drive system.	135

---

Table 6.2: Harmonic contents of motor phase voltages under short-circuit switch fault condition – Analytical and Simulation .....	140
Table 6.3: Harmonic contents of motor phase currents under short-circuit switch fault condition – Analytical and Simulation .....	140
Table 8.1: Simulation conditions of induction motor-drive system.....	184
Table 8.2: Simulation results of harmonic contents of motor phase voltage and current during post-fault limp-home at 30-Hz operation under full-load (8.169 Nm) condition. ....	195
Table 8.3: Simulation results of harmonic contents of motor phase voltage and current during post-fault limp-home at 15-Hz operation under full-load (8.169 Nm) condition. ....	197
Table 8.4: Simulation results of torque pulsations during pre- and post-fault “limp-home” conditions at full-load (8.169 Nm). .....	198
Table 8.5: Simulation results of steady-state motor performance under full-load and half-load conditions for 15-Hz and 12-Hz motor operations. ....	204
Table 8.6: Comparisons between simulation and experimental results for the case of 15-Hz and 12-Hz motor operations. ....	222
Table A.1: Design specifications of 2-hp induction motor. ....	256
Table A.2: Specifications of TI DSP board. ....	262
Table A.3: Features of NI DAQ system.....	269

# CHAPTER 1

---

---

## INTRODUCTION

---

---

### 1.1 Motivation behind This Work

Polyphase induction motors have been the workhorse (main prime movers) for industrial and manufacturing processes as well as numerous propulsion applications [1]. The energization of such motors in these processes and applications can be achieved through the following ways: (1) direct across-the-line starting, (2) soft-starting, and (3) adjustable-speed drive (ASD) control. It is well-known that direct across-the-line starting of induction motors, which offers absolutely no control capability, is characterized by high starting inrush currents and high starting torque pulsations [2]. In certain applications such as conveyor belt drives, these high starting torque pulsations may result in belt slippage, which consequently may lead to undesirable damage to motor-load systems. Frequent direct across-the-line motor starting may introduce significant electrical and thermal stresses on motor bearings and winding components including insulation, heating in motor windings, as well as mechanical stresses on motor cages, shafts and load couplings. The adverse effects due to such stresses on motors may result in undesirable consequences such as squirrel-cage bar breakages, stator winding damage, and inter-turn short-circuit faults, which may lead to catastrophic failures in motors [3].

Accordingly, reduced voltage starters, or the so-called soft starters, are often employed as effective means to reduce high starting currents and torque pulsations through use of thyristor based voltage control [4]-[33]. Likewise, modern PWM-ASDs, which can be considered as an alternative means to soft starting a motor, are also widely adopted in many industrial applications. In fact, the main reasons for their adoption in these applications are owed to the robust control and high performance quality that ASDs offer as compared to soft starters. Nevertheless, using soft starters for reducing high starting currents is a low cost means in comparison to modern ASDs if speed-torque control is not required.

The widespread use of PWM-ASD and soft starter ac motor systems in numerous critical industrial, manufacturing, and transportation applications has escalated the importance and the significance of developing rigorous fault mitigation techniques or fault tolerant / “limp-home” capabilities for such types of systems. Such motor-ASD systems exist in numerous industrial and medical life support systems, electromechanical automation equipment, propulsion and actuation, as well as automotive/transportation, marine, and aerospace systems. On the other hand, motor-soft starter systems can be found in applications that involve systems such as fans, blowers, compressors, centrifugal pumps, elevators and escalators, assembly lines, transport and conveyor-belt systems, as well as heating, ventilation, and air conditioning (HVAC) systems. In these vital and critical applications, the reliability of both ASDs and soft starters is of paramount importance in ensuring a continuous, almost disturbance-free operation and a gentle, judder-free soft starting, respectively, under various possible faulty conditions. Accordingly, such fault tolerant capabilities will entail the reduction in maintenance costs, downtimes, and more importantly the avoidance of unnecessary ASD or soft starter failures, with their potential costly or even perhaps catastrophic consequences. Nevertheless, permanently reduced system performance for short operating times under faulty conditions are sometimes accepted as a compromise, given the fact

that the motor-drive (ASD or soft starter) system continues operating without causing any unnecessary disturbance to the critical load that it is driving.

Surveys on the probability of faults occurring in adjustable-speed drives as well as power electronic equipment such as switch-mode power supply had been conducted and are given in Table 1.1, see [34], and Table 1.2, see [35] and [85], respectively. As one can observe therein, the power semiconductor faults account for around 35% of all faults. In fact, this percentage can be higher if one were to take into account the control circuit faults given in Table 1.1. Such faults may be caused by inverter intermittent misfiring due to defects in control circuit elements or electromagnetic interference. Accordingly, this results in gate-drive open faults, and consequently leads to transistor open-circuit switch faults. Therefore, the need to develop fault-tolerant systems is highly desirable.

Table 1.1: Percentage of component failures in ASD [34].

<b>Major Components</b>	<b>% of Failures</b>
Power Converter Circuits	38
Control Circuits	53
External Auxiliaries	9

Table 1.2: Percentage of component failures in switch-mode power supply [35], [85].

<b>Major Components</b>	<b>% of Failures</b>
DC Link Capacitors	60
Power Transistors	31
Diodes	3
Others	6

Due to the major concern for the need to develop highly reliable and fault-tolerant adjustable speed ac motor-drive systems, extensive research has been dedicated towards this field. Parallel redundancy and conservative design techniques, which are considered as the straightforward solution, have been widely adopted by drive manufacturers to improve their immunity to faults, thereby maintaining the continuity of operation under a variety of faulty conditions. Despite the fact that multiphase (more than three phases) PWM drives [36]-[44], as a means of system redundancy, provide acceptable fault tolerant capability by ensuring a continuous and almost disturbance free operation, the tradeoff lies in the increased system cost and size of such systems.

In order to minimize the cost as a consequence of system redundancy, a lot of attention has been centered on developing intelligent fault mitigation control methods, along with the appropriate hardware modifications to the conventional three-phase adjustable-speed PWM drives [36], [44]-[59], [86]. To further explore the possibility of cost reduction, various reduced-switch-count converter topologies for three-phase ac motor-drive systems have been developed with high reliability due to the reduced number of power switching components [60]-[70]. Other converter topology designs such as matrix converters [71]-[73] or multilevel PWM inverters [74], [75] for three-phase ac motor-drive systems have also been introduced with fault tolerant capability for transistor/switch faults.

Two common types of drive power converter faults that were investigated in [36], [38]-[59], [83], [86] are inverter transistor short-circuit switch-fault ( $F_1$ ) and inverter transistor gate-drive open-circuit fault, that is transistor open-circuit switch-fault ( $F_2$ ), and as depicted in Figure 1.1. A transistor short-circuit switch fault ( $F_1$ ) can lead to catastrophic failure of the drive if the complementary transistor of the same inverter leg is turned-on, resulting in a shoot-through or direct short-circuit of the dc-bus link [83]. Conversely, for a transistor open-circuit switch fault ( $F_2$ ), the drive may still function but at a much inferior performance due to the resulting significant torque pulsations introduced by the consequent asymmetry in the circuit of the motor-

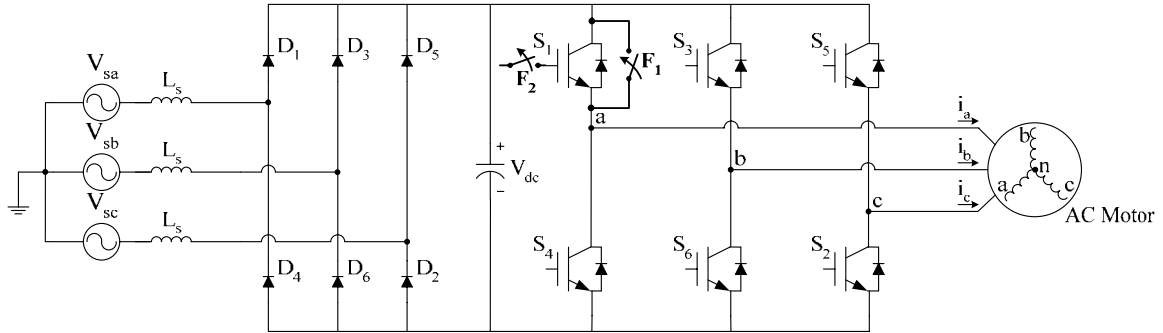


Figure 1.1: Types of inverter switch failure modes under investigation.

drive system and the resulting unipolar nature of one of the motor phase currents [83]. Therefore, a drive fault diagnostic approach is a crucial step in determining the type of fault so that appropriate remedial action can be taken to mitigate the fault at hand. It is important to mention that diagnosis of drive-related faults is not part of the scope of this work. This is due to the fact that various efficient and reliable diagnostic methods have already been conceived by other investigators in the technical literature [76]-[82]. A priori knowledge of the nature of the fault is assumed in this work, so that the proposed measure can be carried out immediately upon the occurrence of such a fault. Even though some of the fault-tolerant solutions presented in [36], [38]-[59], [86] promise the same rated motor performance in so far as the rated torque is concerned, there still exist some demerits in those methods, as will be discussed in detail later-on in this chapter.

On the other hand, to the knowledge of this investigator, no fault-tolerant soft starter has yet been conceived and documented in the technical literature. This may be due to the fact that the SCR/thyristor switch is much more reliable than the IGBT transistor switch because of the high voltage and high current properties that SCRs have [84]. Also, soft starters function at lower switching frequencies as compared to PWM drives. Nevertheless, a soft starter is still prone to failure at some point during the normal operation. Hence, it is crucial to incorporate fault tolerant

features into the existing off-the-shelf soft starter for continuing operation in the event of an SCR switch fault.

In light of the above, the notion of conceiving “limp-home” strategies for both the soft starter and adjustable-speed PWM drive serves as the main motivation factor behind this work, which accordingly led this investigator to pursue his research in this specific area. In fact, the major hurdle to overcome here is the challenge of developing such “limp-home” strategies at a minimum cost increase, and still provides acceptable/reasonable performance. Hence, the main thrust of this work is divided into two parts. The first part focuses on developing a fault-tolerant soft starter based on a novel resilient closed-loop control scheme. The present closed-loop control technique can be employed in conventional three-phase soft starters to enhance the reliability and fault tolerant capability of such soft starter topologies. In the event of a thyristor/SCR open-circuit or short-circuit switch-fault in any one of the phases, the soft starter controller can switch from a conventional open-loop three-phase control scheme to a closed-loop two-phase control mode of operation. The second part of this work is to develop a low-cost adaptive control mitigation or “self-healing/limp-home” strategy for the inverter faults of Figure 1.1 with minimum redundancy. In effect, the proposed approach offers the potential of mitigating any other drive-related faults such as a diode-rectifier short-circuit fault or a dc-link capacitor fault. Furthermore, the present fault mitigation technique requires only minimum hardware modifications to the conventional off-the-shelf six-switch three-phase drives. Literature review covering the preceding research areas is presented next.

## 1.2 Literature Search Surveying Preceding Work

In this section, the various “limp-home” strategies for three-phase ac motor-drive systems under inverter switch faults are briefly reviewed. A categorization of the various “limp-home”

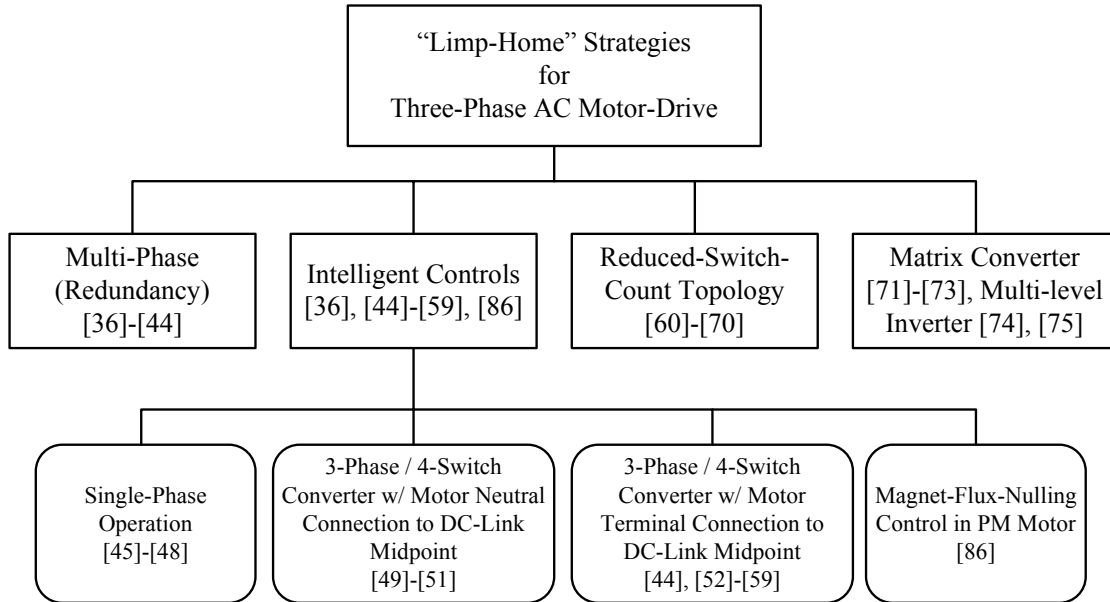
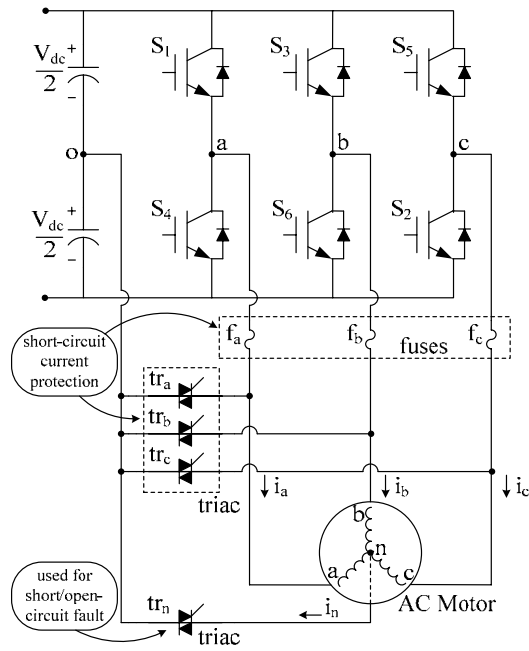


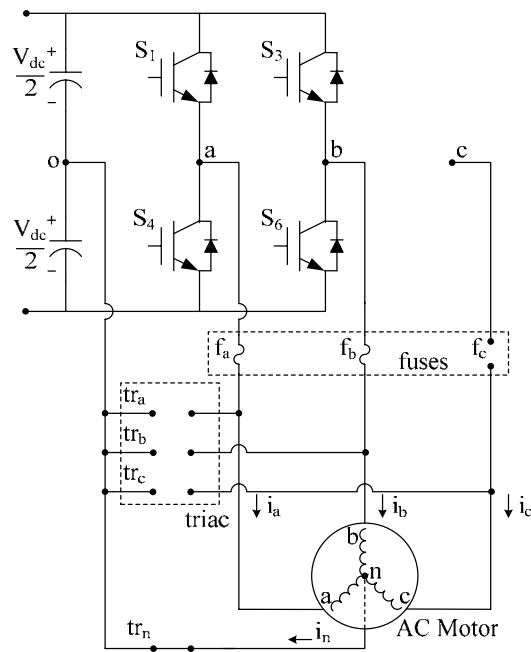
Figure 1.2: Categorization of various “limp-home” strategies for three-phase ac motor-drives.

strategies for three-phase ac motor drives is illustrated in Figure 1.2. It is important to mention that since the goal of this work is to develop fault-tolerant strategies for the standard three-phase adjustable-speed drive, whose configuration is shown in Figure 1.1, only fault-tolerant strategies that are associated with that configuration of Figure 1.1 are being considered and discussed here.

The fault-tolerant inverter topology to be discussed first was proposed by Liu et al. [49], whose configuration is depicted in Figure 1.3. It is based on modifying the post-fault control strategy with the connection of the motor neutral to the mid-point of the split dc-bus capacitor link of the drive. This topology is capable of mitigating both a transistor open-circuit and short-circuit switch fault. It utilizes a conventional three-phase drive with the addition of four triacs or back-to-back connected SCRs, as well as three fast-acting fuses connected in series with the motor. The motor neutral is connected to the mid-point of the split dc-link through a triac,  $tr_n$ . The reason for having the other three triacs, namely,  $tr_a$ ,  $tr_b$ , and  $tr_c$ , as well as the three fuses,  $f_a$ ,  $f_b$ , and  $f_c$ , is for fault isolation purposes [51]. A similar topology capable of mitigating only transistor open-circuit switch faults was proposed by Elch-Heb et al. [50], except without the incorporation



(a) Pre-fault configuration.



(b) Post-fault configuration.

Figure 1.3: Fault-tolerant inverter topology by Liu et al. [49] and Elch-Heb et al. [50].

of the three fuses and the three triacs, namely,  $tr_a$ ,  $tr_b$ , and  $tr_c$ , in the circuit.

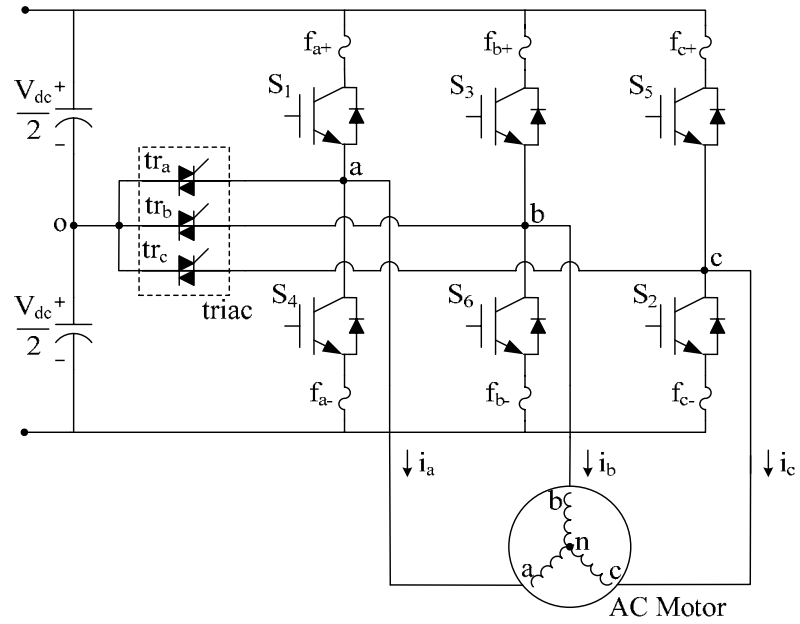
In the pre-fault operation, all triacs are turned-off and the motor-drive system functions in its normal condition. During the post-fault operation, the faulty inverter leg is first isolated using a fault isolation scheme described in [51]. The motor henceforth operates in a two-phase mode with its neutral point connected to the mid-point of the split dc-link by turning-on the triac,  $tr_n$ . The need for the motor neutral point connection is to allow the individual control of the amplitude and phase of the currents in the remaining two healthy phases. In order to maintain the rated motor performance and the same torque production, the currents in the remaining two healthy phases need to be regulated to a magnitude of  $\sqrt{3}$  times their original value, and phase-shifted by  $60^\circ$  with respect to each other. It had been shown that this post-fault control method allows the motor to maintain its normal three-phase performance.

Despite the fact that this fault-tolerant topology ensures the same rated motor performance, there still exist some demerits associated with this method. One drawback is the required accessibility to the motor neutral, which is normally not provided by motor manufacturers except by special request. Also, this method would not be applicable to delta-connected motors. A second drawback is associated with the necessary increase in the fundamental rms motor phase current magnitude in the healthy phases under faulty conditions. This implies that the drive and the motor have to be overrated to withstand this higher level of current for at least a significant period of time. Also, the neutral current is no longer zero. It is comprised of the sum of the currents in the remaining two healthy phases, which results in three times the value of the original phase current during the healthy operation mode. This poses a third drawback owing to the presence of single-phase circulating neutral current through the dc-bus capacitors. This circulating neutral current may cause severe voltage fluctuations that may degrade the performance of the drive in the form of increased winding ohmic losses and motor torque

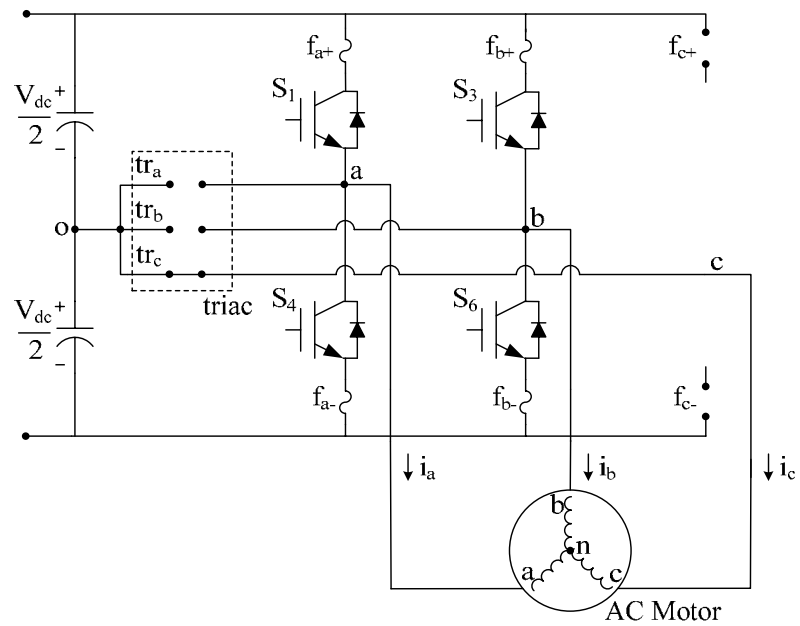
ripples/pulsations. Hence, a larger size dc capacitor is required to sustain the desired voltage level and minimize the dc voltage ripples.

The second fault-tolerant inverter topology to be discussed next was first proposed by Van Der Broeck et al. [52], who named this topology as the “B4 bridge”. His intention was to operate the three-phase induction motor using a component-minimized voltage-fed inverter bridge with only four switching devices. This idea was later adopted by Ribeiro et al. [44], who used it for fault tolerant purposes in a standard six-switch three-phase inverter drive. This configuration of which is depicted in Figure 1.4. This fault-tolerant topology is based on connecting the terminals of the motor to the mid-point of the split dc-bus capacitor link through a set of triacs. This topology is capable of mitigating both a transistor open-circuit and short-circuit switch fault. Other investigators, such as Covic et al. [53], [54], and Blaabjerg et al. [55], [56], had also utilized the “B4” inverter topology with different types of PWM control schemes, in order to compensate for the dc-link voltage ripples as a result of this “B4” configuration.

In the healthy operation of the system in Figure 1.4, the triacs, namely,  $tr_a$ ,  $tr_b$ , and  $tr_c$ , are turned-off and the motor-drive system operates in its normal condition. During the post-fault operation, the faulty inverter leg is first isolated by means of fast-acting fuses, namely  $f_a$ ,  $f_b$ , or  $f_c$  [44]. Thereafter, the terminal of the motor corresponding to the faulty leg is connected to the center of the split dc-bus capacitor link by turning-on the triac of the associated faulty leg of the inverter. It has been reported in [52] and [44] that in order to maintain the rated three-phase motor performance, the dc-bus voltage should be doubled which can be realized through using either a controlled rectifier at the drive front-end or a dc-dc boost converter. Along with that, the motor phase voltages in the two phases, which are not connected to the center of the split dc-link, should be phase-shifted by  $60^\circ e$  with respect to each other. Another potential problem associated with this topology is the single-phase circulating current through the dc-bus capacitor, which may cause severe voltage variations and hence affect the system performance. Hence, an oversized dc



(a) Pre-fault configuration.

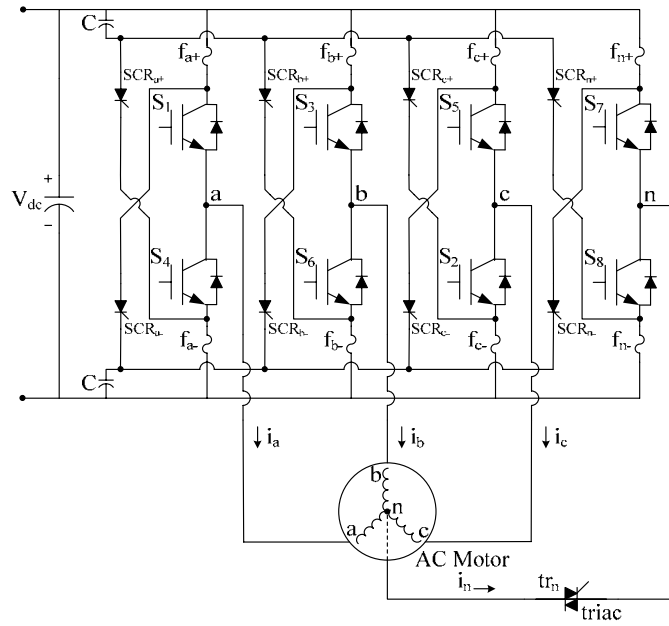


(b) Post-fault configuration.

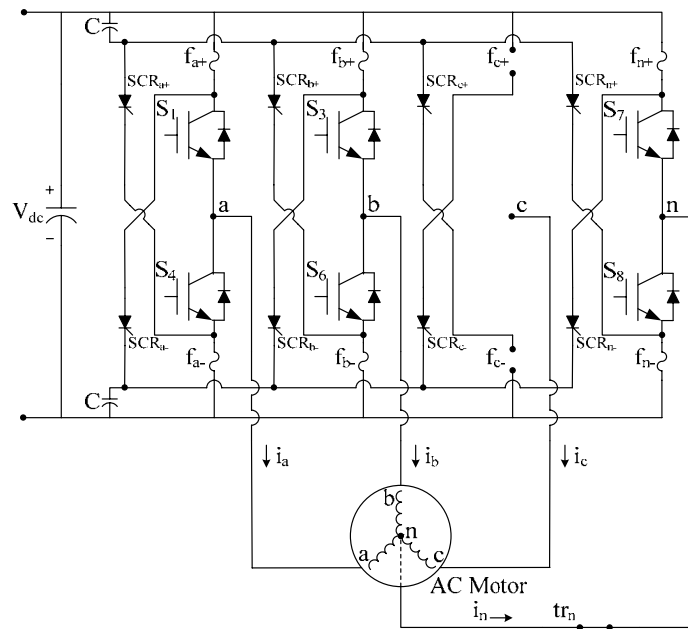
Figure 1.4: Fault-tolerant inverter topology by Van Der Broeck et al. [52] and Ribeiro et al. [44].

capacitor is needed to absorb this single-phase circulating current. Despite the reasonable performance exhibited by the fault-tolerant topologies of Figure 1.3 and Figure 1.4, some of the drawbacks may appear to be intolerable in some motor-drive applications.

The third fault-tolerant inverter topology to be discussed next is based on redundancy concepts which is proposed by Bolognani et al. [40] for permanent-magnet synchronous motor applications, and by Corrêa et al. [42] and Ribeiro et al. [44] for induction motor applications. The fault-tolerant inverter topologies, which were proposed by Bolognani et al. [40], are depicted in Figure 1.5 and Figure 1.6. The only difference in so far as drive configuration is concerned, as compared with that proposed by Corrêa et al. [42] and Ribeiro et al. [44], lies in the fault isolation scheme. Corrêa et al. [42] did not have any fault isolation capability in their topology since it is only intended for mitigating a transistor open-circuit switch fault, while Ribeiro et al. [44] proposed using two fast-acting fuses for each inverter leg that is equivalent to the fault isolation scheme as depicted in Figure 1.4. It is important to mention that the topologies of Figure 1.5 and Figure 1.6 are capable of providing fault tolerance to a transistor open-circuit or short circuit switch fault. The operations of the topologies of Figure 1.5 and Figure 1.6 are straightforward. When either a transistor open-circuit or short-circuit switch fault has been detected and diagnosed, the faulty transistor switch will be first isolated, and the fourth inverter leg will be activated for usage by turning-on the associated triac. In the case of the topology of Figure 1.6, since all three phases of the motor are connected to the inverter during the pre- and post-fault operations, the current amplitude in each of the phases remains the same in order to ensure a smooth torque production. However, for the topology of Figure 1.5, since only two motor phases and the motor neutral are connected to the inverter, the fundamental rms current amplitudes in the motor phases are increased by a factor of  $\sqrt{3}$  in order to maintain the same rated motor performance. This is equivalent to the post-fault operating condition of the topology given in Figure 1.3. Furthermore, the fault-tolerant inverter topologies of Figure 1.5 and Figure 1.6

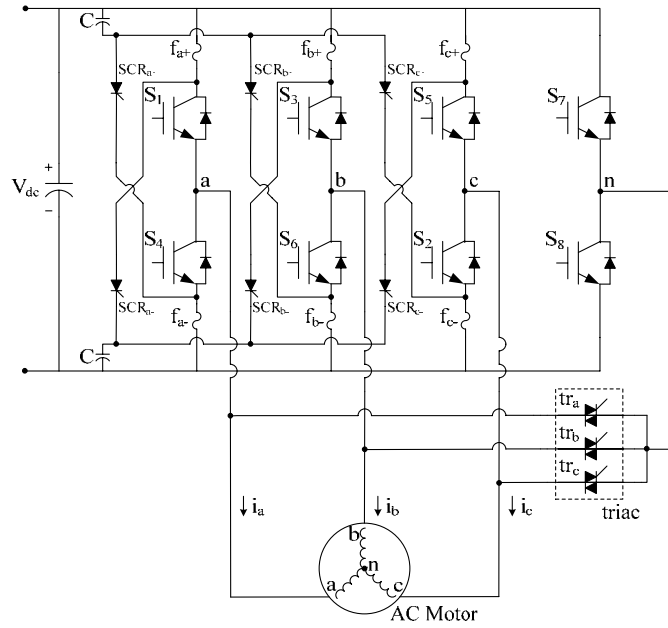


(a) Pre-fault configuration.

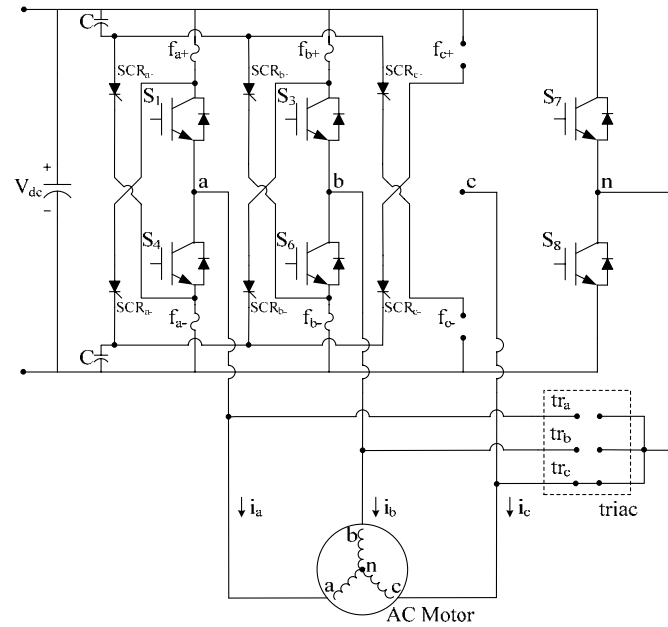


(b) Post-fault configuration.

Figure 1.5: First fault-tolerant inverter topology by Bolognani et al. [40].



(a) Pre-fault configuration.



(b) Post-fault configuration.

Figure 1.6: Second fault-tolerant inverter topology by Bolognani et al. [40].

involve too many circuit components for the fault isolation scheme, which presents a drawback for these methods.

Meanwhile, other investigators, such as Elch-Heb et al. [45] and Kastha et al. [46]-[48], had proposed in their work to operate the three-phase induction motor-drive system in a single-phase mode, in the event of an inverter switch fault. Due to the single-phase motor operation, a pulsating torque at the line current frequency is generated. In order to minimize this torque pulsation, Kastha et al. [46]-[48] proposed injecting odd harmonic voltages at the appropriate phase angles into the motor terminal voltages. This is in order to neutralize the lower-order harmonic pulsating torques by shifting these pulsating torque frequencies to the higher range in the frequency spectrum so that the machine's inertia can filter them substantially and permit satisfactory operation with variable frequency. However, the drawback of this method is its complexity of implementation which requires exact computation of the phase angles of the injected harmonic voltages. Any error in the computation process will result in severe torque pulsation.

Recently, Welchko et al. [86] presented a control method to null the magnet flux in the short-circuited phase of an interior permanent-magnet motor following short-circuit faults in either the inverter drive or the motor stator windings. This was carried out by purposely introducing a zero-sequence current through the phase-current regulators to suppress the current induced in the faulted/shorted phase. However, the downside of the proposed method is the need to increase the currents in the remaining healthy phases by a factor of  $\sqrt{3}$ . Also, for the zero-sequence current to be possible, this requires that each phase of the motor three-phase winding be driven by an H-bridge inverter or, alternatively, employing a six-leg inverter. Such measures will increase the cost of the overall motor-drive system.

In summary, a brief overview of the existing "limp-home" strategies for three-phase ac motor-drive systems has been presented. These methods have their own merits and drawbacks. In

spite of the fact that these methods promise rated motor performance in the event of a switch fault, some of their drawbacks may be intolerable or undesirable in some applications or operating conditions. Again, it should be mentioned that no “limp-home” strategy for the case of soft-starter has yet be conceived and reported in the literature, which makes the work of this dissertation a contribution in this particular area. The objectives and contributions of this dissertation are presented next.

### 1.3 Objectives and Contributions

For fault-tolerant soft starter and adjustable-speed drives to be practical and feasible, both hardware and software must be developed to perform the following tasks: (1) fault detection, (2) fault diagnosis, (3) fault isolation, and (4) remedial action. It is essential to carry out this sequence in the minimum possible time after the onset of a fault, in order to avoid the occurrence of secondary failures. Since fault detection and fault diagnosis of inverter switch faults had already been developed by other investigators [76]-[82], which proved to be simple, efficient, and reliable, the work of this nature lies outside the scope of this dissertation. As for the fault isolation measure, the fault protection system present in off-the-shelf drives is sensitive enough to shut down the complete drive, in the event of a severe fault such as a short-circuit in the transistor switch.

On the other hand, faults occurring in soft starters do not cause immediate permanent damage to the motor-soft starter system. However, the impact of a fault on both the soft starter and the motor will gradually evolve into a severe/damaging stage if the fault is left unattended. Therefore, by monitoring the behavior of the three-phase currents during starting, one could detect and diagnose the type of switch fault. Hence, the core of this dissertation is centered on

developing “limp-home” strategies for both the soft starters and the standard adjustable-speed PWM drives.

Accordingly, the contributions made in this dissertation can be summarized as follows:

1. A closed-form analytical solution is conceived to investigate the transient performance of induction motors during soft starting when experiencing thyristor/SCR switch faults. The two distinct types of failure modes under investigation in this work are: (1) short-circuit SCR fault, and (2) open-circuit SCR fault, which occur only in one phase of the soft starter.
2. A low-cost fault-tolerant approach capable of mitigating SCR open-circuit and short-circuit switch faults for soft starters has been conceived. The conceived approach can be easily retrofitted into the existing commercially-available soft starter with only minimum hardware modifications. Hence, this makes the conceived approach an attractive and feasible means as a potential fault-tolerant solution.
3. An investigation of the impact of inverter switch failure on machine performance is carried out using the averaged switching function modeling concept. Such approach provides a constructive analytical understanding of the extent of these fault effects. Meanwhile, time-domain simulation studies, in parallel with the analytical approach, are also employed to solidify the conclusive outcomes resulting from this study. The two distinct types of inverter transistor switch failure modes under investigation in this work are: (1) a transistor short-circuit switch fault, and (2) a transistor open-circuit switch fault.
4. A low-cost fault-tolerant strategy, based on a quasi-cycloconverter-based topology and control, as a potential solution for overcoming the negative impact of inverter

switch fault on motor performance is conceived. The conceived approach requires minimum hardware modifications at a modest cost to the conventional off-the-shelf three-phase PWM drive, as compared to the existing fault-tolerant topologies proposed by others. In fact, the present approach is also capable of mitigating other drive-related faults that can potentially occur in the diode-rectifier bridge or the dc-link of the drive because of the fact that this approach bypasses the entire drive system, provided that such faults can be safely isolated.

## 1.4 Dissertation Organizations

Following this introduction chapter, this dissertation consists of eight additional chapters. Chapter 2 presents a closed-form analytical solution to study the impact of SCR switch fault of soft starter on the transient performance of the induction motor. The faults under study are SCR short-circuit or open-circuit switch fault occurring only in one phase of the soft starter.

Chapter 3 presents a fault-tolerant solution for mitigating SCR switch fault, while still providing reduced starting inrush currents and consequently reduced starting torque pulsations. This is carried out using a resilient two-phase closed-loop control scheme. In addition, small-signal modeling of the motor-soft starter controller system is developed in order to design the closed-loop control system.

Chapter 4 presents the simulation results of the performance of the fault-tolerant soft starter using the present approach. The simulation results under healthy and faulty conditions are compared with the closed-form analytical results of Chapter 2 to verify the accuracy and value of the analytical results. Harmonic comparisons are carried out for this verification effort.

Chapter 5 presents the experimental test results of the performance of the fault-tolerant soft starter. These test results are compared with both the simulation and analytical results for

validation/verification purposes. Harmonic comparisons are carried out for this verification effort. The test setup of the motor-soft starter system is described in this chapter.

Chapter 6 presents a study of the impact of inverter switch fault, open-circuit and short-circuit type, on the performance of an induction motor. This is carried out using averaged switching function concept. The analytical results are verified by time-domain simulations to solidify the outcomes resulting from this study.

Chapter 7 presents a fault-tolerant solution capable of mitigating inverter switch fault of an adjustable-speed drive. The topology and control algorithm of the present approach are described in detail. Merits and drawbacks of the present approach are also discussed in this chapter.

Chapter 8 presents the simulation and experimental results of the fault-tolerant solution proposed in Chapter 7. Application considerations and opportunities for practical use of the present fault tolerant design are discussed.

Chapter 9, the final chapter of this dissertation, provides a summary of this research work along with some conclusion regarding the significance of the contributions contained in this dissertation. Recommendations for future work to be done are also suggested and discussed.

## 1.5 Summary

In this chapter, the motivation factor which leads to the completion of this work was presented. The problem statement describing the importance of this work towards many industrial applications was also presented. A literature review of the preceding work in the areas of fault-tolerant strategies in adjustable-speed drives was discussed in detail. Finally, the objectives and contributions of this work were summarized, followed by the organization of this dissertation.

## CHAPTER 2

---

---

# TRANSIENT ANALYSIS OF INDUCTION MOTOR-SOFT STARTER

---

---

### 2.1 Introduction

A closed-form solution is presented for the transient performance of induction motors during soft starting when experiencing thyristor/SCR switch faults. Two distinct types of failure modes under investigation in this work are: (1) short-circuit SCR fault, and (2) open-circuit SCR fault, which occur only in one phase of the soft starter. To this author's knowledge, no such analytical work has yet been reported in the technical literature to investigate the impact of switch faults of soft starters on motor performance. It is shown here in this chapter that the use of the conventional open-loop symmetrical-triggering control of the soft starter under faulty condition produces undesired fault response in the machine performance. Closed-form analytical expressions during soft starting transients under healthy and faulty conditions are developed and detailed here. Analytical results along with the corresponding harmonic breakdowns are also set forth in this chapter.

## 2.2 Soft Starters

As mentioned earlier in the previous chapter, soft starter technology is widely employed as effective and low-cost means, as compared to modern PWM adjustable-speed drives, to reduce high starting currents and torque pulsations of medium voltage and large ac motors in numerous critical industrial, manufacturing, and transportation applications through use of thyristor-based voltage control [17]-[33]. The circuit topology and its control scheme are simple and easy to implement, which will be described in the following subsection.

### 2.2.1 Topology

A circuit configuration of the conventional three-phase soft starter is depicted in Figure 2.1. It comprises of a set of back-to-back connected thyristors/SCRs (A1, A2, B1, B2, C1, C2) in series with each phase of the motor's stator phase windings, respectively. Snubbers consisting of series-connected resistors and capacitors are connected in parallel in the circuit to reduce the switching transients. In addition, in commercially available soft starters, a three-phase bypass contactor is usually connected in parallel with the back-to-back thyristors of each phase [31]-[33]. The purpose of this three-phase contactor is to reduce any further thermal stress and power loss imposed on these thyristors after completion of the starting transient of the motor. That is, when the motor reaches its full speed and rated current, the contactor will be "pulled-in" to bypass these thyristors. During this time, all the thyristors will be in their "turned-off" state and the motor will be directly energized from the grid through the bypass contactors.

The controller for the soft starter usually involves using a digital signal processor (DSP) board for programming the control switching algorithm of the SCRs. Pulse transformers are usually utilized as the gate driver for sending the gate pulses to the SCRs, as well as providing electrical galvanic isolations between the DSP board and the SCRs. Besides that, voltage and

current sensors are incorporated in the soft starter for sensing the utility mains voltages and line currents. The inclusion of these sensors serves two purposes. The first purpose is to detect the zero crossings of either the voltages or the currents using a phase-lock loop (PLL), depending on what type of soft starter control scheme is used. The second purpose serves to protect the soft starter against any voltage or current instabilities such as undervoltages or overcurrents.

### 2.2.2 Principles of Operations

In principle, reducing the impressed voltage upon the motor during starting reduces the starting current and torque pulsations. This is due to the fact that the starting torque or locked rotor torque is approximately proportional to the square of the starting current or locked rotor current, and consequently it is proportional to the square of the starting voltage [22]. Therefore, by properly adjusting the applied effective voltage during startup, the locked rotor torque and current can be reduced.

The most common control strategy employed by the soft starter of Figure 2.1 is the open-loop voltage control. Such control approach is widely adopted in commercially available soft starters, as well as soft starter designs reported in the literature [17]-[33]. The voltage control is implemented by adjusting either the delay angle,  $\alpha$ , or the hold-off angle,  $\gamma$ , of the conduction cycle of the oncoming thyristor with respect to either the zero crossing of the supply voltage ( $\alpha$ ) or the zero crossing of the line current ( $\gamma$ ), respectively, as shown in Figure 2.2. The thyristors are then selectively fired to conduct current in the appropriate phase, and naturally commutate off when the current reaches zero. The larger the delay angle,  $\alpha$ , or the hold-off angle,  $\gamma$ , the larger the notch width in the applied motor voltage, which consequently reduces the effective or RMS value of such voltage impressed upon the motor. However, improper control of the  $\alpha$  or  $\gamma$  firing angles may result in relatively high starting torque and current oscillations. Therefore, optimum starting profiles of the  $\alpha$  or  $\gamma$  firing angles have been extensively investigated to produce smooth

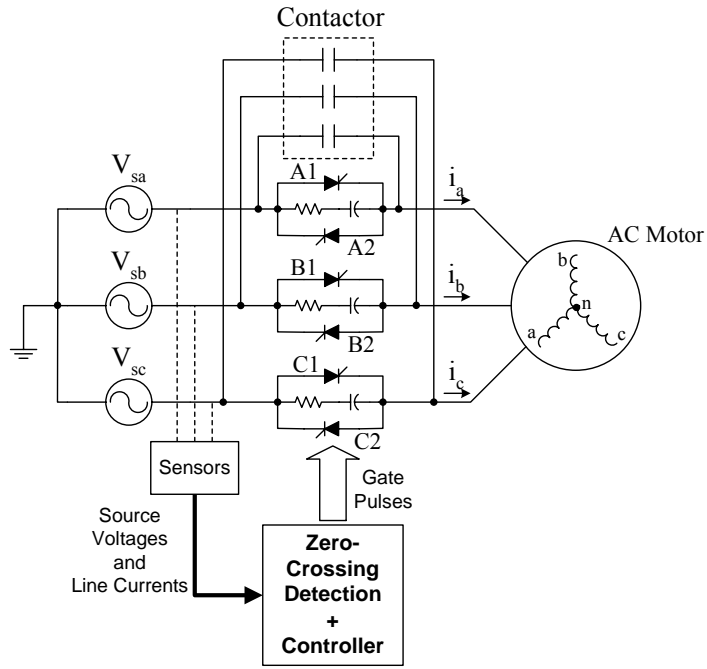


Figure 2.1: Conventional three-phase soft starter topology.

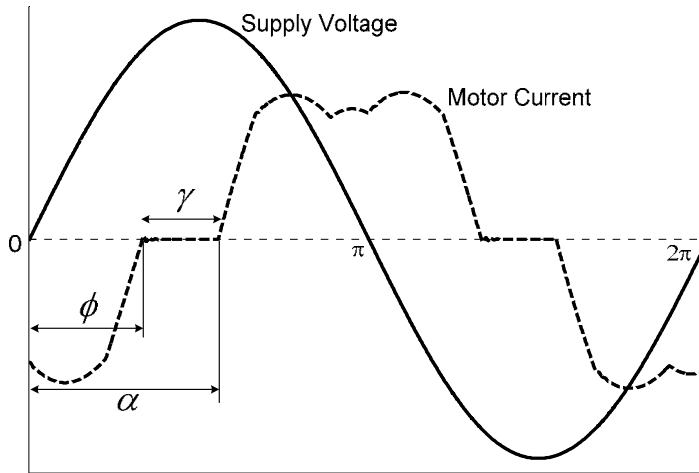


Figure 2.2: Definitions of firing angles.

starting torque and current profiles [17]-[30].

In order to obtain good dynamic characteristics, a symmetrical-triggering firing pulse sequence is necessary. Due to the fact that the thyristor is a half-controlled device, its firing pulse must be synchronized with the ac mains. The six thyristors will be turned on with the proper sequence, and the firing signal is in phase with the zero-crossing of the supply voltage. Since there is an inherent delay associated with a thyristor turn-off, the input current of the motor is not continuous, which results in time harmonics in the machine airgap flux. These generated harmonics are generally odd order harmonic terms.

In the commercially available soft starters, this firing angle profile is preset by the user based on the initial setting of the locked-rotor torque (LRT) and the ramp time, a simple illustration of which is shown in Figure 2.3. The LRT is the initial starting torque that is required to accelerate the motor during starting, and the ramp time is the time it takes for the voltage to go from the initial voltage value at the LRT setting to the maximum full voltage that is being applied to the motor. By adjusting the ramp time, the acceleration time of the motor can be controlled. Accordingly, the firing angle, which controls the amount of applied motor voltage, is reduced gradually depending on the ramp time during the period of starting until the motor has reached its full speed and rated current, whereupon the contactors are closed to bypass the thyristors. Evidently, such predetermined  $\alpha$  or  $\gamma$  firing angle control offers very limited control flexibility. It should be noted from Figure 2.2 that the phase angle,  $\phi$ , is related to the delay angle,  $\alpha$ , and the hold-off angle,  $\gamma$ , by the following relationship:

$$\phi = \alpha - \gamma \quad (2.1)$$

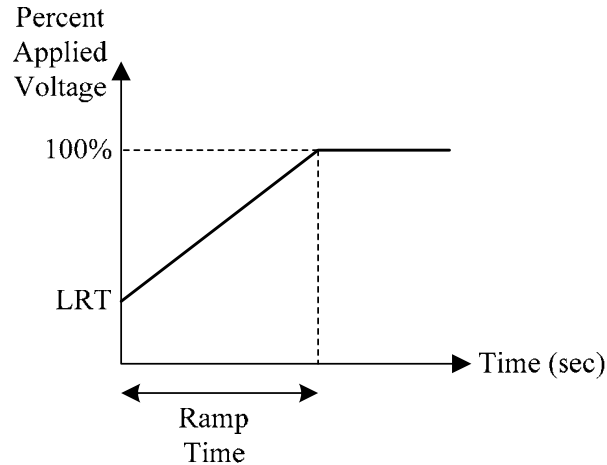


Figure 2.3: Voltage ramp profiles.

## 2.3 Closed-Form Derivation

In this section, the development and derivation of the closed-form solution of the soft starter performance under healthy condition are detailed. The process of formulating a closed-form solution is divided into two parts. The first part involves the derivation of the closed-form expression for the non-sinusoidal phase voltages that are impressed upon the motor windings. The second part involves using the T-equivalent circuit model to obtain the motor phase currents for the fundamental voltage term and each subsequent harmonic voltage term. Superposition is then applied to express the resulting motor phase currents in a Fourier series form.

### 2.3.1 Closed-Form Expressions of Motor Phase Voltages

Equivalent circuits representing the three-phase system of Figure 2.1 for both the 3-phase and 2-phase conduction modes are depicted in Figure 2.4(a) and Figure 2.4(b), respectively. Therein, the motor is represented as a combination of  $RL$  elements and induced back EMF sources. To evaluate the motor voltage of each phase, two cases are considered.

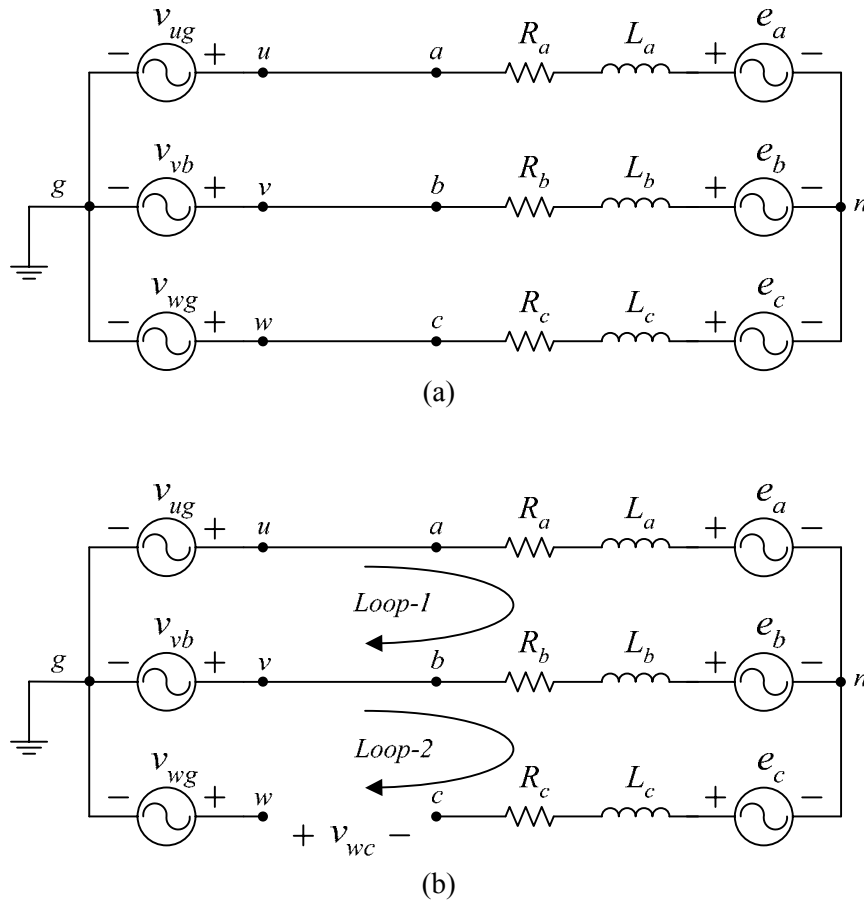


Figure 2.4: (a) 3-phase conduction mode. (b) 2-phase conduction mode.

### Case (I): All 3-phases are conducting currents

Referring to Figure 2.4(a), the motor terminal voltages measured *w.r.t.* ground are the same as the supply voltages, which can be expressed as follows:

$$\begin{aligned}
 v_{ag} &= v_{ug} \\
 v_{bg} &= v_{vg} \\
 v_{cg} &= v_{wg}
 \end{aligned}
 \tag{2.2}$$

Reference should be made to Figure 2.4(a) and Figure 2.4(b) with regard to the subscripts above.

One can also express the motor terminal voltages as the sum of the phase voltages and the neutral voltage, as follows:

$$\begin{aligned}
 v_{ag} &= v_{an} + v_{ng} \\
 v_{bg} &= v_{bn} + v_{ng} \\
 v_{cg} &= v_{cn} + v_{ng}
 \end{aligned} \tag{2.3}$$

Substituting (2.2) into (2.3), and summing the left-hand and right-hand side of the above expression yields the following:

$$v_{ug} + v_{vg} + v_{wg} = v_{an} + v_{bn} + v_{cn} + 3v_{ng} \tag{2.4}$$

For a balanced 3-phase supply and a balanced motor,  $v_{ug} + v_{vg} + v_{wg} = 0$  and  $v_{an} + v_{bn} + v_{cn} = 0$ , which implies  $v_{ng} = 0$ . Accordingly, from (2.2) and (2.3), the motor phase voltages are identical to the supply voltages when all 3-phases are conducting, that is:

$$\begin{aligned}
 v_{an} &= v_{ug} \\
 v_{bn} &= v_{vg} \\
 v_{cn} &= v_{wg}
 \end{aligned} \tag{2.5}$$

### Case (II): Only 2-phases are conducting currents

As may be observed from Figure 2.4(b), only phase-*a* and phase-*b* are conducting currents, while the SCRs of phase-*c* are turned-off. Applying Kirchhoff's Voltage Law in loop-2, the voltage across the turned-off SCRs of phase-*c*,  $v_{wc}$ , is:

$$v_{wc} = v_{wg} - v_{vg} + v_{bn} - e_c \tag{2.6}$$

Note that  $v_{cn} = e_c$  since phase-*c* is not conducting any current. Applying KVL in loop-1, one obtains the following:

$$v_{an} - v_{bn} = v_{ug} - v_{vg} \tag{2.7}$$

For a balanced 3-phase motor,  $v_{an} = -v_{bn} - v_{cn} = -v_{bn} - e_c$ . Hence, one can rewrite (2.7), as follows:

$$v_{bn} = 1/2 \cdot (v_{vg} - v_{ug} - e_c) \quad (2.8)$$

Substituting (2.8) into (2.6) yields the following:

$$v_{wc} = 3/2 \cdot (v_{wg} - e_c) \quad (2.9)$$

From Figure 2.4(b), the motor phase-*c* terminal voltage,  $v_{cg}$ , can be defined as follows:

$$v_{cg} = v_{wg} - v_{wc} \quad (2.10)$$

By substituting (2.9) into (2.10), the motor terminal voltages *w.r.t.* ground, when only phase-*a* and phase-*b* are conducting, can be expressed in terms of the supply voltages and motor back EMF, as follows:

$$\begin{aligned} v_{ag} &= v_{ug} \\ v_{bg} &= v_{vg} \\ v_{cg} &= -(1/2)v_{wg} + (3/2)e_c \end{aligned} \quad (2.11)$$

Similarly, when only phase-*a* and phase-*c* are conducting, one can write:

$$\begin{aligned} v_{ag} &= v_{ug} \\ v_{bg} &= -(1/2)v_{vg} + (3/2)e_b \\ v_{cg} &= v_{wg} \end{aligned} \quad (2.12)$$

and when only phase-*b* and phase-*c* are conducting, one can write:

$$\begin{aligned} v_{ag} &= -(1/2)v_{ug} + (3/2)e_a \\ v_{bg} &= v_{vg} \\ v_{cg} &= v_{wg} \end{aligned} \quad (2.13)$$

In order to acquire the motor phase voltages, one can use (2.3) along with the fact that  $v_{ng} = 1/3 \cdot (v_{ag} + v_{bg} + v_{cg})$  to obtain the following expression:

$$\begin{bmatrix} v_{an} \\ v_{bn} \\ v_{cn} \end{bmatrix} = \begin{bmatrix} 2/3 & -1/3 & -1/3 \\ -1/3 & 2/3 & -1/3 \\ -1/3 & -1/3 & 2/3 \end{bmatrix} \cdot \begin{bmatrix} v_{ag} \\ v_{bg} \\ v_{cg} \end{bmatrix} \quad (2.14)$$

Using (2.11) through (2.14), the motor phase voltages under 2-phase conduction mode for all cases can be evaluated, as follows:

For phase-*a* and phase-*b* conduction only,

$$\begin{aligned} v_{an} &= 1/2 \cdot (v_{ug} - v_{vg} - e_c) \\ v_{bn} &= 1/2 \cdot (v_{vg} - v_{ug} - e_c) \\ v_{cn} &= e_c \end{aligned} \quad (2.15)$$

and for phase-*b* and phase-*c* conduction only,

$$\begin{aligned} v_{an} &= e_a \\ v_{bn} &= 1/2 \cdot (v_{vg} - v_{wg} - e_a) \\ v_{cn} &= 1/2 \cdot (v_{wg} - v_{vg} - e_a) \end{aligned} \quad (2.16)$$

and for phase-*a* and phase-*c* conduction only,

$$\begin{aligned} v_{an} &= 1/2 \cdot (v_{ug} - v_{wg} - e_b) \\ v_{bn} &= e_b \\ v_{cn} &= 1/2 \cdot (v_{wg} - v_{ug} - e_b) \end{aligned} \quad (2.17)$$

Notice that these phase voltages are expressed in terms of only the supply voltages and the back EMFs, which are presumably known quantities.

A typical healthy transient current space-vector polar plot during soft starting is shown in Figure 2.5. As one may observe, there are 12 distinct switching states ( $S_1$ - $S_{12}$ ) in every complete ac power cycle. The machine will only produce a resultant rotating stator mmf when all three phases of the motor are carrying currents. In the event when only two phases are conducting currents, the resultant stator mmf produced by the motor consist of a forward rotating mmf component and a backward rotating mmf component of equal magnitudes. This is due to the fact

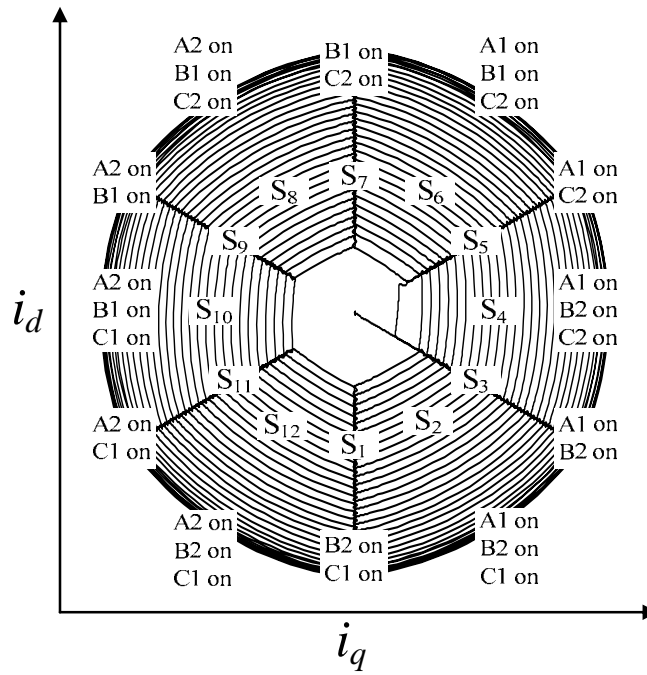


Figure 2.5: *Healthy* transient current space-vector plot during soft starting.

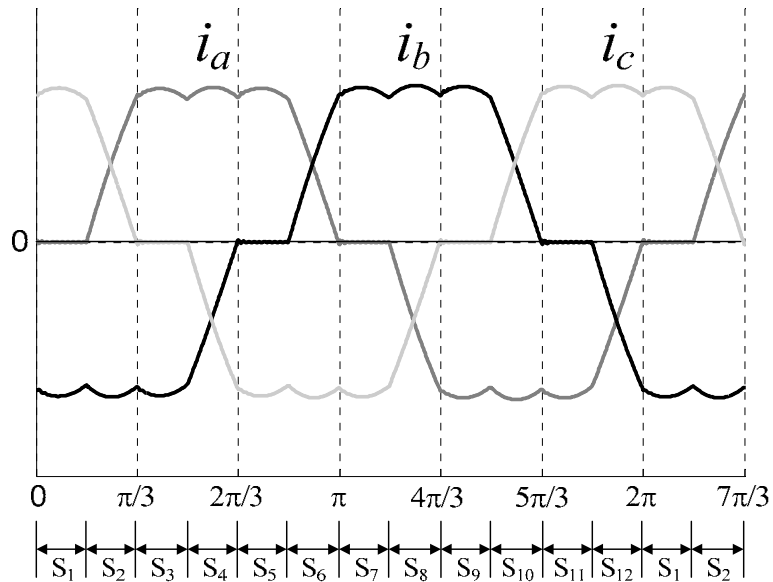


Figure 2.6: *Healthy* transient three-phase currents during soft starting.

that the current flowing into one phase is the same as the current flowing out of another phase. Hence, it will display as a straight line, instead of a quasi-circular outward spiraling locus that follows the transient current built-up, followed by a quasi-circular inward spiraling locus during the transient current decay to its final steady-state value. The corresponding space-vector plot is given in Figure 2.5. It should be noted that Figure 2.5 only presents the transient performance of the motor where the current space-vector is spiraled outwards with increasing speed. A typical healthy transient three-phase current waveform during soft starting is given in Figure 2.6.

By virtue of the 12 distinct switching states, the motor phase voltages over a complete ac cycle can be computed using the above derivations given in (2.5) and (2.15) through (2.17). In light of the half-wave symmetry, the phase-*a* voltage is expressed here over a half cycle, as follows:

$$v_{an} = \begin{cases} e_a, & \phi < \omega t < \alpha \\ v_{ug}, & \alpha < \omega t < \phi + \pi/3 \\ 1/2 \cdot (v_{ug} - v_{vg} - e_c), & \phi + \pi/3 < \omega t < \alpha + \pi/3 \\ v_{ug}, & \alpha + \pi/3 < \omega t < \phi + 2\pi/3 \\ 1/2 \cdot (v_{ug} - v_{wg} - e_b), & \phi + 2\pi/3 < \omega t < \alpha + 2\pi/3 \\ v_{ug}, & \alpha + 2\pi/3 < \omega t < \phi + \pi \end{cases} \quad (2.18)$$

For completeness of this work, the phase-*b* and phase-*c* voltages are also expressed here over a half cycle, as follows:

$$v_{bn} = \begin{cases} 1/2 \cdot (v_{vg} - v_{wg} - e_a), & \phi < \omega t < \alpha \\ v_{vg}, & \alpha < \omega t < \phi + \pi/3 \\ 1/2 \cdot (v_{vg} - v_{ug} - e_c), & \phi + \pi/3 < \omega t < \alpha + \pi/3 \\ v_{vg}, & \alpha + \pi/3 < \omega t < \phi + 2\pi/3 \\ e_b, & \phi + 2\pi/3 < \omega t < \alpha + 2\pi/3 \\ v_{vg}, & \alpha + 2\pi/3 < \omega t < \phi + \pi \end{cases} \quad (2.19)$$

$$v_{cn} = \begin{cases} 1/2 \cdot (v_{wg} - v_{vg} - e_a), & \phi < \omega t < \alpha \\ v_{wg}, & \alpha < \omega t < \phi + \pi/3 \\ e_c, & \phi + \pi/3 < \omega t < \alpha + \pi/3 \\ v_{wg}, & \alpha + \pi/3 < \omega t < \phi + 2\pi/3 \\ 1/2 \cdot (v_{wg} - v_{ug} - e_b), & \phi + 2\pi/3 < \omega t < \alpha + 2\pi/3 \\ v_{wg}, & \alpha + 2\pi/3 < \omega t < \phi + \pi \end{cases} \quad (2.20)$$

Neglecting magnetic saturation and core loss effects, an induction motor can be represented in a T-equivalent circuit model [87], [88], as given in Figure 2.7. During the transient (soft starting) period, the slip of the motor is close to one. Hence,  $\omega L_m \gg \omega L_l + R_r/s$ , which implies that the magnetizing branch of Figure 2.7 can be neglected in the transient analysis. In other words, the motor currents produce negligible flux in the airgap, and the magnitudes of these currents are limited mainly by the leakage reactances. Accordingly, during transient analysis, one can assume negligible induced EMFs in the windings, i.e.  $e_a = e_b = e_c \approx 0$ . Hence, (2.18) through (2.20) can be further simplified by equating the EMF terms to zero. Now, the motor phase voltage expressions depend only on the supply voltages, and hence they can be easily calculated.

A set of healthy three-phase line-to-neutral motor voltage waveforms obtained from the closed-form solutions of (2.18) through (2.20), at  $\phi = 60^\circ$  and  $\alpha = 90^\circ$  is depicted in Figure 2.8. It is important to mention that the waveforms of Figure 2.8 are only valid for transient analysis, which is the subject of this work, due to the fact that the induced EMF in the windings cannot be neglected during the steady state operation. Harmonic breakdown of these motor phase voltages of Figure 2.8, subject to the formulation given in (2.21), are indicated in Table 2.1. The harmonic frequency components of Table 2.1 correspond to the three-phase motor voltages of a case-study being considered here under a healthy condition. In Table 2.1, the magnitude corresponds to  $V_{s(h)}$ , and the phase angle corresponds to  $\theta_{v(h)}$ , in the formulation of (2.21). This table gives the magnitudes and phase angles for the  $a$ ,  $b$ , and  $c$  motor terminal phase voltages.

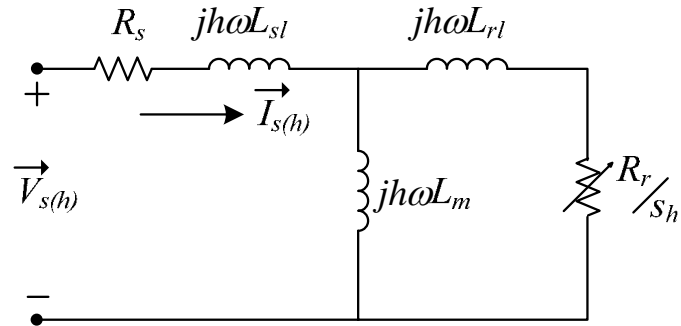


Figure 2.7: T-equivalent circuit model ( $h$  is the harmonic order).

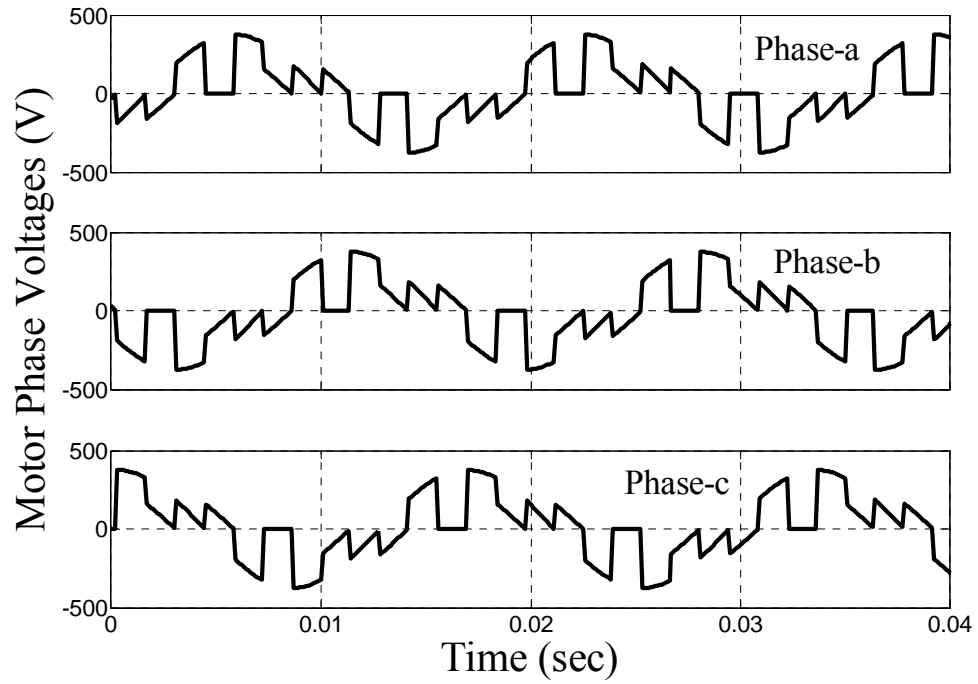


Figure 2.8: Analytical solution of *healthy* three-phase line-to-neutral motor voltage waveforms at operating conditions of  $\phi = 60^\circ$  and  $\alpha = 90^\circ$ .

Table 2.1: Harmonic contents of *healthy* three-phase motor phase voltages obtained from analytical solution.

Harmonic Order	$V_{ma}$		$V_{mb}$		$V_{mc}$	
	Magnitude (Volt)	Phase (radian)	Magnitude (Volt)	Phase (radian)	Magnitude (Volt)	Phase (radian)
1	207.30	-1.784	208.90	2.405	208.10	0.304
3	0	0	0	0	0	0
5	131.40	2.838	131.80	-1.353	131.90	0.745
7	94.11	0.189	93.54	-1.896	94.62	2.293
9	0	0	0	0	0	0
11	17.28	0.959	18.60	-3.130	16.41	-1.014
13	12.45	1.979	11.17	0.017	13.18	-2.063
15	0	0	0	0	0	0
17	35.18	2.854	35.55	-1.331	35.23	0.771
19	31.37	0.189	30.98	-1.886	31.69	2.304
21	0	0	0	0	0	0

### 2.3.2 Closed-Form Expressions of Motor Phase Currents

To obtain closed-form analytical expressions of the motor phase currents, the T-equivalent circuit model for higher-order harmonics is utilized to evaluate the stator currents for the fundamental voltage term and each subsequent harmonic voltage term, see Figure 2.7. Superposition is then applied to express the phase currents in a Fourier series representation.

The non-sinusoidal phase voltages can be expressed in a Fourier series form, as follows:

$$v_s(t) = \sum_{h=1,3,5,7,\dots}^{\infty} V_{s(h)} \cos(h\omega t + \theta_{v(h)}) \quad (2.21)$$

where,  $V_{s(h)}$  and  $\theta_{v(h)}$  are the magnitude and phase of each harmonic term, respectively, and  $h$  is the harmonic order, see Table 2.1 for the harmonic breakdown of the waveforms of Figure 2.8.

For simplicity of the analysis, magnetic saturation and skin effect phenomena are neglected in the derivation process. In other words, both the inductances and resistances of the T-equivalent

circuit model are assumed to be constant during the transient analysis. Accordingly, from Figure 2.7, the motor phase current for each harmonic voltage term can be expressed in phasor form, as follows:

$$\bar{I}_{s(h)} = I_{s(h)} \angle \theta_{i(h)} = \frac{V_{s(h)} \angle \theta_{v(h)}}{Z_{eq}} \quad (2.22)$$

where,  $Z_{eq}$  is

$$Z_{eq} = R_s + jh\omega L_{sl} + \frac{(jh\omega L_m) \cdot (R_r/s_h + jh\omega L_{rl})}{R_r/s_h + jh\omega \cdot (L_m + L_{rl})} \quad (2.23)$$

Knowing the magnitude and phase of each current harmonic term from (2.22), the resulting motor phase currents can be written in Fourier-series time-domain form, as follows:

$$i_s(t) = \sum_{h=1,3,5,7\dots}^{\infty} I_{s(h)} \cos(h\omega t + \theta_{i(h)}) \quad (2.24)$$

An interesting observation can be drawn with regard to the slip term of the motor for higher-order time-harmonics, which can be defined as follows:

$$s_h = \begin{cases} (h\omega_{syn} - \omega_r) / h\omega_{syn}, & \text{for } h = 1, 7, 13, 19\dots \\ (h\omega_{syn} + \omega_r) / h\omega_{syn}, & \text{for } h = 5, 11, 17, 23\dots \end{cases} \quad (2.25)$$

The first expression of (2.25) corresponds to the harmonic components with forward rotating mmf, while the second expression corresponds to the harmonic components with backward rotating mmf. Nevertheless, at higher-order time harmonics, the slip,  $s_h$ , is approaching one, from which one draws the conclusion that the time-harmonics of motor currents have negligible magnetizing components, and therefore produce negligible airgap flux and consequently negligible induced EMFs in the motor windings.

The computed healthy three-phase current waveforms, using (2.22) through (2.25), at transient operating conditions of  $\phi = 60^\circ$ ,  $\alpha = 90^\circ$ , and a motor speed of 200-r/min are shown in

Figure 2.9. The reason for choosing these operating conditions is in light of the fact that during starting, any induction motor is highly inductive. The initial phase displacement angle,  $\phi$ , between the phase voltage and current can be calculated according to (2.23) by setting the slip equal to one and computing the angle of the complex impedance,  $Z_{eq}$ . For this particular 2-hp induction motor under investigation (see Appendix A for motor specifications), the initial phase angle was calculated to be about  $60^\circ$ . Hence this phase angle,  $\phi = 60^\circ$ , is chosen and kept constant throughout the analysis process for simplicity's reason. As for choosing  $\alpha = 90^\circ$  and a speed of 200-r/min, this is to compare and help validate the analytical results by comparison with the simulation results at this particular time instant during the transient period of the simulation, which will be presented later-on in this dissertation. Harmonic contents of these three-phase motor currents of Figure 2.9 are given in Table 2.2.

To further demonstrate the usefulness of the derived closed-form solution, the RMS values of the healthy three-phase currents during the soft starting transient are computed and presented in Table 2.3. In this work, an alpha angle of  $\alpha = 105^\circ$  was chosen as the initial delay/firing angle. This delay angle gradually decreases as the motor speeds up until a final delay angle of  $\alpha = 65^\circ$  is reached. At this point, the RMS values of the currents can no longer be computed from the closed-form expressions owing to the fact that the phase angle,  $\phi$ , is set at  $60^\circ$  during the computation process. Nevertheless, the analytical results of Table 2.3 demonstrate that the three-phase currents are balanced during the starting transient with reduced RMS values. It will be shown later in the simulation chapter that the analytical results begin to deviate from the simulations as the currents are approaching their rated values. This is due to the fact that the induction motor is no longer highly inductive as the motor is approaching its rated speed. Therefore, the phase angle,  $\phi$ , is approaching the power factor angle in the simulations, whereas this angle is kept constant at  $60^\circ$  in the closed-form solution. Another reason is due to the

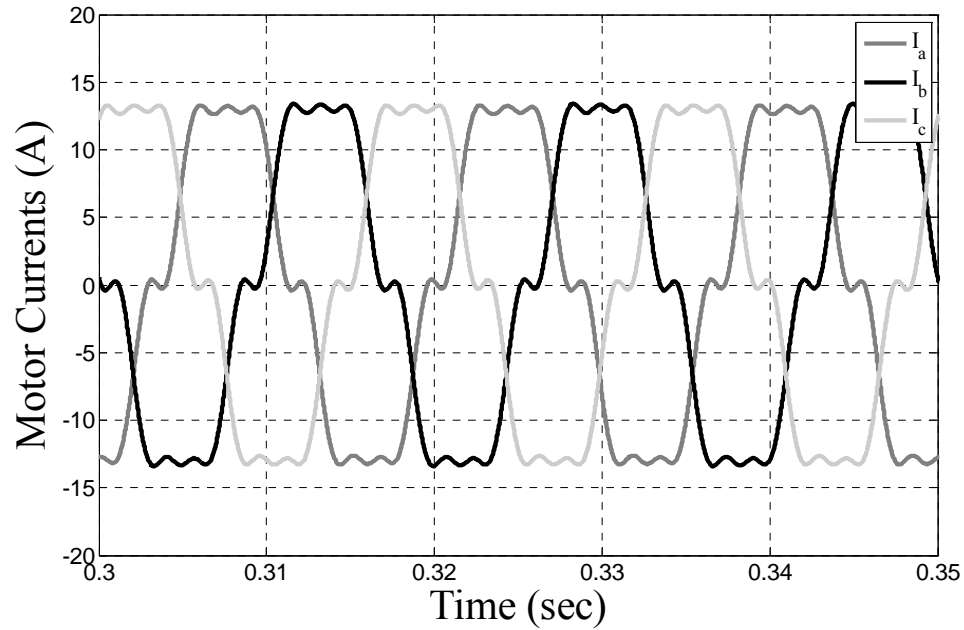


Figure 2.9: Analytical solution of *healthy* three-phase current waveforms at transient conditions of  $\phi = 60^\circ$ ,  $\alpha = 90^\circ$ , and motor speed of 200-r/min.

Table 2.2: Harmonic contents of *healthy* three-phase motor currents obtained from analytical solution.

Harmonic Order	$I_{ma}$		$I_{mb}$		$I_{mc}$	
	Magnitude (Amp)	Phase (radian)	Magnitude (Amp)	Phase (radian)	Magnitude (Amp)	Phase (radian)
1	14.255	-2.869	14.340	1.320	14.326	-0.781
3	0	0	0	0	0	0
5	2.021	1.364	2.027	-2.827	2.028	-0.729
7	1.036	-1.313	1.030	2.886	1.042	0.791
9	0	0	0	0	0	0
11	0.121	-0.568	0.131	1.626	0.115	-2.541
13	0.074	0.445	0.066	-1.516	0.078	2.686
15	0	0	0	0	0	0
17	0.160	1.312	0.162	-2.873	0.160	-0.772
19	0.128	-1.357	0.126	2.852	0.129	0.759
21	0	0	0	0	0	0

Table 2.3: Analytical solution of RMS values of *healthy* three-phase stator currents during the soft starting transient period.

$\alpha$ -Firing Angle (degree)	$I_{ma}$ RMS value (Amp)	$I_{mb}$ RMS value (Amp)	$I_{mc}$ RMS value (Amp)
105	5.75	5.76	5.70
100	7.25	7.24	7.20
95	8.75	8.73	8.69
90	10.08	10.14	10.13
85	11.47	11.52	11.53
80	12.76	12.80	12.82
75	13.82	13.85	13.88
70	14.40	14.40	14.45
65	13.54	13.53	13.58

assumption that the induced EMFs in the windings are negligible in the closed-form analysis, which is no longer valid as the motor is approaching its rated speed. Nevertheless, the objective of this work is to analyze the motor transient performance during soft starting. Therefore, the analytical results presented in Figure 2.9 and Table 2.3 are acceptable for this stage of the work.

## 2.4 Analysis of Failure Modes and Effects

The earlier formulations of the closed-form analytical expressions of the motor phase voltages and currents are employed herein to investigate the impact of failure modes in soft starters on the motor transient performance. Two distinct types of failure modes considered in this work are: (1) short-circuit SCR fault (see Figure 2.10(a)), and (2) open-circuit SCR fault (see Figure 2.10(b)), occurring only in one phase of the soft starter. A short-circuit SCR fault can happen in situations such as loose wire in the circuit or breakdown in the snubber circuit. Conversely, an open-circuit SCR fault can occur due to malfunctions either in the gate driver or the pulse generator of the controller.

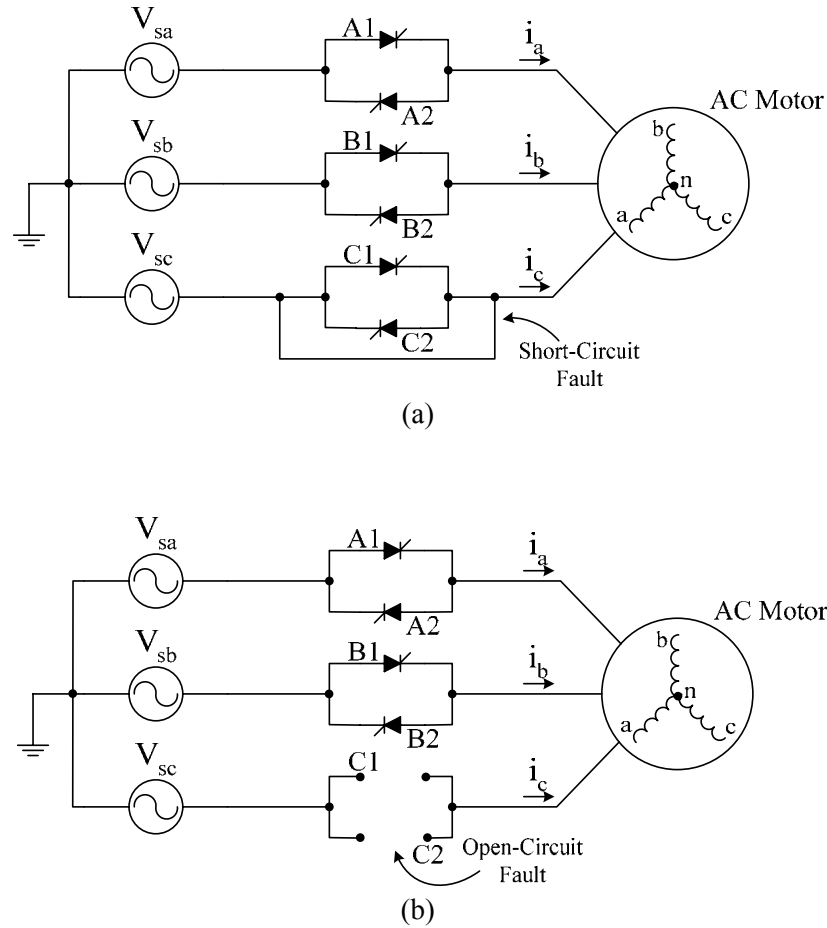


Figure 2.10: Failure modes in soft starter circuit. (a) Short-circuit fault. (b) Open-circuit fault.

### 2.4.1 Short-Circuit SCR Fault

During a short-circuit SCR fault, the motor terminal of phase- $c$  is connected directly to the utility grid, see Figure 2.10(a). As a consequence, the problem of voltage unbalances impressed upon the motor windings arises during starting. This is due to the fact that the motor phase winding without the SCR connection experiences a full applied voltage at its terminal, whereas the other two phases experience reduced voltages impressed upon them during starting. It is well-known that voltage unbalances introduce negative sequence components in the stator currents, which consequently lead to average torque reduction and torque pulsations during the starting transients.

Intuitively, a short-circuit SCR fault is analogous to turning on SCRs C1 and C2 continuously, see Figure 2.10(a). Hence, referring to Figure 2.5, one can deduce that the switching states,  $S_2$ - $S_4$ , will combine to form one switching state. The same can be said for the switching states,  $S_8$ - $S_{10}$ . Accordingly, the 12 switching states under healthy operation will reduce to 8 switching states under a short-circuit SCR fault. A transient current space-vector polar plot during soft starting under a short-circuit SCR switch fault is illustrated in Figure 2.11. Notice in the figure the 8 distinct switching states that were mentioned earlier. Besides that, the shape of the current space-vector is more elliptic and no longer of circular nature as in the healthy case. Furthermore, as one can observe, the magnitude of the current space-vector during starting is higher as compared to the healthy case, see Figure 2.5. Accordingly, this will impose a greater stress on the motor windings, and consequently higher torque pulsations owing to the higher starting currents which contain a negative sequence influence.

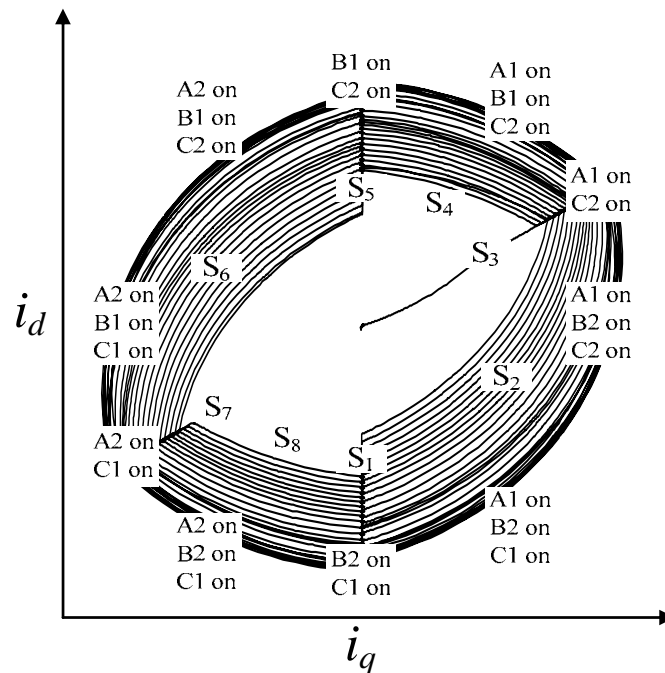


Figure 2.11: Transient current space-vector plot during soft starting under a *short-circuit SCR fault*.

Applying the earlier closed-form derivation of the motor line-to-neutral phase voltages with the switching states of Figure 2.11, the phase-*a* voltage is expressed here over a half cycle, in light of the half-wave symmetry, as follows:

$$v_{an} = \begin{cases} e_a, & \phi < \omega t < \alpha \\ v_{ug}, & \alpha < \omega t < \phi + 2\pi/3 \\ 1/2 \cdot (v_{ug} - v_{wg} - e_b), & \phi + 2\pi/3 < \omega t < \alpha + 2\pi/3 \\ v_{ug}, & \alpha + 2\pi/3 < \omega t < \phi + \pi \end{cases} \quad (2.26)$$

Similarly, voltage expressions for phase-*b* and phase-*c* can be derived in the same manner, which are expressed as follows:

$$v_{bn} = \begin{cases} 1/2 \cdot (v_{vg} - v_{wg} - e_a), & \phi < \omega t < \alpha \\ v_{vg}, & \alpha < \omega t < \phi + 2\pi/3 \\ e_b, & \phi + 2\pi/3 < \omega t < \alpha + 2\pi/3 \\ v_{vg}, & \alpha + 2\pi/3 < \omega t < \phi + \pi \end{cases} \quad (2.27)$$

$$v_{cn} = \begin{cases} 1/2 \cdot (v_{wg} - v_{vg} - e_a), & \phi < \omega t < \alpha \\ v_{wg}, & \alpha < \omega t < \phi + 2\pi/3 \\ 1/2 \cdot (v_{wg} - v_{ug} - e_b), & \phi + 2\pi/3 < \omega t < \alpha + 2\pi/3 \\ v_{wg}, & \alpha + 2\pi/3 < \omega t < \phi + \pi \end{cases} \quad (2.28)$$

The calculated three-phase line-to-neutral motor voltages based on these analytical expressions of (2.26) through (2.28) are illustrated in Figure 2.12, along with the corresponding harmonic frequency breakdown of these voltages which are given in Table 2.4. Examination of Figure 2.12 and Table 2.4 show that the motor voltage waveforms in all phases are unsymmetrical and unbalanced due to the impact of the short-circuit SCR switch fault in phase-*c*.

Using the approach described earlier in attaining the analytical expressions of the motor currents, the calculated three-phase motor currents at transient operating conditions of  $\phi = 60^\circ$ ,  $\alpha = 90^\circ$ , and a motor speed of 400-r/min are given in Figure 2.13, and the corresponding harmonic contents of these currents are given in Table 2.5. The analytical results of Figure 2.13

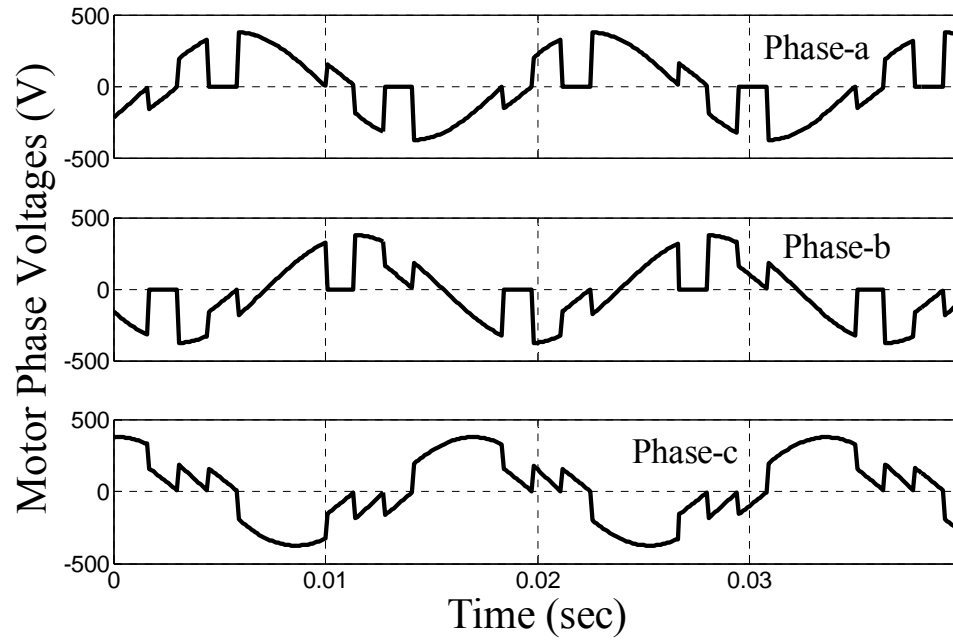


Figure 2.12: Three-phase line-to-neutral motor voltage waveforms from analytical solution under a *short-circuit SCR fault*.

Table 2.4: Harmonic contents of three-phase motor phase voltages obtained from analytical solution under a *short-circuit SCR fault*.

Harmonic Order	$V_{ma}$		$V_{mb}$		$V_{mc}$	
	Magnitude (Volt)	Phase (radian)	Magnitude (Volt)	Phase (radian)	Magnitude (Volt)	Phase (radian)
1	259.30	-1.909	220.80	2.678	318.80	0.475
3	54.98	-0.816	52.48	-0.809	107.50	2.329
5	116.60	2.500	116.20	-1.018	43.55	0.733
7	82.65	0.520	82.85	-2.232	32.03	2.279
9	17.12	-2.519	19.23	-2.429	36.30	0.670
11	15.62	0.639	16.70	-2.847	5.64	-0.914
13	10.67	2.332	9.60	-0.395	4.31	-1.926
15	10.88	-0.820	8.60	-0.698	19.44	2.375
17	31.60	2.509	31.24	-0.995	11.32	0.725
19	27.35	0.511	27.55	-2.227	11.01	2.266
21	6.11	-2.592	7.98	-2.402	14.03	0.657

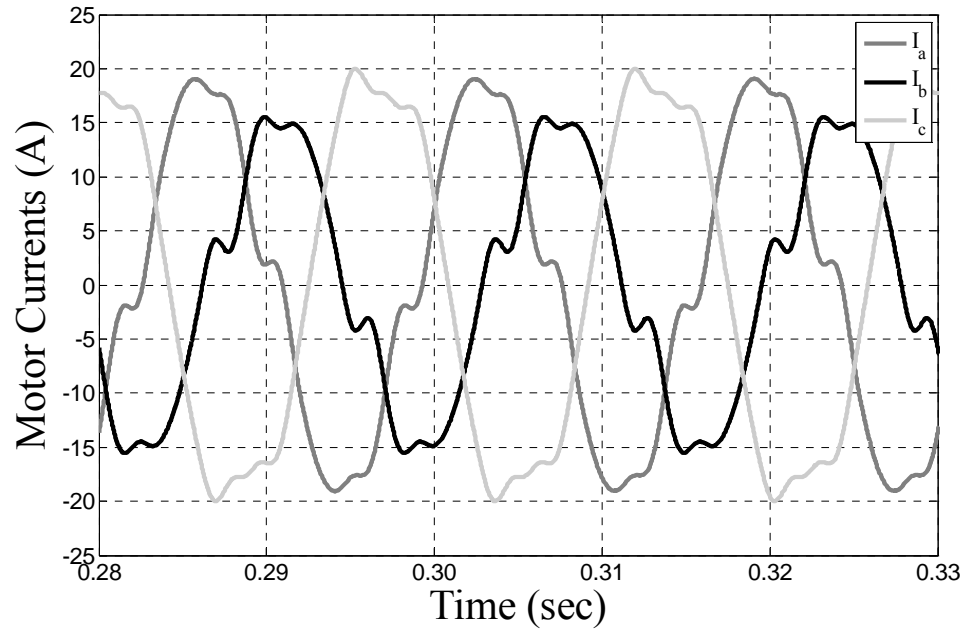


Figure 2.13: Analytical solution of three-phase current waveforms at transient conditions of  $\phi = 60^\circ$ ,  $\alpha = 90^\circ$ , and motor speed of 400-r/min under a *short-circuit SCR fault*.

Table 2.5: Harmonic contents of three-phase motor currents obtained from analytical solution under a *short-circuit SCR fault*.

Harmonic Order	$I_{ma}$		$I_{mb}$		$I_{mc}$	
	Magnitude (Amp)	Phase (radian)	Magnitude (Amp)	Phase (radian)	Magnitude (Amp)	Phase (radian)
1	18.752	-2.994	14.043	1.593	21.666	-0.610
3	1.397	-2.223	1.333	-2.217	2.731	0.921
5	1.793	1.026	1.787	-2.492	0.670	-0.741
7	0.910	-0.982	0.912	2.550	0.353	0.777
9	0.147	2.247	0.165	2.337	0.312	-0.847
11	0.110	-0.888	0.117	1.909	0.040	-2.441
13	0.063	0.798	0.057	-1.929	0.026	2.823
15	0.056	-2.359	0.044	-2.236	0.100	0.836
17	0.144	0.967	0.142	-2.537	0.051	-0.817
19	0.111	-1.034	0.112	2.511	0.045	0.721
21	0.022	2.143	0.029	2.333	0.052	-0.891

Table 2.6: Analytical solution of RMS values of three-phase stator currents under a *short-circuit SCR fault* during the soft starting transient period.

$\alpha$ -Firing Angle (degree)	$I_{ma}$ RMS value (Amp)	$I_{mb}$ RMS value (Amp)	$I_{mc}$ RMS value (Amp)
105	11.41	6.22	13.51
100	12.07	7.47	14.17
95	12.71	8.81	14.82
90	13.26	9.93	15.32
85	13.72	11.04	15.73
80	13.81	11.68	15.81
75	13.01	11.71	15.48
70	10.77	10.21	12.66
65	3.75	4.57	5.14

and Table 2.5 reveal the unbalanced nature of these currents in all phases attributable to the short-circuit SCR switch fault. The RMS values of the three-phase motor currents during the entire soft starting period obtained from closed-form solution are tabulated in Table 2.6. Again, it should be noted that the currents are unbalanced during starting. These unbalanced currents will accordingly lead to undesired torque reduction and transient torque pulsations, as will be demonstrated through simulations in later chapters. Comparing Table 2.6 with Table 2.3, one can deduce that the currents during starting under faulty conditions are higher than in the healthy case.

## 2.4.2 Open-Circuit SCR Fault

An open-circuit fault in the SCR switches can happen when there is a malfunction in the gate driver or the controller that prevents gating of the SCR switches. One common type which is under consideration in this work is depicted in Figure 2.10(b), where both the SCR switches of one phase are inactive. A fault of this nature results in either 2-phase or 1-phase conduction mode during soft starting. Clearly, in the event of 1-phase conduction mode, the motor is incapable of starting since there is no complete path for the current to flow.

As in the case of 2-phase conduction mode, the current flowing into one phase will be equivalent to the current flowing out of another phase, that is  $i_a = -i_b$  in Figure 2.10(b). Suppose that the phase-*a* and phase-*b* winding currents of Figure 2.10(b) are:

$$\begin{aligned} i_a(t) &= I_m \cos(\omega t) \\ i_b(t) &= I_m \cos(\omega t - \pi) \end{aligned} \quad \text{Amps} \quad (2.29)$$

where,  $I_m$  is the peak amplitude of the winding currents.

Considering only the fundamental space harmonic terms, the mmfs of phase-*a* and phase-*b* can be expressed as follows [88]:

$$\begin{aligned} \mathcal{F}_a(\theta) &= \frac{4}{\pi} \left( \frac{N_{ph} k_{w_1}}{p} \right) \left( \frac{i_a}{m} \right) \cos(\theta) \\ \mathcal{F}_b(\theta) &= \frac{4}{\pi} \left( \frac{N_{ph} k_{w_1}}{p} \right) \left( \frac{i_b}{m} \right) \cos(\theta - 2\pi/3) \end{aligned} \quad \text{AT/pole} \quad (2.30)$$

where,  $N_{ph}$  is the effective number of series stator turns per phase,  $p$  is the number of poles,  $m$  is the number of parallel paths per phase, and  $k_{w_1}$  is the fundamental winding factor.

Accordingly, the fundamental resultant mmf corresponding to the phase-*a* and phase-*b* current excitations of (2.29) can be written as follows:

$$\mathcal{F}_{\text{resultant}_1}(\theta, t) = F_{\text{max}_1} \{ \cos(\theta) \cos(\omega t) + \cos(\theta - 2\pi/3) \cos(\omega t - \pi) \} \quad \text{AT/pole} \quad (2.31)$$

where,  $F_{\text{max}_1} = (4/\pi) (N_{ph} k_{w_1} / mp) I_m$  AT/pole.

The resultant mmf of (2.31) can be rewritten by applying the following trigonometric identity:

$$\cos(a) \cos(b) = 1/2 \cdot \cos(a - b) + 1/2 \cdot \cos(a + b) \quad (2.32)$$

which leads to

$$\mathcal{F}_{\text{resultant}_1}(\theta, t) = \left(\frac{\sqrt{3}}{2}\right) F_{\text{max}_1} \left\{ \cos(\theta - \omega t + \pi/6) + \cos(\theta + \omega t + \pi/6) \right\} \quad \text{AT/pole} \quad (2.33)$$

The first term of (2.33) corresponds to the forward traveling mmf wave, whereas the second term of (2.33) represents the backward traveling mmf wave. Evidently, one can conclude from (2.33) that there is no starting torque when the motor is in 2-phase conduction mode during soft starting. Hence, in the event of an open-circuit SCR fault, the motor is incapable of producing a starting torque.

## 2.5 Summary

This chapter of the dissertation contributes to a better understanding of the impacts of SCR switch failures on motor performance by providing closed-form expressions to estimate the motor currents during soft starting. Two distinct types of failure modes investigated here are a short-circuit and an open-circuit SCR switch faults occurring in only one phase of the soft starter. The closed-form analytical studies demonstrate that the short-circuit SCR fault produces undesired fault response on motor performance with unbalanced, high starting currents which accordingly result in high starting torque pulsations. On the contrary, it is shown here that the open-circuit SCR switch fault results in no starting torque from the motor, hence it constitutes a total failure of motor starting. On the other hand, it does not expose the soft starter elements to the severity of motor current unbalances and the severity of motor torque pulsations. Evidently, the use of the conventional open-loop symmetrical-triggering control in a two-phase switching mode under faulty condition contribute to detrimental impacts on motor performance which results in disruption of normal operation of the motor-load system during soft starting. It is important to mention that no such work has yet been reported in the technical literature to investigate the effects of SCR switch faults of soft starters on motor performance. With a better understanding of these fault impacts, remedial strategies can be developed to minimize the negative effects

resulting from such faults during normal soft starting operation, which is presented in the following chapter.

## CHAPTER 3

---

---

# FAULT TOLERANT SOFT STARTER

---

---

### 3.1 Introduction

As demonstrated in the preceding chapter, the use of the conventional open-loop symmetrical-triggering control of the soft starter in two-phase switching mode, under short-circuit SCR switch fault condition produces undesired impacts on machine performance. This situation results in unbalanced and unsymmetrical high currents during soft starting. Furthermore, the conventional soft starter system, such as the commercially available type, is incapable of driving the motor under open-circuit SCR switch fault condition. Accordingly, the soft starter topology and its control algorithm need to be tailored in order to render the soft starter fault tolerant under both open-circuit and short-circuit switch fault conditions in any one of the phases. This is while still providing reduced starting inrush currents, and consequently reduced starting torque transients. In this chapter, the fault tolerant soft starter topology and its resilient closed-loop two-phase control scheme will be set forth. The design procedures of the soft starter controller will also be presented using small-signal modeling approach.

## 3.2 Principles of Fault Tolerant Operations

The main concerns in designing and constructing any fault tolerant system are the potential added cost and feasibility issues. The increased cost of incorporating fault tolerant capabilities into the existing system should always be compared with the cost of damage to the motor-load system when functioning with the existing configuration without such fault tolerant capabilities under faulty conditions. It would not make sense to implement a fault tolerant capability to the existing technology if the added components and manufacturing costs are higher than either the cost of having system redundancy, or the cost of damage to the overall system, when operating under a faulty condition with no remedial action being taken. Hence, a designer should always take these factors into account when designing a fault tolerant system. In the opinion of this investigator, the most cost-effective means is to modify the existing control algorithm to accommodate the impact of a fault while still providing acceptable performance. Such a measure usually involves hardware modifications which need to be performed in a modest and cost-effective manner.

In this work, the proposed fault tolerant soft starter system is designed with minimum hardware modifications to the existing commercially available soft starter. To reiterate, the fault tolerant feature can be easily incorporated into the existing hardware. The added hardware is modest and hence does not increase the size of the existing system with only minimum increase in the component cost. The control algorithm was implemented in a closed-loop form which is more dynamic, effective, and robust in so far as controllability and performance issues are concerned. The proposed scheme is simple and can be easily implemented with the digital signal processing power available in the existing technology. Thus, the proposed controls, along with minimum modification to the hardware circuit topology, present enticing solutions to industries for such technology to be adopted and implemented in their existing products for mitigating

detrimental effects resulting from a faulty soft starter. In fact, by adopting the proposed control technique, a low-cost soft starter with only two-phase switching mode can be developed and produced in the market for consumers at a lower cost with reasonably good performance, as compared to the existing three-phase soft starter products.

### 3.2.1 Modified Topology

The vital part of realizing the fault tolerance of the soft starter through integrating the proposed control algorithm is the amendment of its hardware configuration. Only two significant modifications in terms of hardware were made to the industrial type soft starter of Figure 2.1, which is repeated here for convenience in Figure 3.1. A modified version of the soft starter to accommodate the proposed control technique is illustrated in Figure 3.2. The first modification is the addition of a set of three-phase voltage sensors at the motor end of the soft starter to measure the motor terminal voltages. The reason for having these sensors is that the motor terminal voltage measurement will be employed as one set of the feedback signals for the present closed-loop control scheme. The second modification is the replacement of the existing 3-pole synchronously-controlled modular contactor with three individually-controlled 1-pole contactors, one pole per phase. The main purpose of this modification is such that the contactor of the corresponding SCR phase can be closed in the event of an open-circuit SCR switch fault. This is in order to isolate the faulty SCR phase, as depicted in Figure 3.3. Accordingly, the soft starter can function in a two-phase switching mode using the present two-phase control approach. In the event of a short-circuit SCR fault, the corresponding motor phase is automatically connected directly to the utility mains, and hence the soft starter is already in its two-phase switching mode.

As one can see from the desired hardware modifications to the industrial type soft starter, the suggested changes barely increase the size of the existing system with only minor increase in the component cost. Such design modifications with minimum cost increase are usually acceptable within industrial practice. Due to the asymmetry of the post-fault two-phase thyristors configura-

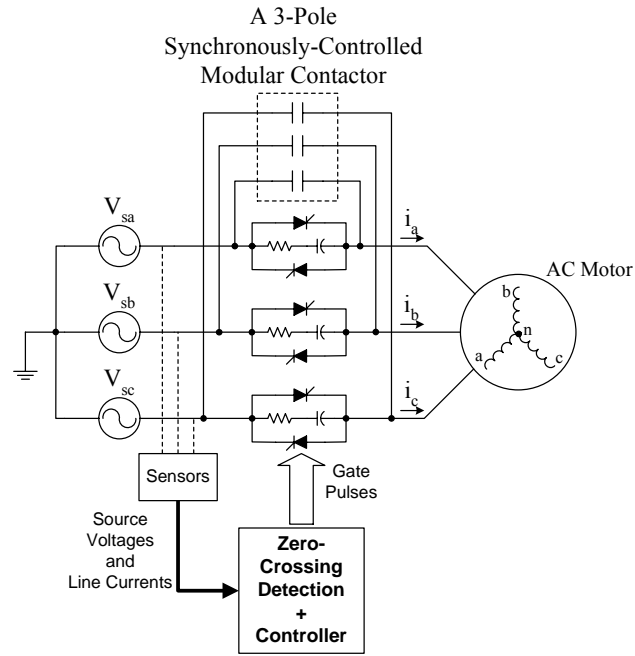


Figure 3.1: Industrial type three-phase soft starter topology.

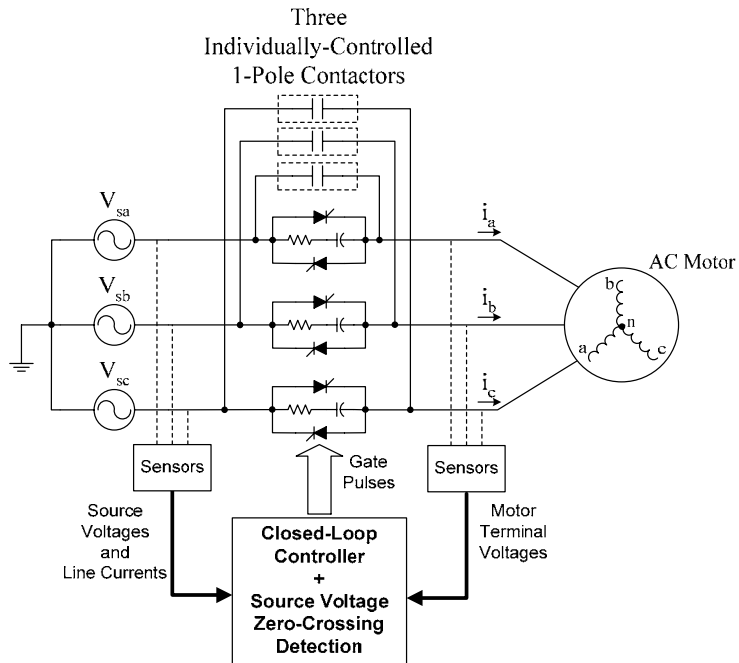


Figure 3.2: Modified version of soft starter with fault tolerance/isolation capabilities.

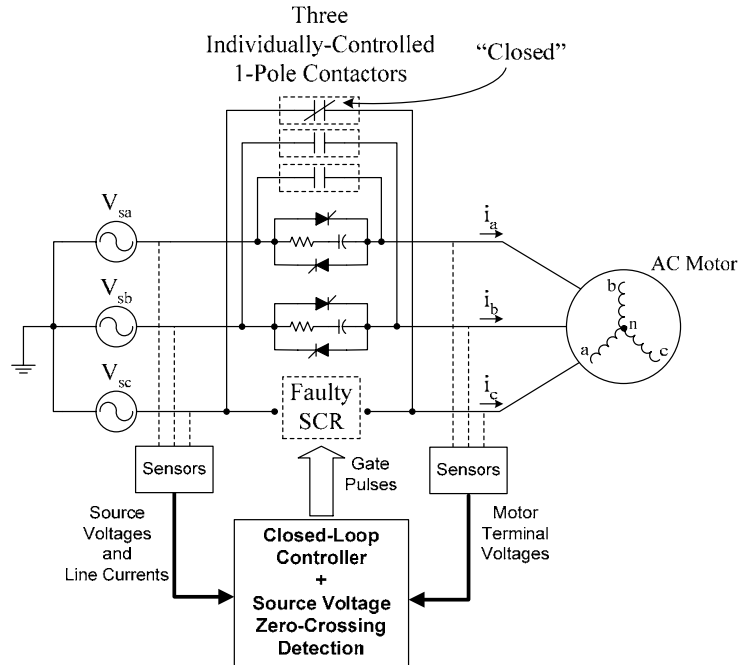


Figure 3.3: Post-fault soft starter configuration.

-tion shown in Figure 3.3, the problem of voltage unbalances impressed upon the motor windings arises during starting. This is due to the fact that the motor phase winding without the SCR connection experiences a full applied voltage, whereas the other two phases experience reduced voltages impressed upon them during starting. It is well-known that voltage unbalances introduce negative sequence components in the stator currents, which consequently lead to torque pulsations during the starting transients. Therefore, the control strategy has to be tailored to control the firing of the thyristors in the remaining two phases independently. This is in order to generate nearly balanced three-phase stator currents during the soft starting period, so that the starting torque pulsations can be alleviated. Hence, a closed-loop type of control is adopted which is presented next.

### 3.2.2 A Resilient Closed-Loop Two-Phase Control Scheme

In order to control the firing of the thyristors in the remaining two healthy phases independently, a new set of firing angles for each of the two phases has to be defined. Such a task

is not easy to achieve using open-loop control, since the firing angle profile will vary with different horsepower motors as well as load conditions. Therefore, closed-loop type of control was adopted here, which will inherently generate the appropriate firing angle profile for the thyristors of each of the two phases under different horsepower motor ratings and different types of load conditions.

The present closed-loop two-phase control scheme is graphically depicted in Figure 3.4 for the post-fault soft starter configuration of Figure 3.3. In this control method, there are two types of feedback control loops, namely a voltage loop and a current loop for each of the remaining two healthy phases. The outputs of these feedback loops represent the changes in the firing angles that will be used to compute the resulting firing (delay) angles, which is defined as follows:

$$\begin{aligned}\alpha_a &= \alpha_{a0} - \alpha_{aV} - \alpha_{aI} \\ \alpha_b &= \alpha_{b0} - \alpha_{bV} - \alpha_{bI}\end{aligned}\tag{3.1}$$

where,  $\alpha_{aV}$  and  $\alpha_{bV}$  are the outputs of the voltage feedback loop,  $\alpha_{aI}$  and  $\alpha_{bI}$  are the outputs of the current feedback loop, and  $\alpha_{a0}$  and  $\alpha_{b0}$  are the initial firing (delay) angles for phase-*a* and phase-*b*, respectively. The resulting firing (delay) angles,  $\alpha_a$  and  $\alpha_b$  computed from (3.1) are used to generate the gate pulses for triggering the thyristors of the two controlled phases. It is of importance to mention that the  $\alpha$ -control approach [29] is adopted here in lieu of the  $\gamma$ -control approach [23]. This is due to the fact that the motor phase currents are unbalanced and unsymmetrical during the starting transient period, as was discussed in the preceding chapter. Consequently, the zero crossings of the currents will accordingly vary in all three phases. Therefore, the control response will become unstable if the  $\gamma$ -control method, which is dependent on the zero crossings of the line currents, is adopted. On the other hand, the zero crossings of the ac mains voltages are symmetrical and phase-shifted by  $120^\circ e$  from each other in all three phases, regardless of both the conditions of the soft starter and the electric motor. Hence, the  $\alpha$ -

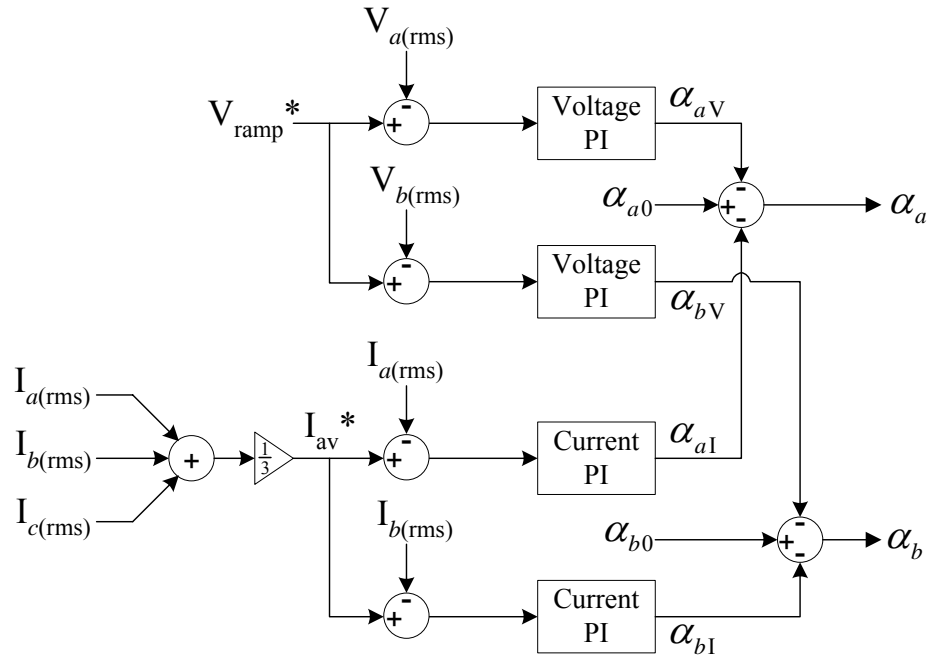


Figure 3.4: Present closed-loop two-phase control for fault tolerant soft starter.

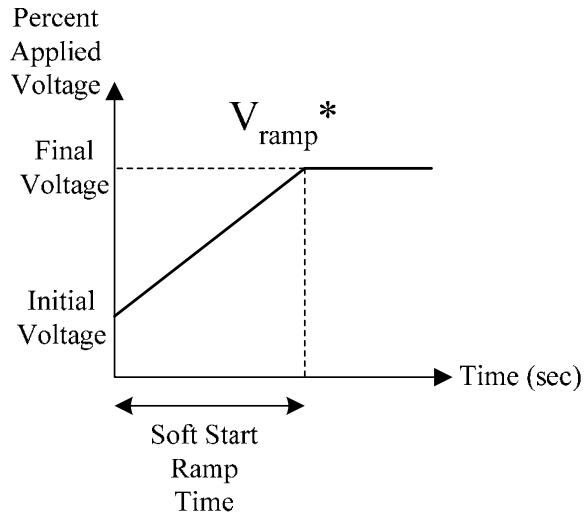


Figure 3.5: Reference voltage ramp profile.

control approach, which relies on the zero crossings of the mains voltages, provides a much more stable control response and thus it is employed in the present control approach.

The voltage feedback loop is used to control the starting acceleration profiles of the motor currents and torque. It controls the duration of the starting period which varies for different types of applications. A user-selected voltage ramp profile,  $V_{\text{ramp}}^*$ , is used as a reference command, as shown in Figure 3.5. It consists of an initial voltage setting, a final voltage setting, and a soft start (ramp) time setting. The user presets the initial phase voltage percentage that will be impressed upon the motor windings during the start-up process. Typically, a heavier load which requires a higher starting torque will need a higher initial impressed voltage. The final voltage setting will typically be the rated phase voltage of the motor. In addition, the soft start (ramp) time setting will determine the duration of the starting period before the motor establishes its rated speed. This voltage ramp profile,  $V_{\text{ramp}}^*$ , is analogous to the user-setting being utilized in industrial-type soft starters, where the user presets the initial locked rotor torque percentage and the soft start (ramp) time [31]-[33]. Once the voltage ramp profile,  $V_{\text{ramp}}^*$ , has been predefined during the start-up process, the effective (rms) values of the measured motor terminal voltages for the two controlled phases,  $V_{a(\text{rms})}$  and  $V_{b(\text{rms})}$ , are computed online during the motor starting transients. These values are then compared with the voltage reference profile,  $V_{\text{ramp}}^*$ , and the errors are conditioned by a set of voltage Proportional-Integral (PI) regulators. The outputs of the PI regulators represent the first part of the firing (delay) angles,  $\alpha_{aV}$  and  $\alpha_{bV}$ , see (3.1), for phase-*a* and phase-*b* firing (delay) angles,  $\alpha_a$  and  $\alpha_b$ , respectively.

With only the voltage feedback loop, the motor will still exhibit unbalanced starting currents, and consequently significant starting torque pulsations. Accordingly, in order to ensure nearly balanced three-phase motor currents during starting, a current feedback loop is utilized, see Figure 3.4. The effective (rms) values of the three-phase motor currents,  $I_{a(\text{rms})}$ ,  $I_{b(\text{rms})}$ , and  $I_{c(\text{rms})}$ ,

are measured and the average value of these currents,  $I_{av}^*$ , is used as the current reference command for the current controller, which is expressed as follows:

$$I_{av}^* = \frac{I_{a(rms)} + I_{b(rms)} + I_{c(rms)}}{3} \quad (3.2)$$

The average current,  $I_{av}^*$ , is compared with the measured effective (rms) motor currents of the two controlled phases,  $I_{a(rms)}$  and  $I_{b(rms)}$ , and the errors are conditioned by a set of current PI regulators. Here, the outputs of the PI regulators represent the second part of the firing angles,  $\alpha_{a1}$  and  $\alpha_{b1}$ , for phase-*a* and phase-*b* firing angles,  $\alpha_a$  and  $\alpha_b$ , respectively, see (3.1). By regulating the rms values of the two controlled phase currents,  $I_{a(rms)}$  and  $I_{b(rms)}$ , to be near the average current value,  $I_{av}^*$ , the rms value of the third phase current,  $I_{c(rms)}$ , is automatically adjusted to be the average current,  $I_{av}^*$ , so as to satisfy the condition of (3.2). As a result, a nearly balanced three-phase current condition is realized through this approach, which will in turn provide reduced starting torque transients. Meanwhile, in order to start up the motor from zero speed, an initial firing angle for each of the two controlled phases is commanded and is represented in Figure 3.4 as  $\alpha_{a0}$  and  $\alpha_{b0}$ . The final firing (delay) angle profiles for the two-phase control for triggering the two-phase thyristors are defined as given in (3.1).

### 3.3 Small-Signal Modeling of Motor-Soft Starter Controller

In this section, a small-signal model representing the motor-soft starter controller is developed. More specifically, the derivations of the open-loop and closed-loop (feedback) system transfer functions of the small-signal model consisting of the controller and the plant (induction motor + soft starter) are detailed here. A simplified control system representing the motor-soft starter of Figure 3.3, as well as the control algorithm of Figure 3.4 is shown here in Figure 3.6. It

consists of the transfer function of the plant,  $G_p(s)$ , the transfer function of the controller,  $G_c(s)$ , the reference inputs,  $I(s)^*$  and  $V(s)^*$ , and the system outputs,  $I(s)$  and  $V(s)$ . The plant is composed of a soft starter and an induction motor. Since the soft starter is a nonlinear electrical system, it is represented here by a nonlinear expression:  $V_{rms} = f(\alpha)$ , the derivation of which will be discussed in detail later on in this section. As for the induction motor, a simplified transfer function of it is also derived and presented here. On the other hand, the controller consists of a set of PI regulators for the voltage and current loops with unity feedback. It is the reason of tuning the PI regulators that the small-signal model of Figure 3.6 is being developed and analyzed for transient response and stability purposes.

As one may observe from the control system of Figure 3.6, there are two feedback loops, namely the voltage and current loops, which are operating in a parallel fashion. As was mentioned earlier, these two feedback loops serve different purposes. The voltage loop is responsible for the starting acceleration of the motor, while the current feedback loop is accountable for mitigating the unbalanced effects of the starting currents under thyristor switch fault condition. As a consequence, these two feedback loops are independent of one another, and hence the control feedback loop of each can be designed in an individual manner. Nevertheless, the motor can still function with only one feedback loop available, but at a much inferior performance such as having starting torque pulsations. Therefore, in designing the controller of Figure 3.6, the control system can be segregated into two separate individual control systems accountable for the voltage and current loops, as illustrated in Figure 3.7 and Figure 3.8, respectively. In doing so, the process of designing both the voltage and current regulators is simplified with only a single input and a single output in the control systems of both Figure 3.7 and Figure 3.8.

Upon observation of the voltage control loop as depicted in Figure 3.7, the plant of this voltage control system is now represented by the soft starter. This is due to the fact that the main

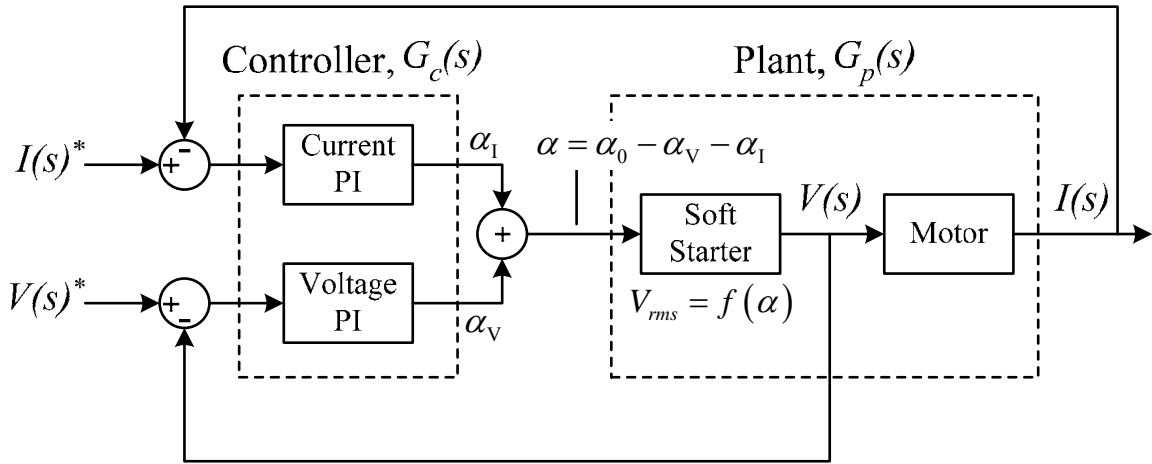


Figure 3.6: Simplified control system representation of motor-soft starter controller.

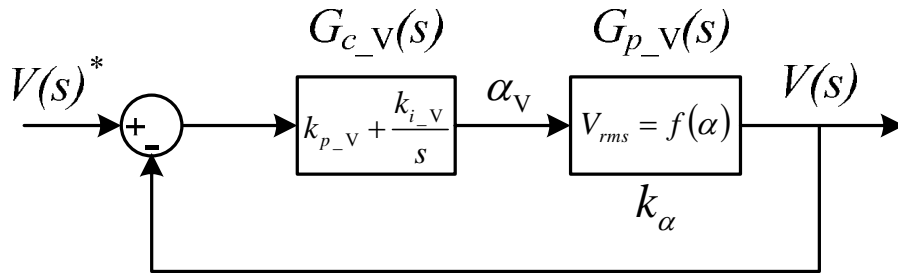


Figure 3.7: Voltage control loop.

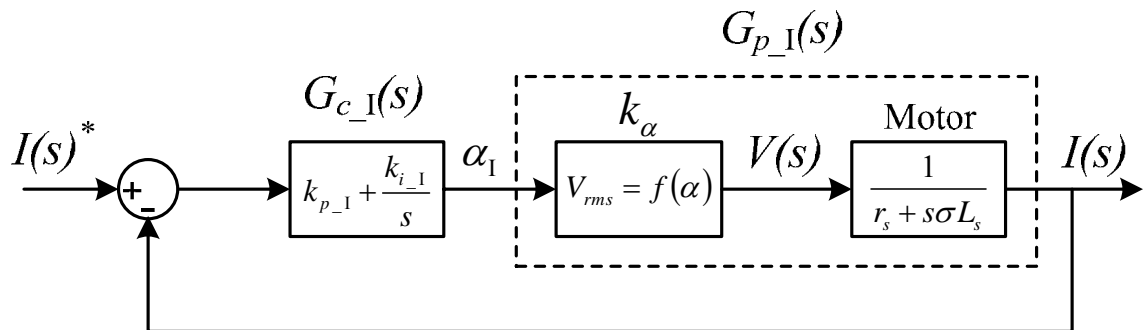


Figure 3.8: Current control loop.

thrust of the soft starter is to provide voltage excitation, which is dependent on the firing/delay angle profile, to the motor. Due to its nonlinear nature, the plant (or soft starter) is represented by a nonlinear expression:  $V_{rms} = f(\alpha)$ . Meanwhile, the controller consists of only the voltage PI regulator with a unity voltage feedback loop. On the other hand, in the current control system as shown in Figure 3.8, the plant consists of both the soft starter and the motor, and the controller is now a current PI regulator with a unity current feedback loop. The details of derivation of the corresponding small-signal models are set forth next.

### 3.3.1 Transfer Function of Controller

The transfer function of the PI controller is straightforward, and it is defined for the voltage and current loops,  $G_{c\_v}(s)$  and  $G_{c\_i}(s)$ , respectively, as follows:

$$G_{c\_v}(s) = k_{p\_v} + \frac{k_{i\_v}}{s} \quad (3.3)$$

$$G_{c\_i}(s) = k_{p\_i} + \frac{k_{i\_i}}{s} \quad (3.4)$$

where,  $k_{p\_v}$  and  $k_{p\_i}$  are the proportional gains, and  $k_{i\_v}$  and  $k_{i\_i}$  are the integral gains of the voltage and current controllers, respectively.

Owing to the separate control loop for the voltage and current controllers, the corresponding  $k_p$  and  $k_i$  can be easily designed to achieve the selected bandwidth at the crossover frequency where the gain of the open-loop transfer function equals unity using linear control theory. The design procedures are detailed in the coming section.

### 3.3.2 Transfer Function of Induction Motor

In an induction motor, the set of differential equations in  $dq$  representation that govern the instantaneous relationship between the voltages and currents in the synchronously rotating frame of reference can be expressed in the following manner [87]:

$$\begin{aligned}
v_{qs}^e &= r_s i_{qs}^e + \frac{d\lambda_{qs}^e}{dt} + \omega_e \lambda_{ds}^e \\
v_{ds}^e &= r_s i_{ds}^e + \frac{d\lambda_{ds}^e}{dt} - \omega_e \lambda_{qs}^e \\
0 &= r_r i_{qr}^e + \frac{d\lambda_{qr}^e}{dt} + (\omega_e - \omega_r) \lambda_{dr}^e \\
0 &= r_r i_{dr}^e + \frac{d\lambda_{dr}^e}{dt} - (\omega_e - \omega_r) \lambda_{qr}^e
\end{aligned} \tag{3.5}$$

where,

$$\begin{aligned}
\lambda_{qs}^e &= L_s i_{qs}^e + L_m i_{qr}^e \\
\lambda_{ds}^e &= L_s i_{ds}^e + L_m i_{dr}^e \\
\lambda_{qr}^e &= L_r i_{qr}^e + L_m i_{qs}^e \\
\lambda_{dr}^e &= L_r i_{dr}^e + L_m i_{ds}^e
\end{aligned} \tag{3.6}$$

Here,  $L_s = L_{ls} + L_m$  and  $L_r = L_{lr} + L_m$ , where,  $L_{ls}$  is the stator phase leakage inductance,  $L_{lr}$  is the referred rotor phase leakage inductance, and  $L_m$  is the magnetizing inductance in the T-equivalent circuit of an induction machine [88]. The first two equations of (3.5) correspond to the  $dq$  stator windings, while the last two equations of (3.5) correspond to the  $dq$  rotor windings. The equations of (3.6) represent the  $dq$  stator and rotor flux linkages. Meanwhile, the terms,  $\omega_e$  and  $\omega_r$ , denote the synchronous speed and the rotor speed in electrical radians/second, respectively. The superscript  $e$  indicates the synchronously rotating reference frame.

Under a balanced sinusoidal condition, the “synthetic”  $dq$  windings in the synchronously rotating reference frame will rotate at the same speed as the airgap magnetic field distribution. Hence, this results in a dc value representation of all the currents, voltages, and flux linkages associated with the  $dq$  stator and rotor windings (note that  $\omega_{slip} = \omega_e - \omega_r$ ). Accordingly, this makes the design process of the PI regulator a much easier task than designing using other reference frames.

From (3.6), one can rewrite the  $dq$  rotor winding currents from the  $dq$  rotor winding flux linkage terms, as follows:

$$\begin{aligned} i_{qr}^e &= \frac{\lambda_{qr}^e - L_m i_{qs}^e}{L_r} \\ i_{dr}^e &= \frac{\lambda_{dr}^e - L_m i_{ds}^e}{L_r} \end{aligned} \quad (3.7)$$

By substituting (3.7), as well as the  $dq$  stator winding flux linkage terms of (3.6) into the  $dq$  stator winding voltage expressions of (3.5), one obtains the following [89]:

$$\begin{aligned} v_{qs}^e &= r_s i_{qs}^e + \underbrace{\frac{d}{dt} \left[ \left( L_s - \frac{L_m^2}{L_r} \right) i_{qs}^e \right]}_{v_{qs}^{e'}} + \underbrace{\frac{d}{dt} \left( \frac{L_m}{L_r} \lambda_{qr}^e \right) + \omega_e \left[ \frac{L_m}{L_r} \lambda_{dr}^e + \left( L_s - \frac{L_m^2}{L_r} \right) i_{ds}^e \right]}_{\text{Compensation/Decoupling Terms}} \\ v_{ds}^e &= r_s i_{ds}^e + \underbrace{\frac{d}{dt} \left[ \left( L_s - \frac{L_m^2}{L_r} \right) i_{ds}^e \right]}_{v_{ds}^{e'}} + \underbrace{\frac{d}{dt} \left( \frac{L_m}{L_r} \lambda_{dr}^e \right) - \omega_e \left[ \frac{L_m}{L_r} \lambda_{qr}^e + \left( L_s - \frac{L_m^2}{L_r} \right) i_{qs}^e \right]}_{\text{Compensation/Decoupling Terms}} \end{aligned} \quad (3.8)$$

In the  $q$ -axis voltage equation of (3.8), only the first two terms on the right hand side are due to the  $q$ -axis current,  $i_{qs}^e$ . The next two terms of the same equation can be considered as the compensation or decoupling terms [89]. The same can be stated for the  $d$ -axis voltage equation.

Assuming the compensation or decoupling effect is perfect, the new  $dq$ -axis voltage equations can be expressed as follows [89]:

$$\begin{aligned} v_{qs}^{e'} &= r_s i_{qs}^e + \sigma L_s \frac{di_{qs}^e}{dt} \\ v_{ds}^{e'} &= r_s i_{ds}^e + \sigma L_s \frac{di_{ds}^e}{dt} \end{aligned} \quad (3.9)$$

where,  $\sigma = 1 - L_m^2 / L_s L_r$ . Hence, the induction motor (plant) can be simply represented by the above equation as defined in (3.9). The resulting voltage space vector,  $\vec{v}_s$ , can therefore be written in the following manner:

$$\vec{v}_s = v_{qs}^{e'} + jv_{ds}^{e'} = r_s \vec{i}_s + \sigma L_s \frac{d\vec{i}_s}{dt} \quad (3.10)$$

Accordingly, a per-phase motor model can be represented by the transfer function block diagram as depicted in Figure 3.9.

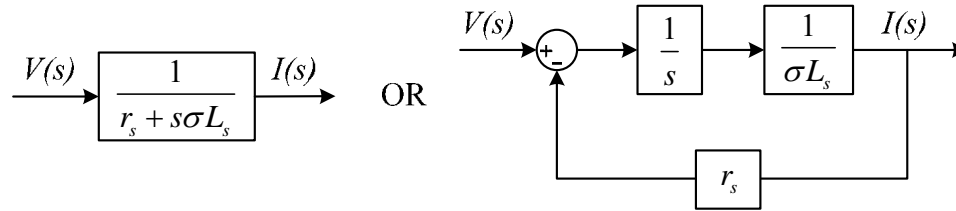


Figure 3.9: Transfer function of per-phase induction motor model.

### 3.3.3 Nonlinear Representation of Soft Starter

In order to incorporate the electrical behavior of a soft starter into the small-signal model representing the control system of Figure 3.6, a mathematical expression describing the nonlinear nature of the soft starter is derived and detailed here. The main thrust of the soft starter is to provide voltage excitation to the motor, where the rms value of this impressed voltage is dependent on the firing angle profile. Meanwhile, as one can see from Figure 3.6, the outputs of the voltage and current PI controllers yield  $\alpha_v$  and  $\alpha_1$ , respectively. This results in the firing angles,  $\alpha = \alpha_0 - \alpha_v$  and  $\alpha = \alpha_0 - \alpha_1$  for the voltage and current PI controllers, respectively, where  $\alpha_0$  denotes the initial firing angle. As a result, a mathematical expression which describes the relationship between the impressed rms voltage and the firing angle is developed here.

The closed-form expression of the motor line-to-neutral voltage was derived in the previous chapter and is given here in the following expression for phase-*a* over a complete cycle:

$$v_{an} = \begin{cases} e_a, & \phi < \omega t < \alpha \\ v_{ug}, & \alpha < \omega t < \phi + \pi/3 \\ 1/2 \cdot (v_{ug} - v_{vg} - e_c), & \phi + \pi/3 < \omega t < \alpha + \pi/3 \\ v_{ug}, & \alpha + \pi/3 < \omega t < \phi + 2\pi/3 \\ 1/2 \cdot (v_{ug} - v_{vg} - e_b), & \phi + 2\pi/3 < \omega t < \alpha + 2\pi/3 \\ v_{ug}, & \alpha + 2\pi/3 < \omega t < \phi + \pi \\ e_a, & \phi + \pi < \omega t < \alpha + \pi \\ v_{ug}, & \alpha + \pi < \omega t < \phi + 4\pi/3 \\ 1/2 \cdot (v_{ug} - v_{vg} - e_c), & \phi + 4\pi/3 < \omega t < \alpha + 4\pi/3 \\ v_{ug}, & \alpha + 4\pi/3 < \omega t < \phi + 5\pi/3 \\ 1/2 \cdot (v_{ug} - v_{vg} - e_b), & \phi + 5\pi/3 < \omega t < \alpha + 5\pi/3 \\ v_{ug}, & \alpha + 5\pi/3 < \omega t < \phi + 2\pi \end{cases} \quad (3.11)$$

where, the induced back emfs,  $e_a = e_b = e_c \approx 0$  during the soft starting transients, and  $v_{ug}$ ,  $v_{vg}$ , and  $v_{wg}$  represent the ac mains voltages, which are expressed as follows:

$$\begin{aligned} v_{ug}(t) &= V_m \cos(\omega t) \\ v_{vg}(t) &= V_m \cos(\omega t - 2\pi/3) \\ v_{wg}(t) &= V_m \cos(\omega t - 4\pi/3) \end{aligned} \quad (3.12)$$

Accordingly, from the above equations of (3.11) and (3.12), the rms value of the phase- $a$  voltage,  $V_{rms}$ , can be computed using the following expression:

$$V_{rms} = \sqrt{\frac{1}{2\pi} \int_{\phi}^{\phi+2\pi} v_{an}^2 d\theta} \quad (3.13)$$

After performing the necessary mathematical steps, the resulting  $V_{rms}$  can be expressed by the following nonlinear expression:

$$V_{rms} = \frac{V_m}{\sqrt{2\pi}} \sqrt{\pi + \frac{3}{2}\phi - \frac{3}{2}\alpha + \frac{3}{4}\sin(2\alpha) - \frac{3}{4}\sin(2\phi)} \quad (3.14)$$

Examination of (3.14) reveals that the only variable is the angle,  $\alpha$ , since  $V_m$  represents the peak magnitude of the ac mains voltage (in this case,  $V_m = \sqrt{2} \times 265$  Volt) and  $\phi$  is chosen to be  $60^\circ$

(or  $\pi/3$  rad) during the soft starting transients, as was mentioned earlier in the preceding chapter. It should also be noted that by selecting  $\alpha_0 = 120^\circ$  along with the fact that the  $\alpha$  firing/delay angle ranges from  $60^\circ$  to  $120^\circ$  during the starting transients, this results in  $\alpha_v$  and  $\alpha_1$  ranging from  $0^\circ$  to  $60^\circ$ . A plot of the motor phase voltage (rms) versus  $\alpha_v$  from  $0^\circ$  to  $60^\circ$  using (3.14) is depicted in Figure 3.10. As one can notice from Figure 3.10, at the point of  $\alpha_v = \phi = 60^\circ$ , the SCRs are fully on, which entails the rms voltage value of  $265 V_{rms}$  for a line-to-line utility voltage of  $460 V_{rms}$ .

Despite the nonlinear nature of the soft starter, a linear relationship between the rms motor phase voltage and the firing angle can be approximately realized at a selected operating point which results in:  $V_{rms} = k_\alpha \alpha_v$  and  $V_{rms} = k_\alpha \alpha_1$ , for the voltage and current loops, respectively, see Figure 3.7 and Figure 3.8. It should be emphasized that the units of  $\alpha_v$  and  $\alpha_1$  are in radians per second when computing the gain  $k_\alpha$ . Such linearization simplifies the design process in such a way that linear control systems theory can be employed. Here,  $\alpha_v$  and  $\alpha_1$  are assumed to have the same operating point. In this design process, an operating point is chosen where  $\alpha_v = \alpha_1 = 30^\circ$  or  $\pi/6$  rad. Hence, the constant  $k_\alpha$  can be calculated using (3.14). As a result, the linear transfer function of the soft starter at the chosen operating point can be approximately expressed for the voltage and current loops, respectively, as follows:

$$\begin{aligned} \frac{V_{rms}(s)}{\alpha_v(s)} &= k_\alpha \\ \frac{V_{rms}(s)}{\alpha_1(s)} &= k_\alpha \end{aligned} \quad (3.15)$$

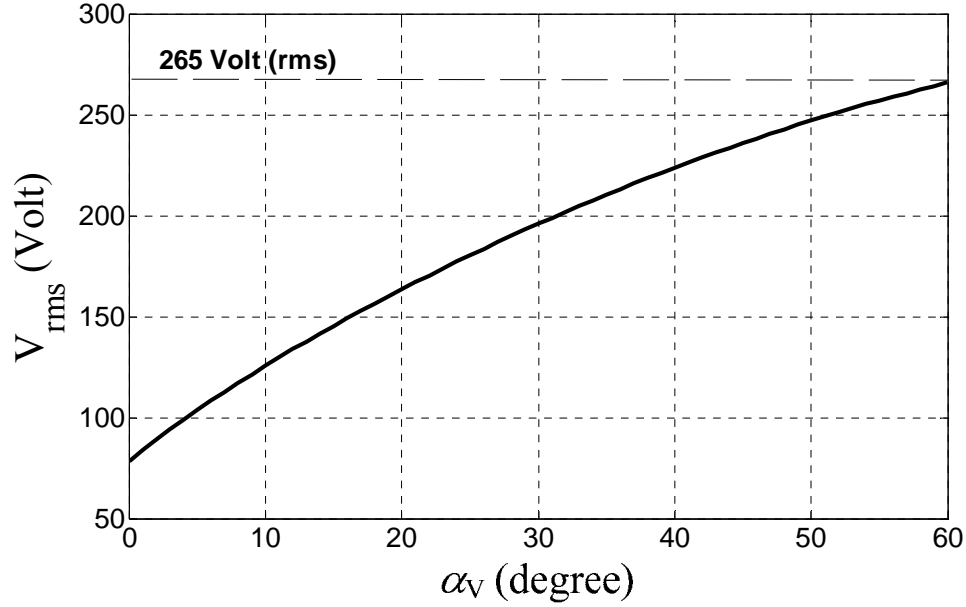


Figure 3.10: A plot of motor phase voltage (rms) versus  $\alpha_V$  using Equation (3.14).

### 3.3.4 Small-Signal Model Representation of Overall System

From the previously derived transfer function of each individual subsystem of Figure 3.6, a small-signal model of the voltage and current control loops can thus be developed. More specifically, the open-loop and closed-loop transfer functions of the voltage and current control loops are derived.

For the voltage control loop of Figure 3.7, the open-loop,  $G_{OL\_V}(s)$ , and the closed-loop,  $G_{CL\_V}(s)$ , transfer functions can be written as follows:

$$G_{OL\_V}(s) = G_{c\_V}(s)G_{p\_V}(s) = \left( k_{p\_V} + \frac{k_{i\_V}}{s} \right) (k_\alpha) = \frac{k_\alpha k_p s + k_\alpha k_i}{s} \quad (3.16)$$

$$G_{CL\_V}(s) = \frac{G_{OL\_V}}{1 + G_{OL\_V}} = \frac{k_\alpha k_p s + k_\alpha k_i}{(1 + k_\alpha k_p) s + k_\alpha k_i}$$

Meanwhile, for the current control loop of Figure 3.8, the open-loop,  $G_{OL\_1}(s)$ , and the closed-loop,  $G_{CL\_1}(s)$ , transfer functions can be expressed in the following manner:

$$G_{OL\_1}(s) = G_{c\_1}(s)G_{p\_1}(s) = \left(k_{p\_1} + \frac{k_{i\_1}}{s}\right)(k_\alpha) \left(\frac{1}{r_s + s\sigma L_s}\right) = \frac{k_\alpha k_p s + k_\alpha k_i}{\sigma L_s s^2 + r_s s} \quad (3.17)$$

$$G_{CL\_1}(s) = \frac{G_{OL\_1}}{1 + G_{OL\_1}} = \frac{k_\alpha k_p s + k_\alpha k_i}{\sigma L_s s^2 + (r_s + k_\alpha k_p)s + k_\alpha k_i}$$

The design procedures for obtaining  $k_p$  and  $k_i$  of the voltage and current PI regulators at selected bandwidth are detailed next.

## 3.4 Design Procedures of Soft Starter PI Controllers

The overall motor-soft starter system is designed at a desired bandwidth to provide good dynamic and fast transient responses to any changes in the reference input to the soft starter controller. Certain design conditions and criteria are assumed here in order to simplify the overall design process. In addition, since the soft starter is a nonlinear system, a certain operating point is selected so that the overall system is assumed to be linear around that selected operating point, thus allowing the basic concepts of linear control theory to be applied. Once the controller has been designed, the entire system is simulated under large-signal conditions to evaluate the adequacy, stability, and response of the controller, which will be presented in the following chapter.

### 3.4.1 Voltage Control Loop

In selecting the gain constants of the PI controller of the voltage control loop of Figure 3.7, the following are the design criteria:

- Crossover frequency of  $G_{OL\_v}(s)$ ,  $f_c = 500$  Hz.

- Phase Margin (PM) of  $G_{OL\_v}(s)$ ,  $\phi_{PM} = 120^\circ$ .

The crossover frequency,  $f_c$ , is defined as the frequency at which the gain of the open-loop transfer function equals unity, that is  $|G_{OL\_v}(s)| = 0$  dB. On the other hand, the phase margin,  $\phi_{PM}$ , is defined as the phase angle of the open-loop transfer function that is measured with respect to  $-180^\circ$  at the crossover frequency [90]. For a satisfactory dynamic transient response without any instabilities or oscillations, the phase margin should be chosen to be greater than  $45^\circ$  [90]. Meanwhile, the bandwidth (BW) of the overall closed-loop feedback system is defined as the frequency at which the gain of the closed-loop transfer function drops to  $-3$  dB. In some practical applications, the bandwidth of the closed-loop feedback system is approximately equal to the crossover frequency,  $f_c$  [90]. Hence, for a fast dynamic transient response by the control system, the bandwidth of the closed-loop system should be high, which indicates that the crossover frequency of the open-loop system should be designed to be high. In this design work, the crossover frequency,  $f_c$ , was selected to be 500 Hz so that the overall bandwidth of the voltage control loop is high enough to dynamically respond to changes in the reference input voltage.

Based on the aforementioned design criteria, the following two equations at the crossover frequency can be defined:

$$\begin{aligned} |G_{OL\_v}(s)|_{s=j\omega_c} &= \left| \frac{k_\alpha k_p s + k_\alpha k_i}{s} \right|_{s=j\omega_c} = 1 \\ \angle G_{OL\_v}(s)|_{s=j\omega_c} &= \angle \left( \frac{k_\alpha k_p s + k_\alpha k_i}{s} \right) \Bigg|_{s=j\omega_c} = -\pi + \phi_{PM} \text{ (rad)} \end{aligned} \quad (3.18)$$

where,  $\omega_c = 2\pi f_c$  is the angular crossover frequency in rad/sec. By solving these two equations above, one can acquire the gain constants,  $k_p$  and  $k_i$ , of the voltage control loop at the selected design conditions as given in the following expressions:

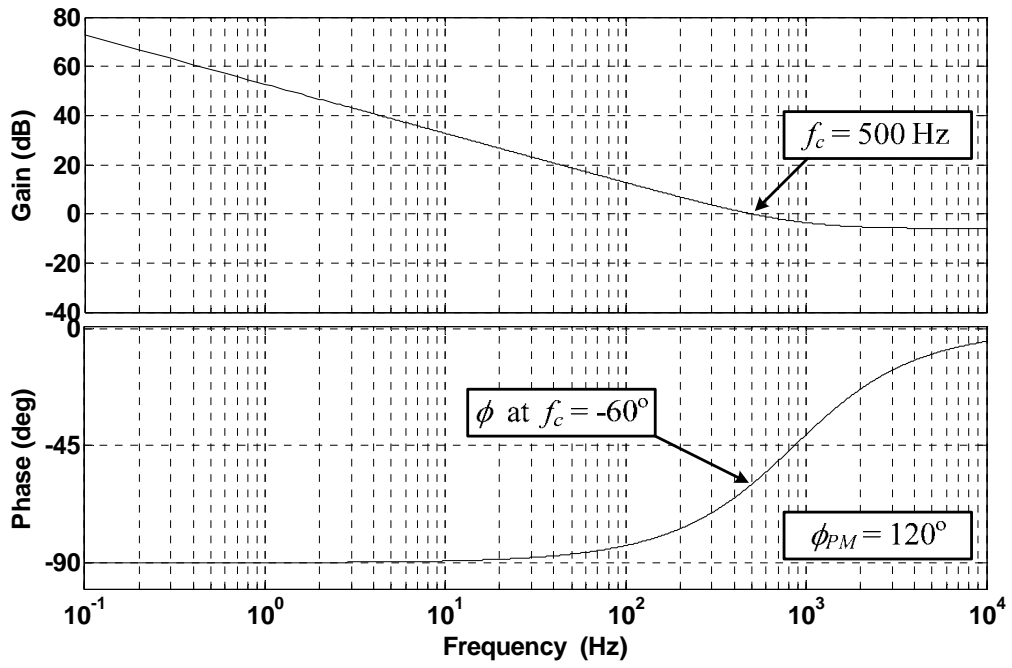
$$\begin{aligned}
 k_p &= \frac{1}{2k_\alpha} \\
 k_i &= \frac{\sqrt{3}\omega_c}{2k_\alpha}
 \end{aligned}
 \tag{3.19}$$

As discussed in earlier sections, the gain  $k_\alpha$  which represents the linear transfer function gain of the soft starter is computed at a selected operating point with the following conditions:  $\alpha = \alpha_0 - \alpha_v = 120^\circ - 30^\circ = 90^\circ$  or  $\pi/2$  rad,  $\phi = 60^\circ$  or  $\pi/3$  rad, and  $V_m = \sqrt{2} \times 265$  Volt. Accordingly, the gain  $k_\alpha$  was calculated from (3.14) and (3.15), resulting in a value,  $k_\alpha \approx 374$ . With this gain, knowing that  $\omega_c = 2\pi f_c = 2\pi \times 500$  rad/sec, the PI gain constants of the voltage control loop were calculated and found to be:  $k_p \approx 0.0013$  and  $k_i \approx 7.27$ .

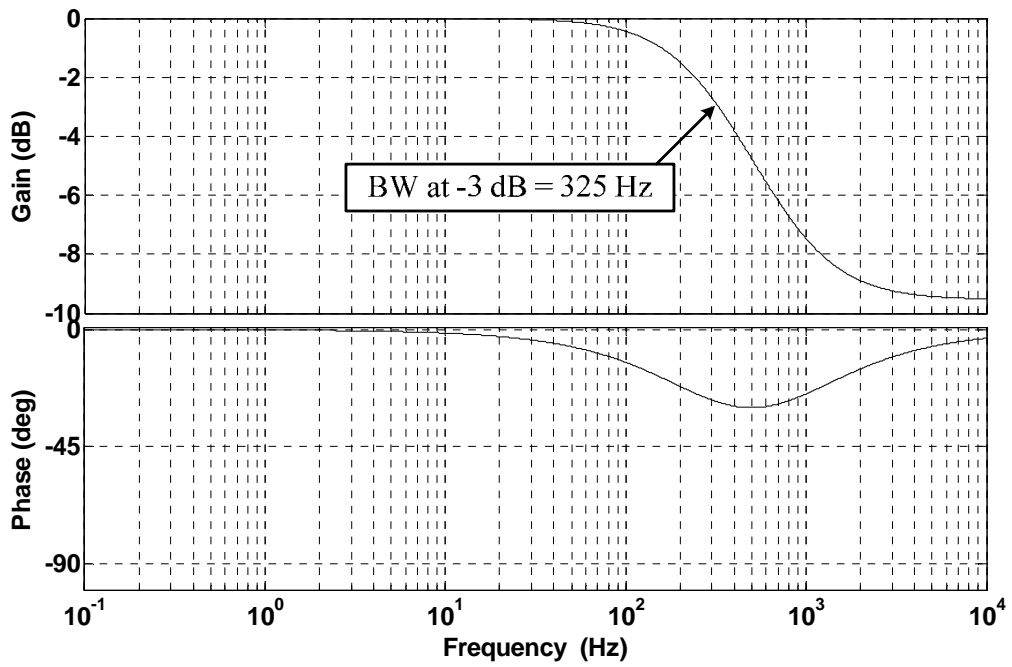
Using the computed gain constants of the voltage PI controller, the corresponding bode plots of the open-loop and closed-loop transfer functions of the voltage control loop system are depicted in Figure 3.11(a) and Figure 3.11(b), respectively. As one can observe from Figure 3.11(a), the desired crossover frequency,  $f_c$ , and the phase margin,  $\phi_{PM}$ , have been achieved, according to the design criteria, at 500 Hz and  $120^\circ$ , respectively. The subsequent bandwidth (BW) of the voltage control loop system of Figure 3.7 was found to be 325 Hz, as indicated in Figure 3.11(b). This bandwidth is adequately enough for the soft starter to respond to any variations in the reference input voltage profile. It should also be noticed from Figure 3.11(b) that the gain of the voltage control loop system is at its maximum, that is  $|G_{CL_v}(s)| = 0$  dB, within its bandwidth.

### 3.4.2 Current Control Loop

The current control loop of Figure 3.8 was designed in a similar manner to the voltage control loop. The following are the design criteria:



(a)



(b)

Figure 3.11: Bode plot of voltage control feedback loop system. (a) Open-loop transfer function. (b) Closed-loop transfer function.

- Crossover frequency of  $G_{OL\_1}(s)$ ,  $f_c = 500$  Hz .
- Phase Margin (PM) of  $G_{OL\_1}(s)$ ,  $\phi_{PM} = 90^\circ$  .

The open-loop transfer function of the current control feedback loop, which is given earlier in (3.17), is written here, as follows:

$$G_{OL\_1}(s) = G_{c\_1}(s)G_{p\_1}(s) = \frac{k_\alpha k_p s + k_\alpha k_i}{s(\sigma L_s s + r_s)} \quad (3.20)$$

To select the gain constants of the PI controller in the current control loop, a simple design procedure, which results in a phase margin of  $90^\circ$  as stated above in the design criteria, was implemented as follows:

**Step (1):** Select the zero of (3.20) to cancel its corresponding pole.

Under this condition,

$$\frac{k_i}{k_p} = \frac{1}{\sigma \tau_e} \Rightarrow k_p = \sigma \tau_e k_i \quad (3.21)$$

where,  $\tau_e = L_s/r_s$  is the electrical time constants. This consequently results in the following transfer function:

$$G_{OL\_1}(s) = \frac{k_\alpha k_i / r_s}{s} \quad (3.22)$$

Examination of (3.22) indicates that the phase margin,  $\phi_{PM}$ , is  $90^\circ$  which satisfies the above given design criteria.

**Step (2):** Compute the crossover frequency such that  $\left|G_{OL\_1}(s)\right|_{s=j\omega_c} = \left|\frac{k_\alpha k_i / r_s}{s}\right|_{s=j\omega_c} = 1$ .

This yields  $\omega_c = k_\alpha k_i / r_s$ . Using this equation along with (3.21), one can solve for the PI gain constants of the current control feedback loop of Figure 3.8, which are expressed as follows:

$$k_p = \frac{\sigma \tau_e r_s \omega_c}{k_\alpha} \quad (3.23)$$

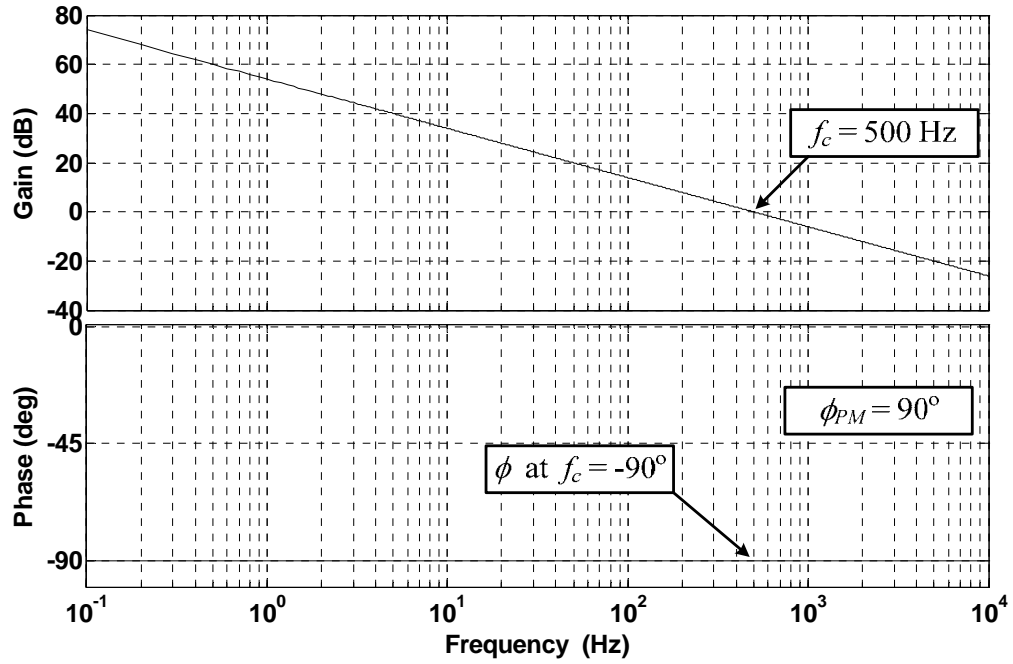
$$k_i = \frac{r_s \omega_c}{k_\alpha}$$

Using the same  $k_\alpha$  as was computed earlier, along with the given machine parameters of the case-study 2-hp induction motor (see Appendix A), the PI gain constants of the current control loop were computed to be,  $k_p \approx 0.3$  and  $k_i \approx 32.3$ .

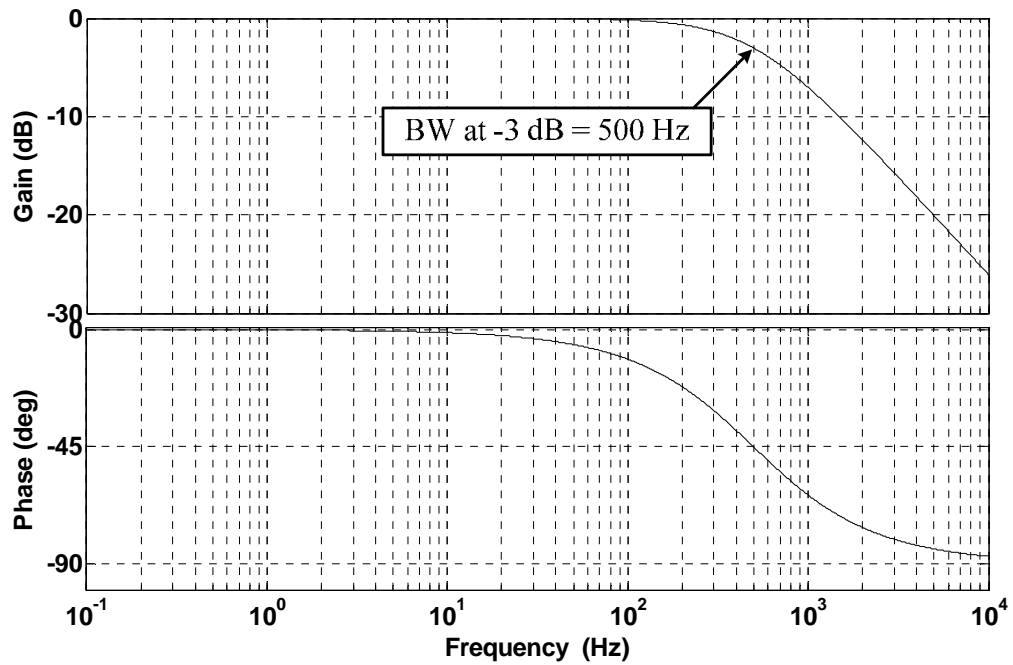
With the calculated  $k_p$  and  $k_i$  of the current PI regulator, the bode plots of the open-loop and closed-loop transfer functions of the associated current control feedback loop system of Figure 3.8 are illustrated in Figure 3.12(a) and Figure 3.12(b), respectively. Evidently, from both the bode plots of the open-loop and closed-loop transfer functions, the crossover frequency,  $f_c$ , and the bandwidth (BW) have been realized at 500 Hz, which fulfills the design criteria.

## 3.5 Summary

Low-cost fault tolerant solution capable of mitigating thyristor open and short-circuit switch faults for soft starters has been presented in this chapter. Minimum hardware modifications are required for the existing commercially available soft starter in order for the fault tolerant operation to be possible. It should be emphasized that such essential modifications do not significantly increase the cost and size of the existing system. One of the essential changes involves adding a set of three-phase voltage transducers on the motor end of the soft starter for acquiring the motor terminal voltages needed for fault tolerant control purposes. The second hardware modification involves the replacement of the existing 3-pole synchronously-controlled modular bypass contactor with a set of individually-controlled 1-pole contactors for all three



(a)



(b)

Figure 3.12: Bode plot of current control feedback loop system. (a) Open-loop transfer function. (b) Closed-loop transfer function.

phases. These contactors are used for fault isolation purposes in such a way that the soft starter can switch into a two-phase switching mode in the event of an SCR switch fault occurring in any one of the phases. As for the proposed two-phase control approach, two types of feedback control loops were adopted. Namely, these are the voltage and current feedback loops, respectively. The voltage feedback control is responsible for the starting acceleration of the motor, while the current feedback loop is responsible for mitigating the unbalanced effects of the starting currents under thyristor switch fault condition. In fact, by adopting the proposed control technique, a low-cost soft starter with only two-phase switching mode can be developed and produced in the market for consumers at a lower cost with reasonably good performance, as compared to the existing three-phase soft starter products.

In addition, small-signal modeling of the motor-soft starter controller system was developed. More specifically, the open-loop and closed-loop transfer functions of the voltage and current control feedback loop systems were derived. The main thrust of this small-signal modeling approach is to design the PI regulators in the voltage and current loops so as to achieve the desired bandwidth to render a good dynamic and fast transient response. Upon designing the PI controllers, the entire system was simulated under large-signal conditions to evaluate the stability and response of the controllers, which are presented in the next chapter.

## CHAPTER 4

---

---

# CIRCUIT SIMULATIONS OF FAULT TOLERANT SOFT STARTER

---

---

### 4.1 Introduction

In the preceding chapters, closed-form analytical solutions as well as proposed fault tolerant operating principles of soft starters under SCR switch fault conditions were presented. These closed-form solutions under healthy and faulty conditions were verified here using dynamic simulations that were carried out using a commercial circuit simulation software package, namely *Matlab-Simulink*. A 2-hp, 460-volt, 4-pole, three-phase induction motor was used as the target for these verification efforts, providing valuable results that raise confidence in the accuracy and value of the analytical results. Meanwhile, motor performance under fault tolerant control operations was also evaluated here using dynamic simulations. The simulation work indicates promising results that illustrate reduced starting torque pulsations under SCR switch fault condition through using the present two-phase control technique. Using the calculated gain constants of the PI regulators, the control system exhibits stable response to the increasing voltage in the reference input ramp during soft starting. Hence, this validates the accuracy of the

controller design approach. Accordingly, such promising results demonstrate the soundness and efficacy of the present control scheme.

## 4.2 Circuit Simulation Model

The simulation work was carried out in a *Matlab-Simulink* environment [91]. The power circuit structure of the induction motor-soft starter system is depicted in Figure 4.1. A 2-hp, 4-pole, 3-phase induction motor was used as the simulation target, whose machine parameters correspond to the design characteristics of the test motor in the experimental work. The motor properties of this 2-hp induction motor are given in Appendix A, and they are repeated here for convenience in Table 4.1. The motor was simulated in the  $dq$  frame of reference representation. Meanwhile, the load is of the fan type:  $T_L = k_L \omega_m^2$ , where  $\omega_m$  denotes the motor speed in mechanical radians per second, and  $k_L$  is the load coefficient in  $\text{Nm}/(\text{mech. rad}/\text{sec})^2$ .

On the other hand, the soft starter consists of three sets of back-to-back connected thyristors, which can be readily obtained from the Power System Blockset toolbox in *Simulink*. The parallel-connected  $RC$  elements for each phase have the following values:  $R = 500\Omega$  and  $C = 0.01\mu F$ . Meanwhile, the utility input voltage and line impedance values are given in Table 4.2. The line impedances are selected at 4.8% of the base impedance for both the line resistance and line inductance. This is in order to match the transformer power ratings currently present in the test laboratory.

The control block diagram of the proposed closed-loop two-phase control scheme is depicted in Figure 4.2. An input reference voltage ramp is preset at an initial voltage of 200-Volt, a final voltage of 265-Volt, and a soft start ramp time of 0.5 seconds. The PI regulators are designed with the values obtained from the previous chapter. They are  $k_p = 0.0013$  and  $k_i = 7.27$  for the

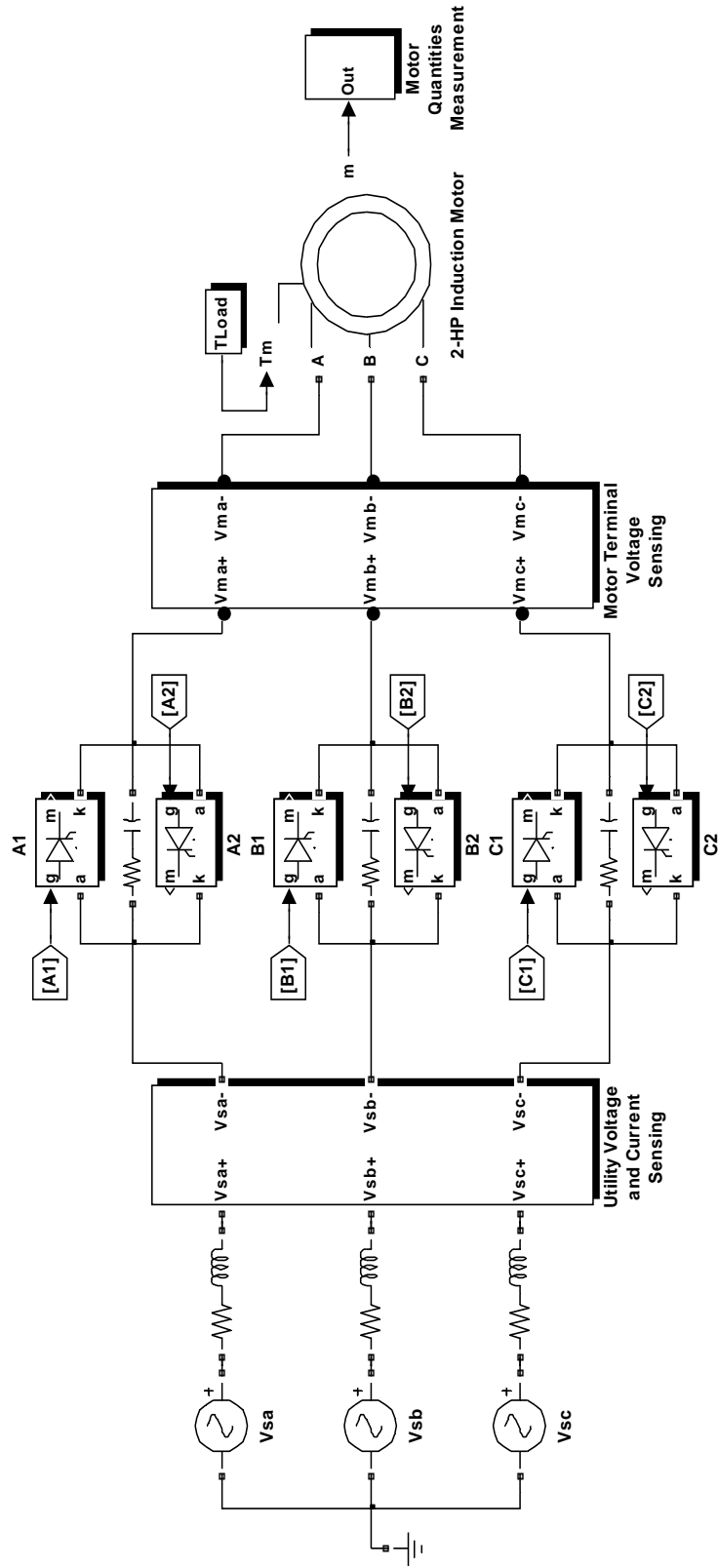


Figure 4.1: Schematic of motor-soft starter power structure in *Matlab-Simulink* [91].

Table 4.1: Design properties of 2-hp induction motor.

Rated Power	2 hp (1492 Watts)
Rated Voltage (Line-Line)	460 Volts
Rated Current	3.0 Amps
Rated Frequency	60 Hz
Rated Speed	1744 r/min
Rated Torque	8.169 Nm
Phase	3
Number of Poles	4
Stator Resistance, $R_s$	3.850 $\Omega$
Rotor Resistance, $R_r$	2.574 $\Omega$
Stator Leakage Inductance, $L_{ls}$	17.5594 mH
Rotor Leakage Inductance, $L_{lr}$	17.5594 mH
Magnetizing Inductance, $L_m$	0.372674 H
Moment of Inertia, $J$	0.028 kg.m <sup>2</sup>
Load Coefficient, $k_L$	$0.24493 \times 10^{-3}$ Nm/(m. rad/s) <sup>2</sup>

Table 4.2: Utility grid input parameters.

Utility Power	15 kW
Utility Input Voltage	460 Volts
Utility Input Current	18 Amps (rms)
Frequency	60 Hz
Line Resistance (4.8%)	0.7082 $\Omega$
Line Inductance (4.8%)	1.8786 mH

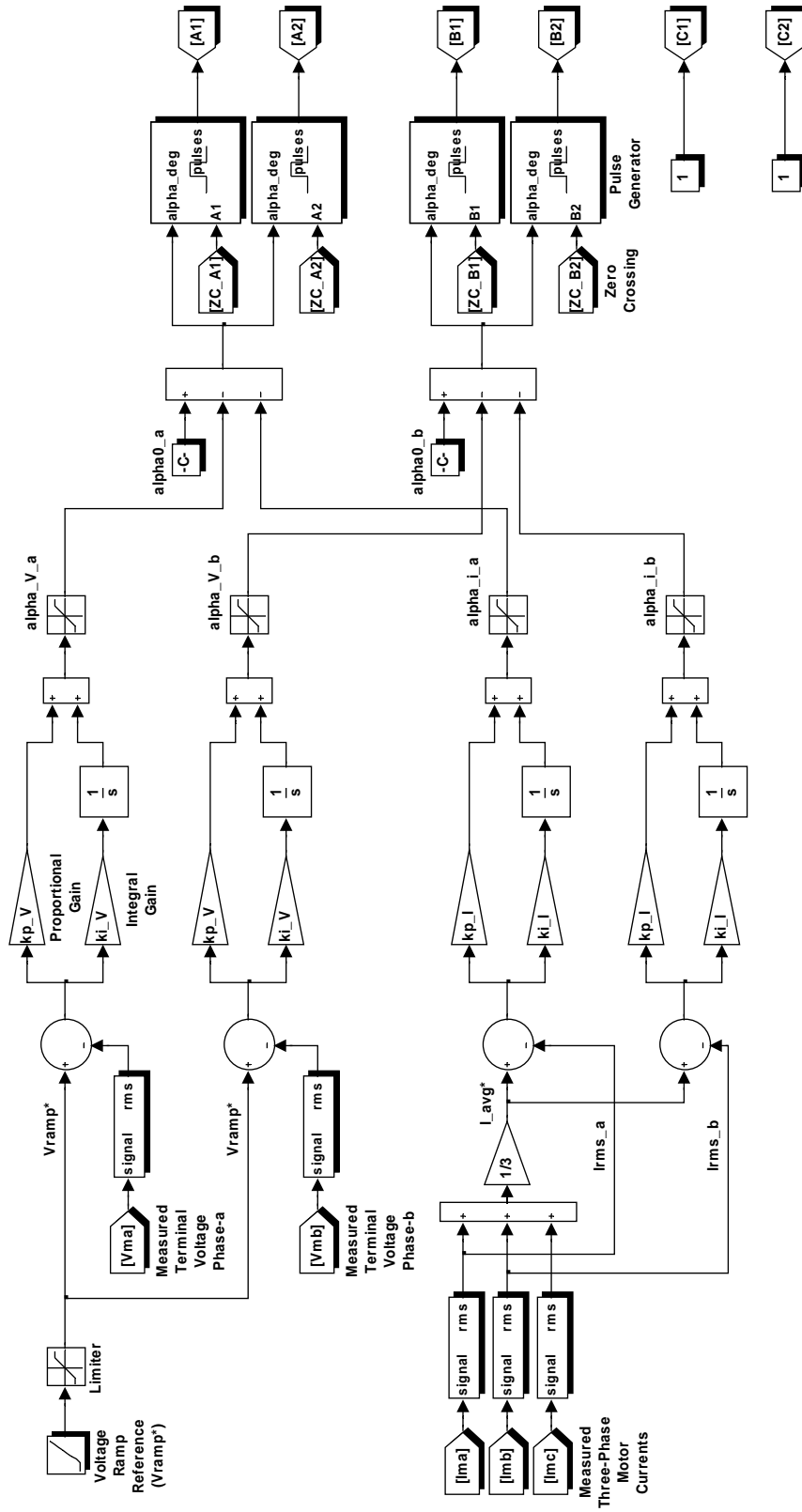


Figure 4.2: Block diagram of soft starter controller in *Matlab-Simulink* [91].

voltage PI controllers, and  $k_p = 0.3$  and  $k_i = 32.3$  for the current PI controllers. The initial firing/delay angles are set at  $110^\circ$ . The resulting firing/delay angles are fed into a set of pulse generators for synthesizing a train of gate pulses (high = 1, low = 0) for triggering the SCRs. In order to simulate the two-phase controls, an active high signal is fed into the gate of both the SCRs of phase-*c* so that the switches are turned-on at all time, see Figure 4.2. Finally, the simulation is carried out at a time step of  $10\mu\text{sec}$  (or a sampling frequency of 100 kHz).

## 4.3 Verifications between Closed-Form Analytical and Simulation Results

For convenience of the readers, the closed-form analytical results presented in Chapter 2 of this dissertation are repeated here for verification purposes with the simulation results. It is important to note that the simulation results presented here are obtained at nearly the same operating conditions that were utilized to compute the closed-form analytical results. In addition, open-loop symmetrical-triggering control was employed here in the simulation.

### 4.3.1 Healthy Condition

The three-phase line-to-neutral motor voltage waveforms obtained from closed-form solutions, along with the corresponding simulation waveforms under healthy condition at  $\phi = 60^\circ$  and  $\alpha = 90^\circ$  are depicted in Figure 4.3(a) and Figure 4.3(b), respectively. As one may observe, the calculated waveforms are in good agreement with the simulation waveforms. It is important to mention that the waveforms of Figure 4.3(a) are only valid for transient analysis, which is the subject of this work, due to the fact that the induced EMF in the windings cannot be neglected during the steady state operation.

The computed healthy three-phase current waveforms and the corresponding simulation waveforms at transient operating conditions of  $\phi = 60^\circ$ ,  $\alpha = 90^\circ$ , and a motor speed of 200-r/min are shown in Figure 4.4(a) and Figure 4.4(b). It can be seen from Figure 4.4 that the analytical waveforms match reasonably well with the simulation waveforms, in so far as the profiles and peak magnitudes are concerned. For further comparisons, the harmonic contents of the motor phase voltages of Figure 4.3 and the motor phase currents of Figure 4.4 are given in Table 4.3 and Table 4.4, respectively. Again, as one can see from the harmonic comparisons, the analytical results are in close agreement with the simulation results.

The RMS values of the three-phase currents during the entire soft starting period obtained from analytical solutions and dynamic simulations are depicted in Figure 4.5. As may be observed from the figure, the analytical results are congruent with the simulation results during soft starting. However, the analytical results begin to deviate from the simulations as the currents are approaching their rated values. This is due to the fact that the induction motor is no longer highly inductive as the motor is approaching its rated speed. Therefore, the phase angle,  $\phi$ , is approaching the power factor angle in the simulations, whereas this angle is kept constant at  $60^\circ$  in the closed-form solution. Another reason is due to the assumption that the induced EMFs in the windings are negligible in the closed-form analysis, which is no longer valid as the motor is approaching its rated speed. Nevertheless, the objective of this work is to analyze the motor transient performance during soft starting. Therefore, the analytical results presented here are acceptable for this stage of the work.

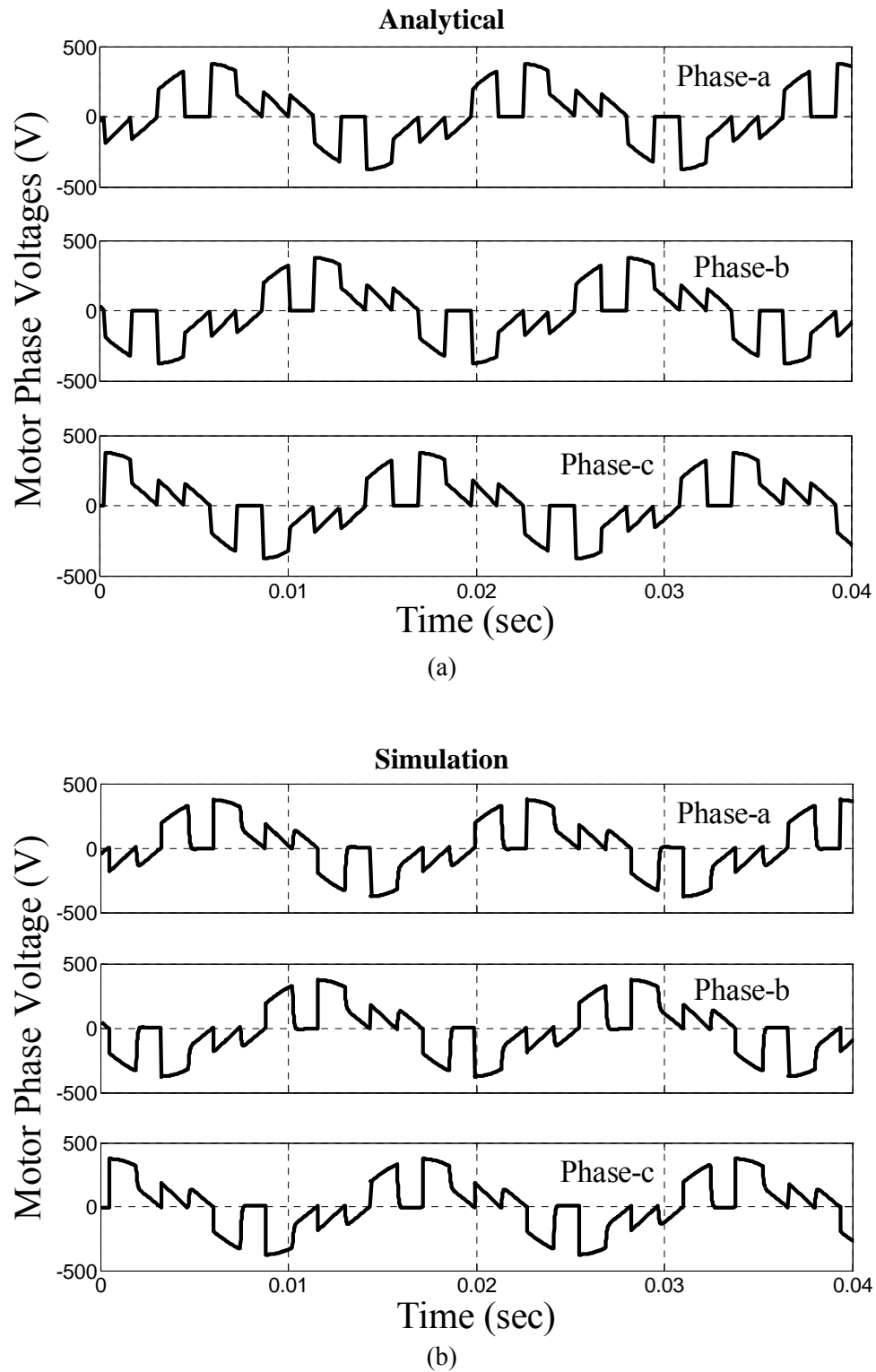


Figure 4.3: *Healthy* three-phase line-to-neutral motor voltage waveforms at operating conditions of  $\phi = 60^\circ$  and  $\alpha = 90^\circ$ . (a) Analytical. (b) Simulation.

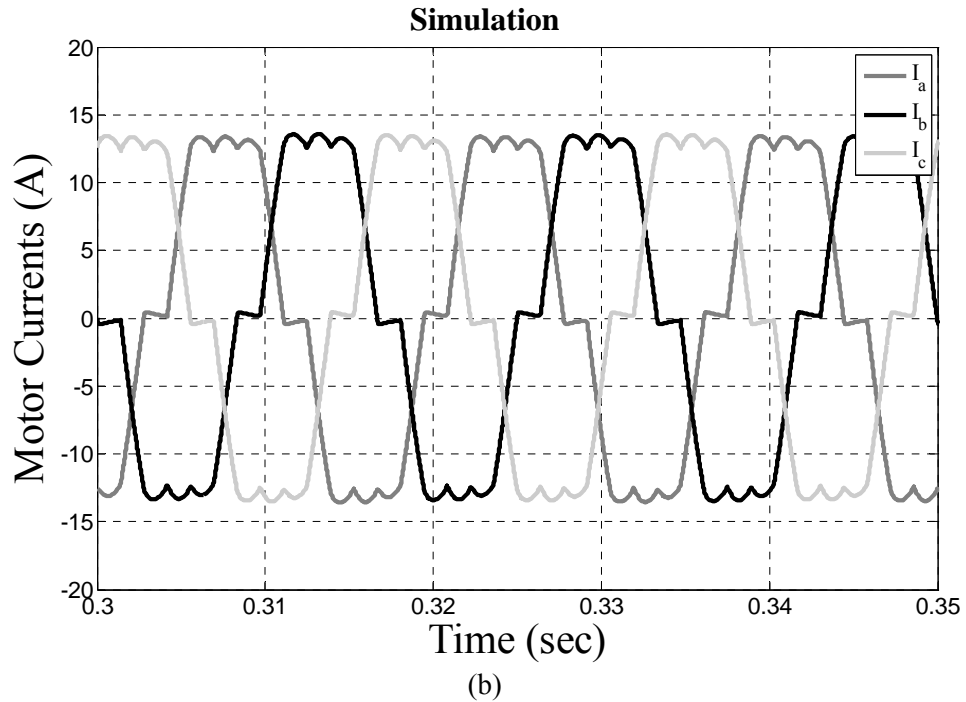
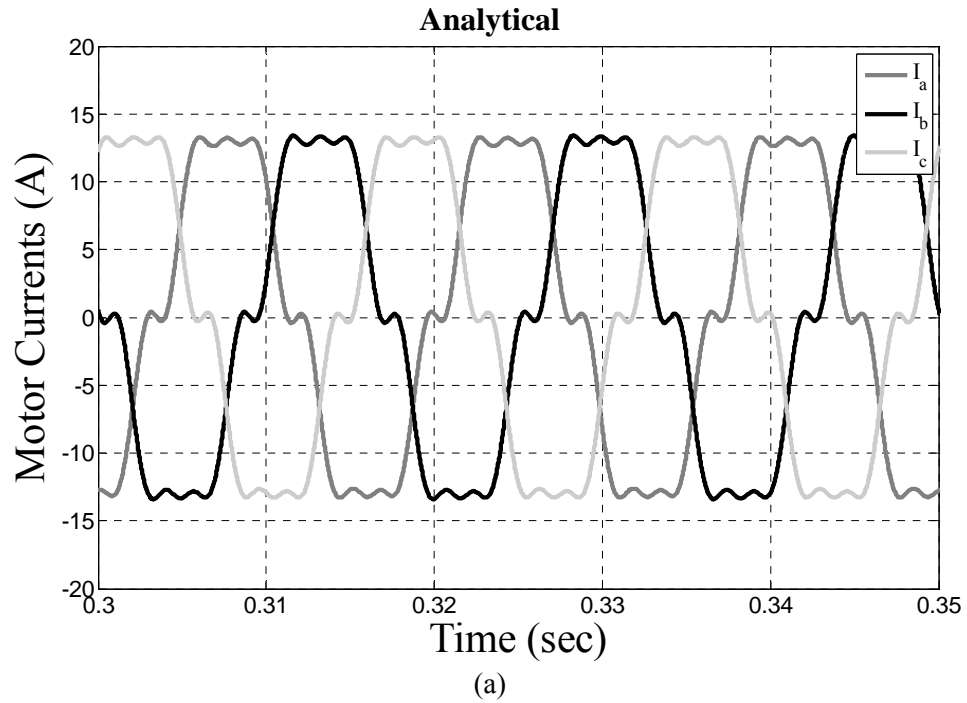


Figure 4.4: *Healthy* three-phase current waveforms at transient conditions of  $\phi = 60^\circ$ ,  $\alpha = 90^\circ$ , and motor speed of 200-r/min. (a) Analytical. (b) Simulation.

Table 4.3: Harmonic contents of *healthy* three-phase motor phase voltages – Analytical and Simulation.

Harmonic Order	Analytical			Simulation		
	$V_{ma}$ (Volt)	$V_{mb}$ (Volt)	$V_{mc}$ (Volt)	$V_{ma}$ (Volt)	$V_{mb}$ (Volt)	$V_{mc}$ (Volt)
1	207.30	208.90	208.10	206.22	207.75	207.20
3	0	0	0	0	0	0
5	131.40	131.80	131.90	134.97	134.23	133.66
7	94.11	93.54	94.62	97.38	97.95	98.68
9	0	0	0	0	0	0
11	17.28	18.60	16.41	21.37	21.68	21.40
13	12.45	11.17	13.18	9.49	8.14	9.57
15	0	0	0	0	0	0
17	35.18	35.55	35.23	37.33	36.55	36.01
19	31.37	30.98	31.69	34.11	34.62	35.37
21	0	0	0	0	0	0

Table 4.4: Harmonic contents of *healthy* three-phase motor currents – Analytical and Simulation.

Harmonic Order	Analytical			Simulation		
	$I_{ma}$ (Amps)	$I_{mb}$ (Amps)	$I_{mc}$ (Amps)	$I_{ma}$ (Amps)	$I_{mb}$ (Amps)	$I_{mc}$ (Amps)
1	14.255	14.340	14.326	14.212	14.180	14.234
3	0	0	0	0	0	0
5	2.021	2.027	2.028	2.077	2.035	2.032
7	1.036	1.030	1.042	1.073	1.085	1.109
9	0	0	0	0	0	0
11	0.121	0.131	0.115	0.151	0.159	0.157
13	0.074	0.066	0.078	0.056	0.054	0.059
15	0	0	0	0	0	0
17	0.160	0.162	0.160	0.169	0.161	0.154
19	0.128	0.126	0.129	0.139	0.137	0.149
21	0	0	0	0	0	0

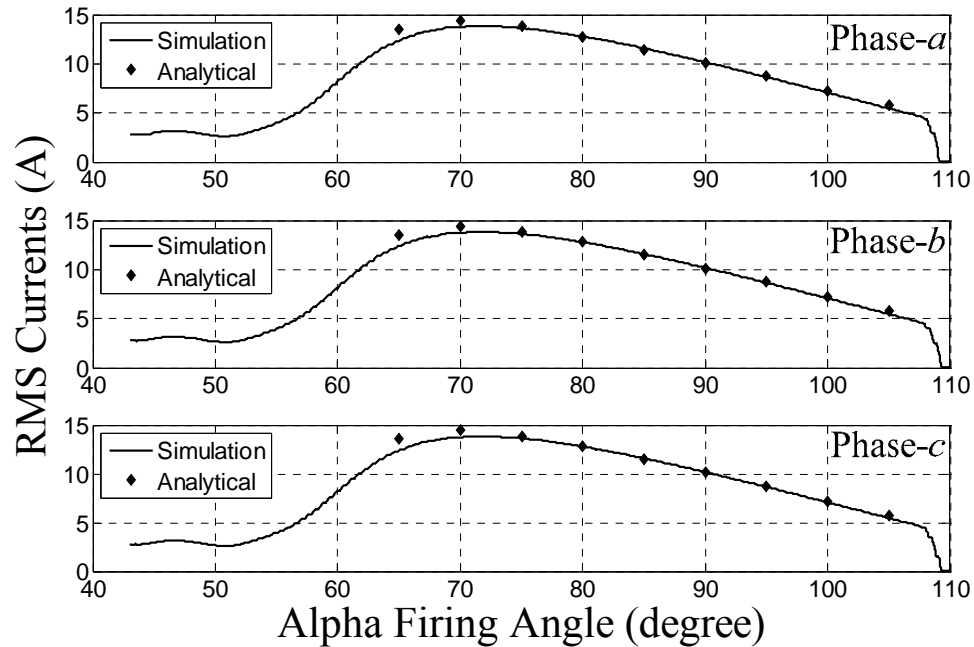


Figure 4.5: RMS values of *healthy* three-phase stator currents from analytical solution and dynamic simulation.

### 4.3.2 Short-Circuit SCR Switch Fault Condition

The analytical waveforms of the three-phase line-to-neutral motor voltages, and the corresponding simulation waveforms are illustrated in Figure 4.6(a) and Figure 4.6(b), respectively. From the figures, one can state that the analytical waveforms are in good agreement with the simulation waveforms, in so far as the profiles are concerned. Meanwhile, the computed currents and its associated simulated three-phase motor currents at transient operating conditions of  $\phi = 60^\circ$ ,  $\alpha = 90^\circ$ , and a motor speed of 400-r/min are shown in Figure 4.7(a) and Figure 4.7(b), respectively. As one can observe, there is a certain degree of similarity between the analytical and simulation waveforms. Furthermore, the harmonic breakdown of the motor phase voltages of Figure 4.6 and the motor phase currents of Figure 4.7 are given in Table 4.5 and Table 4.6, respectively. As one can observe from the harmonic comparisons, the analytical results match fairly well with the simulation results, except for some of the higher-order harmonic

components for which the analytical results tend to over-estimate or under-estimate the higher harmonic amplitudes. This may be due to the simplifying assumptions built into the analytical model derivations. The RMS values of the three-phase currents during the entire soft starting period obtained from analytical solutions and dynamic simulations are depicted in Figure 4.8. Notice that the currents are unbalanced during starting which can be further validated by the simulated three-phase currents under a short-circuit SCR switch fault, as illustrated in Figure 4.8. These unbalanced currents will accordingly lead to undesired transient torque pulsations, as will be demonstrated next.

Evidently, from the aforementioned results, the simulation work has confirmed the key analytical results of this investigation. Such efforts validate the fidelity of the closed-form analytical approach, which provides an alternative means of acquiring the transient motor performance in lieu of pursuing the simulation approach.

## 4.4 Motor Performance under Fault Tolerant Operations

In this section, the motor performance resulting from using the resilient closed-loop two-phase control technique is compared with that when using the conventional symmetrical-triggering open-loop three-phase as well as two-phase controls. The main thrust is to demonstrate the efficacy of the present approach under switch fault conditions over the open-loop control approach, with minimum starting torque transient.

The conventional three-phase soft starter using open-loop voltage control was first simulated. The results of the three-phase motor currents are shown in Figure 4.9(a). As one may observe therein, the motor currents have smooth starting profiles as the firing angle is decreasing, with low starting currents. To demonstrate the voltage unbalance effects due to open-loop two-

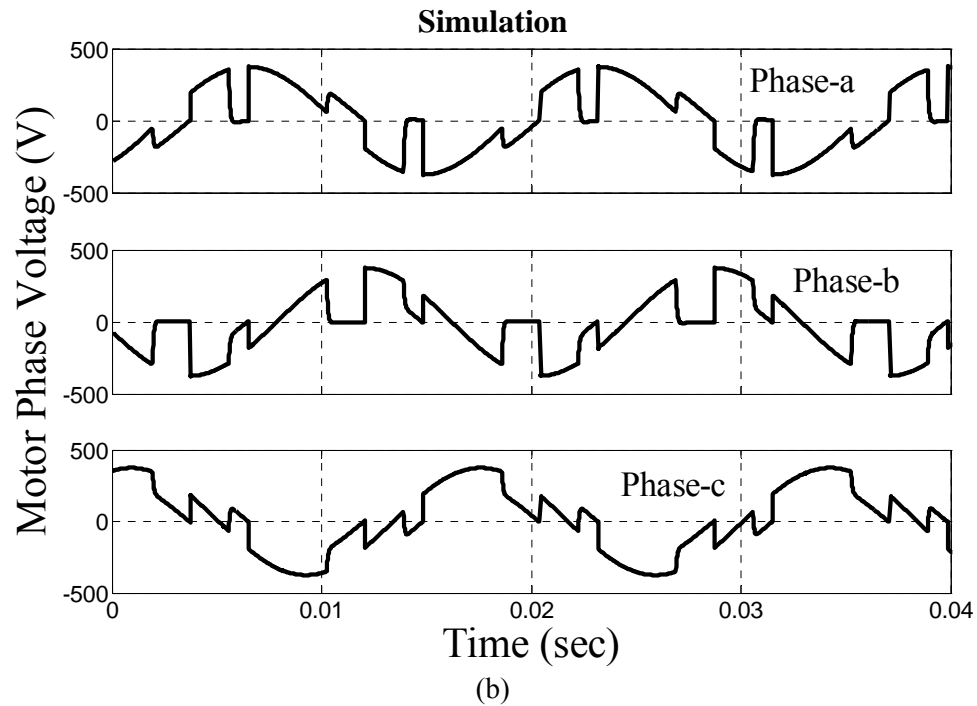
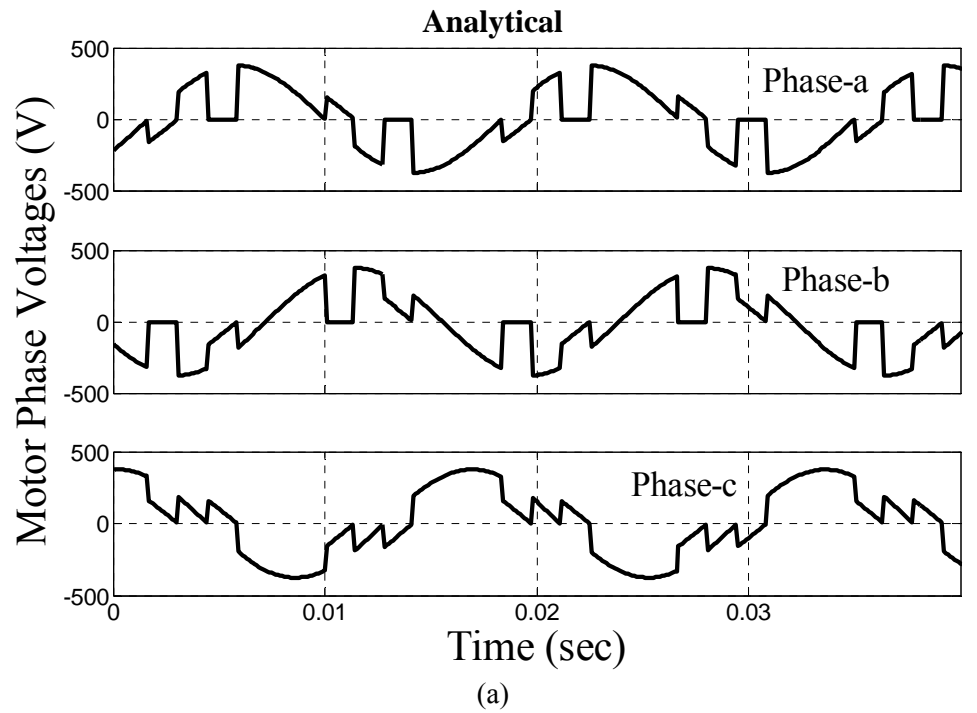


Figure 4.6: Three-phase line-to-neutral motor voltage waveforms at operating conditions of  $\phi = 60^\circ$  and  $\alpha = 90^\circ$  under a *short-circuit SCR fault*. (a) Analytical. (b) Simulation.

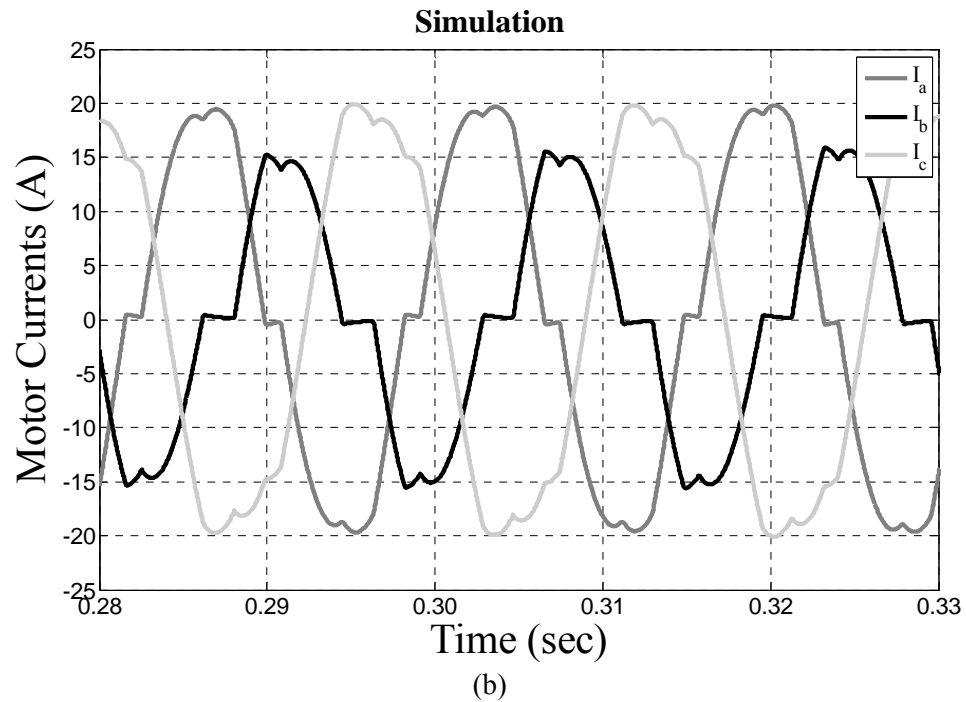
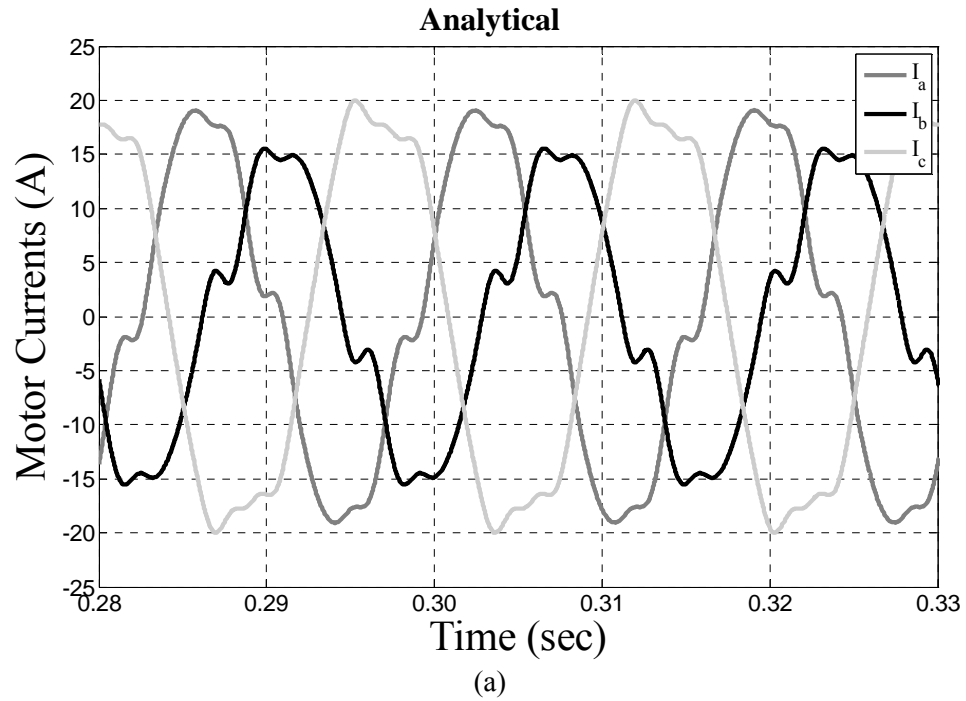


Figure 4.7: Three-phase current waveforms at transient conditions of  $\phi = 60^\circ$ ,  $\alpha = 90^\circ$ , and motor speed of 400-r/min under a *short-circuit SCR fault*. (a) Analytical. (b) Simulation.

Table 4.5: Harmonic contents of three-phase motor phase voltages under a *short-circuit SCR fault* – Analytical and Simulation.

Harmonic Order	Analytical			Simulation		
	$V_{ma}$ (Volt)	$V_{mb}$ (Volt)	$V_{mc}$ (Volt)	$V_{ma}$ (Volt)	$V_{mb}$ (Volt)	$V_{mc}$ (Volt)
1	259.30	220.80	318.80	270.97	200.22	300.35
3	54.98	52.48	107.50	48.46	41.81	102.99
5	116.60	116.20	43.55	117.73	124.22	39.75
7	82.65	82.85	32.03	75.70	72.70	36.03
9	17.12	19.23	36.30	49.33	20.35	29.35
11	15.62	16.70	5.64	35.88	27.28	28.45
13	10.67	9.60	4.31	41.29	44.65	6.55
15	10.88	8.60	19.44	4.82	15.20	17.05
17	31.60	31.24	11.32	3.73	4.96	2.30
19	27.35	27.55	11.01	9.32	13.15	7.18
21	6.11	7.98	14.03	9.48	15.35	14.73

Table 4.6: Harmonic contents of three-phase motor currents under a *short-circuit SCR fault* – Analytical and Simulation.

Harmonic Order	Analytical			Simulation		
	$I_{ma}$ (Amps)	$I_{mb}$ (Amps)	$I_{mc}$ (Amps)	$I_{ma}$ (Amps)	$I_{mb}$ (Amps)	$I_{mc}$ (Amps)
1	18.752	14.043	21.666	19.621	13.413	20.740
3	1.397	1.333	2.731	1.350	1.300	2.605
5	1.793	1.787	0.670	1.807	1.892	0.628
7	0.910	0.912	0.353	0.806	0.760	0.381
9	0.147	0.165	0.312	0.417	0.157	0.261
11	0.110	0.117	0.040	0.253	0.205	0.206
13	0.063	0.057	0.026	0.247	0.269	0.034
15	0.056	0.044	0.100	0.027	0.068	0.082
17	0.144	0.142	0.051	0.017	0.019	0.005
19	0.111	0.112	0.045	0.035	0.045	0.026
21	0.022	0.029	0.052	0.037	0.062	0.055

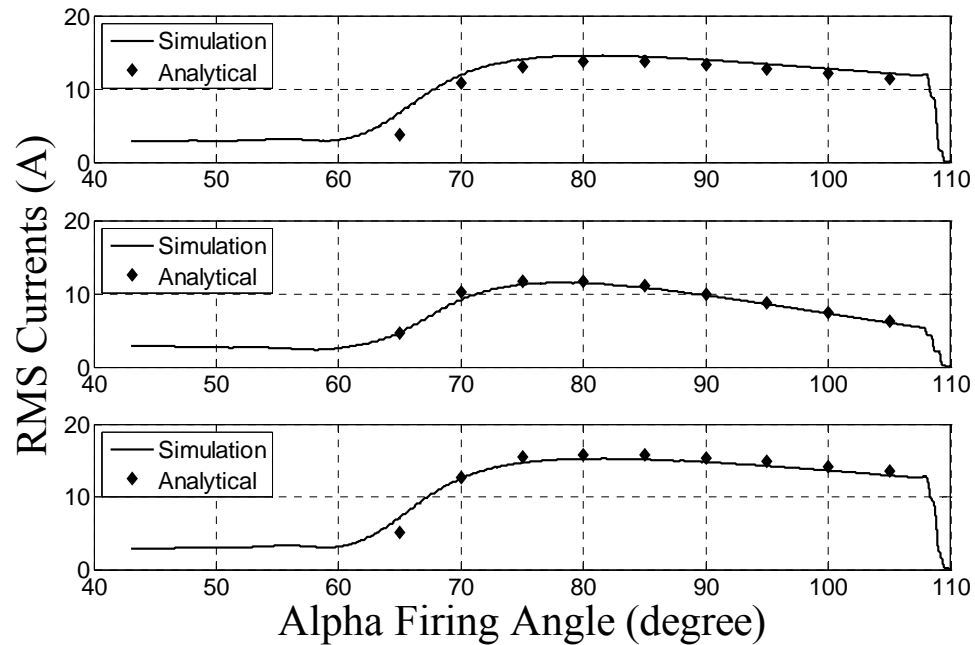


Figure 4.8: RMS values of three-phase stator currents from analytical solution and dynamic simulation under a *short-circuit SCR fault*.

phase operation, the control method applied to the three-phase soft starter was utilized except that one phase of the back-to-back thyristors is always maintained in the “on” state. In reality, this is equivalent to isolating the faulty switch by closing the corresponding by-pass contactor so that there is a direct electrical connection between the ac mains and the associated motor phase. The results of the motor phase currents are depicted in Figure 4.9(b). Notice the high motor current unbalances during the starting transients. This is not the case for the present closed-loop two-phase control, the results of which are illustrated in Figure 4.9(c). As may be noted in Figure 4.9(c), the three-phase motor currents have reasonably smooth starting profiles, which indicate significant starting transient improvement, in comparisons to that of Figure 4.9(b) due to open-loop two-phase control. Even though the currents of Figure 4.9(c) have a higher breakdown current value than that of Figure 4.9(b), the starting inrush currents are lower as compared to that of Figure 4.9(b).

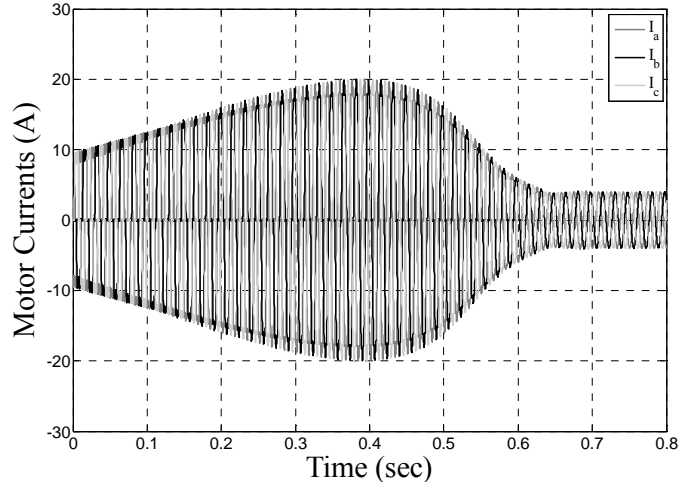
To further demonstrate the fineness of the present approach, the current space-vector plots of the motor currents in the form of  $\vec{i}_s = i_q + ji_d = 2/3 \cdot (i_a + i_b e^{j2\pi/3} + i_c e^{j4\pi/3})$  are given in Figure 4.10(a), (b), and (c), for the three-phase open-loop, the two-phase open-loop, and the proposed two-phase closed-loop controls, respectively. The current space-vector plot due to three-phase open-loop control, see Figure 4.10(a), exhibits a circular locus with the 12 distinct switching states. On the other hand, the two-phase open-loop control results in an elliptic locus with higher starting currents, as shown in Figure 4.10(b). Notice the 8 distinct switching states that the locus presents due to this control method. An improved starting transient of the current space-vector plot with a circular locus can be observed from Figure 4.10(c) for the proposed closed-loop two-phase control approach.

The developed motor torque profiles for all three control cases are depicted in Figure 4.11. Again, one can see a smooth starting profile with minimum torque pulsations in Figure 4.11(a). However, this is not the case under open-loop two-phase control, as can be observed from Figure 4.11(b). An improved starting torque profile for the proposed approach is illustrated in Figure 4.11(c). It can be seen from the figure that the starting torque pulsations are significantly reduced as compared to those of Figure 4.11(b).

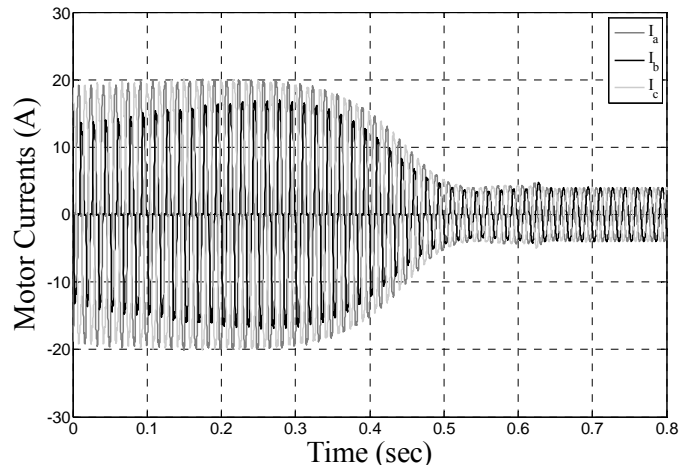
## 4.5 Summary

The first part of this chapter is to verify the accuracy of the closed-form analytical results versus the simulation results. It has been shown that the analytical results are in good correspondence with the simulation results, which raises confidence in the fidelity and value of the analytical approach. Such efforts provide an alternative means of analyzing the transient performance of the motor besides using the simulation approach. The second part of the work involves comparing the motor performance under three different control cases, namely, three-

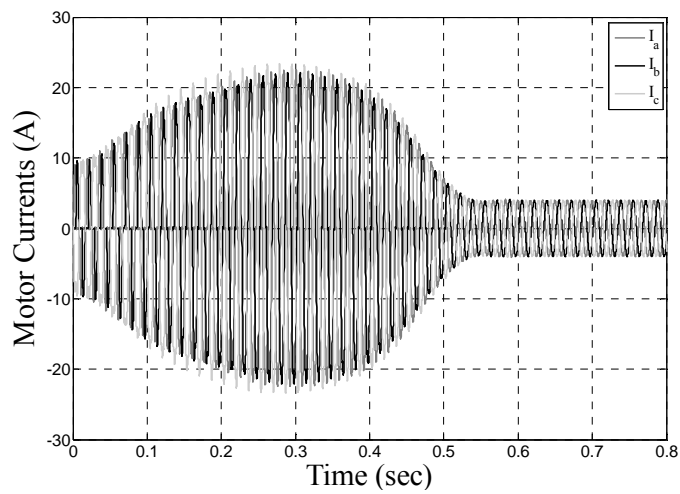
phase open-loop, two-phase open-loop, and proposed two-phase closed-loop controls. The present fault tolerant resilient control has demonstrated reduced starting inrush currents, and consequently reduced starting torque pulsations under thyristor fault in one phase of the soft starter, as compared to the two-phase open-loop control case. These promising results demonstrate the feasibility of the proposed strategy for improving the reliability of an industrial-type three-phase soft starter system at a modest cost increase.



(a)



(b)



(c)

Figure 4.9: Simulation results of three-phase current waveforms. (a) 3-phase open-loop control. (b) 2-phase open-loop control. (c) Proposed 2-phase closed-loop control.

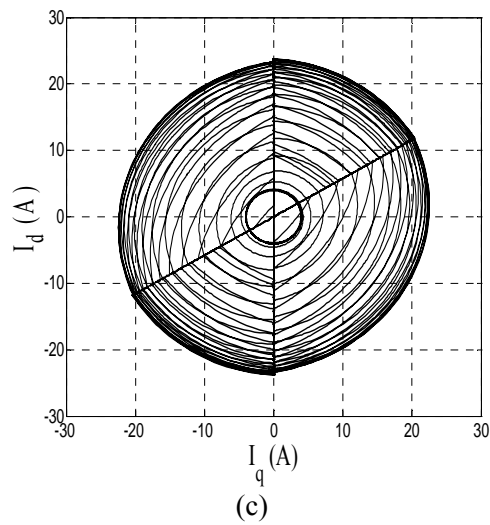
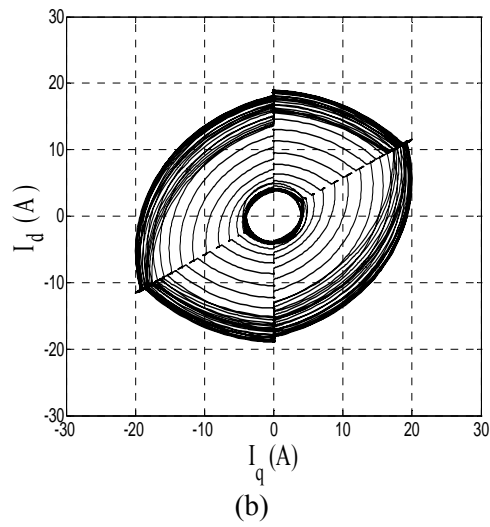
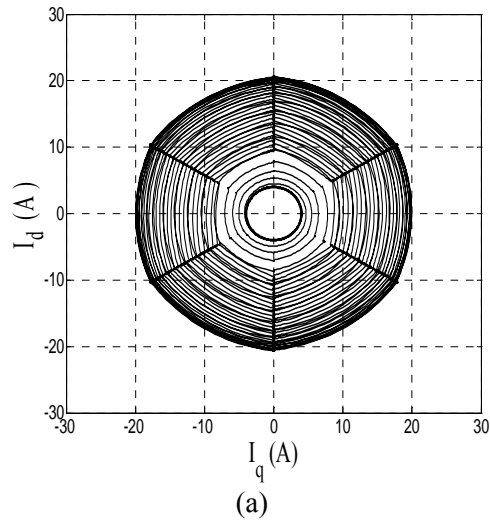
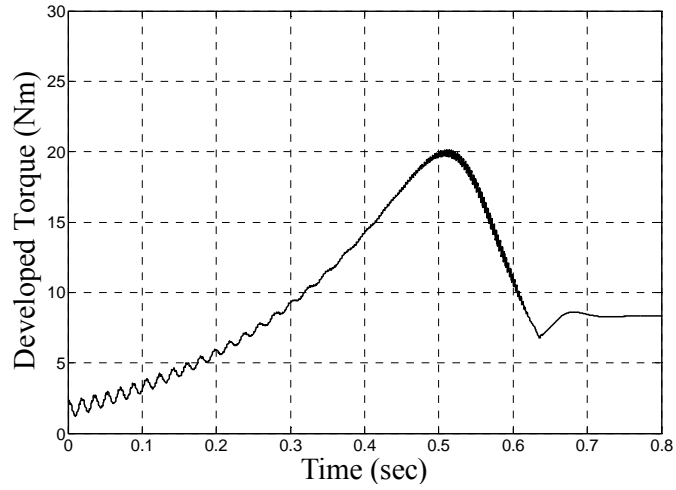
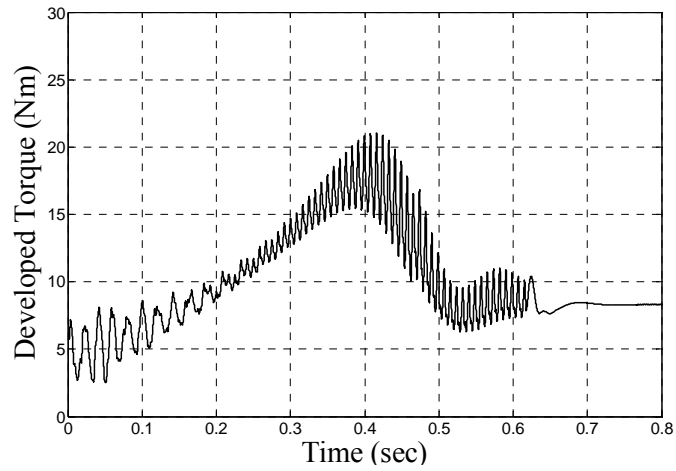


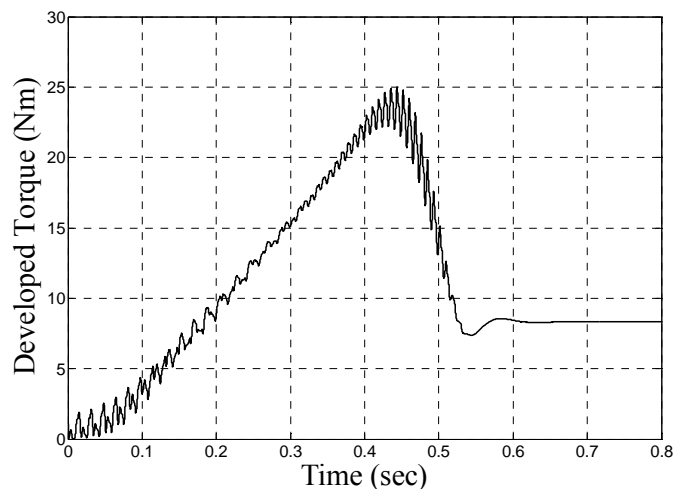
Figure 4.10: Simulation results of current space-vector plots. (a) 3-phase open-loop control. (b) 2-phase open-loop control. (c) Proposed 2-phase closed-loop control.



(a)



(b)



(c)

Figure 4.11: Simulation results of motor developed torque. (a) 3-phase open-loop control. (b) 2-phase open-loop control. (c) Proposed 2-phase closed-loop control.

## CHAPTER 5

---

---

# HARDWARE EXPERIMENTS OF FAULT TOLERANT SOFT STARTER

---

---

### 5.1 Introduction

With the analytical and simulation portions of the present fault tolerant soft starter, including the theoretical design of the soft starter controller, accomplished and documented in the foregoing chapters, one is now at a stage of presenting the hardware experimental results. The test operating conditions, as well as the controller design parameters, were set as close as possible to their values given earlier in association with the simulation conditions. This was done for comparison purposes between the simulation results given in Chapter 4 and the test results which will be given here. For these purposes, some of the analytical and simulation results presented earlier are repeated here for the convenience of the reader. The target test motor chosen for the experimental testing is the 2-hp, 4-pole, three-phase induction motor, whose machine parameters were given earlier in Chapter 4 and were used in the simulation work. Evidently from the experimental results as will be shown later on, the fault tolerant control scheme alleviates the starting torque pulsations under SCR switch fault condition. Accordingly, such promising results demonstrate

the feasibility and validity of the present approach. In the following, the hardware prototype is first described, followed by the test results.

## 5.2 Hardware Prototype

The configuration of the experimental setup is shown schematically in Figure 5.1. The setup consists of a 460-Volt utility grid supply feeding a three-phase SCR bridge, which acts as a soft starter to supply controlled voltages to a three-phase induction motor during soft starting. The power rating of the SCR bridge is chosen such that the direct-online-starting current of the target motor is within the limit of the current rating of the chosen SCRs. Typically, the maximum current amplitude (rms) during line-starting of a motor is about 6 to 8 times of the motor rated current value [22]. On the other hand, for the case of soft starting, typically the maximum current amplitude (rms) is measured to be about 3 to 5 times that of the motor rated current value [22]. The SCR bridge was mounted on a oversized heat sink, originally intended for a 15-hp drive, see Figure 5.2(a). With this oversized heat sink, along with the use of a fan as the cooling mechanism, the thermal issues of the power structure were not of major concern. Snubber circuits in the form of  $RC$  elements were also incorporated to reduce any switching transients caused by the process of commutation of the SCRs. Meanwhile, a DSP-based control board from Texas Instruments (Model: TMS320F2812) were utilized to control the switching sequences of the SCR switches [92]. Voltage and current feedbacks through the use of analog signal conditioning circuits and current transducers (from LEM) are fed into the analog inputs of the DSP board, and the firing pulses in the form of digital signals were accordingly generated. The gate drive interface between the high power stages of the switches and the low power stages of the DSP was realized by means of a set of pulse transformers. The main purpose of such type of interface is to provide electrical galvanic isolations between the high and low power stages, as well as to provide sufficient currents to the gates of the SCRs for turning-on. The EMI/EMC noise of the

present hardware prototype was minimized through the use of decoupling capacitors in various parts of the signal conditioning circuits. Digital software-based low-pass filters, of the 5<sup>th</sup> order Butterworth type [93], were also implemented in the DSP to suppress any EMI noise that might be imposed on the measured signals. The data measurement was carried out using a data acquisition (DAQ) system from National Instruments (Model: PCI-6052E) at a data measurement sampling rate of 50 kSamples/sec [94]. This system allows measurements of up to 8 analog signals, which are virtually impossible to achieve from an ordinary oscilloscope. Again, the hardware prototype of the present configuration is depicted in Figure 5.2(a). Detailed designs and specifications of the present hardware prototype, including circuit design and component selections, are described in Appendix A of this dissertation.

As mentioned earlier, the test motor is a 2-hp, 4-pole, three-phase induction motor, with a full-load rating of 8.169 Nm at a rated speed of 1744 r/min. This is the same motor that had been used during the simulation process of this work. The motor is coupled to a dynamometer from Magtrol Corporation through a love joy coupler, as shown in Figure 5.2(b). This Magtrol dynamometer, which functions as a mechanical load, is capable of supplying up to 12 Nm. It is important to mention that the load torque supplied by this dynamometer is a constant type, which is different from the fan type of load used in the earlier simulation work in Chapter 4. The specifications of the hardware prototype are listed in Figure 5.1, as well as in Table 5.1. For further details, Appendix A should be consulted.

As was indicated in Chapter 3 of this dissertation, the present control scheme requires the use of PI controllers for closed-loop feedback control purposes. The DSP-based controller proportional gains for both the voltage and current feedback loops were selected to be the same as those obtained from the theoretical analysis carried out in Chapter 3 and those used in the circuit simulations. That is,  $k_p = 0.0013$  for the voltage loop, and  $k_p = 0.3$  for the current loop. However, the DSP-based controller integral gains which were obtained from the theoretical

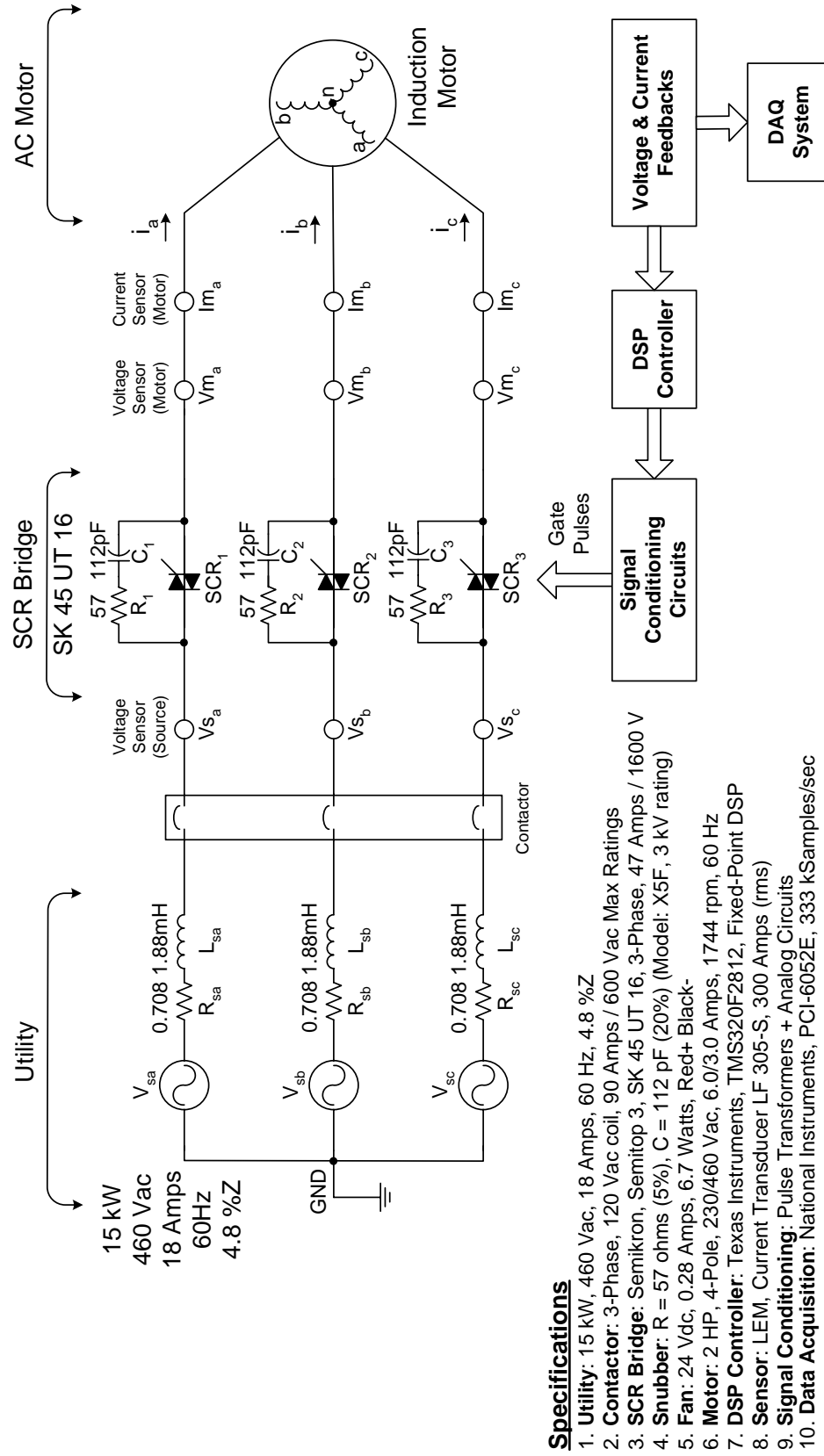


Figure 5.1: Schematic of experimental setup of induction motor-soft starter system.

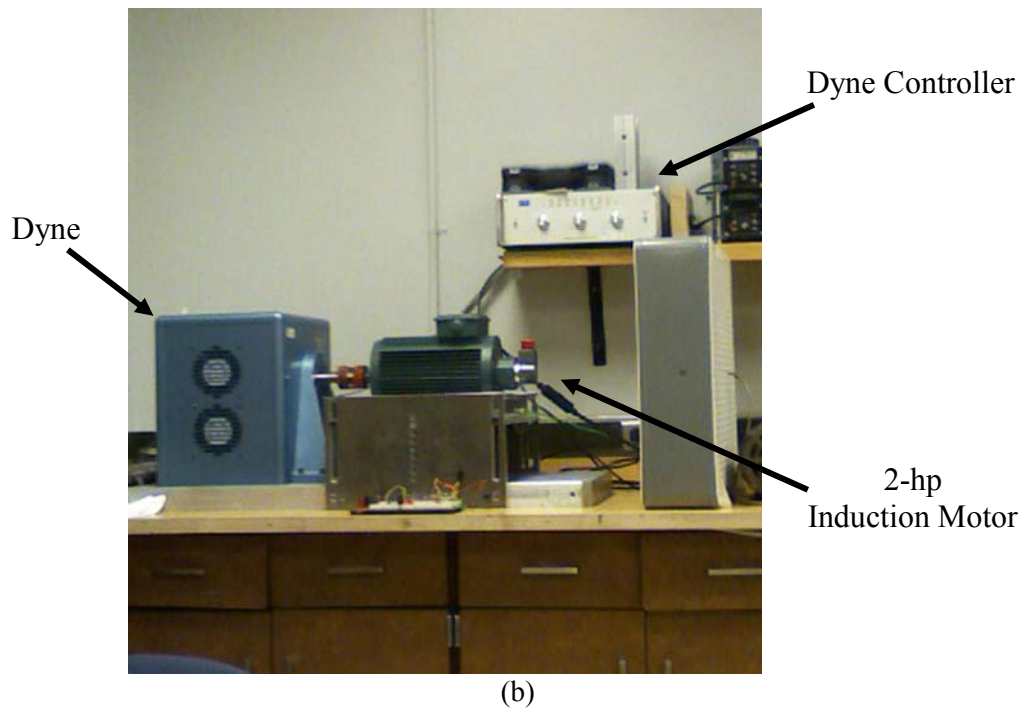
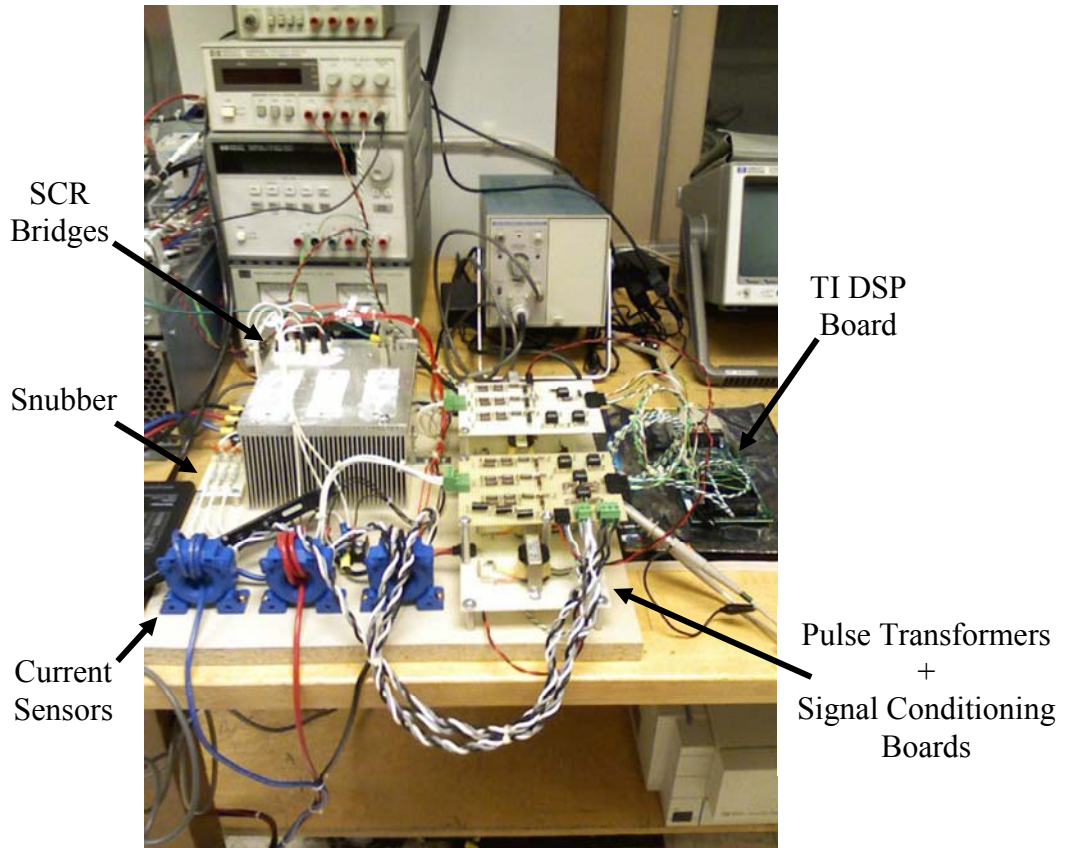


Figure 5.2: Test rigs. (a) Soft starter. (b) Induction motor and dynamometer.

Table 5.1: Specifications of hardware prototype.

<b>Utility</b>	
Utility Input Voltage (Line-To-Line)	460 Volts
Frequency	60 Hz
Line Resistance (4.8%)	0.7082 $\Omega$
Line Inductance (4.8%)	1.8786 mH
<b>SCR Bridge</b>	
Current / Voltage Ratings (Max)	47 Amps / 1600 Volts (rms)
Snubber Circuits	R = 57 $\Omega$ , C = 112 $\mu$ F
<b>Induction Motor</b>	
Rated Power	2 hp (1492 Watts)
Rated Voltage (Line-To-Line)	460 Volts
Rated Current	3.0 Amps
Rated Frequency	60 Hz
Rated Speed	1744 r/min
Rated Torque	8.169 Nm
Phase	3
Number of Poles	4
<b>Dynamometer (Magtrol)</b>	
Mechanical Load (Constant Type)	Up to 12 Nm
<b>DSP Board (TI TMS320F2812)</b>	
Execution Cycle	10 kHz
Digital Low-pass Filter	5 <sup>th</sup> order Butterworth type
PI Gains for Voltage Loop	$k_p = 0.0013$ , $k_i = 0.5$
PI Gains for Current Loop	$k_p = 0.3$ , $k_i = 1.5$
Anti-windup Gains for Both Loops	$k_c = 0.2$
<b>DAQ System (NI PCI-6052E)</b>	
System Sampling Rate	333 kSamples/sec
Actual Measurement Rate	50 kSamples/sec
Number of Analog Input Channels	8
<b>Current Transducer</b>	
Current Rating (Max)	300 Amps (rms)

analysis, that is,  $k_i = 7.27$  for the voltage loop and  $k_i = 32.3$  for the current loop, have been first reduced by a factor of 10. The reason for doing so is due to the fact that the circuit simulation was carried out at a sampling frequency of 100 kHz, while the interrupt service routine in the DSP main program is executing at 10 kHz. Hence, the designed integral gains need to be reduced by one order of magnitude [90]. Further fine tuning, for the purposes of stabilizing the control loop, as well as reducing noise susceptibility, results in the following integral gains:  $k_i = 0.5$  for the voltage loop and  $k_i = 1.5$  for the current loop. In addition, an anti-windup scheme was also incorporated into the PI controller design. This is to avoid instability in the PI controller due to saturation in the integral loop, especially during start up when the error between the reference input and the control output is large [90]. The anti-windup gains for both the voltage and current loops were accordingly chosen to be  $k_c = 0.2$ .

## 5.3 Experimental Results

### 5.3.1 Comparisons with Simulation and Analytical Results

In Chapter 4 of this dissertation, the simulation results were compared with the analytical results obtained from Chapter 3 under both healthy and faulty conditions. The resulting comparisons indicated a good degree of similarity/agreement between the analytical and simulation results. In this chapter, those results are repeated here for comparison with the experimental test results for further verification purposes. This is in order to validate and demonstrate the accuracy/fidelity of the analytical work being done thus far.

The test results of the healthy three-phase motor line-to-neutral voltages during soft starting under full-load condition are depicted in Figure 5.3(a), along with the corresponding simulation and analytical results given in Figure 5.3(b) and Figure 5.3(c), respectively. Notice the close

agreement between each individual waveform for phases-*a*, *b*, and *c*. The corresponding healthy three-phase motor currents under the same condition for the test, simulation, and analytical work are shown in Figure 5.4(a), (b), and (c), respectively. It can be observed from Figure 5.4 that there is a reasonable degree of agreement between those waveforms. Furthermore, the harmonic contents of the motor phase voltages of Figure 5.3 and the motor phase currents of Figure 5.4 are given in Table 5.2 and Table 5.3, respectively. Again, there is a considerable degree of similarity between the trends of the harmonic components of the test, simulation, and analytical results, except for some of the higher-order harmonics, and third harmonic as well as its multiples 9<sup>th</sup>, 15<sup>th</sup>, etc. This may be due to the fact that the machine's magnetic core saturation effects are neglected in the simulation and analytical work, while such saturation effects are inherently present in the actual test motor. This is also the reason for the presence of a positive-sequence 3<sup>rd</sup> harmonic component and its multiples, as indicated in the test columns of the voltage and current in both tables.

Meanwhile, the experimental work was repeated in the event of an SCR short-circuit switch fault, by turning-on the SCRs of phase-*c* continuously, to emulate the effect of a bypass contactor that would have been used in practice. The measured results of the three-phase motor phase voltages are depicted in Figure 5.5(a). The associated simulation and analytical results are given in Figure 5.5(b) and (c), respectively. Again, therein, one can notice the similarity between those voltage waveforms in so far as the profiles are concerned. The experimental results also show the unsymmetrical nature of the voltage waveforms under faulty condition. The corresponding three-phase motor currents obtained from test, simulation, and analytical work under faulty condition are illustrated in Figure 5.6(a), (b), and (c), respectively. It can be noticed from the test results in Figure 5.6(a) that the measured currents exhibit the same unbalanced nature as the simulation and analytical results, when subjected to a short-circuit switch fault. In addition, the harmonic breakdown of the motor phase voltages of Figure 5.5 and the motor phase currents of Figure 5.6

are listed in Table 5.4 and Table 5.5, respectively. Again, upon comparison, there is a certain degree of agreement in trend among these results, except for some of the higher-order harmonic components due to the effects of the machine's magnetic saturation being present in the test, and as mentioned earlier neglected in both the simulation and analytical models. The fact that the impressed voltages on the motor windings are unbalanced, under faulty condition, is also a contributing factor to the presence of the positive-sequence 3<sup>rd</sup> harmonic component and its multiples in the test, simulation, and analytical results, see Table 5.4 and Table 5.5.

It should be mentioned here that due to the inaccessibility of the motor neutral connection, the measured motor line-to-neutral voltages presented herein in the test data were indirectly acquired through the use of the line-to-line voltage measurements, assuming a balanced three-phase motor, which would lead to line-to-neutral voltages which can be expressed and computed as follows:

$$\begin{aligned}v_{an} &= \frac{1}{3}(v_{ab} - v_{ca}) \\v_{bn} &= \frac{1}{3}(v_{bc} - v_{ab}) \\v_{cn} &= \frac{1}{3}(v_{ca} - v_{bc})\end{aligned}\tag{5.1}$$

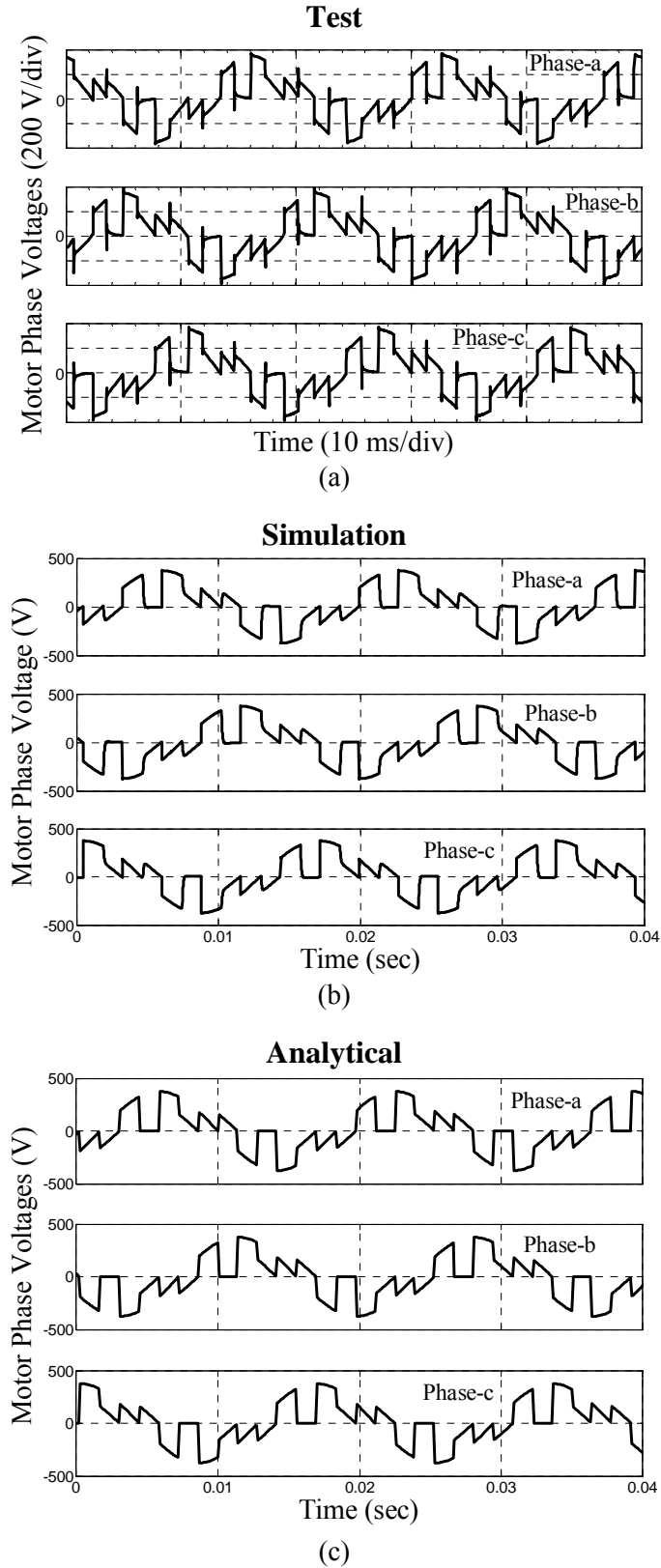


Figure 5.3: *Healthy* three-phase line-to-neutral motor voltage waveforms. (a) Test. (b) Simulation. (c) Analytical.

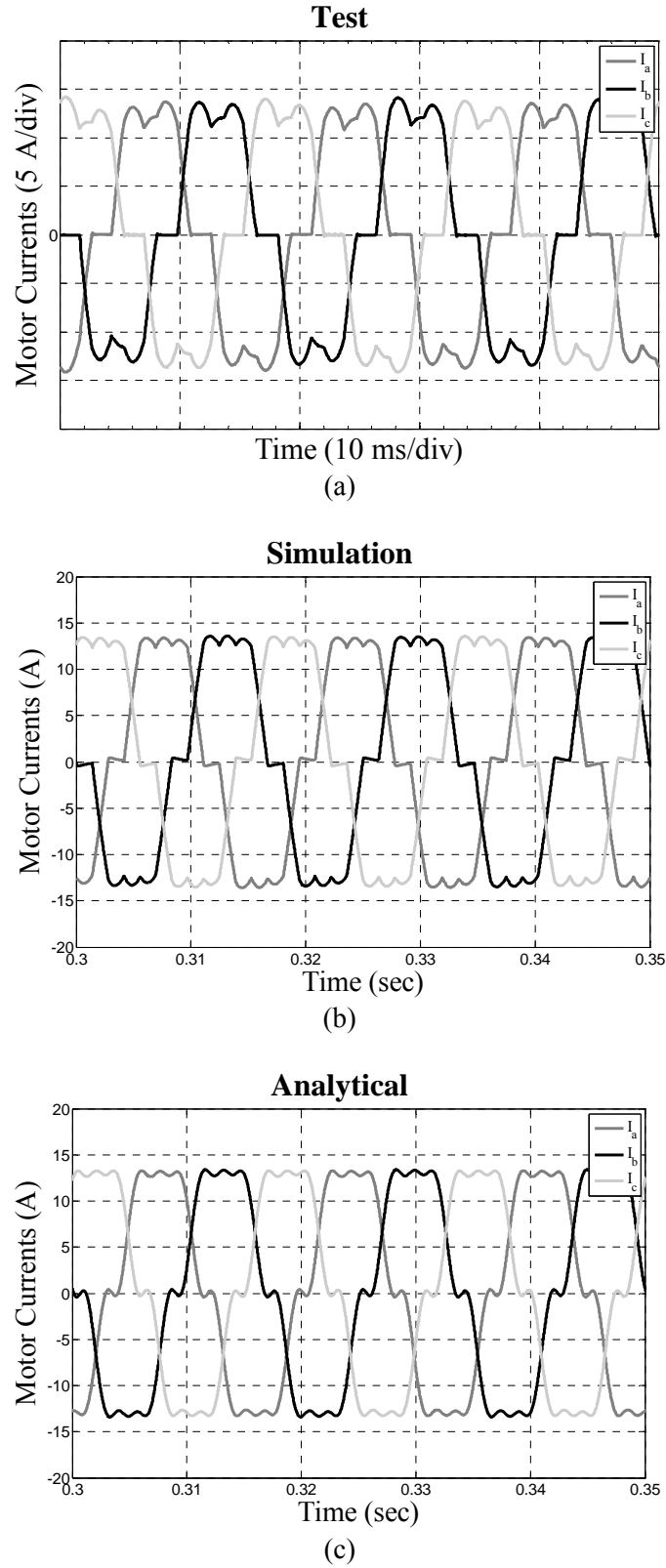


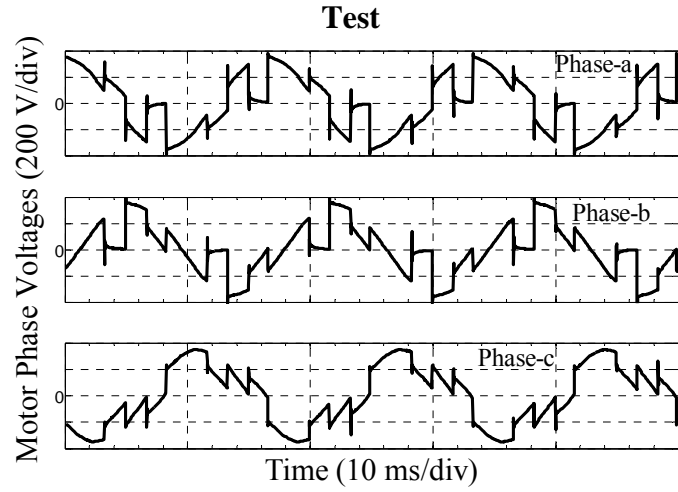
Figure 5.4: *Healthy* three-phase current waveforms. (a) Test. (b) Simulation. (c) Analytical.

Table 5.2: Harmonic contents of *healthy* three-phase motor phase voltages – Test, Simulation, and Analytical.

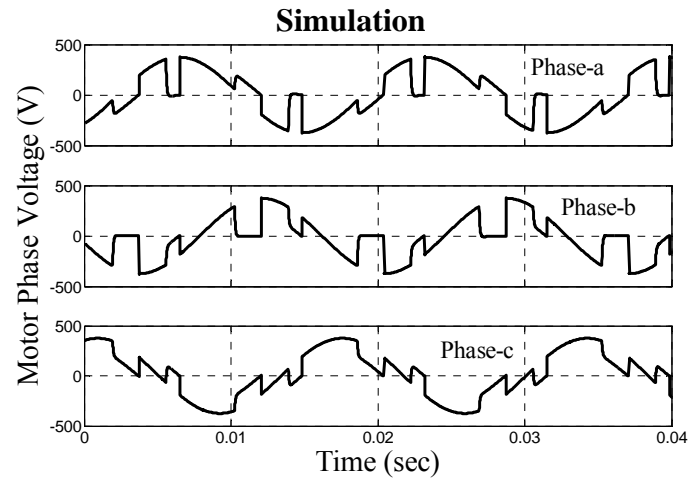
Harmonic Order	Test			Simulation			Analytical		
	$V_{ma}$ (Volt)	$V_{mb}$ (Volt)	$V_{mc}$ (Volt)	$V_{ma}$ (Volt)	$V_{mb}$ (Volt)	$V_{mc}$ (Volt)	$V_{ma}$ (Volt)	$V_{mb}$ (Volt)	$V_{mc}$ (Volt)
1	197.91	197.10	199.35	206.22	207.75	207.20	207.30	208.90	208.10
3	8.31	8.51	8.77	0	0	0	0	0	0
5	118.22	123.95	127.16	134.97	134.23	133.66	131.40	131.80	131.90
7	86.95	88.52	86.25	97.38	97.95	98.68	94.11	93.54	94.62
9	5.16	5.89	4.92	0	0	0	0	0	0
11	25.85	25.05	26.82	21.37	21.68	21.40	17.28	18.60	16.41
13	22.95	24.45	23.94	9.49	8.14	9.57	12.45	11.17	13.18
15	4.76	4.51	4.92	0	0	0	0	0	0
17	27.55	24.90	29.90	37.33	36.55	36.01	35.18	35.55	35.23
19	25.60	24.62	22.03	34.11	34.62	35.37	31.37	30.98	31.69
21	3.12	2.86	3.35	0	0	0	0	0	0

Table 5.3: Harmonic contents of *healthy* three-phase motor currents – Test, Simulation, and Analytical.

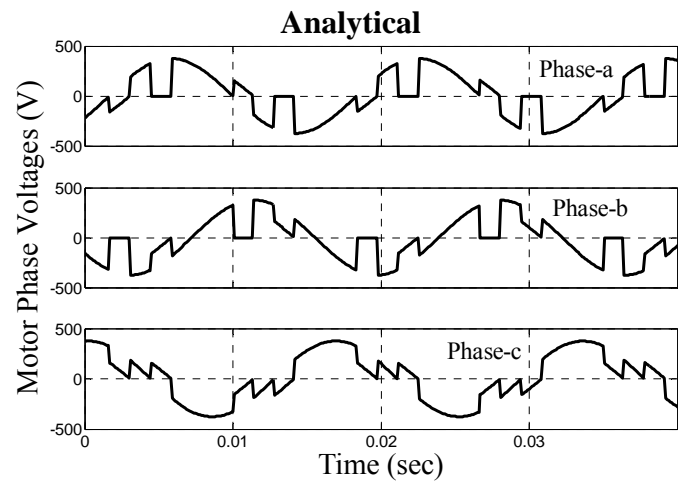
Harmonic Order	Test			Simulation			Analytical		
	$I_{ma}$ (A)	$I_{mb}$ (A)	$I_{mc}$ (A)	$I_{ma}$ (A)	$I_{mb}$ (A)	$I_{mc}$ (A)	$I_{ma}$ (A)	$I_{mb}$ (A)	$I_{mc}$ (A)
1	13.681	13.550	13.793	14.212	14.180	14.234	14.255	14.340	14.326
3	0.208	0.246	0.265	0	0	0	0	0	0
5	2.680	2.781	2.824	2.077	2.035	2.032	2.021	2.027	2.028
7	0.956	0.985	0.889	1.073	1.085	1.109	1.036	1.030	1.042
9	0.112	0.168	0.090	0	0	0	0	0	0
11	0.245	0.309	0.341	0.151	0.159	0.157	0.121	0.131	0.115
13	0.178	0.101	0.193	0.056	0.054	0.059	0.074	0.066	0.078
15	0.089	0.055	0.095	0	0	0	0	0	0
17	0.152	0.118	0.146	0.169	0.161	0.154	0.160	0.162	0.160
19	0.112	0.110	0.092	0.139	0.137	0.149	0.128	0.126	0.129
21	0.056	0.044	0.069	0	0	0	0	0	0



(a)



(b)



(c)

Figure 5.5: Three-phase line-to-neutral motor voltage waveforms under a *short-circuit SCR fault*.  
 (a) Test. (b) Simulation. (c) Analytical.

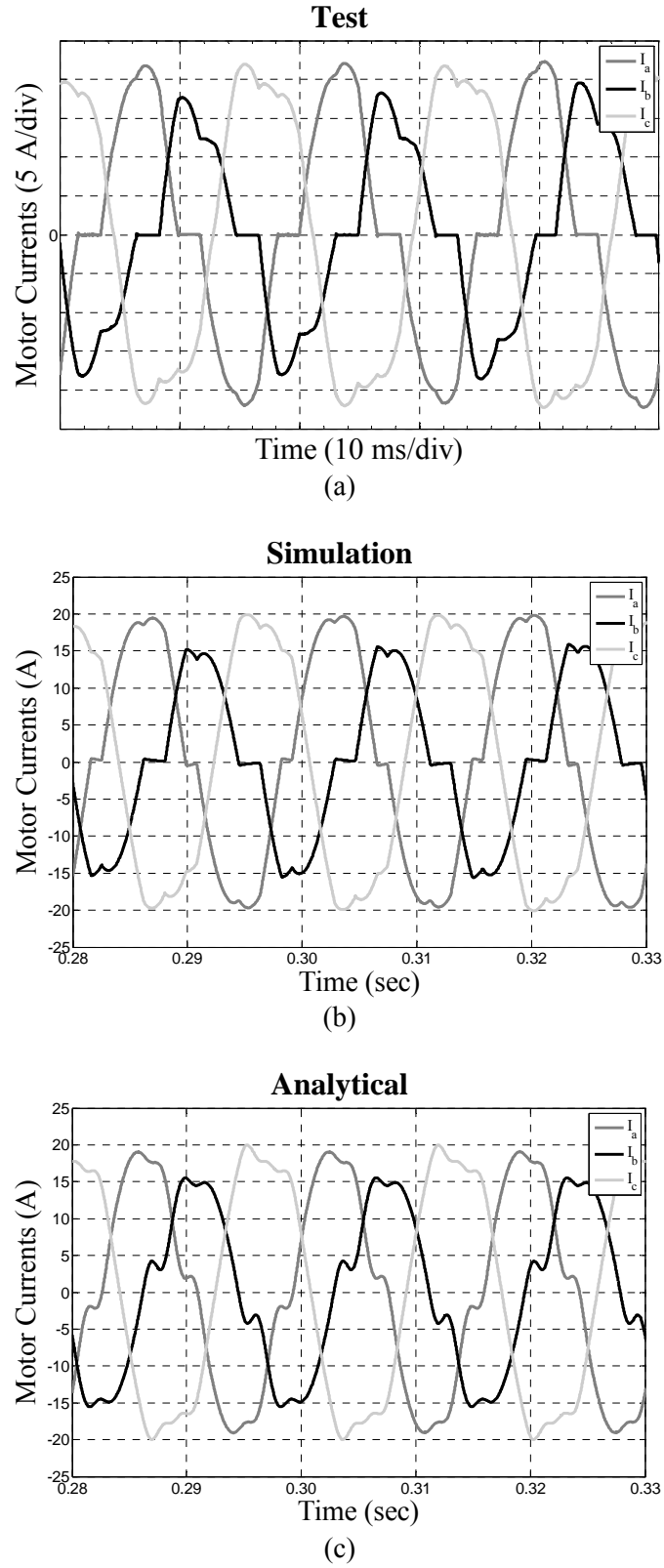


Figure 5.6: Three-phase current waveforms under a *short-circuit SCR fault*. (a) Test. (b) Simulation. (c) Analytical.

Table 5.4: Harmonic contents of three-phase motor phase voltages under a *short-circuit SCR fault* – Test, Simulation, and Analytical.

Harmonic Order	Test			Simulation			Analytical		
	$V_{ma}$ (Volt)	$V_{mb}$ (Volt)	$V_{mc}$ (Volt)	$V_{ma}$ (Volt)	$V_{mb}$ (Volt)	$V_{mc}$ (Volt)	$V_{ma}$ (Volt)	$V_{mb}$ (Volt)	$V_{mc}$ (Volt)
1	282.35	240.68	335.55	270.97	200.22	300.35	259.30	220.80	318.80
3	60.61	56.23	99.70	48.46	41.81	102.99	54.98	52.48	107.50
5	118.20	115.25	43.67	117.73	124.22	39.75	116.60	116.20	43.55
7	89.38	84.26	45.25	75.70	72.70	36.03	82.65	82.85	32.03
9	36.85	30.95	25.68	49.33	20.35	29.35	17.12	19.23	36.30
11	32.45	25.22	2.85	35.88	27.28	28.45	15.62	16.70	5.64
13	44.32	45.31	2.15	41.29	44.65	6.55	10.67	9.60	4.31
15	18.42	14.52	14.01	4.82	15.20	17.05	10.88	8.60	19.44
17	18.31	12.75	17.92	3.73	4.96	2.30	31.60	31.24	11.32
19	13.96	8.18	9.32	9.32	13.15	7.18	27.35	27.55	11.01
21	8.46	9.95	2.72	9.48	15.35	14.73	6.11	7.98	14.03

Table 5.5: Harmonic contents of three-phase motor currents under a *short-circuit SCR fault* – Test, Simulation, and Analytical.

Harmonic Order	Test			Simulation			Analytical		
	$I_{ma}$ (A)	$I_{mb}$ (A)	$I_{mc}$ (A)	$I_{ma}$ (A)	$I_{mb}$ (A)	$I_{mc}$ (A)	$I_{ma}$ (A)	$I_{mb}$ (A)	$I_{mc}$ (A)
1	21.280	16.452	23.045	19.621	13.413	20.740	18.752	14.043	21.666
3	1.821	1.543	2.424	1.350	1.300	2.605	1.397	1.333	2.731
5	2.023	1.631	0.740	1.807	1.892	0.628	1.793	1.787	0.670
7	1.255	1.060	0.458	0.806	0.760	0.381	0.910	0.912	0.353
9	0.351	0.311	0.246	0.417	0.157	0.261	0.147	0.165	0.312
11	0.225	0.192	0.075	0.253	0.205	0.206	0.110	0.117	0.040
13	0.249	0.252	0.008	0.247	0.269	0.034	0.063	0.057	0.026
15	0.125	0.152	0.188	0.027	0.068	0.082	0.056	0.044	0.100
17	0.095	0.066	0.078	0.017	0.019	0.005	0.144	0.142	0.051
19	0.039	0.031	0.048	0.035	0.045	0.026	0.111	0.112	0.045
21	0.024	0.042	0.020	0.037	0.062	0.055	0.022	0.029	0.052

### 5.3.2 Motor Performance under Fault Tolerant Operations

In this section, the experimental results of motor performance resulting from using the resilient closed-loop two-phase control technique are compared with those when using the conventional symmetrical-triggering open-loop three-phase control approach as well as two-phase control approach. The open-loop three-phase control approach and two-phase control approach were carried out under the conditions of an initial locked-rotor torque percentage of 40%, and a soft start ramp time of 5 seconds. On the other hand, for the case of the proposed closed-loop two-phase control technique, the test conditions were set at an initial voltage of 200-Volt, a final voltage of 265-Volt, and a soft start ramp time of 5 seconds. The PI controller gains were those given in Table 5.1. The initial firing delay angles for all cases were set at  $110^\circ$ . Finally, all the testing was carried out under full-load motor condition.

Due to limited laboratory facilities, the present dynamometer setup of Figure 5.2(b) is not equipped with a torque transducer. Therefore, an implicit method of obtaining the motor airgap or developed torque was utilized here which can be expressed in terms of the measured motor quantities, as follows [95]:

$$T_{airgap} = T_{dev} = \frac{P}{2\sqrt{3}} \left\{ (i_a - i_b) \int [v_{ca} - R_s(i_c - i_a)] dt - (i_c - i_a) \int [v_{ab} - R_s(i_a - i_b)] dt \right\} \quad (5.2)$$

where,  $P$  is the number of poles, and  $R_s$  is the stator equivalent series resistance per phase. As one can see from (5.2), the motor airgap or developed torque can be implicitly computed using the measured motor quantities, which can be easily accessible from the present DAQ system.

First, the test results obtained under direct-line-starting are given in Figure 5.7(a) and (b) for the motor phase currents and airgap (developed) torque, respectively, under normal/healthy motor condition. As expected, the starting transients are characterized by high inrush currents and high

torque pulsations. Next, the test waveforms of the three-phase motor currents under conventional soft-starter 3-phase open-loop control, along with the corresponding simulation waveforms are depicted in Figure 5.8(a) and (b), respectively. As one can observe from both figures, the test and simulation waveforms are in good agreement with one another in so far as the starting profiles are concerned. The currents from both figures, test and simulations, have a starting value of around 10 Amps and a peak value of around 20 Amps. The corresponding motor airgap (developed) torque profiles computed from the experiment and simulation current and voltage data are shown in Figure 5.9(a) and (b), respectively. One can notice that the test waveform of the torque profile, see Figure 5.9(a), consists of more ripple contents than that of the simulation of Figure 5.9(b), which can be attributed to a number of possible factors. The first factor can be due to the fact that the machine's magnetic core saturation was neglected in the simulation process owing to the use of the  $dq$  reference frame representation of the induction motor, in which this assumption of linearity is inherent. In reality, during starting, a motor is subjected to considerable magnetic saturation effects owing to the high starting transient currents, which leads to the presence of space/time harmonics imposed on the currents, and consequently the torque. The second factor may be due to drift problems in the integrator terms of the torque expression of (5.2), which can be attributed to the presence of small dc offsets in the measurements of the voltages and currents. These dc offsets or errors, which can be caused by either the sensor itself or the data acquisition system, will accumulate during the integration process associated with obtaining the torque indirectly through the use of (5.2). As a result, these cumulative errors introduce noises in the computation process. Nevertheless, both the measured and simulated motor torques have similar starting profiles. One should also notice that the average starting torque values from both the test and simulation are around 2 Nm, and their maximum values are both around 20 Nm, see Figure 5.9. Meanwhile, one can notice a discrepancy in the time scales of both the test (400 ms/div) and simulation (100 ms/div) waveforms of Figure 5.8 and Figure 5.9. This is mainly due to the different types of load used in the experimental and simulation work. Since a constant load torque

( $\sim 8$  Nm) was utilized in the experimental test, it is anticipated that the motor will take longer to accelerate and reach its steady-state condition, as compared to the simulation results in which a fan load was used to provide a mechanical load torque of 8.169 Nm at the rated speed.

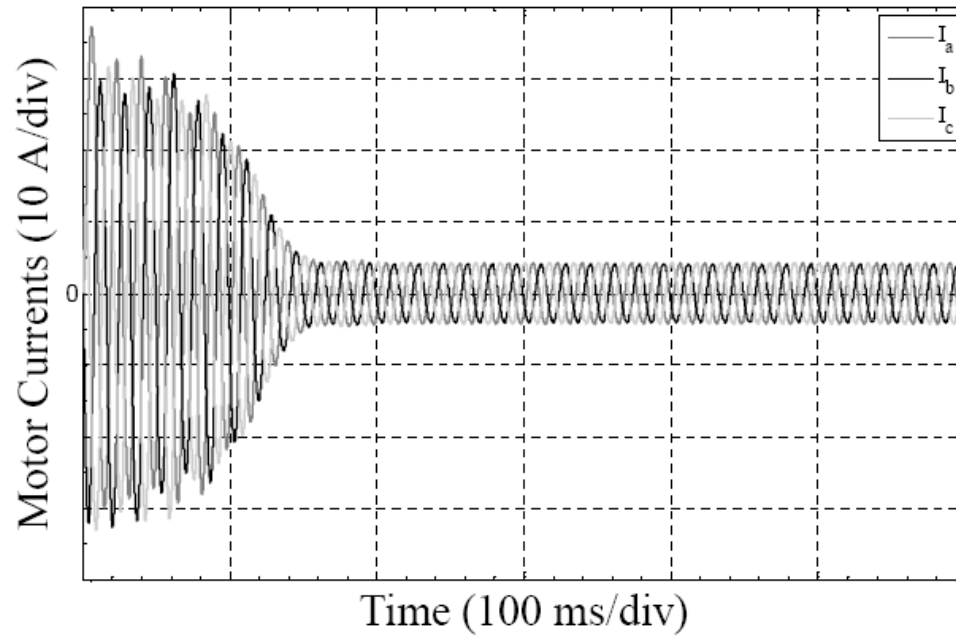
The experiment was repeated under the same operating condition, except that the SCRs of phase-*c* were always set in the “on” mode of operation. This is in order to emulate a short-circuit switch fault. The measured and simulated three-phase motor currents are depicted in Figure 5.10(a) and (b), respectively. Again, the test waveforms match quite well with the simulation waveforms, with similar unbalanced nature during starting. The corresponding measured and simulated motor airgap (developed) torques, under 2-phase open-loop control, are given in Figure 5.11(a) and (b), respectively. Notice the pulsations present in the measured torque profile of Figure 5.11(a). Moreover, there is a certain degree of similarity between the test and simulation results, in so far as the starting profiles, torque pulsations, as well as the average starting torque (around 5 to 6 Nm) and the maximum torque (around 21 to 22 Nm). Again, as mentioned earlier, the discrepancy in the time scales of both the test (400 ms/div) and simulation (100 ms/div) results is due to the fact that different types of load were used in the test (a constant load torque of around 8 Nm) and simulation (a fan load providing 8.169 Nm at the rated speed).

In the final test of this work, the experiment was repeated under the same condition as the previous case, that is the SCRs of phase-*c* are always maintained in the “on” state, while utilizing the 2-phase closed-loop control technique. The experimental results of the three-phase motor currents using such control technique are illustrated in Figure 5.12(a), along with the corresponding simulated currents given in Figure 5.12(b). In spite of the fact that the measured currents do not precisely match with the simulated currents, the test waveforms still exhibit smooth starting profiles with low starting inrush currents in both test and simulation, regardless of the short-circuit switch fault. The consequent measured and simulated torque profiles are depicted in Figure 5.13(a) and (b), respectively. As may be observed from the measured torque profile of

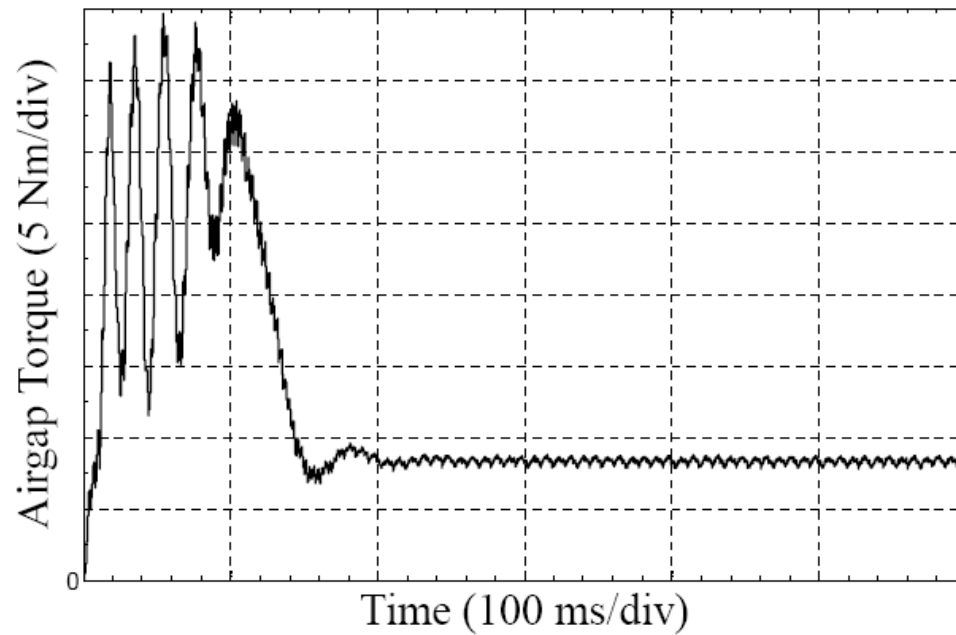
Figure 5.13(a), the starting torque pulsations are alleviated as a result of the present control approach. Furthermore, the measured torque shows a smooth starting profile, which is in relatively good agreement with the simulation case. Accordingly, the proposed control method demonstrates its fault tolerant capability in the event of SCR switch faults, with reduced starting currents and torque ripples. These claims by this investigator are strongly supported by the experimental test results presented herein.

## 5.4 Summary

In the first part of this chapter, the measured results during the soft starting transients under healthy and short-circuit switch fault conditions were compared with the analytical and simulation results presented in Chapters 2 and 4, respectively. The objective is to verify the accuracy of the analytical work that was carried out earlier in Chapter 2. The resulting comparisons indicate good agreements between the test, simulation, and analytical waveforms. The second part of this chapter involves comparing the motor performance obtained from both the experiment and simulation, under 3-phase open-loop, 2-phase open-loop, as well as the proposed 2-phase closed-loop controls. Overall, the experimental test results match reasonably well with the simulation results. It is evident from both the test and simulation results given in this chapter that the proposed fault tolerant soft starter has demonstrated its efficacy and practicability for improving the reliability of an industrial-type three-phase soft starter system at a modest cost increase.

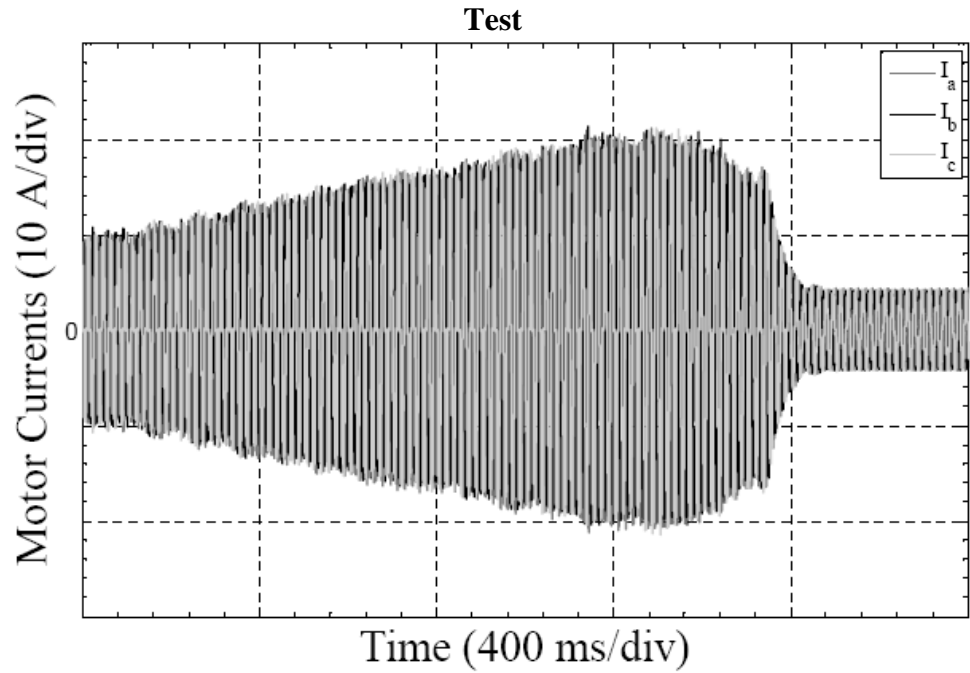


(a)

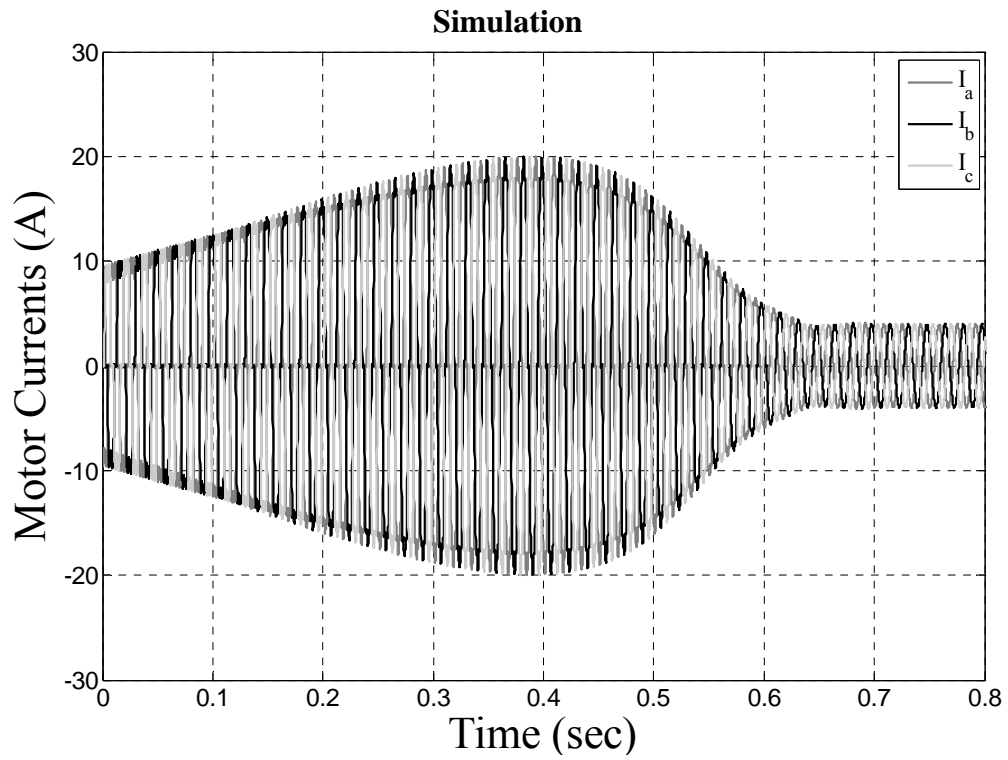


(b)

Figure 5.7: Test results obtained under *direct-line-starting*. (a) Three-phase motor currents. (b) Motor developed torque.



(a)



(b)

Figure 5.8: Three-phase motor currents obtained under *3-Phase Open-Loop Control*. (a) Test. (b) Simulation.

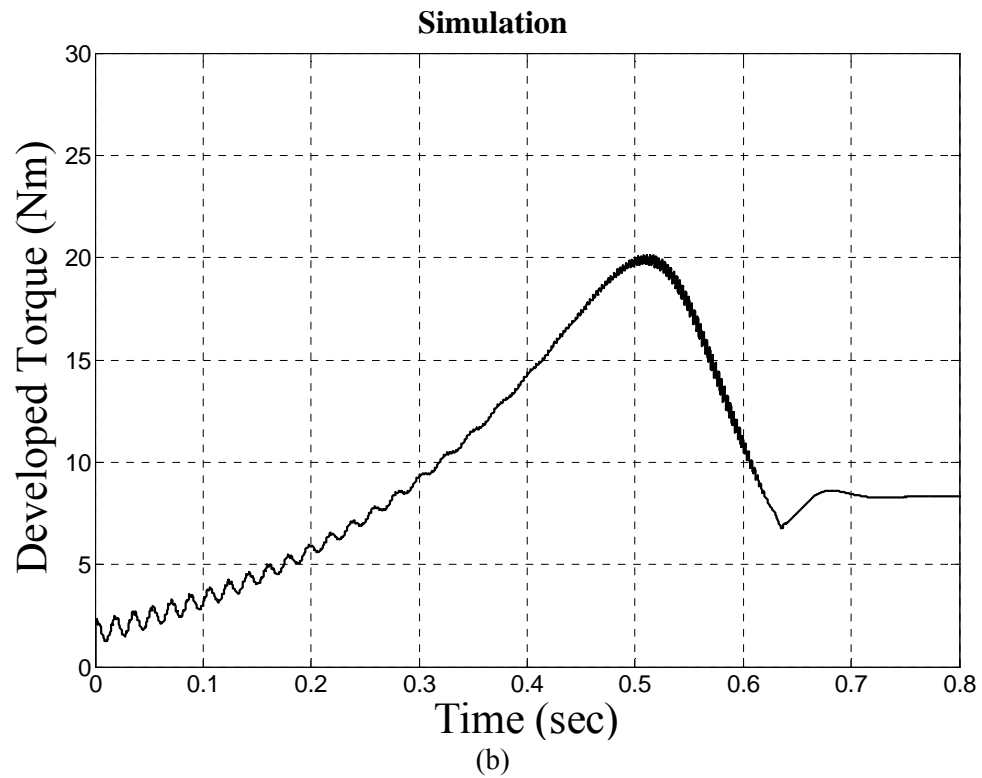
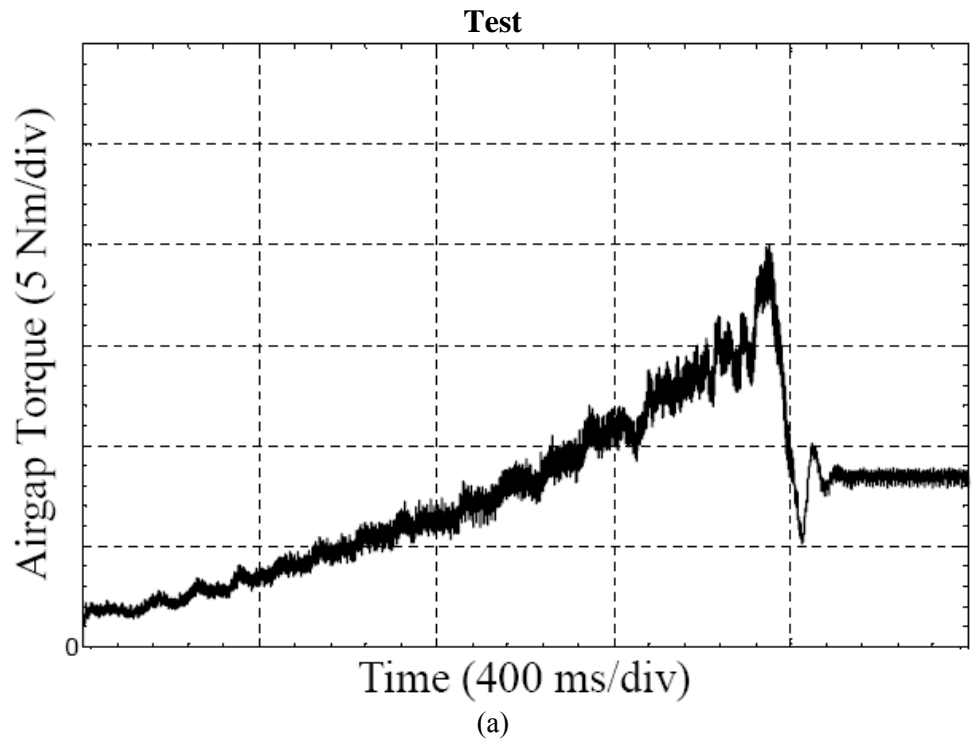


Figure 5.9: Motor developed torque obtained under *3-Phase Open-Loop Control*. (a) Test. (b) Simulation.

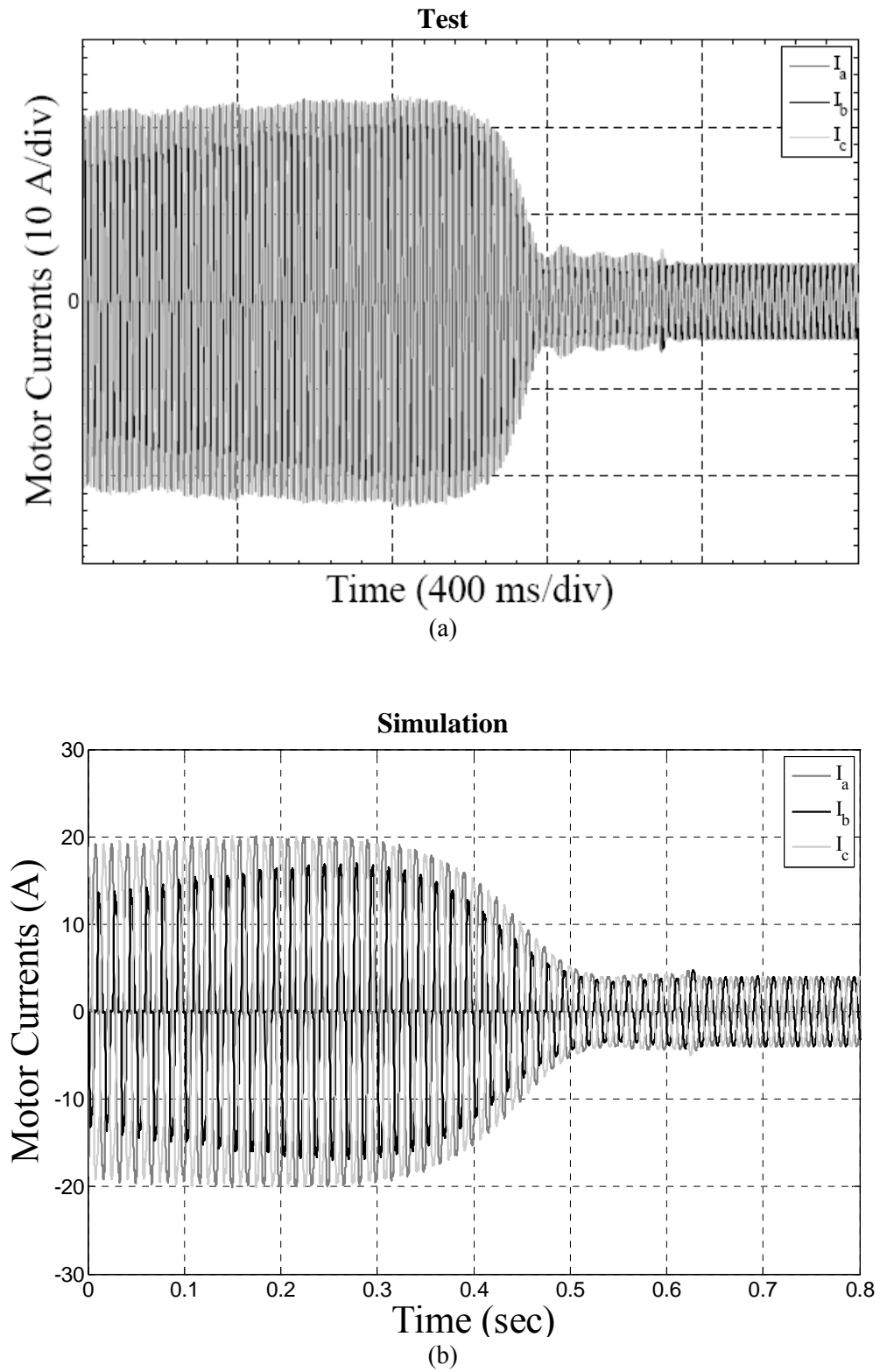


Figure 5.10: Three-phase motor currents obtained under *2-Phase Open-Loop Control*. (a) Test. (b) Simulation.

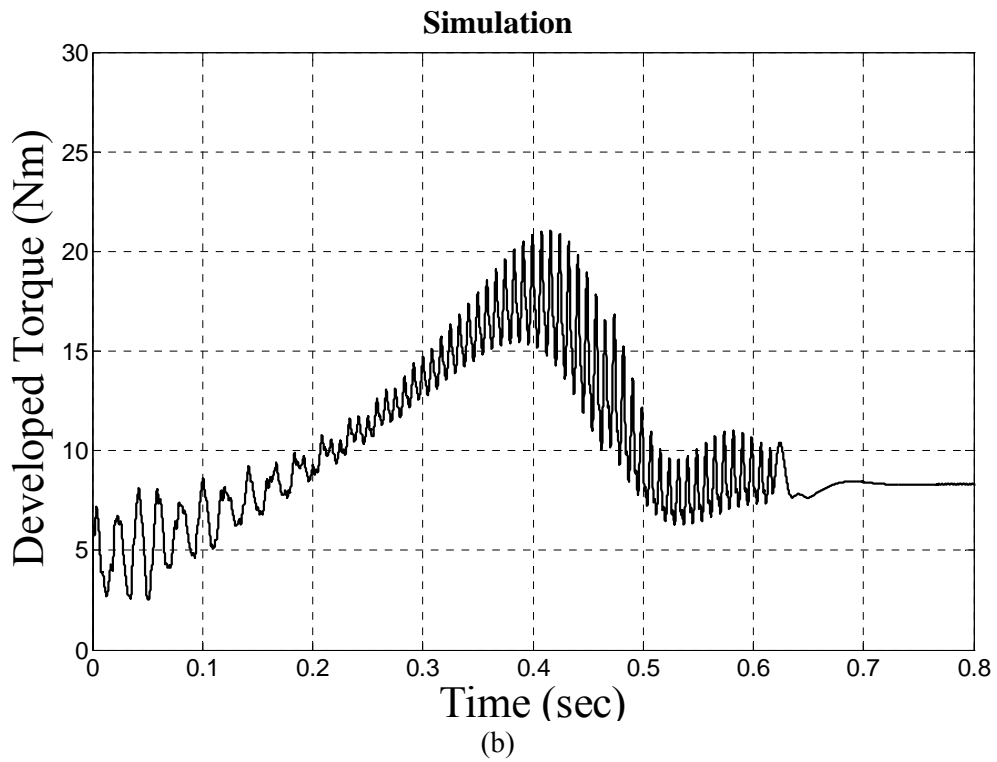
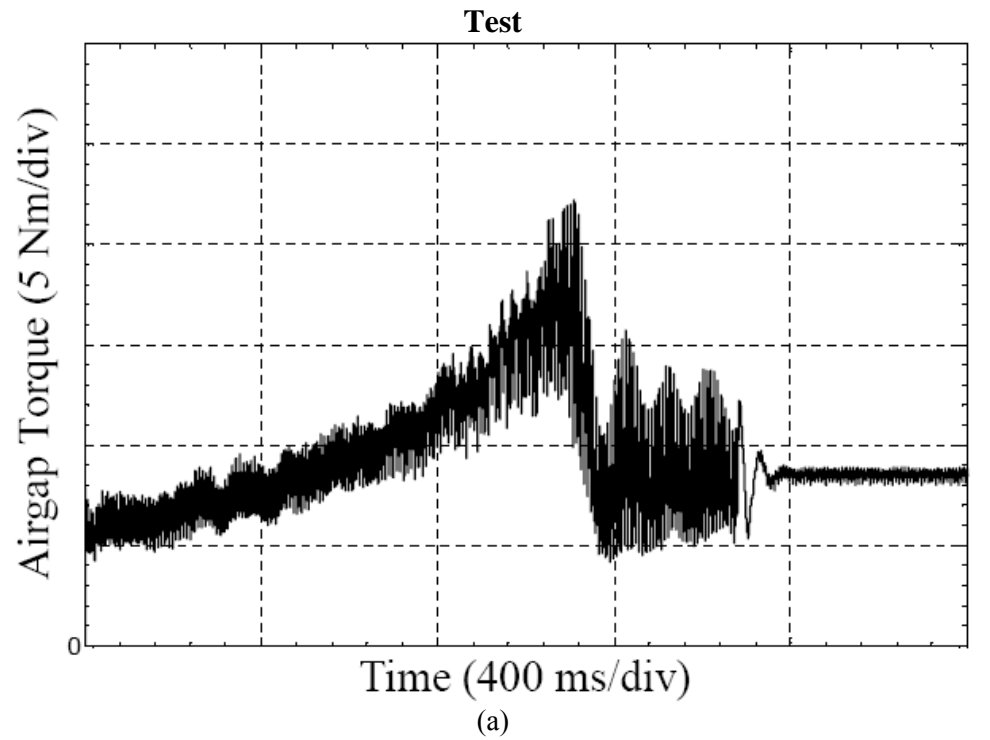


Figure 5.11: Motor developed torque obtained under *2-Phase Open-Loop Control*. (a) Test. (b) Simulation.

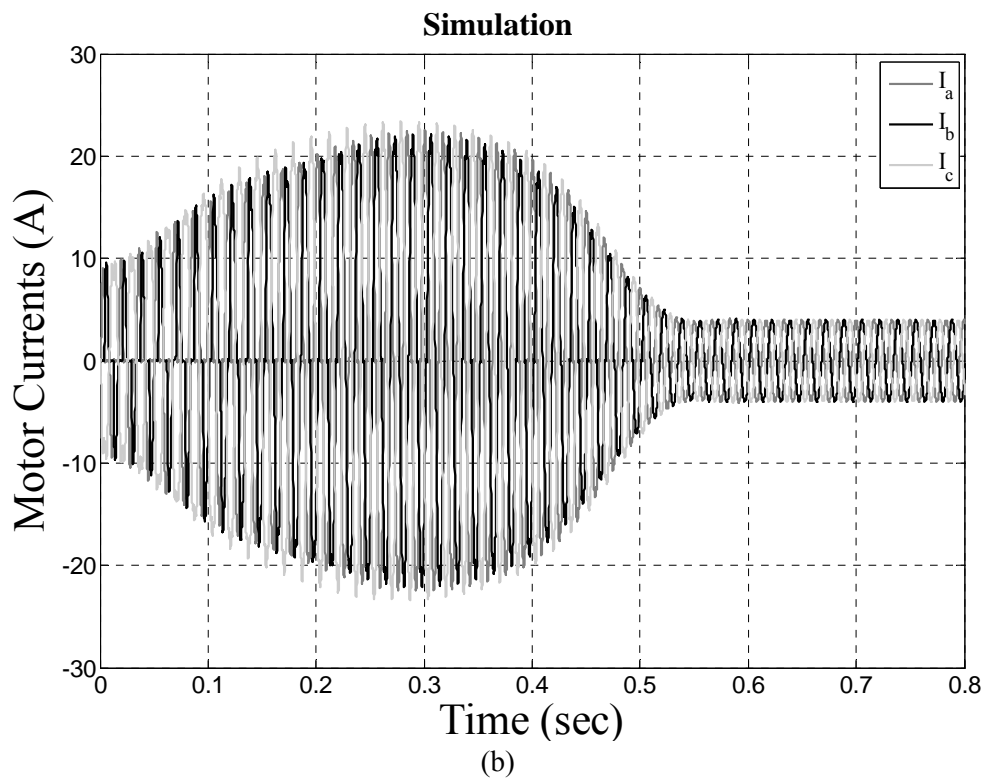
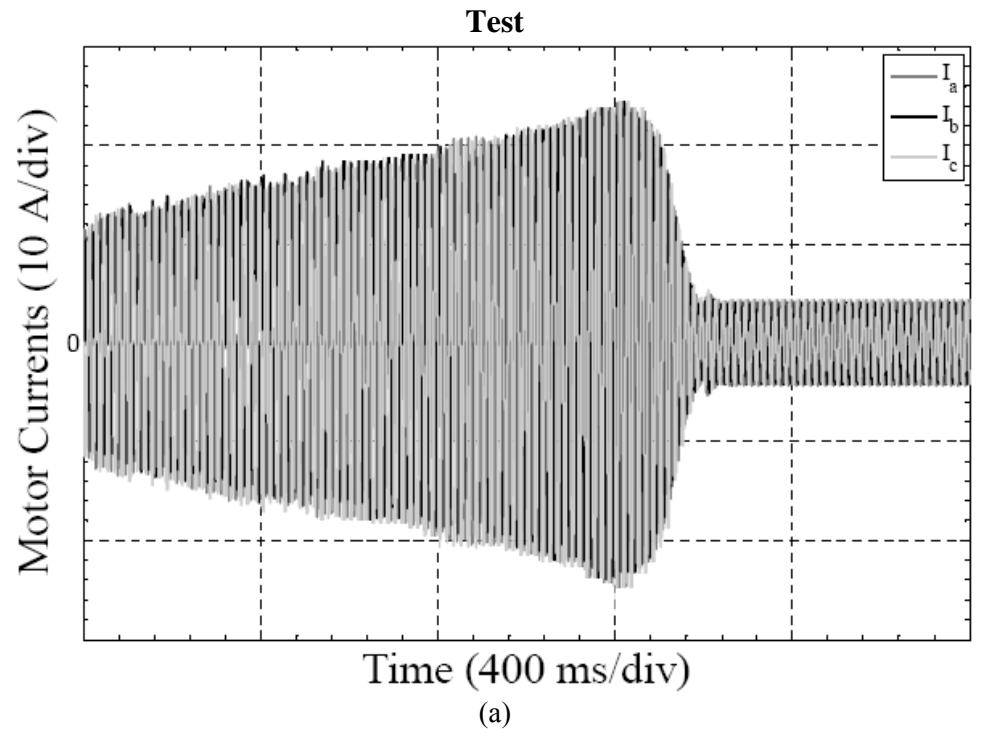


Figure 5.12: Three-phase motor currents obtained under *2-Phase Closed-Loop Control*. (a) Test. (b) Simulation.

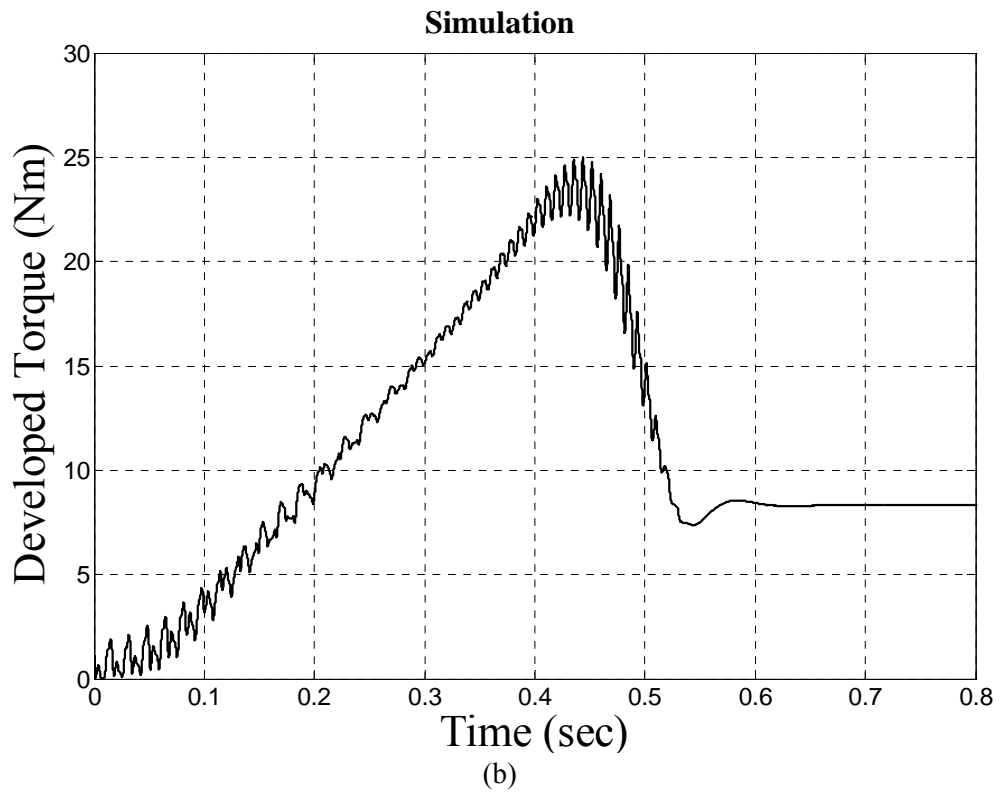
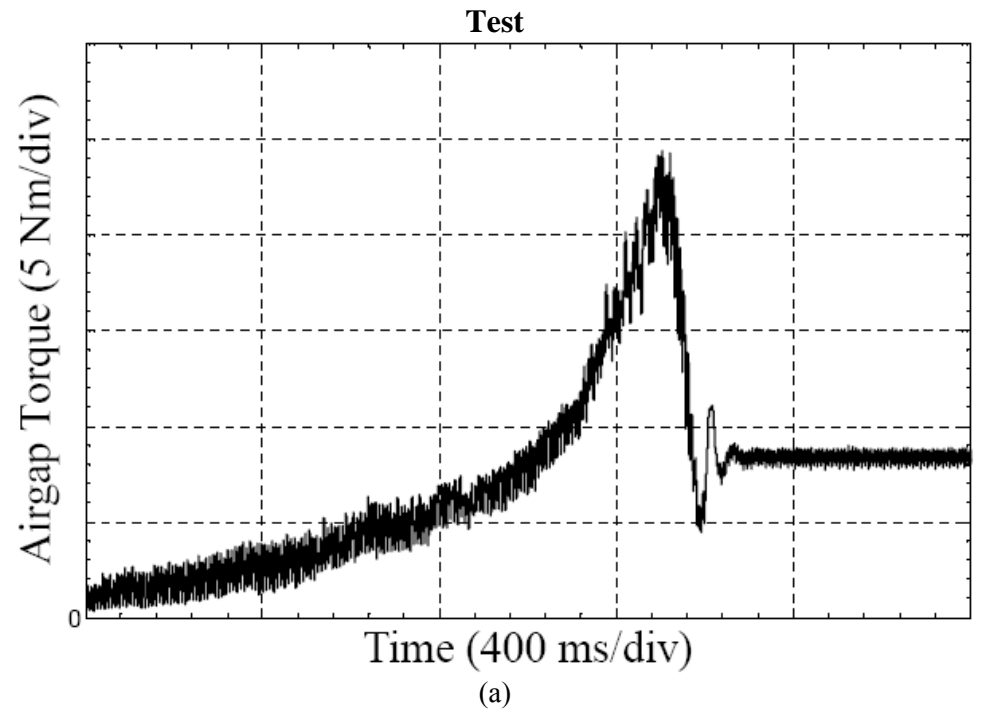


Figure 5.13: Motor developed torque obtained under *2-Phase Closed-Loop Control*. (a) Test. (b) Simulation.

## CHAPTER 6

---

---

# ANALYSIS OF FAILURE MODE AND EFFECT OF INVERTER SWITCH FAULTS ON MOTOR PERFORMANCE

---

---

### 6.1 Introduction

One of the most common types of drive system faults is the loss of a power transistor switch in one of the legs of the inverter which can be caused by either an open-circuit or short-circuit fault. In practice, a short-circuit switch fault occurs more frequently than an open-circuit switch fault [96], [97]. The open-circuit transistor switch fault is commonly due to either a malfunction in one of the PWM output ports of the controller that is transmitting the switching patterns, or sequences to the transistors, or a malfunction in the gate drive. On the other hand, the short-circuit transistor switch fault can be caused by a breakdown of the snubber circuit or a loose wire, resulting in a short-circuit fault. More specifically, the short-circuit transistor switch fault can lead to a catastrophic failure of the drive if the complementary transistor switch of the same leg is closed, resulting in a shoot-through or direct short-circuit of the dc bus link. On the contrary, for the open-circuit transistor switch fault, the motor-drive system will still function but at a much

inferior performance due to the significant torque pulsations introduced by the resulting asymmetry in the electrical circuit of the motor-drive system.

In this chapter, a closer look at the impacts of such inverter failure modes on machine performance is carried out. This is realized by means of the averaged switching function modeling concept [98]. Such approach provides a constructive analytical understanding of the extent of these fault effects. Meanwhile, time-domain simulation studies, in parallel with the analytical approach, are also employed to solidify the conclusive outcomes resulting from this study. Two distinct types of inverter transistor switch failure modes under investigation in this work are: (1) a transistor short-circuit switch fault ( $F_1$ ), and (2) a transistor open-circuit switch fault ( $F_2$ ), see Figure 6.1. It is important to mention that for the case of a transistor short-circuit switch fault ( $F_1$ ), the complementary transistor switch of the corresponding inverter leg is turned-off. This is in order to avoid shoot-through or direct short-circuit of the dc bus link. The motor performance resulting from this action is accordingly investigated.

## 6.2 Averaged Switching Function Model

In this section, an averaged switching function model representation of an inverter circuit of a three-phase standard drive was introduced [98]. This model allows one to easily compute the design parameters, such as the voltage and current ratings of the power semiconductor devices, which will serve as an easy-to-design tool for system design, stress evaluations, and component selections. Moreover, the numerical convergence and long “run-time” problems associated with detailed time-domain simulation models can be avoided. In this work, the inverter circuit switching function model is adopted to investigate and visualize the extent of the impacts of inverter transistor switch faults on the performance of induction motors.

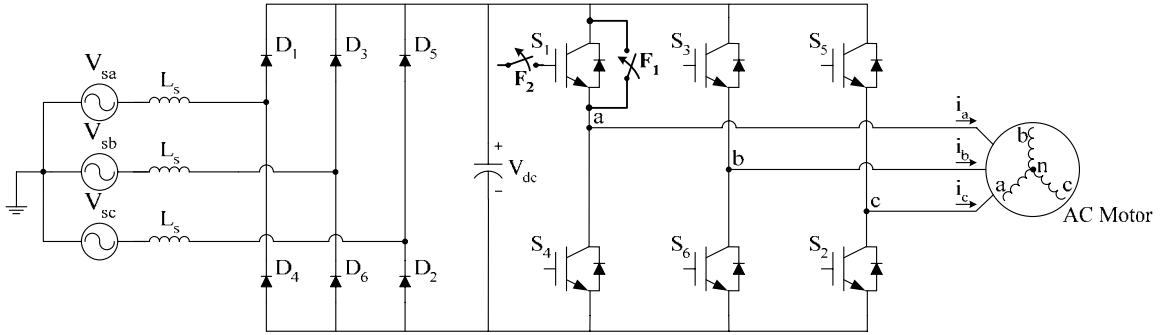


Figure 6.1: Types of inverter switch failure modes under investigation.

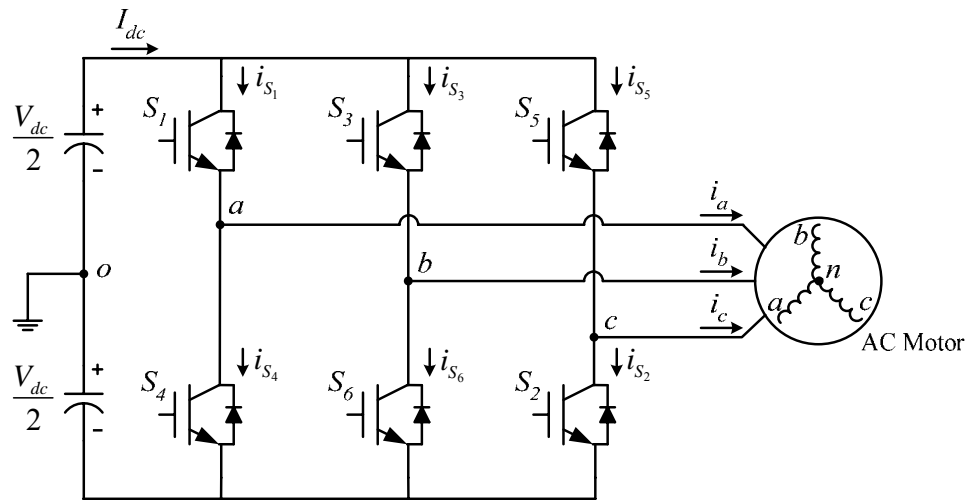


Figure 6.2: Inverter circuit.

## 6.2.1 Motor Phase Voltage Representations

A schematic of the drive inverter circuit is shown here in Figure 6.2. It consists of six power transistors connected with six anti-parallel diodes ( $S_1 \sim S_6$ ). The dc bus link consists of two dc capacitors, and they are usually of the electrolytic type due to their high capacitance values and high voltage ratings. The mid-point of the dc link is assumed here as the reference ground, which is denoted in Figure 6.2 as “o”.

Referring to Figure 6.2, the pole voltages measured *w.r.t.* the reference ground can be expressed as follows:

$$\begin{aligned} v_{ao} &= v_{an} + v_{no} \\ v_{bo} &= v_{bn} + v_{no} \\ v_{co} &= v_{cn} + v_{no} \end{aligned} \quad (6.1)$$

where,  $v_{an}, v_{bn}, v_{cn}$  represent the motor phase voltages, and  $v_{no}$  is usually referred to as the common-mode voltage. References should be made to Figure 6.2 with regard to the subscripts above. Summing up the left-hand and right-hand sides of (6.1), one obtains the following:

$$v_{ao} + v_{bo} + v_{co} = v_{an} + v_{bn} + v_{cn} + 3v_{no} \quad (6.2)$$

For a balanced motor,  $v_{an} + v_{bn} + v_{cn} = 0$ . Hence, (6.2) can be rewritten as follows:

$$v_{no} = \frac{1}{3}(v_{ao} + v_{bo} + v_{co}) \quad (6.3)$$

By substituting (6.3) in (6.1), the motor phase voltages can be expressed in the following manner:

$$\begin{aligned} v_{an} &= v_{ao} - v_{no} = \frac{1}{3}(2v_{ao} - v_{bo} - v_{co}) \\ v_{bn} &= v_{bo} - v_{no} = \frac{1}{3}(2v_{bo} - v_{ao} - v_{co}) \\ v_{cn} &= v_{co} - v_{no} = \frac{1}{3}(2v_{co} - v_{ao} - v_{bo}) \end{aligned} \quad (6.4)$$

## 6.2.2 Averaged Switching Function Formulations

The development of the PWM inverter can be greatly simplified by using the averaged switching function model. This is due to the fact that the PWM switching frequency is much larger than the power frequency of the desired inverter ac output voltages. Accordingly, one can assume almost sinusoidal (rippleless) output waveforms since the higher-order frequency time harmonics can be easily filtered out by the inherent low-pass filtering capability of the motor windings, and the lower-order frequency space-induced time harmonic effects due to winding layouts and core saturations are neglected during the analysis process.

In the analysis, the power switches are assumed ideal as is common in preliminary functional analysis of switching power converters [98]. These assumptions include: (a) negligible forward voltage drop of the switches in their on-state; (b) sufficient on-state current carrying capacity and off-state voltage blocking capacity commensurate and compatible with the current and voltage ratings of the system, respectively; and (c) negligible transition periods between the “turn-on” and “turn-off” states of the switches which permit repetitive high frequency switching. In order to maintain continuity of the three phase currents connected to the poles, only one of the switches connected to any given pole is turned-on. In other words, at any given instant of time, no two switches of the same inverter leg can be turned-on (which results in a shoot-through) or turned-off.

Mathematically, these constraints may be expressed using switching function formulations [98]. Let  $H_j(t)$ ,  $j = 1, 2, 3, 4, 5, 6$ , be the switching function of each of the corresponding switches,  $S_1 \sim S_6$ , respectively. Furthermore,  $H_j(t)$  is expressed in a binary format, that is  $H_j(t) = 1$  when a switch is turned-on, and  $H_j(t) = 0$  when a switch is turned-off. Accordingly, in light of the constraints mentioned earlier, one can state the following switching function conditions for inverter leg-*a*, leg-*b*, and leg-*c*, respectively, as follows:

$$\begin{aligned}
H_1 + H_4 &= 1 \\
H_3 + H_6 &= 1 \\
H_5 + H_2 &= 1
\end{aligned} \tag{6.5}$$

Using the switching functions defined above, the pole voltages of Figure 6.2 can be described as follows:

$$\begin{aligned}
v_{ao} &= H_1(V_{dc}/2) + H_4(-V_{dc}/2) \\
v_{bo} &= H_3(V_{dc}/2) + H_6(-V_{dc}/2) \\
v_{co} &= H_5(V_{dc}/2) + H_2(-V_{dc}/2)
\end{aligned} \tag{6.6}$$

Depending on the switching states, equation (6.6) indicates that the pole voltages,  $v_{ao}, v_{bo}, v_{co}$ , only can have the values of either  $V_{dc}/2$  or  $-V_{dc}/2$  at any given time instant. In addition, the states of the switching functions depend on the types of pulse-width modulation (PWM) schemes being used. For simplicity of explanation, a carrier-based PWM, or the so-called sine-triangle PWM, scheme is utilized here [84].

Considering only the power switch,  $S_1$ , of Figure 6.2, the corresponding pole voltage,  $v_{ao} = H_1(V_{dc}/2)$ , is graphically illustrated in Figure 6.3. The switching states of  $H_1$ , at any given time instant, depend on the comparison outcome between the reference signal,  $V_{ref}$ , and the carrier (or triangle) signal,  $V_{carrier}$ . In other words,  $H_1$  can be defined in the following manner:

$$H_1 = \begin{cases} 1 & \text{for } V_{ref} > V_{carrier} \\ 0 & \text{otherwise} \end{cases} \tag{6.7}$$

Here, the reference signal,  $V_{ref}$ , represents the duty ratio,  $d_a$ , that varies in a sinusoidal fashion which also represents the desired fundamental inverter output ac voltage waveform. On the other hand, the carrier signal,  $V_{tri}$ , is a triangle wave that varies between -1 and 1 with a switching frequency,  $f_{sw}$ . In practice, each of these variables is typically scaled such that the actual voltage level makes the best use of the hardware on which it is implemented.

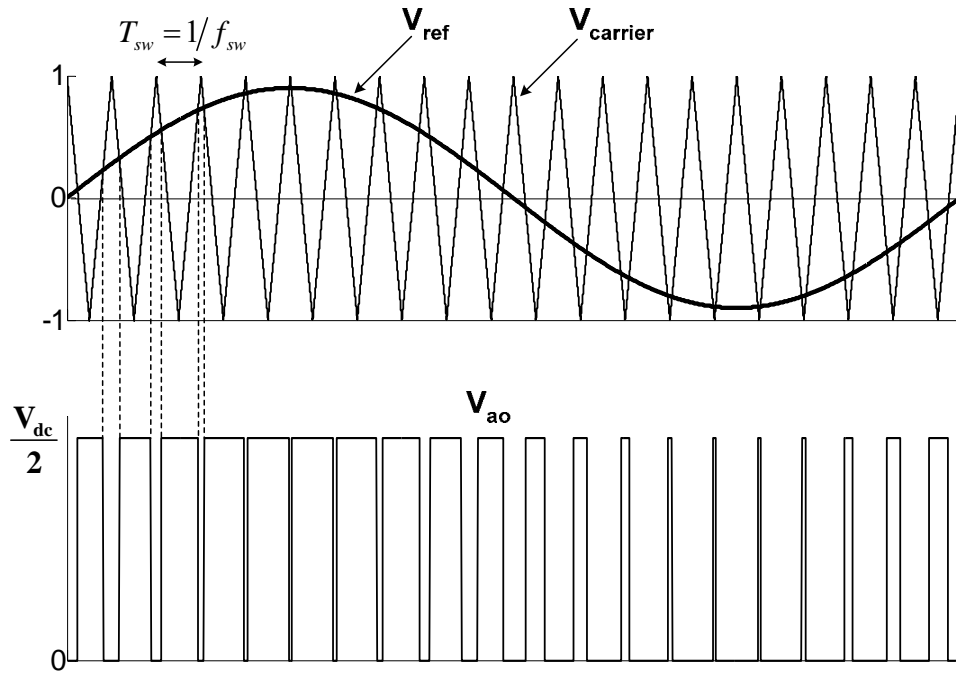


Figure 6.3: PWM switching function,  $H_I$ , of switch,  $S_I$ , of inverter leg- $a$ .

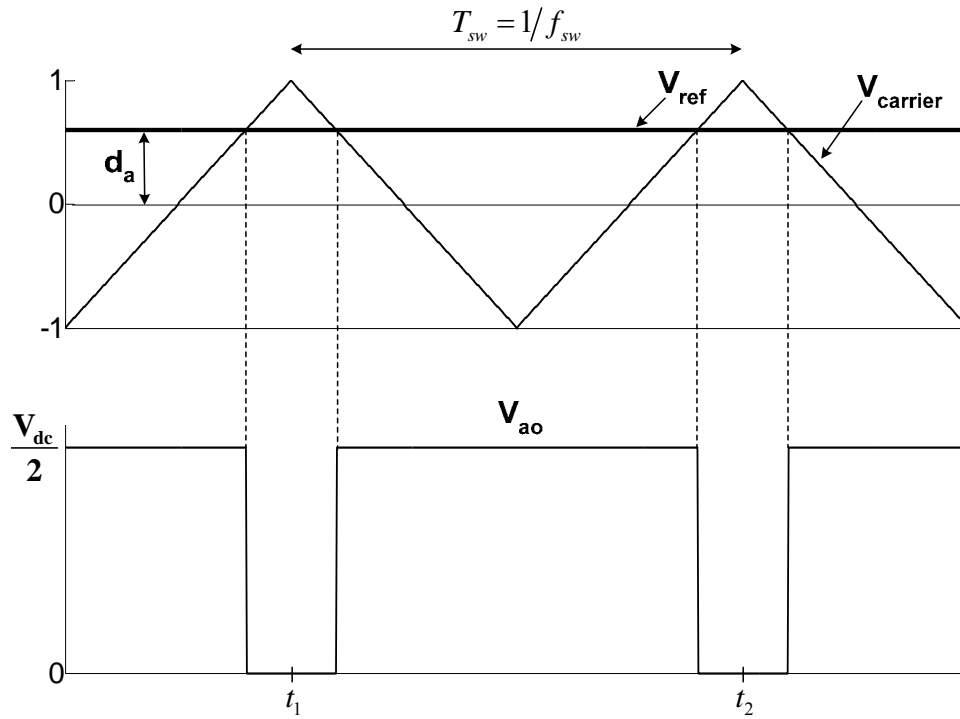


Figure 6.4: Switching function expressed over a switching period of switch,  $S_I$ .

Assuming that the switching frequency,  $f_{sw}$ , is sufficiently large, the duty ratio or  $V_{ref}$  of Figure 6.3 will appear as constant throughout a switching period,  $T_{sw}$ , as depicted in Figure 6.4. Therein, the duty ratio,  $d_a$ , is shown as being constant even though it is in fact sinusoidal. This is because of the assumption that the triangle wave is assumed to have a much higher switching frequency than the duty ratio signal,  $d_a$ , (or  $V_{ref}$ ). For the purposes of analysis, it is convenient to define the averaged switching function,  $\hat{H}_1$ , of  $H_1$ , that is, the average value over of a period of time,  $T_{sw}$ , as follows:

$$\hat{H}_1(t) = \frac{1}{T_{sw}} \int_{t_1}^{t_2} H_1(t) dt \tag{6.8}$$

where,  $t_2 - t_1 = T_{sw}$ . From (6.8) and Figure 6.4, it can be demonstrated that the averaged switching function,  $\hat{H}_1$ , can be expressed in the following manner:

$$\hat{H}_1 = \frac{1}{2}(1 + d_a) \tag{6.9}$$

Using the earlier defined constraints which state that  $H_1 + H_4 = 1$ , the averaged switching function of  $H_4$ , that is  $\hat{H}_4$ , is given as follows:

$$\hat{H}_4 = 1 - \hat{H}_1 = \frac{1}{2}(1 - d_a) \tag{6.10}$$

In real practice, as mentioned earlier, the duty ratio,  $d_a$ , is not constant and it is in fact sinusoidal. Accordingly, one can choose a balanced set of desired three-phase duty ratio (modulating) signals with amplitude,  $m_a$ , ( $0 < m_a < 1$ ), and angular frequency,  $\omega = 2\pi f$ , that produce a set of sinusoidal, fundamental inverter output waveforms, as follows:

$$\begin{aligned} d_a(t) &= m_a \cos(\omega t) \\ d_b(t) &= m_a \cos(\omega t - 2\pi/3) \\ d_c(t) &= m_a \cos(\omega t - 4\pi/3) \end{aligned} \tag{6.11}$$

The amplitude,  $m_a$ , of the duty ratio signal is also referred to as the modulation index. By varying the modulation index and the angular frequency, one can vary the amplitude and frequency of the desired fundamental component of the inverter output waveforms.

Accordingly, using the modulating signals as defined in (6.11), the averaged switching functions,  $\hat{H}_1 \dots \hat{H}_6$ , of all six switches,  $S_1 \sim S_6$ , respectively, can be expressed as follows:

$$\begin{aligned}
 \hat{H}_1(t) &= \frac{1}{2}(1 + m_a \cos(\omega t)) \\
 \hat{H}_2(t) &= \frac{1}{2}(1 - m_a \cos(\omega t - 4\pi/3)) \\
 \hat{H}_3(t) &= \frac{1}{2}(1 + m_a \cos(\omega t - 2\pi/3)) \\
 \hat{H}_4(t) &= \frac{1}{2}(1 - m_a \cos(\omega t)) \\
 \hat{H}_5(t) &= \frac{1}{2}(1 + m_a \cos(\omega t - 4\pi/3)) \\
 \hat{H}_6(t) &= \frac{1}{2}(1 - m_a \cos(\omega t - 2\pi/3))
 \end{aligned} \tag{6.12}$$

By substituting the averaged switching functions of (6.12) into (6.6), one obtains the following fundamental harmonic terms for the three-phase pole voltages:

$$\begin{aligned}
 v_{ao} &= \frac{1}{2} m_a V_{dc} \cos(\omega t) \\
 v_{bo} &= \frac{1}{2} m_a V_{dc} \cos(\omega t - 2\pi/3) \\
 v_{co} &= \frac{1}{2} m_a V_{dc} \cos(\omega t - 4\pi/3)
 \end{aligned} \tag{6.13}$$

Substituting the pole voltages as defined in (6.13) into (6.4) yield the following set of expressions for the fundamental motor phase voltages, as follows:

$$\begin{aligned}
 v_{an} &= \frac{1}{2} m_a V_{dc} \cos(\omega t) \\
 v_{bn} &= \frac{1}{2} m_a V_{dc} \cos(\omega t - 2\pi/3) \\
 v_{cn} &= \frac{1}{2} m_a V_{dc} \cos(\omega t - 4\pi/3)
 \end{aligned} \tag{6.14}$$

Examinations of (6.13) and (6.14) reveal a few important observations. First, in order to synthesize a set of desired fundamental components of the motor line-to-neutral voltages ( $v_{an}, v_{bn}, v_{cn}$ ), one can realize these by specifying the desired reference duty ratio signals with the preferred modulation index and output fundamental frequency. Second, only the fundamental harmonic terms of the motor phase voltages are in congruence with those fundamental harmonic terms of the pole voltages. This condition only holds true for a balanced three-phase motor. Third, the maximum line-to-neutral motor voltage that one can realize from using the sine-triangle PWM scheme in this work is  $V_{dc}/2$ .

From the above illustrations, the outputs of a three-phase inverter circuit can be simply described by a set of three-phase voltage expressions as given in (6.14) for the case of the sine-triangle PWM scheme. The use of the switching function concept is extremely useful in analyzing the behavior of switching power converters in general, as well as simplifying the control design process in the small-signal environment. In the following sections, focus will be made on the study of the impacts of inverter transistor switch faults on motor performance using both the averaged switching function modeling concept, as well as the time-domain simulation approach.

### 6.3 Analysis of Failure Modes and Effects

In this section, the failure impacts of inverter transistor switch faults on the performance of induction motors are investigated. Two distinct types of failure modes considered in this work are: (1) a transistor short-circuit switch fault, and (2) a transistor open-circuit switch fault, see

Figure 6.1. Analytical and simulation results, along with insights and discussions, are presented here to provide a constructive understanding of the extent of the severity caused by such faults.

### 6.3.1 Short-Circuit Switch Fault

As mentioned earlier, a transistor short-circuit switch fault can instigate a catastrophic failure in the electric drive system if the complementary transistor switch of the corresponding inverter leg is turned-on, resulting in a shoot-through of the dc bus link. In this work, the running performance of the motor when the complementary healthy transistor switch is turned-off in the event of detecting a short-circuit switch fault in the same inverter leg is investigated. For the sake of this analysis, a short-circuit fault is assumed to occur at switch  $S_j$ , hence switch  $S_d$  is turned-off.

Having the pole of the inverter leg- $a$  tied directly to the positive rail of the dc link due to a short-circuit fault, and assuming the PWM switching patterns of the remaining two healthy inverter legs, that is leg- $b$  and leg- $c$ , remain unaltered during pre- and post-fault conditions, the fundamental terms of the three-phase pole voltages, based on the earlier derivations, can be written as follows:

$$\begin{aligned} v_{ao} &= \frac{1}{2}V_{dc} \\ v_{bo} &= \frac{1}{2}m_a V_{dc} \cos(\omega t - 2\pi/3) \\ v_{co} &= \frac{1}{2}m_a V_{dc} \cos(\omega t - 4\pi/3) \end{aligned} \tag{6.15}$$

Accordingly, the motor line-to-neutral voltage of phase- $a$  can be acquired using the earlier derived voltage expression, that is  $v_{an} = (2v_{ao} - v_{bo} - v_{co})/3$ , which yields the following:

$$v_{an} = \frac{1}{3}V_{dc} + \frac{1}{6}m_a V_{dc} \cos(\omega t) \tag{6.16}$$

Likewise, voltage expressions for phase-*b* and phase-*c* can also be determined in a similar fashion, that is  $v_{bn} = (2v_{bo} - v_{ao} - v_{co})/3$  and  $v_{cn} = (2v_{co} - v_{ao} - v_{bo})/3$ . Hence, one obtains the following voltage expressions for phase-*b* and phase-*c*, respectively, as follows:

$$\begin{aligned} v_{bn} &= -\frac{1}{6}V_{dc} + \frac{\sqrt{7}}{6}m_aV_{dc} \cos(\omega t - \phi - \pi/2) \\ v_{cn} &= -\frac{1}{6}V_{dc} + \frac{\sqrt{7}}{6}m_aV_{dc} \cos(\omega t + \phi + \pi/2) \end{aligned} \tag{6.17}$$

where,  $\phi = \tan^{-1}(1/3\sqrt{3})$ .

Examinations of (6.16) and (6.17) indicates the presence of a significant dc (unidirectional) component term in all the phase voltages. Due to an isolated motor neutral, these dc (unidirectional) offsets in all phases will add up to zero. In addition, a close observation of both (6.16) and (6.17) reveals that the dc component term is larger in magnitude than the fundamental harmonic term in all the phase voltages. Such phenomenon introduces a significant negative impact on the motor running performance. This is due to the fact that the dc voltage terms will introduce a set of dc current terms in the corresponding phase currents, which will in turn generate a resultant dc or stationary magnetic field in the machine. Since the dc magnetic field is dominant over the rotating fundamental magnetic field, a significant braking torque will be produced. Such phenomenon results in the motor speed to drop sharply. Furthermore, the electromagnetic interaction between the dc component of the stator current and the fundamental component of the rotor magnetic field generates a pulsating torque at a frequency equal to the fundamental stator current frequency. Accordingly, this results in an oscillating torque with a zero average torque and speed. A fault of such type introduces a high degree of severity due to the high circulating dc (unidirectional) current in the motor windings. Consequently, this will cause a temperature rise in the windings owing to excessive losses, and insulation breakdowns will eventually occur. Using (6.16) and (6.17), these dc currents can be computed as follows:

$$\begin{aligned}
 I_{a(dc)} &= \frac{V_{dc}/3}{R_s} \\
 I_{b(dc)} &= -\frac{V_{dc}/6}{R_s} \\
 I_{c(dc)} &= -\frac{V_{dc}/6}{R_s}
 \end{aligned} \tag{6.18}$$

where,  $R_s$  is the stator equivalent series resistance per phase. It should be noted that the inductance terms in the T-equivalent circuit model are “shorted” (or zero) under dc condition, which entails the expressions as delineated in (6.18).

### 6.3.1.1 Circuit Simulation Model

The simulation work was again carried out using *Matlab-Simulink* software package [91]. The power circuit structure of the induction motor-drive system is depicted in Figure 6.5. The same 2-hp, 4-pole, 3-phase induction motor, that was used as the simulation target in the earlier chapters, was again employed here in these simulations. Its machine parameters are given in Appendix A. The power stages of the drive system consist of a three-phase diode rectifier bridge at the drive front-end for the purpose of converting voltages from ac to dc, a split dc link capacitor bank to act as an energy storage device and a dc filter, followed by a three-phase inverter bridge for converting voltages from dc to ac in order to supply the motor. The snubber circuits, which are not shown in the schematic, are implicitly defined inside the blocks of both the rectifier and inverter bridges. The PWM modulation scheme is of the sine-triangle type. The motor was simulated in the  $dq$  frame of reference representation under rated load (8.169 Nm) and rated speed (1744 r/min) conditions. Meanwhile, the load is of the fan type:  $T_L = k_L \omega_m^2$ , where  $\omega_m$  denotes the motor speed in mechanical radians per second, and  $k_L$  is the load coefficient in Nm/(mech. rad/sec)<sup>2</sup>. The complete simulation parameters and conditions are given in Table 6.1.

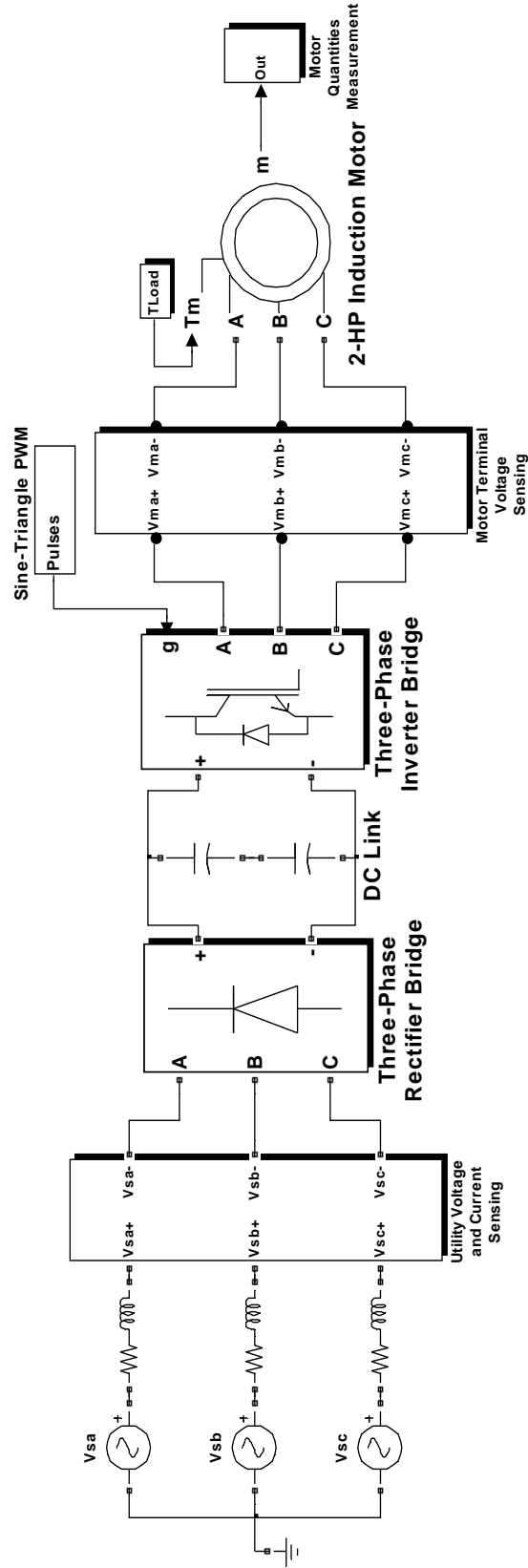


Figure 6.5: Schematic of induction motor-drive power structure in *Matlab-Simulink* [91].

Table 6.1: Simulation conditions of induction motor-drive system.

<b>Utility</b>	
Utility Input Voltage (Line-To-Line)	460 Volts
Frequency	60 Hz
Line Resistance (4.8%)	0.7082 $\Omega$
Line Inductance (4.8%)	1.8786 mH
<b>DC Link (2 capacitors in series)</b>	
Capacitance Value	2000 $\mu$ F per capacitor
<b>Induction Motor</b>	
Rated Power	2 hp (1492 Watts)
Rated Voltage (Line-To-Line)	460 Volts
Rated Current	3.0 Amps
Rated Frequency	60 Hz
Rated Speed	1744 r/min
Rated Torque	8.169 Nm
Phase	3
Number of Poles	4
Stator Resistance, $R_s$	3.850 $\Omega$
Rotor Resistance, $R_r$	2.574 $\Omega$
Stator Leakage Inductance, $L_{ls}$	17.5594 mH
Rotor Leakage Inductance, $L_{lr}$	17.5594 mH
Magnetizing Inductance, $L_m$	0.372674 H
Moment of Inertia, $J$	0.028 kg.m <sup>2</sup>
<b>Load (<math>T_L = k_L \omega_m^2</math>)</b>	
Load Coefficient, $k_L$	$0.24493 \times 10^{-3}$ Nm/(m. rad/s) <sup>2</sup>
<b>PWM Controller</b>	<b>Carrier-Based Sine-Triangle</b>
Modulation Index, $m_a$	0.9
Switching Frequency	5 kHz

### 6.3.1.2 Analytical and Simulation Results

The analytical waveforms of the three-phase motor line-to-neutral voltages obtained using (6.16) and (6.17), under transistor short-circuit switch fault at  $S_1$ , are shown here in Figure 6.6(a), under the conditions of  $m_a = 0.9$  and  $V_{dc} = 610$  Volts. This is in order to match with the simulation operating conditions. Again, it should be noted that the complementary transistor switch,  $S_4$ , was turned-off in order to avoid a shoot-through. The corresponding simulation results of the motor line-to-neutral voltages, at a low-pass filtering cutoff frequency of 120-Hz, are depicted in Figure 6.6(b). The purpose of filtering the voltage waveforms is to be able to meaningfully compare them with the analytical results that neglect the lower-order frequency space/machine induced time harmonics, as well as the higher-order frequency time harmonics due to the PWM switching. It can be observed from Figure 6.6 that the analytical waveforms are in good agreement with the simulation waveforms. The FFT frequency spectra of the associated simulated three-phase voltage waveforms are illustrated in Figure 6.7. The dc and the fundamental harmonic voltage terms of all phases computed using (6.16) and (6.17), as well as those obtained from the simulation frequency spectra of Figure 6.7 are given in Table 6.2. Again, the analytical and simulation values match quite well with one another.

The simulation results of the three-phase motor currents during pre- and post-fault conditions are depicted in Figure 6.8. As one can observe therein, a severe transient occurs at the time instant when the fault is introduced at  $t = 1.3$  sec. As was expected from the earlier analysis, a large positive dc (unidirectional) current is present in phase- $a$ , and this dc current is divided equally between phase- $b$  and phase- $c$ , as was shown in Figure 6.8. The FFT frequency spectra of the corresponding motor phase currents during post-fault condition are illustrated in Figure 6.9 for all three phases. Again, notice the large dc current components present in all phases. To verify the earlier analysis, the dc current terms were acquired analytically using (6.18), and they are given in Table 6.3, along with the simulation values obtained from Figure 6.9.

Therein, the close agreement between the analytical and simulation results confirms or validates the earlier analytical study.

To further investigate the motor performance during post-fault condition, the motor speed and developed torque profiles are depicted in Figure 6.10(a) and Figure 6.11(a), respectively. The associated FFT frequency spectra during post-fault condition are also shown in Figure 6.10(b) and Figure 6.11(b), respectively. It can be observed from the speed profile, upon the occurrence of fault at  $t = 1.3$  sec, that the braking torque introduced by the dc magnetic field causes the speed to drop sharply. In addition, as mentioned above, the electromagnetic interactions between the resultant stator dc field and the resultant rotor fundamental rotating field introduce a pulsating torque, and subsequent speed ripples, at the fundamental power frequency. This phenomenon can be observed from the FFT spectra as was illustrated in Figure 6.10(b) and Figure 6.11(b) for the speed and torque profiles, respectively. Notice in the FFT spectrum of the torque profile shown in Figure 6.11(b), the fundamental component of the pulsating torque has a peak value of 79Nm, which is substantially high as compared to the average torque (8.2Nm) of the motor during the pre-fault (healthy) state.

Evidently, the extent of the fault severity due to a short-circuit switch fault on the motor performance has been shown to be severe. Hence, fault isolation along with remedial action need to be performed in a minimum of elapse time in order to maintain, to the fullest extent, the desirable motor performance characteristics during normal operation. This remedial action will be detailed in the next chapter.

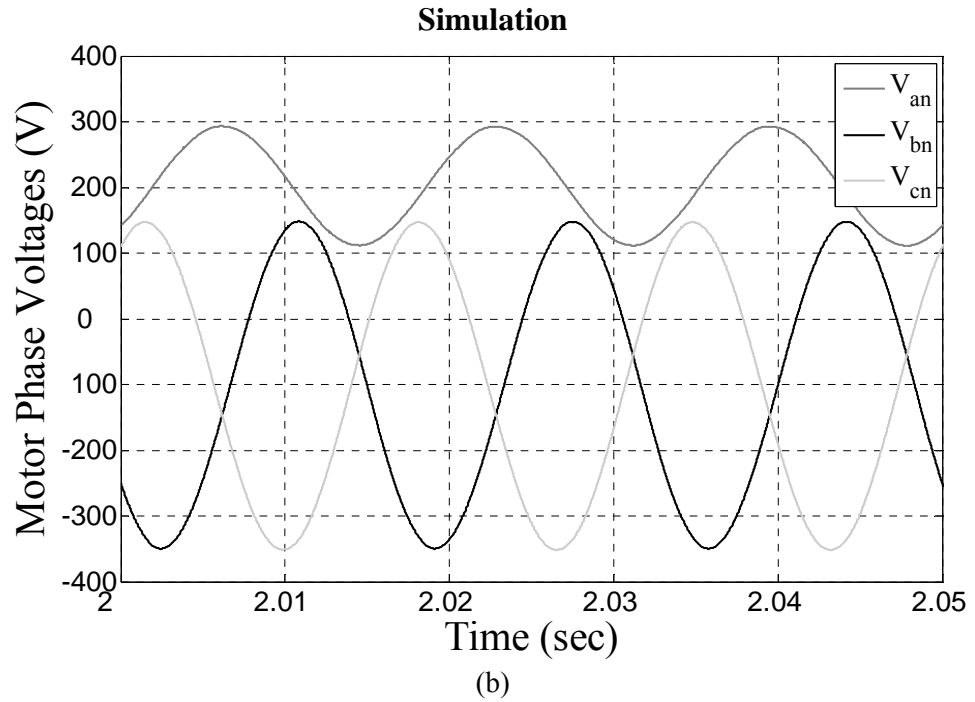
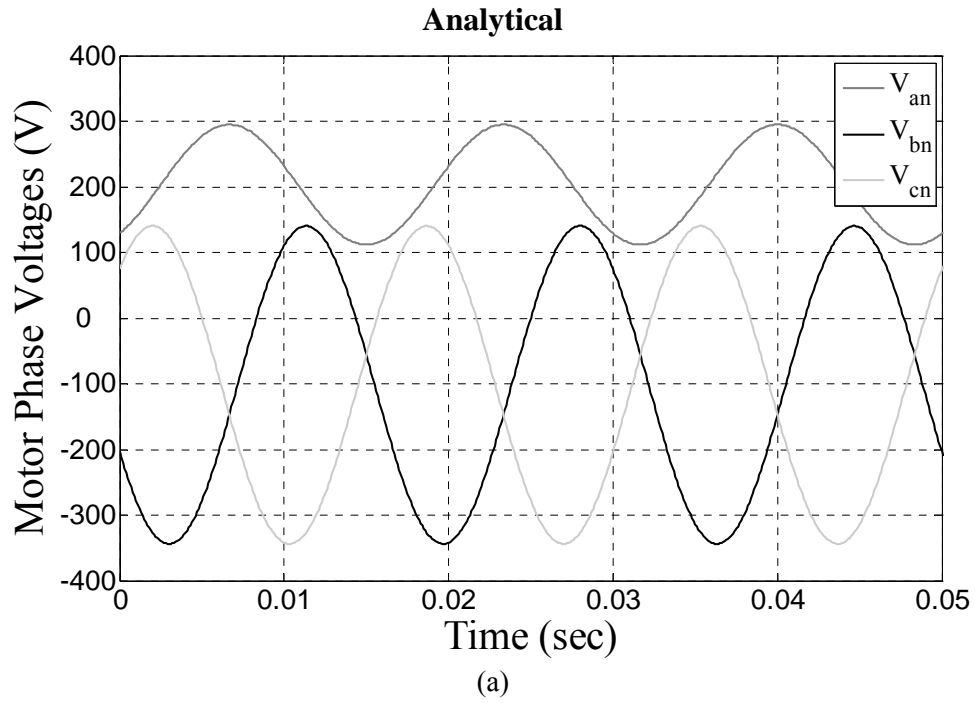
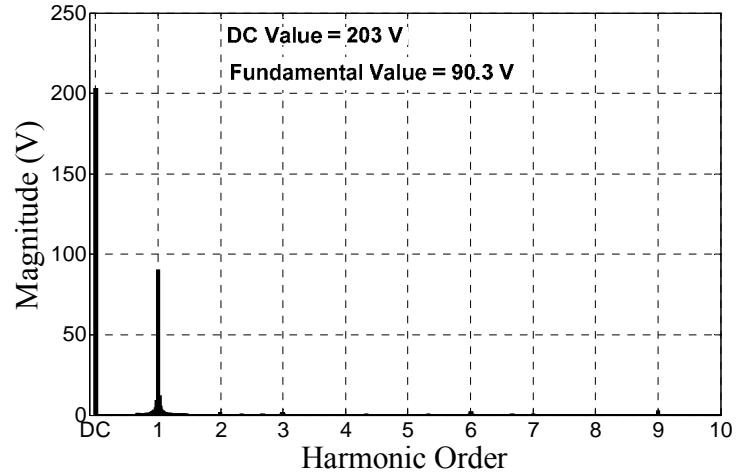
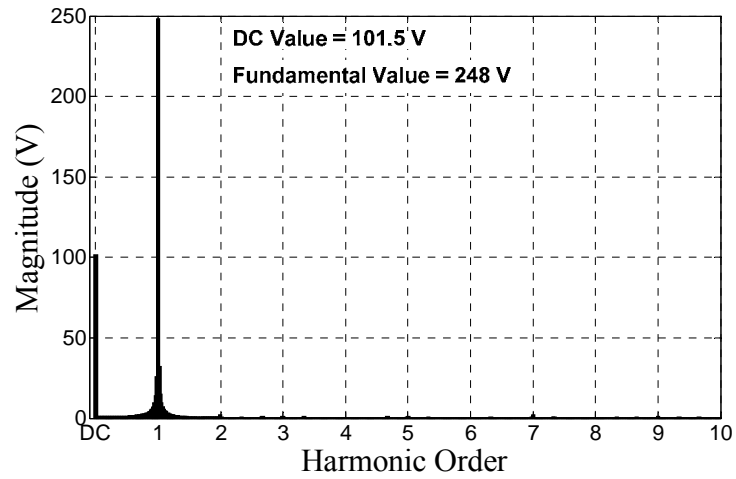


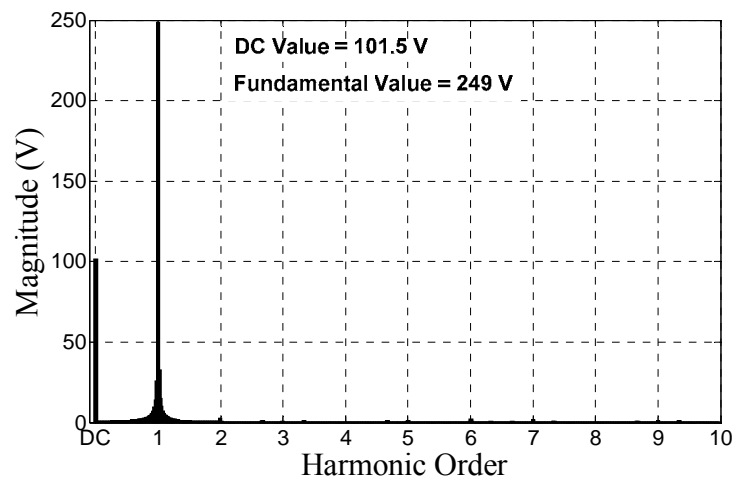
Figure 6.6: Three-phase motor phase voltages during short-circuit switch fault condition. (a) Analytical. (b) Simulation.



(a)



(b)



(c)

Figure 6.7: FFT spectra of simulated three-phase motor phase voltages during short-circuit switch fault condition. (a) Phase-a. (b) Phase-b. (c) Phase-c.

Table 6.2: Harmonic contents of motor phase voltages under short-circuit switch fault condition – Analytical and Simulation

	Analytical		Simulation	
	DC (V)	Fundamental (V)	DC (V)	Fundamental (V)
$v_{an}$	203.3	91.5	203	90.3
$v_{bn}$	-101.7	242.1	-101.5	248
$v_{cn}$	-101.7	242.1	-101.5	249

Table 6.3: Harmonic contents of motor phase currents under short-circuit switch fault condition – Analytical and Simulation

	Analytical	Simulation
	DC (A)	DC (A)
$i_a$	52.8	52
$i_b$	-26.4	-26
$i_c$	-26.4	-26

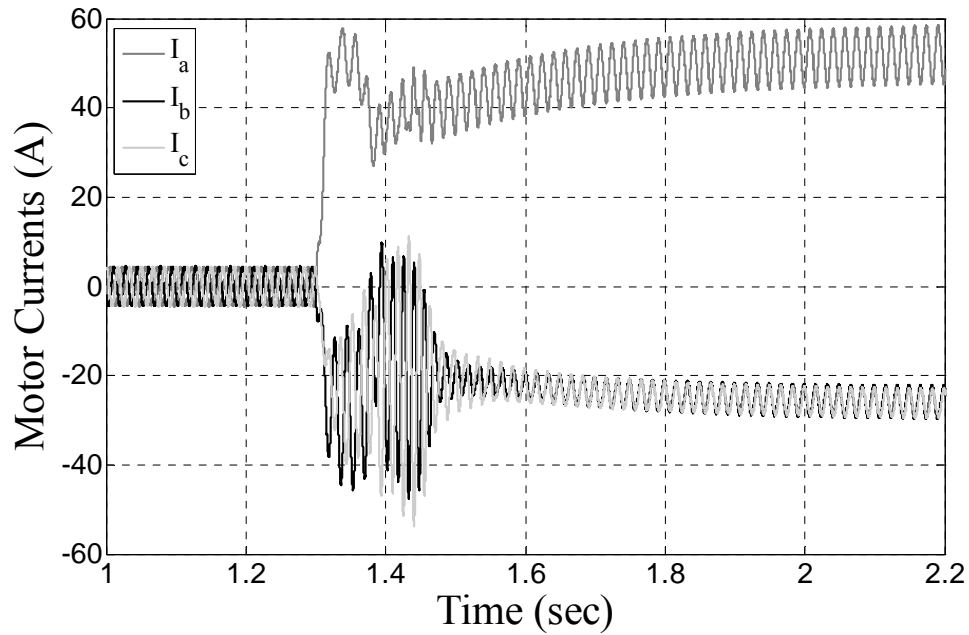
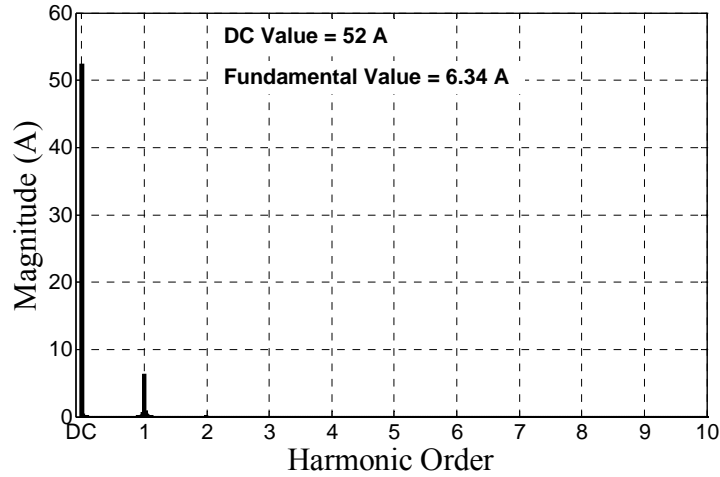
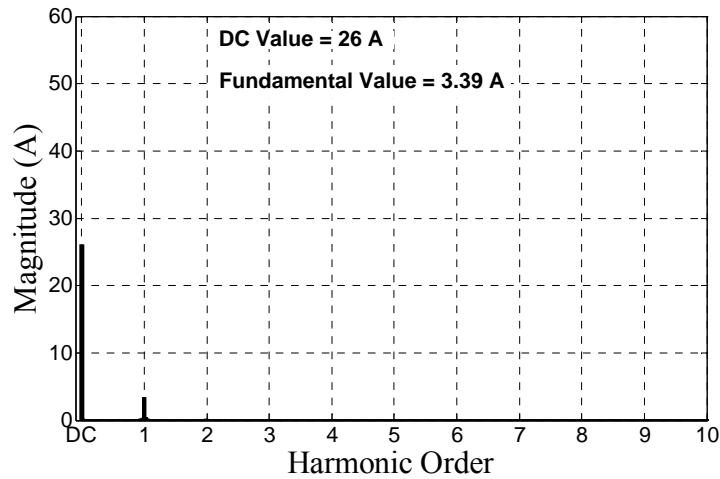


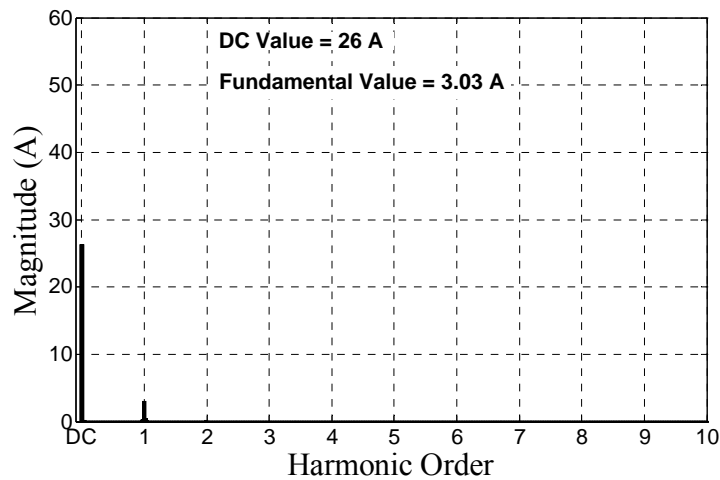
Figure 6.8: Simulation results of three-phase motor currents during pre- and post-fault short-circuit switch fault conditions (fault occurs at  $t = 1.3 \text{ sec}$ ).



(a)



(b)



(c)

Figure 6.9: FFT spectra of simulated three-phase motor currents during short-circuit switch fault condition. (a) Phase-a. (b) Phase-b. (c) Phase-c.

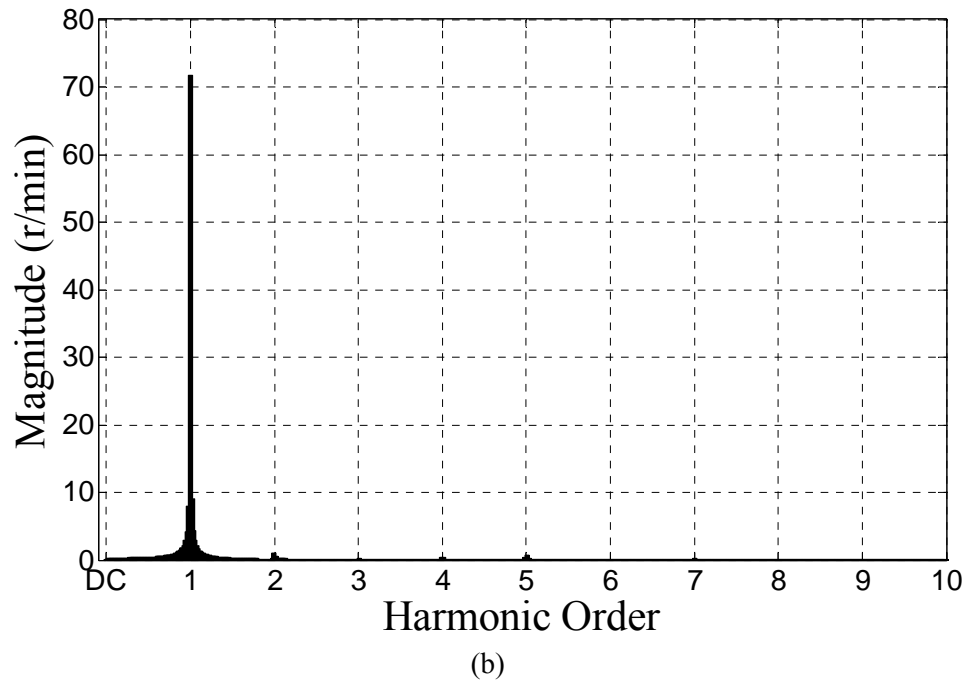
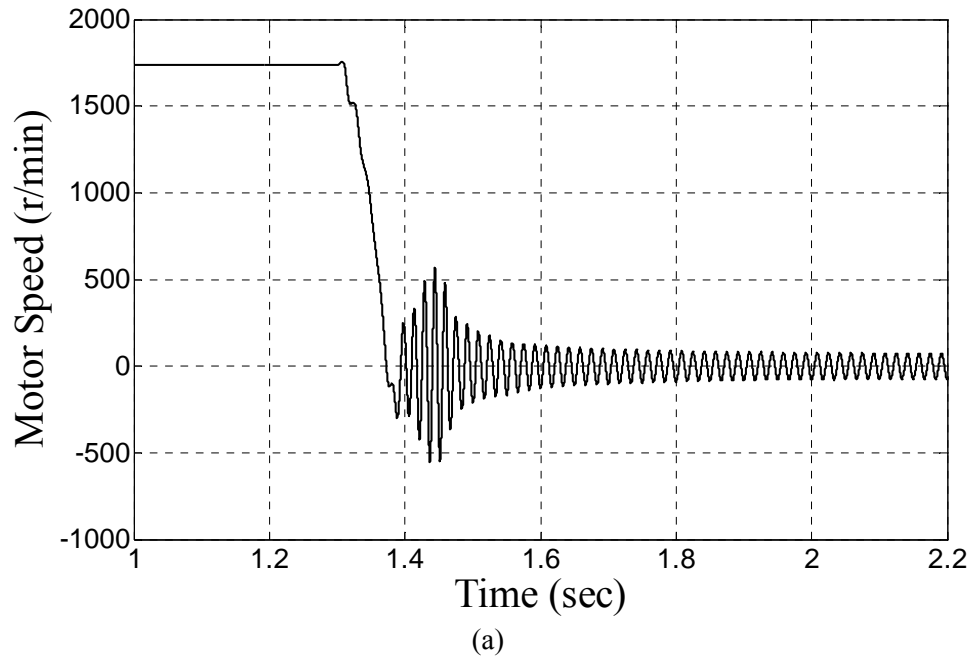


Figure 6.10: Simulation results of motor speed during short-circuit switch fault condition (fault occurs at  $t = 1.3$  sec). (a) Time-domain profile during pre- and post-fault. (b) FFT spectrum during post-fault.

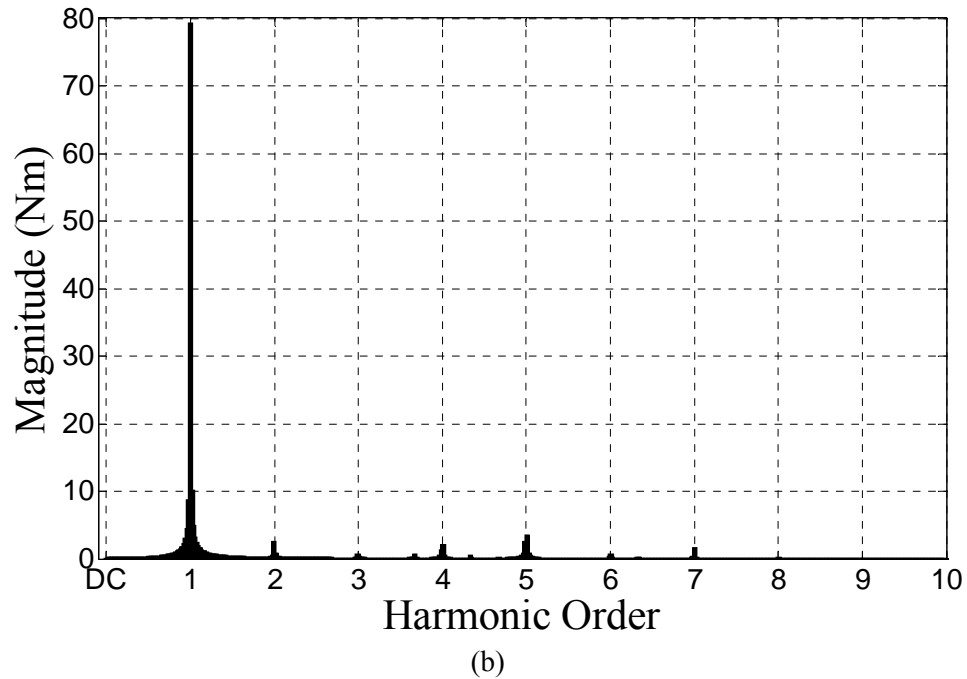
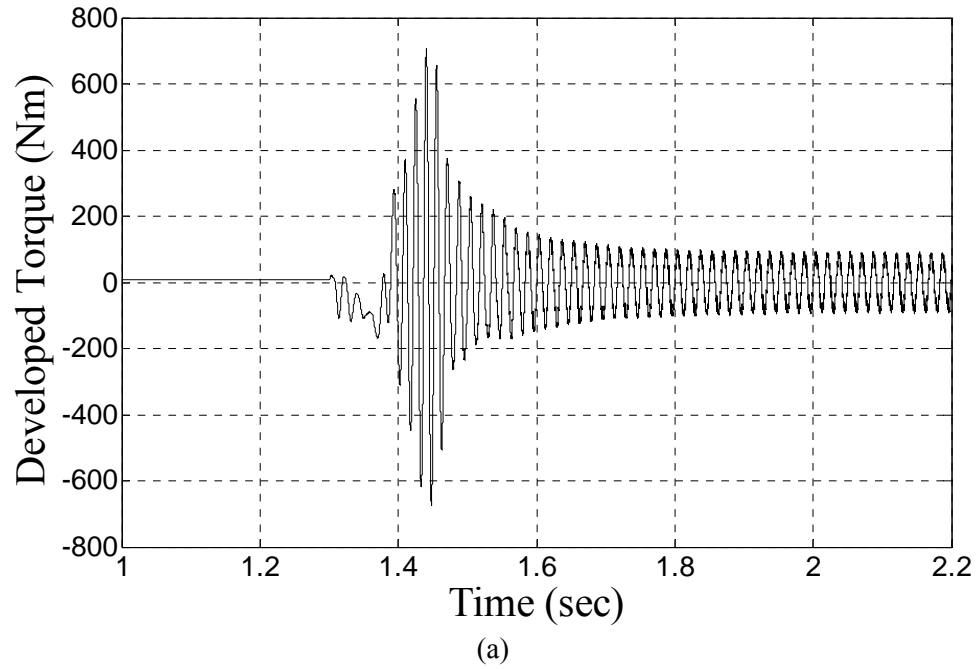


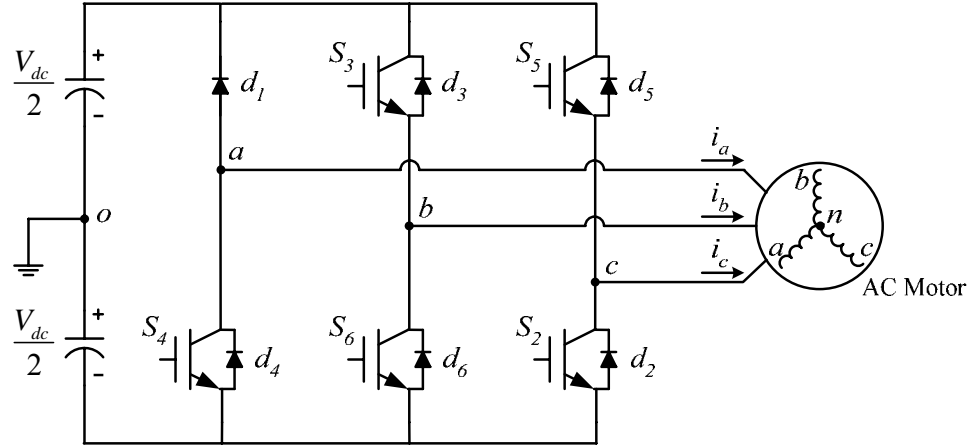
Figure 6.11: Simulation results of motor developed torque during short-circuit switch fault condition (fault occurs at  $t = 1.3$  sec). (a) Time-domain profile during pre- and post-fault. (b) FFT spectrum during post-fault.

### 6.3.2 Open-Circuit Switch Fault

Failure in either one of the PWM digital output ports of a DSP board or one of the isolation amplifiers of the gate drive can lead to an open-circuit fault in the transistor switch, as shown in Figure 6.1. A transistor open-circuit switch fault is a less severe type of fault as compared to the short-circuit switch fault. Nevertheless, such type of inverter fault will still generate disturbances in the form of pulsating electromagnetic torque and a substantial dc component in the stator winding currents. This dc current component will cause thermal problems, such as temperature rise, in the windings. Eventually, insulation breakdown will occur if the fault is left unmitigated. For the sake of analysis, an open-circuit fault occurring in switch,  $S_1$ , is considered in this work.

A misfiring of the transistor switch,  $S_1$ , will result in an inverter circuit topology, as illustrated in Figure 6.12. Intuitively, through the observation of Figure 6.12, one can state that there will not be any positive current flow into the motor for phase- $a$  after the fault occurrence, due to the absence or malfunction of switch  $S_1$ . Hence, the resulting post-fault phase- $a$  current,  $i_a$ , will consist of a dc (unidirectional) current component. If the motor has an isolated (floating) neutral connection, this dc (unidirectional) current term will be divided between the currents of the remaining two phases. As previously mentioned, the consequence of having a dc (unidirectional) current circulating in the motor windings leads to the significant presence of motor torque pulsations.

In the circuit of Figure 6.12, the pole voltage of phase- $a$  is determined based on the phase- $a$  current,  $i_a$ , and the switching patterns associated with the switch,  $S_4$ . If the switching patterns of  $S_4$ , as well as the other switches of phase- $b$  and phase- $c$ , remain the same after the fault occurrence, the pole voltages,  $v_{ao}, v_{bo}, v_{co}$ , can be defined based on the earlier derivations of the averaged switching functions, assuming that current is positive when flowing into the motor terminal, as follows:


 Figure 6.12: Inverter circuit topology with an open-circuit fault at switch  $S_1$ .

$$v_{ao} = \begin{cases} -\frac{V_{dc}}{2} & \text{for } i_a > 0 & \text{(State-1)} \\ -\frac{V_{dc}}{2} & \text{for } i_a < 0 \text{ and } S_4 \text{ is ON} & \text{(State-2)} \\ \frac{V_{dc}}{2} & \text{for } i_a < 0 \text{ and } S_4 \text{ is OFF} & \text{(State-3)} \\ \frac{1}{2}(v_{bo} + v_{co} + 3e_a) & \text{for } i_a = 0 & \text{(State-4)} \end{cases}$$

$$v_{bo} = \frac{1}{2} m_a V_{dc} \cos(\omega t - 2\pi/3)$$

$$v_{co} = \frac{1}{2} m_a V_{dc} \cos(\omega t - 4\pi/3)$$
(6.19)

where,  $e_a$  represents the back emf of the phase- $a$  motor winding.

As one can see from (6.19), there are four different states associated with the pole voltage of phase- $a$ . The first state, namely State-1, implies that  $v_{ao} = -V_{dc}/2$  when  $i_a > 0$ . It should be noted that this state only takes place when the phase- $a$  current is positive during the time instant of the fault occurrence. Hence, this state represents the time interval between the fault instant and the first zero-crossing instant of the phase- $a$  current,  $i_a$ . During this time interval, the free-wheeling diode,  $d_4$ , will conduct current.

The next two states, namely State-2 and State-3, occur during the negative half cycle of the phase-*a* current. In these states, the phase-*a* pole voltage,  $v_{ao}$ , alternates between  $V_{dc}/2$  and  $-V_{dc}/2$ , depending on the switching patterns. Accordingly, from the averaged switching function derivation, the line-to-neutral voltages of all three phases can be defined as follows:

$$\left. \begin{aligned} v_{an} &= \frac{1}{2} m_a V_{dc} \cos(\omega t) \\ v_{bn} &= \frac{1}{2} m_a V_{dc} \cos(\omega t - 2\pi/3) \\ v_{cn} &= \frac{1}{2} m_a V_{dc} \cos(\omega t - 4\pi/3) \end{aligned} \right\} \text{ for State-2 and State-3} \quad (6.20)$$

Notice that the three-phase voltages of (6.20) take the healthy form as given previously in (6.14).

The last state, namely State-4, takes place when  $i_a$  is zero, owing to the inaction of switch  $S_1$ . Therefore, during this state, the motor phase-*a* line-to-neutral voltage is equal to its back emf, that is,  $v_{an} = e_a$ . By virtue of the following expressions,  $v_{ao} = v_{an} + v_{no}$  and  $v_{no} = (v_{ao} + v_{bo} + v_{co})/3$ , the pole voltage of phase-*a* is as defined in (6.19). That is,  $v_{ao} = (v_{bo} + v_{co} + 3e_a)/2$ . Using (6.4), the line-to-neutral voltages of all three phases can be expressed as follows:

$$\left. \begin{aligned} v_{an} &= e_a \\ v_{bn} &= \frac{1}{2}(v_{bo} - v_{co} - e_a) \\ v_{cn} &= \frac{1}{2}(v_{co} - v_{bo} - e_a) \end{aligned} \right\} \text{ for State-4} \quad (6.21)$$

It is important to point out that only State-2 through State-4 are still valid after the on-set of the fault transient.

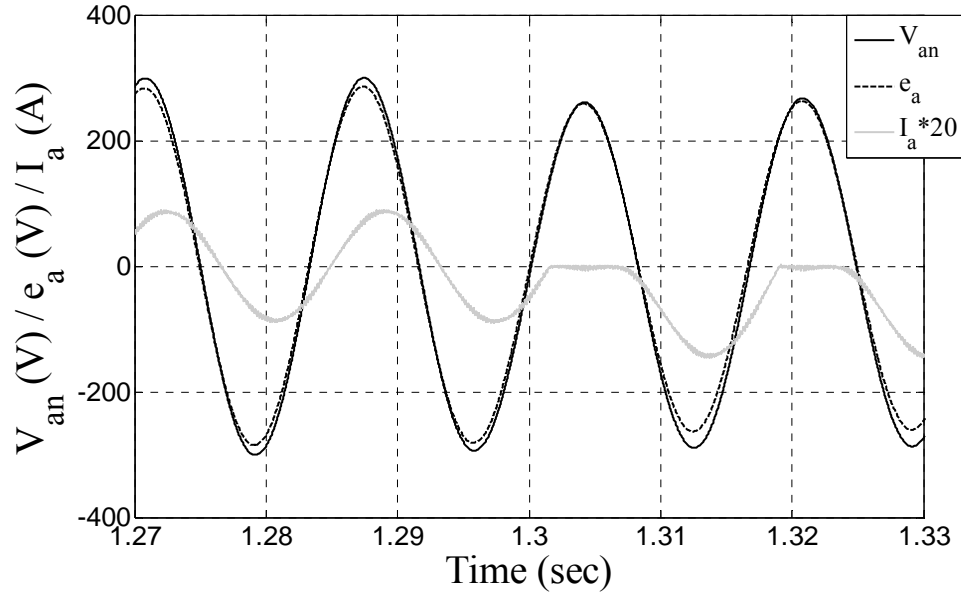


Figure 6.13: Simulation waveforms of motor quantities during pre- and post-fault conditions (open-circuit switch fault occurred at switch  $S_I$  at  $t = 1.3$  sec).

Pictorial representations of the motor phase- $a$  voltage ( $v_{an}$ ), back emf ( $e_a$ ), and current ( $i_a$ ) during pre- and post-fault conditions were obtained through simulation and are depicted in Figure 6.13. Here, the open-circuit switch fault occurred at switch  $S_I$  at  $t = 1.3$  sec. Note that the phase current,  $i_a$ , is multiplied by a factor of 20 for better and clearer visualization. As one can observe therein, the fault occurred when the current is negative. Hence, State-1 will never be in effect during the post-fault period. In addition, when the current is equal to zero (State-4), the phase- $a$  voltage (shown by the solid line in Figure 6.13) is in congruence with its back emf (shown by the dotted line), which is in agreement with the foregoing development as given in (6.21). Moreover, in the same figure, during the negative half cycle of the motor phase current (State-2 and State-3), the phase- $a$  voltage,  $v_{an}$ , reverts to its healthy form, which again corresponds to the earlier development as delineated in (6.20). An important observation worth noting from Figure 6.13 is the presence of the negative dc (unidirectional) offsets in both the phase current and voltage. Notwithstanding this fact, these dc (unidirectional) offsets are smaller in magnitude than their

respective fundamental components. Thus, the braking torque will have less significant effect. Nevertheless, a pulsating torque, at the fundamental power cycle frequency, with significant negative impact on motor performance will still be present.

### 6.3.2.1 Simulation Results

Simulation results are presented here to demonstrate the impact of the failure of an open-circuit switch fault on the motor performance. The 2-hp induction motor-drive system under study was simulated here in a *Matlab-Simulink* environment [91], see Figure 6.5, with the associated simulation conditions which were given in Table 6.1. The open-circuit fault location is assumed at switch,  $S_I$ , and the fault occurrence was introduced at time,  $t = 1.3 \text{ sec}$ . Meanwhile, the controller is of the open-loop constant volts per hertz PWM type, and the motor operation was simulated under full-load condition, that is at an output torque of 8.169 Nm.

The simulation waveforms of the three-phase motor currents during pre- and post-fault conditions are plotted in Figure 6.14(a) and Figure 6.14(b), respectively. As one can observe from the post-fault result of Figure 6.14(b), a malfunction (open-circuit) of the switch,  $S_I$ , results in the elimination of any positive current flow in phase- $a$  of the stator windings of the motor. Consequently, a dc (unidirectional) offset is imposed on the current of phase- $a$ , and this dc (unidirectional) current is divided between the paths of the remaining two phases, provided that the motor has a floating neutral connection. It should also be noted that due to the unbalanced voltage excitations at the motor terminals as a result of the fault, negative sequence components will also be introduced in the motor currents.

Meanwhile, the corresponding FFT frequency spectra of the motor phase currents are shown in Figure 6.15(a) for the healthy case, and Figure 6.15(b) through (d) for the faulty case. Despite the presence of the dc (unidirectional) current offsets in all three phases, their magnitudes are smaller than their respective fundamental components, as depicted in Figure 6.15(b) through (d).

Hence, the possibility of a motor stall is unlikely, which is not the case for a transistor short-circuit switch fault as was previously illustrated in this chapter. Observation of Figure 6.15(b) through (d) also indicates the presence of lower-order time harmonics imposed on the motor currents. This can best be explained by examining the simulation waveform of the dc link voltage and its corresponding FFT spectra, as illustrated in Figure 6.16(a) and Figure 6.16(b) and its close-up (zoom) depiction in Figure 6.16(c), respectively. In a healthy three-phase electric drive, the dc link voltage is composed of a dc component, as well as higher-order harmonic frequency components that are multiple of six. However, as a consequence of asymmetry in the inverter circuit, lower-order harmonics are generated in the dc link, particularly the fundamental harmonic component at the main power cycle frequency. This can be observed in both the time-domain waveform, see Figure 6.16(a), and the close-up view of the FFT spectrum, see Figure 6.16(c), respectively.

To demonstrate the effects of these dc link harmonics on the motor phase voltages and currents, the previously derived averaged-switching-function model is invoked. Considering a dc bus voltage with dc, 1<sup>st</sup>, and 2<sup>nd</sup> harmonic components, one can write the dc bus voltage expression as follows:

$$V_{dc}(t) = V_{dc_0} + V_{dc_1} \cos(\omega t + \phi_1) + V_{dc_2} \cos(2\omega t + \phi_2) \quad (6.22)$$

where,  $V_{dc_0}$  is the average dc bus voltage,  $V_{dc_1}$  and  $V_{dc_2}$  represent the peak magnitudes of the first (fundamental) and second harmonic components, whereas,  $\phi_1$  and  $\phi_2$ , represent their respective phase angles. By substituting (6.22) in (6.14), one can obtain the three-phase line-to-neutral voltages, that is,  $v_{an}$ ,  $v_{bn}$ , and  $v_{cn}$ , as follows:

$$\begin{aligned}
v_{an} &= \frac{1}{2} m_a \underbrace{\left[ V_{dc_0} + V_{dc_1} \cos(\omega t + \phi_1) + V_{dc_2} \cos(2\omega t + \phi_2) \right]}_{V_{dc}(t)} \cos(\omega t) \\
v_{bn} &= \frac{1}{2} m_a \underbrace{\left[ V_{dc_0} + V_{dc_1} \cos(\omega t + \phi_1) + V_{dc_2} \cos(2\omega t + \phi_2) \right]}_{V_{dc}(t)} \cos(\omega t - 2\pi/3) \\
v_{cn} &= \frac{1}{2} m_a \underbrace{\left[ V_{dc_0} + V_{dc_1} \cos(\omega t + \phi_1) + V_{dc_2} \cos(2\omega t + \phi_2) \right]}_{V_{dc}(t)} \cos(\omega t - 4\pi/3)
\end{aligned} \tag{6.23}$$

Using the trigonometric identity,  $\cos(a)\cos(b) = 1/2 \cdot \cos(a-b) + 1/2 \cdot \cos(a+b)$ , one can rewrite (6.23) in the following manner:

$$\begin{aligned}
v_{an} &= \underbrace{\frac{1}{2} m_a V_{dc_0} \cos(\omega t)}_{\text{Positive-Sequence Fundamental Term}} + \frac{1}{4} m_a V_{dc_1} \left[ \underbrace{\cos(\phi_1)}_{\text{dc Term}} + \underbrace{\cos(2\omega t + \phi_1)}_{\text{Positive-Sequence 2nd Harmonic Term}} \right] \\
&\quad + \frac{1}{4} m_a V_{dc_2} \left[ \underbrace{\cos(\omega t + \phi_2)}_{\text{Negative-Sequence Fundamental Term}} + \underbrace{\cos(3\omega t + \phi_2)}_{\text{Positive-Sequence 3rd Harmonic Term}} \right] \\
v_{bn} &= \underbrace{\frac{1}{2} m_a V_{dc_0} \cos(\omega t - 2\pi/3)}_{\text{Positive-Sequence Fundamental Term}} + \frac{1}{4} m_a V_{dc_1} \left[ \underbrace{\cos(\phi_1 + 2\pi/3)}_{\text{dc Term}} + \underbrace{\cos(2\omega t + \phi_1 - 2\pi/3)}_{\text{Positive-Sequence 2nd Harmonic Term}} \right] \\
&\quad + \frac{1}{4} m_a V_{dc_2} \left[ \underbrace{\cos(\omega t + \phi_2 + 2\pi/3)}_{\text{Negative-Sequence Fundamental Term}} + \underbrace{\cos(3\omega t + \phi_2 - 2\pi/3)}_{\text{Positive-Sequence 3rd Harmonic Term}} \right] \\
v_{cn} &= \underbrace{\frac{1}{2} m_a V_{dc_0} \cos(\omega t - 4\pi/3)}_{\text{Positive-Sequence Fundamental Term}} + \frac{1}{4} m_a V_{dc_1} \left[ \underbrace{\cos(\phi_1 + 4\pi/3)}_{\text{dc Term}} + \underbrace{\cos(2\omega t + \phi_1 - 4\pi/3)}_{\text{Positive-Sequence 2nd Harmonic Term}} \right] \\
&\quad + \frac{1}{4} m_a V_{dc_2} \left[ \underbrace{\cos(\omega t + \phi_2 + 4\pi/3)}_{\text{Negative-Sequence Fundamental Term}} + \underbrace{\cos(3\omega t + \phi_2 - 4\pi/3)}_{\text{Positive-Sequence 3rd Harmonic Term}} \right]
\end{aligned} \tag{6.24}$$

The first term given in all three voltage expressions of (6.24) represents the fundamental positive-sequence component which contributes to the fundamental (useful) magnetic flux distribution in the airgap. The corresponding second and third terms of (6.24) represent a dc offset and a 2<sup>nd</sup> harmonic positive-sequence term, respectively. These terms are resulting from the effect of the 1<sup>st</sup>

harmonic component of the dc link voltage. The last two terms given in all three voltage expressions of (6.24), which are due to the effect of the 2<sup>nd</sup> harmonic dc voltage term, represent a fundamental negative-sequence term and a 3<sup>rd</sup> harmonic positive-sequence term, respectively.

Accordingly, the motor phase currents will be expected to consist of harmonic components of corresponding nature to the order of harmonics that are given in (6.24). This is clearly confirmed upon examination of the FFT spectra, as depicted in Figure 6.15(b) through (d). Therein, the only harmonic term that is not shown in those spectral figures is the fundamental negative-sequence component which leads to a flux component that is traveling in the airgap at an angular synchronous frequency of  $-\omega$ . It should be noted that the negative-sequence terms will produce a negative torque (opposite to the motor's rotation), which will reduce the overall average torque of the motor. Also, one should not confuse the 3<sup>rd</sup> harmonic positive-sequence term given in (6.24) with the traditional 3<sup>rd</sup> harmonic component referred to as common-mode or zero-sequence component, where  $i_{a_3} = i_{b_3} = i_{c_3} = I_{m_3} \cos(3\omega t)$ , in which case, along with the other triple (9, 15, 21, 27, ..., etc.) harmonic components, do not exist in this motor-drive fault setup. This is due to the fact that the motor has a floating neutral point connection, constituting no path for such harmonic currents. The remaining lower-order time harmonics of the motor phase currents shown in the spectral Figure 6.15(b)-(d), that is harmonic components higher than the 3<sup>rd</sup> order, can be explained in a similar manner using (6.22) and (6.23) by taking into account the other higher harmonic terms of the dc link voltage.

The simulation results of the developed motor torque profile along with its corresponding FFT spectra during pre- and post-fault conditions are given in Figure 6.17(a) and Figure 6.17(b) and (c), respectively. The corresponding motor speed profile is also shown here in Figure 6.18. As one can observe from the torque profile, see Figure 6.17(a), and speed profile, see Figure 6.18, the effects of the presence of pulsations or ripples are clearly evident. These pulsations or ripples are oscillating at a combination of several harmonic frequencies, with the main oscillating term

being attributed to the fundamental harmonic term having a frequency equal to the power cycle frequency. The cause of this torque component pulsating at  $\omega_{syn}$  can best be described through a set of pictorial illustrations of the airgap flux and rotor magnetic field space-vectors, as depicted in Figure 6.19. It should be noted that the harmonic components, including the dc component, of the airgap flux and rotor magnetic field space-vectors are originating from the harmonic components of the stator currents, the spectra of which are depicted in Figure 6.15. In conventional machine theory, it is known that in an induction machine, the airgap flux and the rotor magnetic field consist of harmonic components that are rotating at the same angular frequency (angular synchronous speed). Hence, according to Figure 6.19(a), the relative speed between the dc flux of the airgap and the fundamental positive-sequence harmonic component of the rotor field, and vice versa, is  $\omega_{syn}$ . Therefore, both of these interactions will produce a torque component that pulsates at the fundamental harmonic frequency,  $\omega_{syn}$ . On the other hand, in Figure 6.19(b), the interactions between the dc airgap flux and the fundamental negative-sequence harmonic component of the rotor field, and vice versa, will also produce a negative pulsating torque at  $\omega_{syn}$ . Moreover, it can be seen from Figure 6.19(c) that the interactions between the positive-sequence airgap fundamental flux and the 2<sup>nd</sup> harmonic component of the rotor field, and vice versa, will also produce a positive torque pulsation at  $\omega_{syn}$ . The same phenomenon can be stated with regard to the interactions between the positive-sequence 2<sup>nd</sup> and 3<sup>rd</sup> harmonic components of the airgap flux and the rotor field. Accordingly, the cumulative effects of these electromagnetic interactions between the airgap flux and rotor field will result in a torque component pulsating at  $\omega_{syn}$ . It should be noticed that the interactions between harmonic components rotating at the same frequency produce a non-pulsating (or average) torque. A similar argument can also be carried out to determine the cause of the other harmonic torque components given in Figure 6.17(c). Meanwhile, it was calculated from the simulated torque profile of Figure

6.17(a) that the peak-to-peak torque ripple is found to be about 190% of the post-fault average torque. Clearly, this indicates that the continuous operation of the motor-drive system, upon the occurrence of the fault, is highly undesirable in many applications. This is in order to avoid mechanical damage to the motor bearings and shaft, as well as the mechanical load system.

In order to further investigate the motor performance due to an open-circuit switch fault, the current space-vector locus, obtained by plotting  $i_d$  versus  $i_q$  current components, under different locations of the faulty transistor switch are plotted and shown here, along with the healthy case, in Figure 6.20. It can be seen from these figures that the current space-vector locus under different faulty switch locations exhibit different patterns, which are far from matching the circular locus under healthy condition. Previous investigators have made use of these types of pattern indicators to detect and locate the specific whereabouts of the open-circuit switch fault in an adjustable-speed drive [76]-[82].

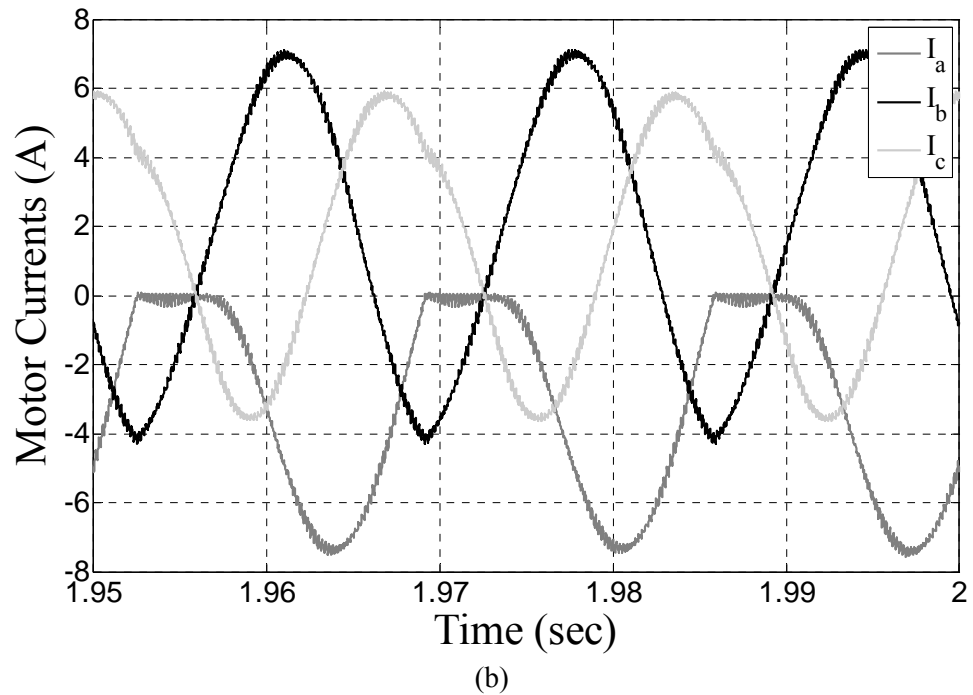
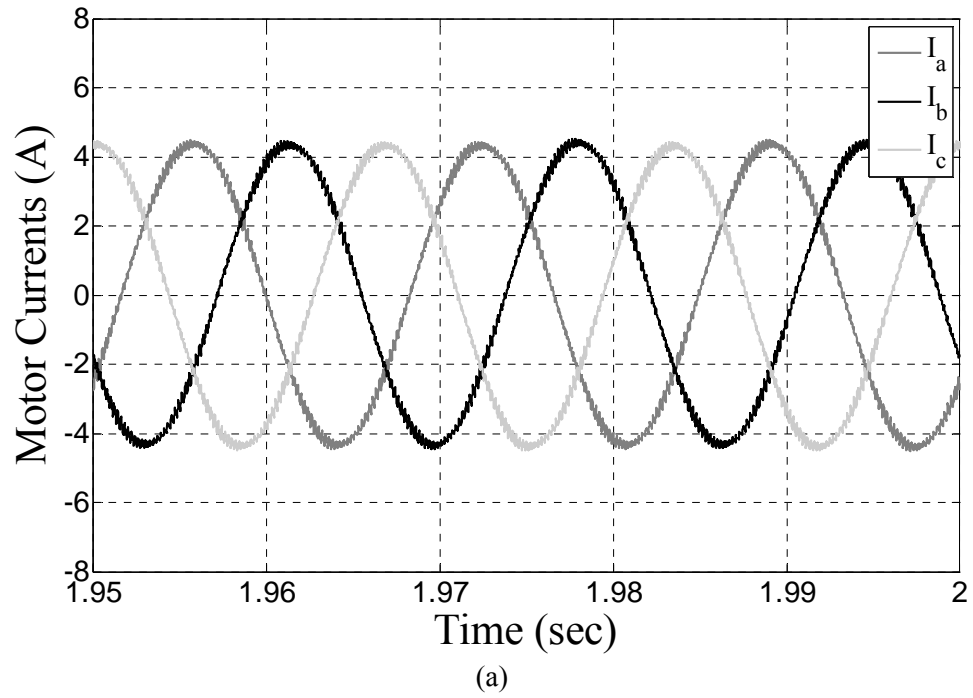
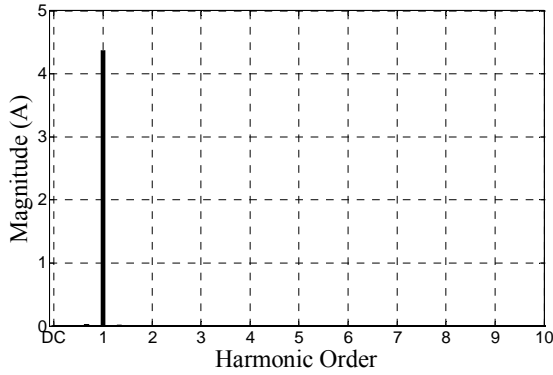
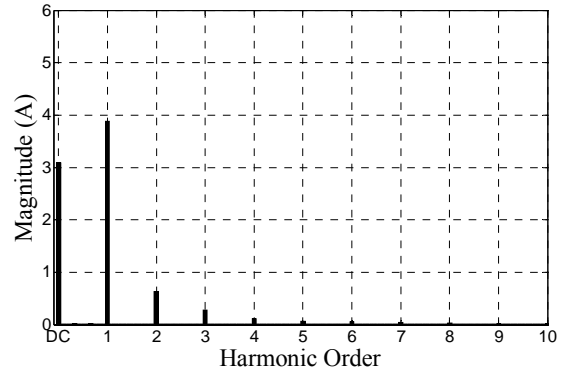


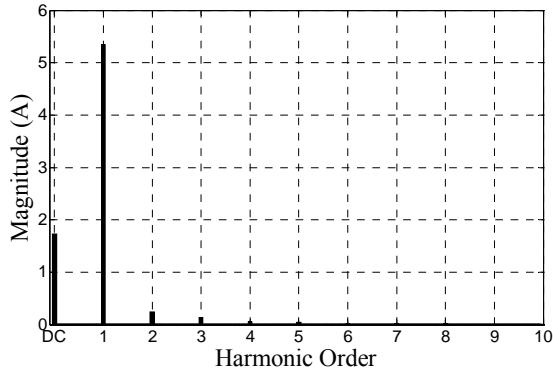
Figure 6.14: Simulation results of three-phase motor currents during pre- and post-fault open-circuit switch fault conditions. (a) Healthy. (b) Post-Fault.



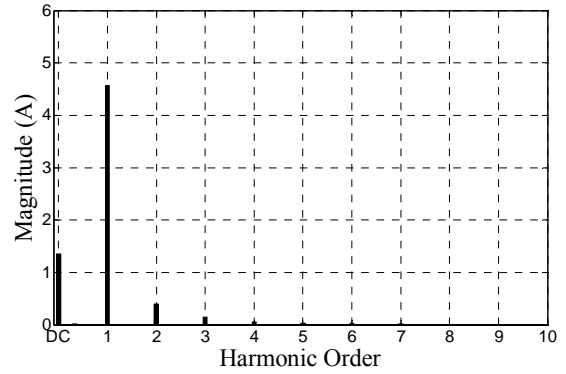
(a) Healthy case in all phases.



(b) Faulty case of  $i_a$ .

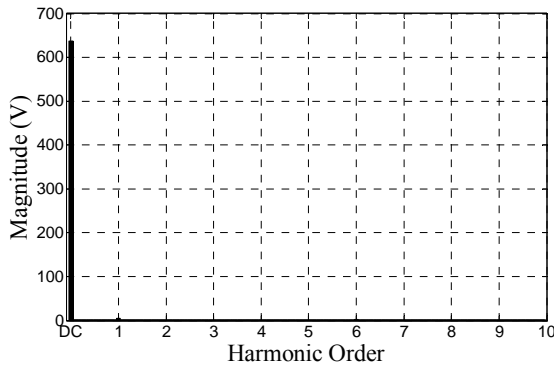
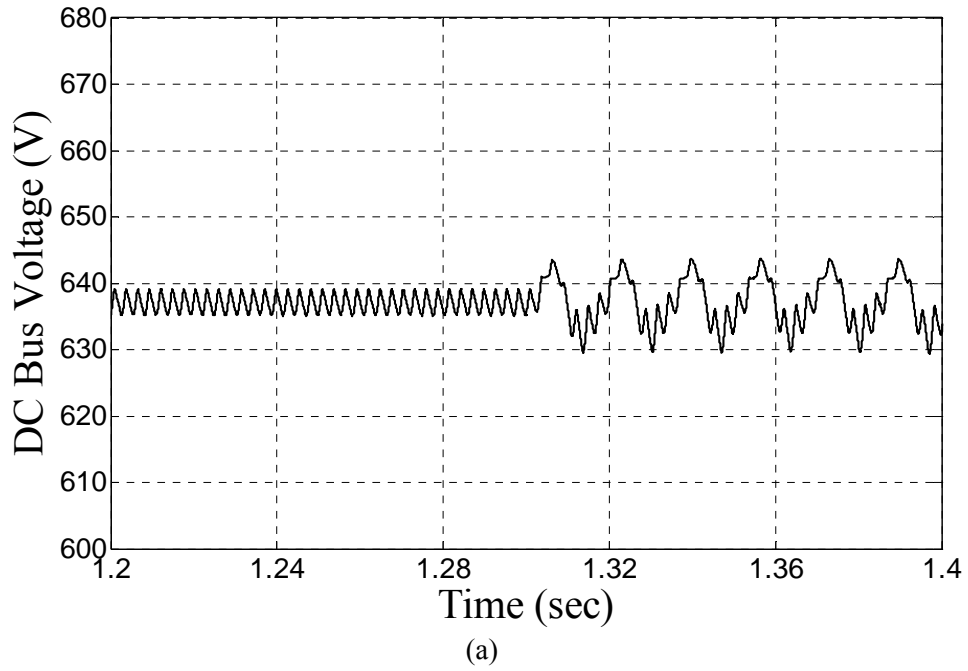


(c) Faulty case of  $i_b$ .

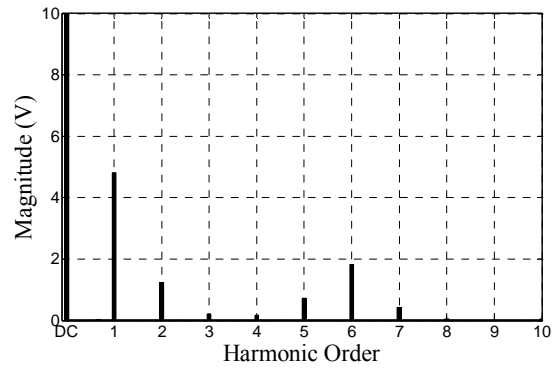


(d) Faulty case of  $i_c$ .

Figure 6.15: FFT spectra of simulated three-phase motor currents during open-circuit switch fault condition. (a) Healthy case in all phases. (b) Faulty case of  $i_a$ . (c) Faulty case of  $i_b$ . (d) Faulty case of  $i_c$ .

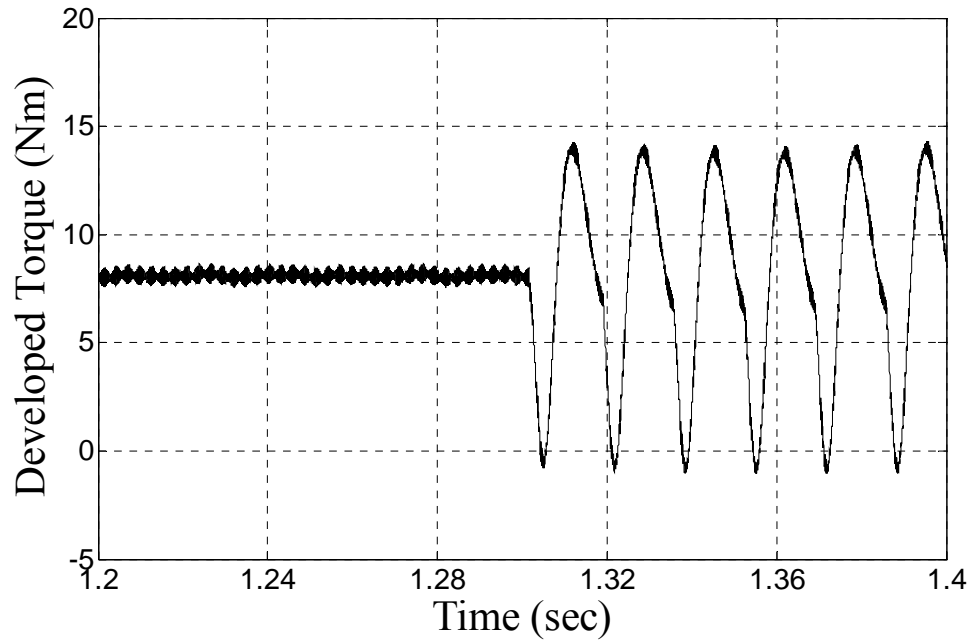


(b) Post-fault.

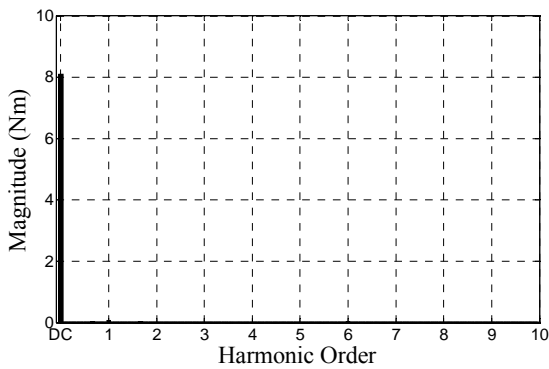


(c) Close-up view of Figure (b).

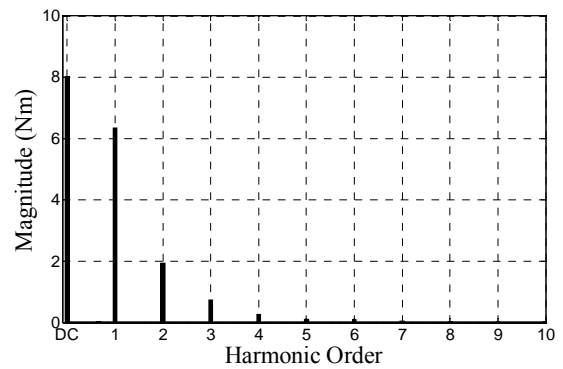
Figure 6.16: Simulation results of dc link voltage during open-circuit switch fault condition (fault occurs at  $t = 1.3 \text{ sec}$ ). (a) Time-domain profile during pre- and post-fault. (b) FFT spectrum during post-fault. (c) Close-up view of FFT spectrum of Figure (b).



(a)



(b) Pre-fault.



(c) Post-fault.

Figure 6.17: Simulation results of motor developed torque during open-circuit switch fault condition (fault occurs at  $t = 1.3 \text{ sec}$ ). (a) Time-domain profile during pre- and post-fault. (b) FFT spectrum during pre-fault. (c) FFT spectrum during post-fault.

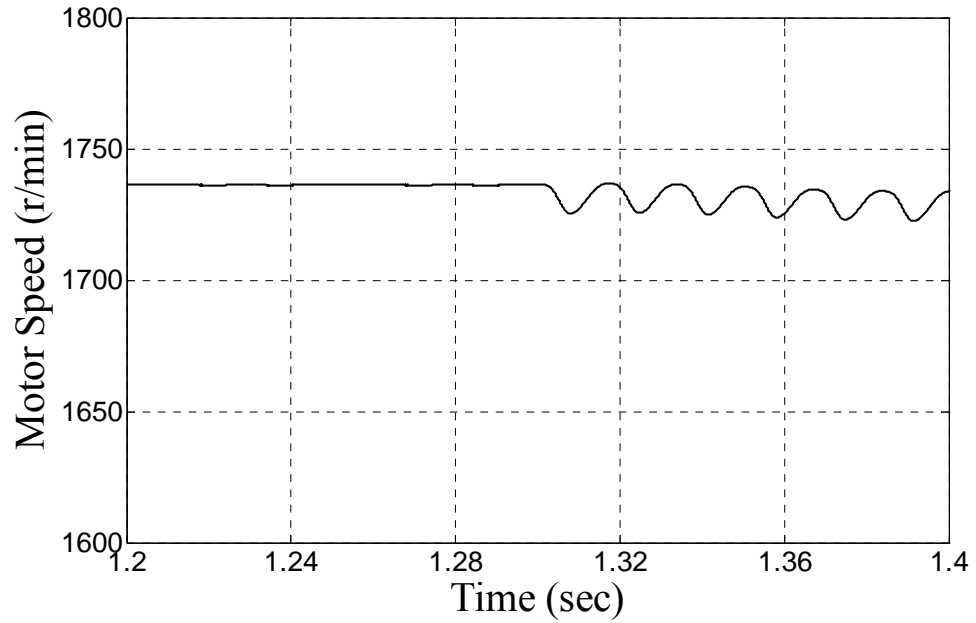


Figure 6.18: Simulation results of motor speed during pre- and post-fault open-circuit switch fault conditions (fault occurs at  $t = 1.3$  sec).

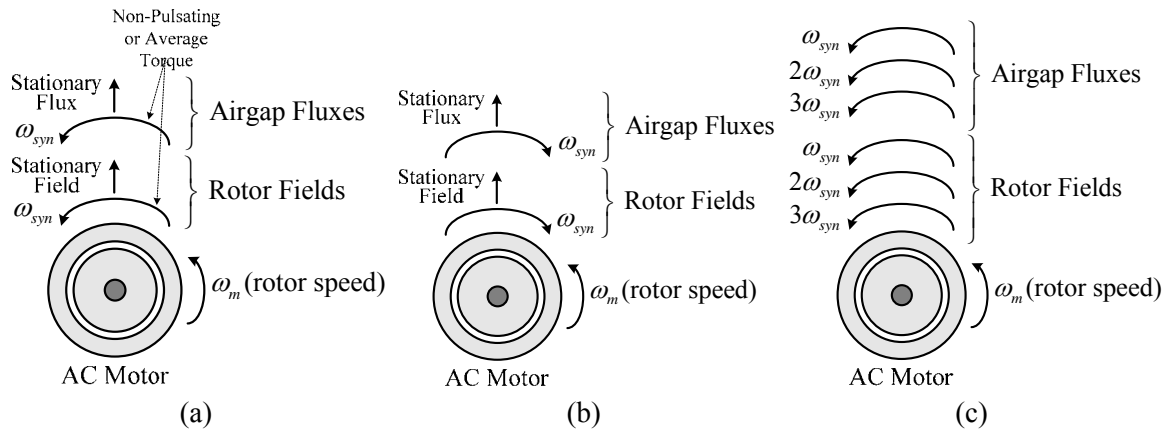


Figure 6.19: The origination of torque pulsations at a frequency,  $\omega_{syn}$ . (a) Interactions between dc flux/field and positive-seq. 1<sup>st</sup> harmonic. (b) Interactions between dc flux/field and negative-seq. 1<sup>st</sup> harmonic. (c) Interactions between positive-seq. 1<sup>st</sup>, 2<sup>nd</sup>, and 3<sup>rd</sup> harmonics.

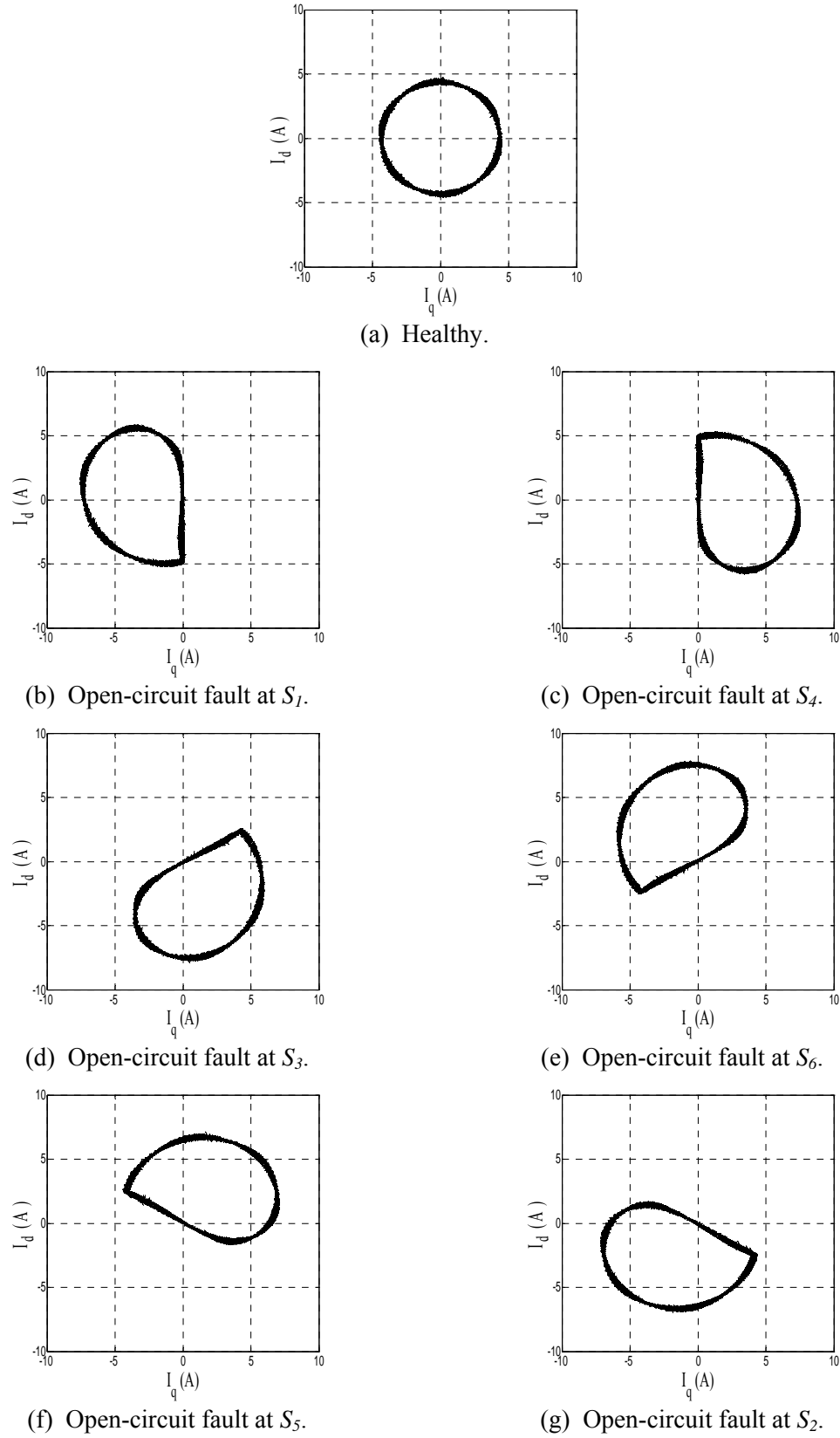


Figure 6.20: Simulation results of current space-vector locus.

## 6.4 Summary

The main purpose of this chapter was to contribute to a better understanding of the impact of various inverter faults, more specifically transistor/switch failures, on motor performance using a combination of time-domain simulations and analytical derivations based on averaged switching function modeling concepts. The two distinct types of inverter failure modes investigated herein are: (1) a transistor short-circuit switch fault, and (2) a transistor open-circuit switch fault. In the event of a short-circuit switch fault, the complementary switch of the same inverter leg has to be instantaneously turned-off upon the on-set of such a fault in order to avoid the catastrophic event of a dc link shoot-through situation. The resulting inverter circuit reconfiguration was accordingly investigated. It was found from the study that the short-circuit switch fault produces a severe fault impact on the motor performance. A dc (unidirectional) offset of high magnitude is imposed on the motor current of each phase, which results in a braking torque that causes the motor speed to drop sharply. In addition, huge torque pulsations are also generated as a result of such an event. Moreover, the presence of a high magnitude circulating dc (unidirectional) current in the motor windings will eventually lead to insulation failure if the motor is left unattended. As a consequence, such a fault will require immediate shut-down of the motor-drive system in order to prevent secondary failures.

On the other hand, it was demonstrated here that an open-circuit switch fault will still permit the operation of the motor-drive system, but at a much inferior performance due to the presence of significant torque pulsations. It was found from this specific simulation case study that the peak-to-peak torque pulsations were computed to be about 190% of the post-fault average torque for the case-study 2-hp motor. This clearly indicates that the operation of the motor-drive system, after the fault occurrence, can only be extended for a short period of time. This is in order to avoid damages to the mechanical portions of the motor-drive system. Analytical studies were also

presented in this work to determine the causes of these torque pulsations. In the opinion of this investigator, a detailed understanding of these fault impacts on machine performance is essential when one proceeds to the design stage of developing remedial strategies for such types of faults, which will be presented in the forthcoming chapter.

## CHAPTER 7

---

---

# A QUASI-CYCLOCONVERTER-BASED TOPOLOGY AND CONTROL FOR INVERTER FAULT MITIGATION

---

---

### 7.1 Introduction

The main idea leading to the development of the present approach as a potential solution for motor-drive inverter switch fault mitigation was attributed to a discovery by this investigator, while implementing the control algorithm of soft starters in the earlier work. Therein, it was discovered by this investigator that proper control of the SCRs of the previously given topology of a soft-starter, see Figure 7.1, in a specific switching pattern can produce a set of three-phase positive-sequence voltages with a fundamental frequency other than the input supply frequency. It was this specific discovery that led this investigator to conceive of the notion that such a finding may serve as a potential remedial solution for inverter faults, by connecting the three-phase SCR bridge whose configuration is shown in Figure 7.1 in parallel with the drive. In the event of a fault, the drive will shut down by its own fault protection system, and the SCR bridge will bypass the faulty drive to continue operation of the motor using the present control method.

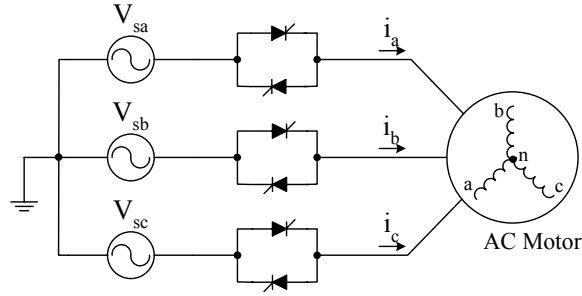
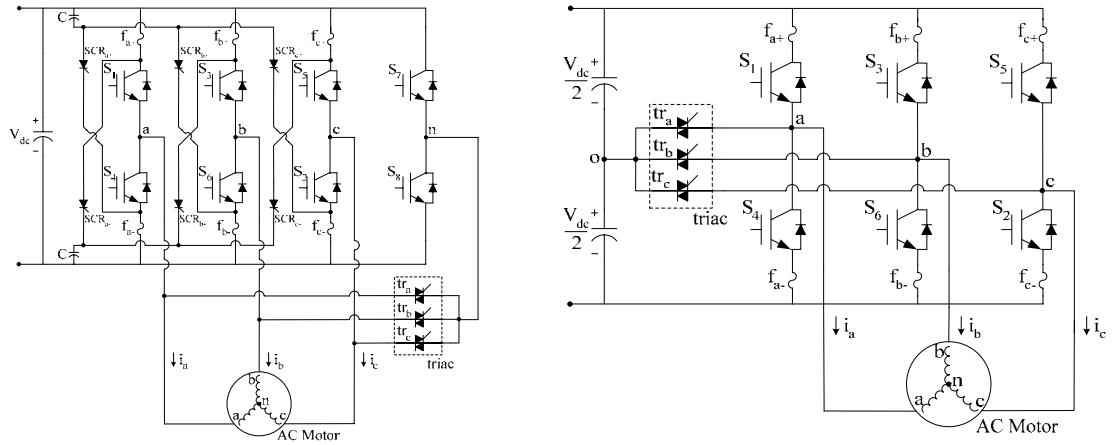
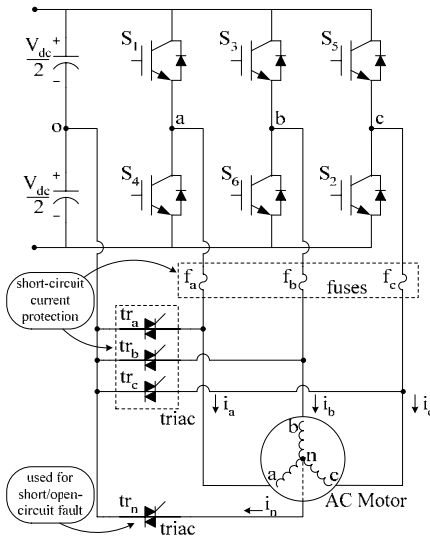


Figure 7.1: SCR voltage-controlled topology.



(a) Proposed by Bolognani et al. [40].

(b) Proposed by Van Der Broeck et al. [52] and Ribeiro et al. [44].



(c) Proposed by Liu et al. [49] and Elch-Heb et al. [50].

Figure 7.2: Different types of existing fault tolerant inverter topologies.

This idea of fault mitigation appeared to this investigator to be promising, in light of a thorough investigation which was carried out on the existing fault tolerant solutions that were previously proposed by other researchers [38]-[59], and which were discussed in detail earlier in Chapter 1. For the convenience of the reader, these topologies proposed by earlier investigators are depicted here in Figure 7.2. As mentioned earlier in Chapter 1, each of the topologies of Figure 7.2 has its own merits and drawbacks. The merit of these topologies is their ability to maintain continuous operation of the machine in the event of an inverter fault. On the other hand, the drawbacks range from having the need for a redundant inverter leg for the topology of Figure 7.2(a), oversizing the dc capacitors and doubling the dc link voltage for the topology of Figure 7.2(b), to the need for a motor neutral connection as well as oversizing the dc link capacitors for the topology of Figure 7.2(c).

Examination of those inverter topologies reveals one common thing. Namely that is the mechanism, which enables the change in the status of the inverter into its post-fault configuration in order to allow the fault mitigation control to be applied thereafter, consists of three sets of back-to-back connected SCRs which resembles the configuration shown in Figure 7.1. Accordingly, in comparison with the existing topologies of Figure 7.2, the present remedial approach, based on the SCR bridge configuration of Figure 7.1, will not introduce any additional cost on top of what had already been proposed by others in Figure 7.2. However, it will be demonstrated later on that in order for the motor to operate at more selectable frequencies, additional two sets of back-to-back connected SCRs are essential, resulting in a total of five sets of back-to-back connected SCRs, as depicted in Figure 7.3. Nevertheless, the present approach is still worth the effort for achieving a potential remedial solution for the case of inverter faults.

In fact, the present fault mitigation approach has the following attributes: (1) does not require the accessibility of the neutral point of the motor which is normally not provided by motor manufacturers except by special request, (2) does not need to double the dc bus voltage which can

only be realized through either a dc-dc boost converter or an active rectifier at the drive front-end, and (3) does not need to oversize the dc link capacitors in order to sustain the desired voltage level and minimize the voltage ripples due to the single-phase current circulating through the capacitors. Another appealing feature of this new approach is its ability of potential use for mitigating any other drive-related faults such as faults occurring in the diode rectifier bridge or the dc-link capacitor because of the fact that this approach bypasses the entire drive system, provided that such faults can be safely isolated. Despite the aforementioned merits, due to its unique control operation, the present topology is only suitable for low-speed type of motor applications, such as vehicle and ship propulsion systems, cement mills, mine hoists, rolling mills and the like, where high torque at low speed is indispensable [101]. In addition, the appearance of a pulsating torque will be evident from the motor performance as a result of the present approach. Details of these will be explained further later-on in this chapter.

In light of the present topology structure and its operating principles, one can consider it as an ac-to-ac frequency changer, or “cycloconverter”. The basic function of a cycloconverter is to convert directly the incoming supply frequency to some different output frequency [99]. For most practical purposes, the maximum attainable useful output frequency is less than the input frequency. Hence, this is a fundamental limitation of a cycloconverter. The operation of a cycloconverter is carried out by controlling the switching patterns of a plurality of static SCR switches connected directly between the input ac system and the motor [99]. Unlike the standard PWM drives, there is basically no energy storage element present in the converter. In real applications, the cycloconverter is generally adopted for high power drive applications, in the range of MegaWatts, such as power mills for grinding purposes in mineral processing plants [102]. This is because of the high voltage and high current withstand ratings of SCR switches. A typical three-phase cycloconverter consists of 6 SCR switches for each phase, resulting in a total of 18 SCR switches. Hence, the present topology of Figure 7.3, with a total of 10 SCRs, can be

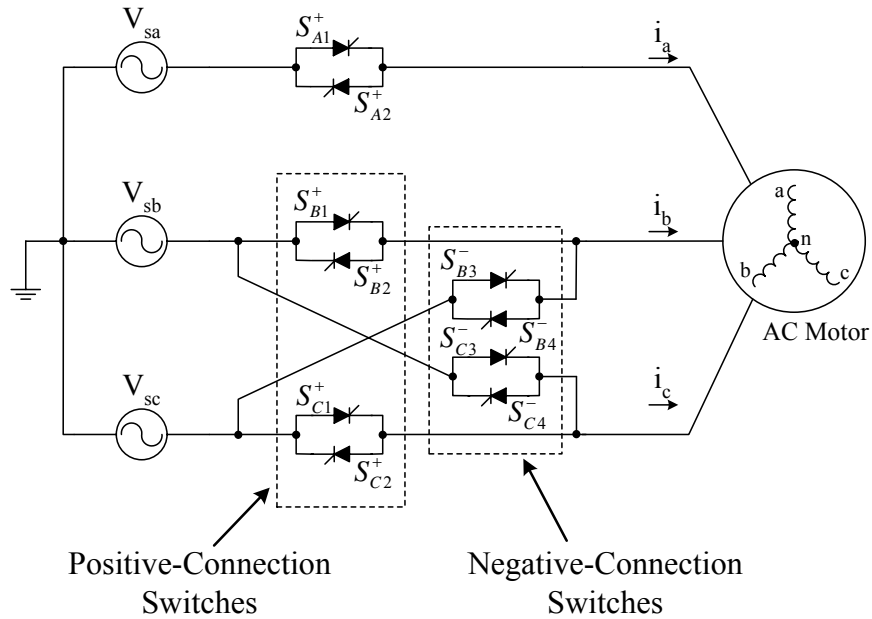


Figure 7.3: Present topology based on quasi-cycloconverter configuration.

considered as a quasi-cycloconverter, or a reduced-switch-count cycloconverter, for three-phase modes of operation.

In the event that during the post-fault operation the motor has to be brought to a halt, before starting up again from standstill, the present topology can function as a soft-starter during the initial speed ramp-up. This is before switching to the commanded speed using the present control approach. The use of soft-starting is to reduce any high starting inrush currents, and consequently any stressful high starting torque pulsations. Furthermore, by controlling the frequency and “depth” of phase modulation of the firing angles of the SCRs, it is possible to control the frequency and amplitude of the fundamental component of the output voltages. Hence, the operation of the present topology resembles, to a certain extent, the operation of a typical volts-per-hertz PWM drive. The only difference lies in the limitation of the present topology to operate in a higher frequency range and with better torque performance. Nevertheless, this investigator perceives that there is still a place in real practice for the present topology to “stand out” as a potential means of mitigating any drive-related faults, based on its low-cost requirements as well

as other merits that were previously mentioned above. Accordingly, the present topology with its unique operation can be considered as a high-performance soft-starter and a moderate-performance drive. Such technology is well-suited for users who are unwilling to bear the burden of the high price of a typical PWM drive, and still hope to achieve with reduced requirements the performance of variable speed operation at a lower affordable cost. In the following, the basic principles of operation of the present topology and its control technique are set forth in detail.

## 7.2 Present Fault Mitigation Topology and Control

### 7.2.1 Operating Principle of Present Topology

The present solution for mitigating inverter faults is based on the topology given earlier in Figure 7.3, and is re-illustrated here in Figure 7.4 with the inclusion of a standard PWM drive. In this configuration, besides the PWM drive, the three-phase motor terminals are connected to the ac supply mains terminals through a group of back-to-back connected SCRs. These SCRs are segregated into two sets. The first set, namely “positive-connection switches”, consists of SCRs that were labeled as  $S_{B1}^+$ ,  $S_{B2}^+$ ,  $S_{C1}^+$ , and  $S_{C2}^+$ . On the other hand, the second set of SCRs, namely “negative-connection switches”, were labeled as  $S_{B3}^-$ ,  $S_{B4}^-$ ,  $S_{C3}^-$ , and  $S_{C4}^-$ . Notice that including the operation of the  $S_{A1}^+$  and  $S_{A2}^+$  set, the phase sequencing of the first set yields an *abc* positive sequence switching. Meanwhile, including the operation of the  $S_{A1}^+$  and  $S_{A2}^+$  set, the phase sequencing of the second set yields an *acb* negative sequence switching. The main objective of having positive-connection switches as well as negative-connection switches is not to achieve forward or backward rotation control of the motor. In fact, its purpose is to provide a speed control at more selectable frequencies such that the sequence of the fundamental components of the voltages received at the motor terminals shall always possess a positive-sequence orientation

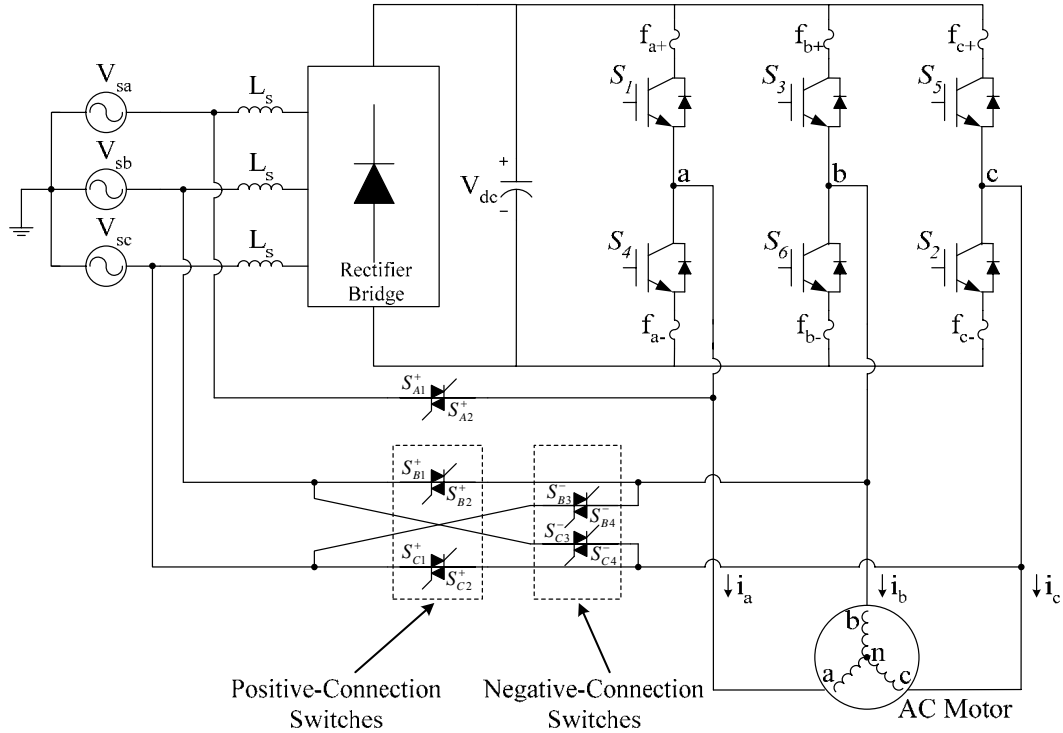


Figure 7.4: Present topology for inverter fault mitigation.

in order to produce forward rotation of the motor. Nevertheless, the function of the negative-connection switches can also provide a reverse rotation control of the motor, if both forward and reverse rotations of the motor are essential for the specific application.

In the healthy pre-fault condition, the motor-drive system is assumed to be operating at rated supply frequency under its normal rated conditions, with all the SCRs in the “turn-off” state. In the event of an inverter fault, regardless of an open-circuit or short-circuit type, the whole drive is completely shut down using its own fault protection/detection system by turning-off all the solid-state power switches. In situations where the drive protection system could not react immediately to a short-circuit switch fault, fast-acting fuses need to be incorporated in each inverter leg in order to provide another means of isolating the fault [44]. In such a case, the remaining healthy solid-state power switches will have to be accordingly commanded to revert to their “turn-off” state. Thereafter, the set of SCRs corresponding to the “positive-connection switches” are turned-

on (whereas, the SCRs associated with the “negative-connection switches” are turned-off) for a normal forward rotating mode, which leads to the bypass transfer whereupon the motor is fed directly from the ac supply mains. In order to maintain synchronization and to avoid any interruption at the point of bypass transfer, the reference (modulating) waveforms employed in the pulse-width modulation scheme of the drive have to be in synchronism with the ac supply mains voltages using a phase-locked loop (PLL) scheme [100]. Again, it should be emphasized that regardless of which set of switches are in action, the SCRs of phase-*a*, namely  $S_{A1}^+$  and  $S_{A2}^+$ , will always be a part of the switching process, in order to provide a balanced three-phase operation.

In order to realize fault tolerant operation in the adjustable-speed mode, besides the rated frequency of the ac supply mains, a discrete-frequency control method is utilized here. Due to its unique control scheme, the present approach is only suitable for low-speed motor applications. It had been discovered by this investigator that selectively triggering of the SCRs in a specific pattern can produce a set of three-phase voltages, and consequently three-phase currents, having a fundamental output frequency,  $f_o$ , which is an integer fraction of the frequency of the ac supply mains,  $f_s$ . That is, the output frequency,  $f_o = (1/2)f_s, (1/4)f_s, (1/5)f_s, (1/7)f_s, (1/8)f_s, (1/10)f_s, \dots$ , etc. In other words,  $f_o = f_s/N$ , where,  $N = 2, 4, 5, 7, 8, 10, 11, 13, 14, 16, 17, 19, 20, 22, 23, 25, \dots$ , etc. Notice that frequencies where  $N = 3, 6, 9, 12, 15, \dots$ , etc. are unavailable for reasons explained below.

A set of example current patterns at selected frequencies down to  $(1/8)f_s$  are graphically illustrated in Figure 7.5. As one can observe therein, by triggering the SCRs in a specific pattern to produce a set of current pulses, one can obtain fundamental frequencies, as shown by the dotted lines of Figure 7.5, that are lower than the ac supply mains frequency,  $f_s$ . Hence, this resembles very much the performance of a cycloconverter, which is the reason for referring to the

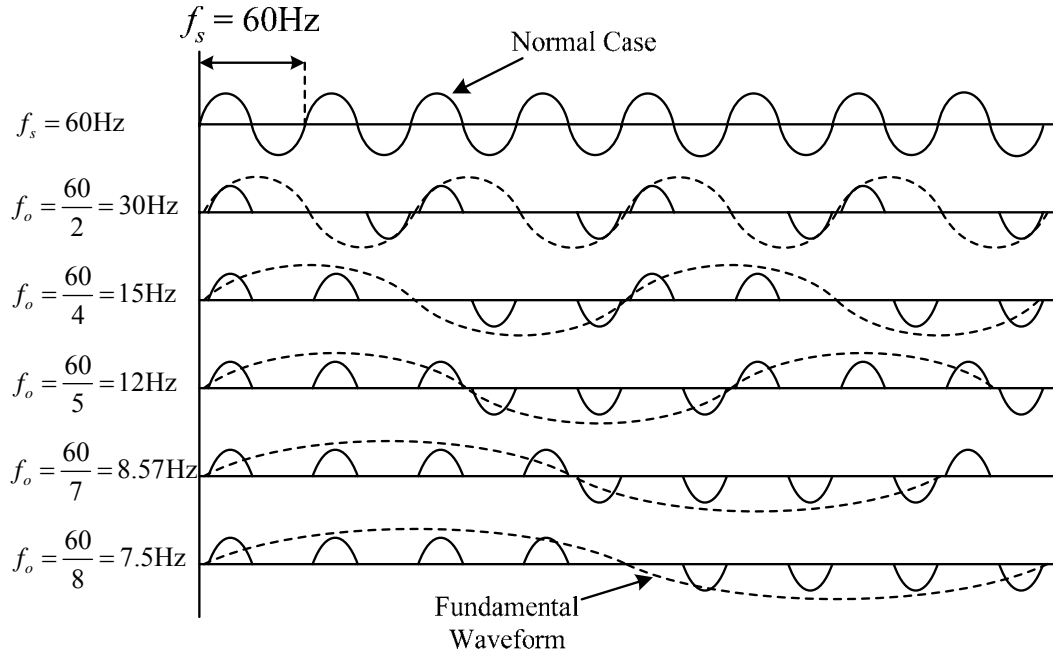


Figure 7.5: Example current patterns using discrete-frequency control for adjustable-speed mode operation for a supply mains frequency,  $f_s = 60\text{Hz}$ .

present topology as a quasi-cycloconverter-based topology. Since the available frequencies resulting from this discrete-frequency control method are equal to or lower than half the rated supply frequency, the present fault tolerant approach is mainly applicable to situations where low speed operation is acceptable such as in emergency “limp-home” situations in vehicles and other propulsion applications.

The importance of having two separate sets of SCRs, see Figure 7.3 and Figure 7.4, is explained in the following discussion. Assuming a set of balanced, three-phase positive-sequence, one per-unit waveforms, to be expressible as follows:

$$\begin{aligned}
 v_A(t) &= \cos(\omega_o t) \\
 v_B(t) &= \cos(\omega_o t - 2\pi/3) \\
 v_C(t) &= \cos(\omega_o t - 4\pi/3)
 \end{aligned} \tag{7.1}$$

where,  $\omega_o = 2\pi f_o$ , is the commanded output angular frequency, one can express the ac supply mains angular frequency,  $\omega_s = 2\pi f_s$ , and  $\omega_o = \omega_s/N$ . Here,  $N$  is the set of acceptable integers given above. Consequently, using (7.1), one can express a set of balanced, three-phase supply mains voltages at the angular frequency,  $\omega_s$ , in the following manner:

$$\begin{aligned} v_{sa}(t) &= V_m \cos(N\omega_o t) = V_m \cos(\omega_s t) \\ v_{sb}(t) &= V_m \cos\left[N(\omega_o t - 2\pi/3)\right] = V_m \cos(\omega_s t - 2\pi N/3) \\ v_{sc}(t) &= V_m \cos\left[N(\omega_o t - 4\pi/3)\right] = V_m \cos(\omega_s t - 4\pi N/3) \end{aligned} \quad (7.2)$$

where,  $V_m$  is the voltage peak (maximum) amplitude of the ac supply mains. As one can observe in (7.2), the lag phase angles for phase-*b* and phase-*c* of the supply mains voltages determine the overall voltage sequence order, whether it is an (*abc*) positive or an (*acb*) negative sequence. In other words, for positive-sequence order,  $N = 3k + 1$ ; while for negative-sequence order,  $N = 3k + 2$ ; and for zero-sequence order,  $N = 3k + 3$ , where  $k = 0, 1, 2, 3, 4, 5, \dots$ , etc. Hence, this implies that in order to produce a set of three-phase, positive-sequence output voltage waveforms at an output frequency,  $f_o = f_s/N$ , the sequence order of the ac supply mains needs to be varied depending on the commanded output frequency,  $f_o$ . It is always considered in any situation that the supply mains voltages always preserve a positive-sequence manner. Therefore, in order to obtain a negative-sequence order of voltages from the ac supply mains, two phases of the ac supply mains need to be interchanged. This can be realized using the set of “negative-connection switches” for shifting the phase order of the ac supply mains, as depicted in both Figure 7.3 and Figure 7.4. Clearly, it serves no purpose to achieve a zero-sequence order of voltages from the ac supply mains for motor rotation. Hence, the available output frequencies that can be obtained from using the proposed discrete-frequency control method can only be realized for  $N = 2, 4, 5, 7, 8, 10, 11, 13, 14, 16, 17, 19, 20, \dots$ , etc. This means that for the low-speed type of

motor applications, there is a wider range of frequency to be selected, excluding  $N$  being a multiple of “3”, which would lead to zero-sequence type  $abc$  voltages.

In order to re-emphasize the above concept, a graphical illustration is given in Figure 7.6(a) and Figure 7.6(b) for 15-Hz and 30-Hz output waveforms, respectively. As shown in both figures, the output waveforms have an amplitude of two per-units for clarity of demonstration purposes, and they are labeled as  $v_A$ ,  $v_B$ , and  $v_C$ . Meanwhile, the input supply mains have an amplitude of one per-units also for clarity of demonstration purposes, and they are labeled as  $v_{sa}$ ,  $v_{sb}$ , and  $v_{sc}$ . It can be seen from both figures that the output waveforms at either 15-Hz or 30-Hz frequency are shown in a positive-sequence manner. On the other hand, the 60-Hz supply mains are shown in a positive-sequence manner for the case of 15-Hz output (that is  $N = 4$ ), and a negative-sequence manner for the case of 30-Hz output (that is  $N = 2$ ). That is, for  $N = 4$ , the ac supply has to appear to the motor through the SCR bridge in its  $(abc)$  positive-sequence form to provide a positive-sequence output set of voltages at the commanded frequency,  $f_o$ . Meanwhile, for  $N = 2$ , the ac supply has to appear to the motor through the SCR bridge in its  $(acb)$  negative-sequence form to provide a positive-sequence output set of voltages at the commanded frequency,  $f_o$ .

### 7.2.2 Discrete-Frequency Control Algorithm

The main objective behind this discrete-frequency control approach is to selectively trigger or turn-on the SCRs in a specific pattern in order to achieve the desired output waveforms at the commanded frequency,  $f_o = f_s/N$ . To demonstrate this concept, the switching patterns (trigger signals) for the SCRs,  $S_{A1}^+$  and  $S_{A2}^+$ , of phase- $a$  at commanded output frequencies of 30-Hz ( $N = 2$ ), 15-Hz ( $N = 4$ ), and 12-Hz ( $N = 5$ ) are shown in Figure 7.7(a), (b), and (c), respectively. As one may observe therein, each output frequency requires a different switching pattern for the turn-on of the SCRs in order to realize the desired motor current pattern. Furthermore, each of the SCR

firing pulses is phase-delayed by an angle,  $\alpha$ , with respect to the zero-crossing of the supply voltage before the corresponding SCR is triggered/turned-on. The choice of the value of  $\alpha$  depends on the motor load condition, with lower values for heavier loads. It should also be noted that the angle,  $\alpha$ , dictates the fundamental amplitude of the output voltage waveforms. Hence, by adjusting the frequency of the triggering pulse as well as the value of the angle,  $\alpha$ , one can control both the frequency and amplitude of the output voltages impressed upon the motor to render the performance of the bridge resembling the operating principle of a constant volts-per-hertz control of a standard adjustable-speed drive.

The block diagram of the discrete-frequency control algorithm is depicted in Figure 7.8. The desired output voltage frequency,  $f_o$ , applied at the motor terminals at integer fractions of the supply mains frequency,  $f_s$ , is first commanded, see Figure 7.8. Thereafter, a set of three-phase positive-sequence waveforms,  $v_{ref}$ , at the commanded output frequency,  $f_o = f_s/N$ , is synthesized as a result. Again, notice that  $N$  is an integer that is not a multiple of 3. Hence,  $N = 2, 4, 5, 7, 8, 10, 11, 13, 14, \dots$ , etc. This set of three-phase waveforms,  $v_{ref}$ , is used as reference waveforms for generating a set of positive-sequence voltages applied at the motor terminals. In order to ensure a proper sequencing of the triggering pulses during low-speed operation, these reference waveforms have to be in synchronism with the ac supply mains voltages in such a way that the reference waveforms have the same zero crossings as the corresponding supply voltages, as shown previously in Figure 7.6. This is carried out by sensing the ac supply mains voltages,  $v_{sa}$ ,  $v_{sb}$ , and  $v_{sc}$ , and applying the PLL routine to attain the three angles of the supply voltages for all three phases, that is  $\theta_a$ ,  $\theta_b$ , and  $\theta_c$  [100]. With these set of angles,  $\theta_a$ ,  $\theta_b$ , and  $\theta_c$ , and the commanded frequency,  $f_o$ , the reference waveforms,  $v_{ref}$ , for each of the phases,  $a$ ,  $b$ , and  $c$ , can be synthesized accordingly.

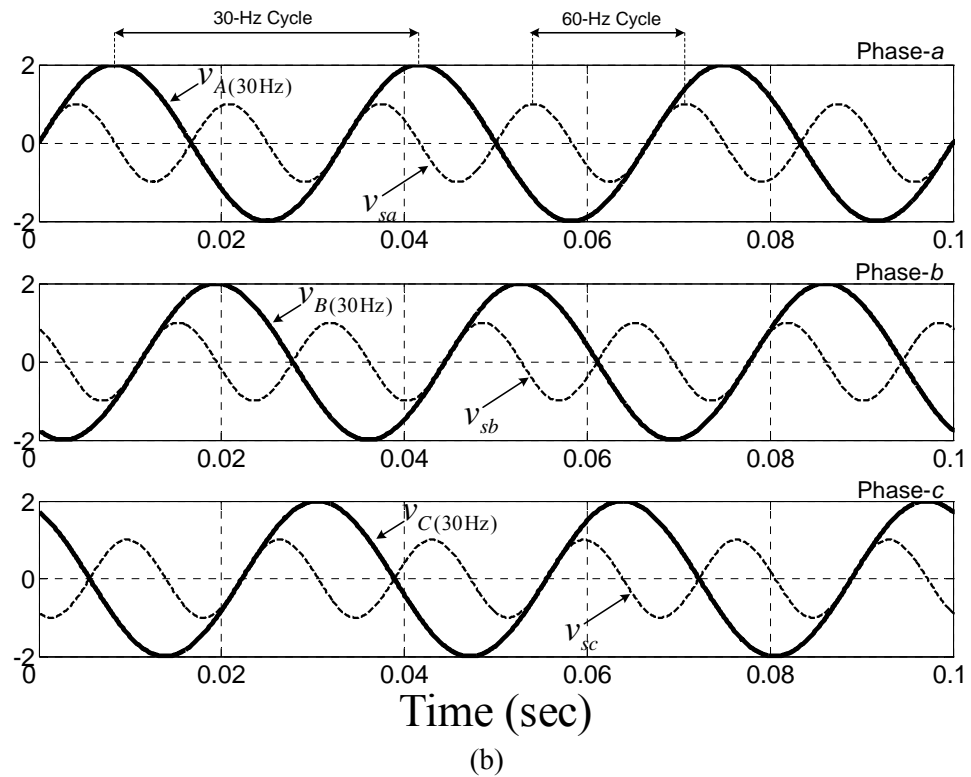
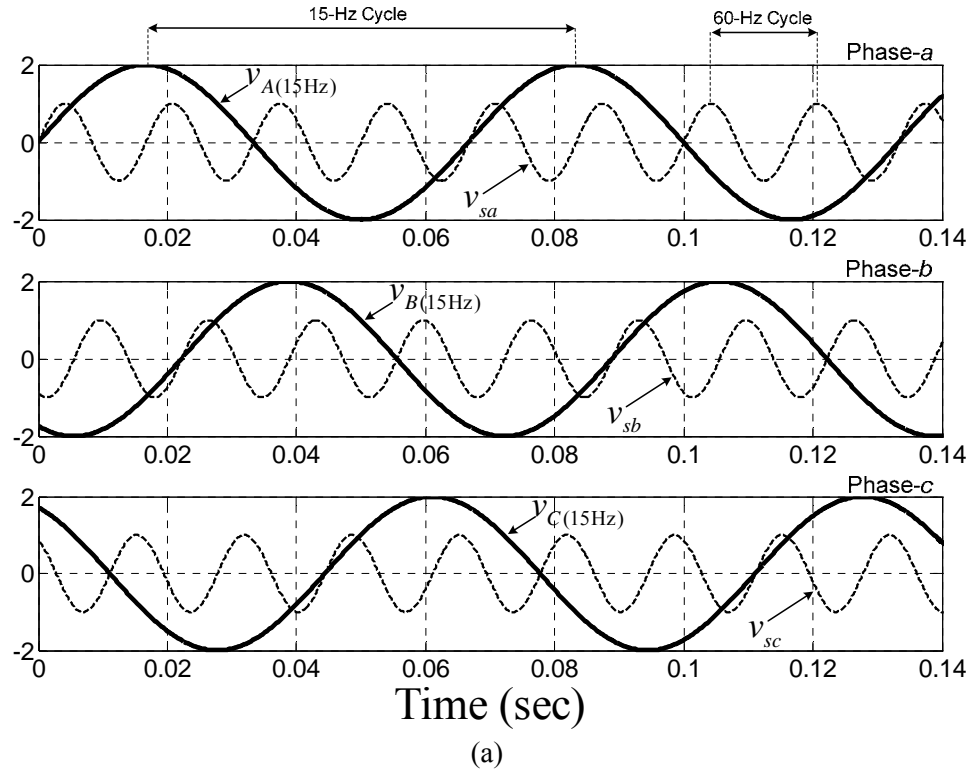


Figure 7.6: Graphical illustrations on the sequence order of input supply mains to achieve output waveforms with different frequency. (a) 15-Hz output. (b) 30-Hz output.

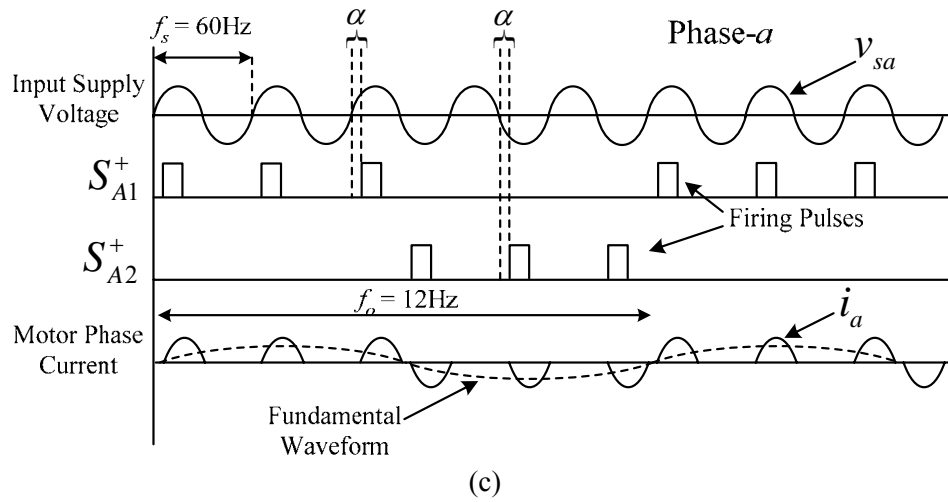
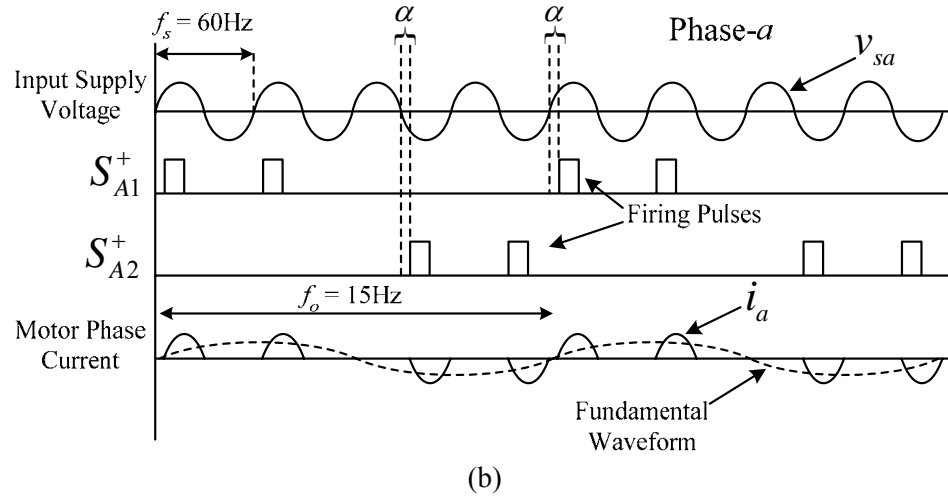
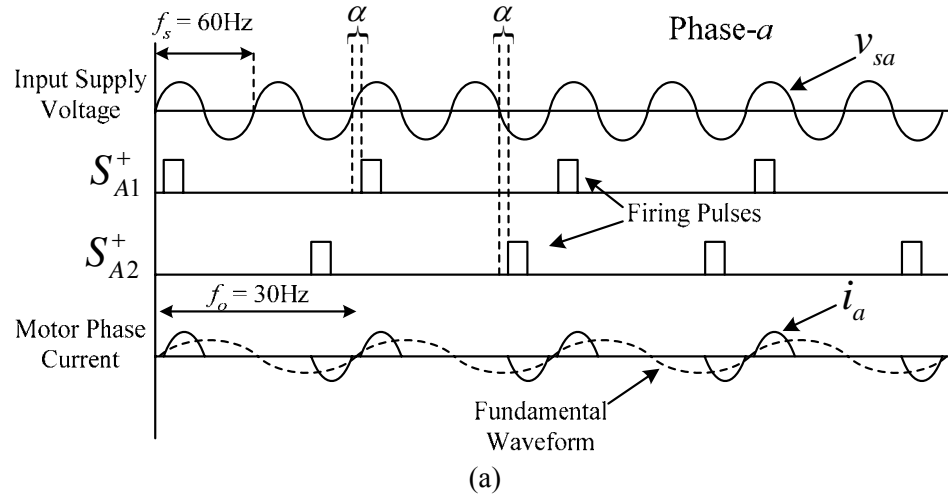


Figure 7.7: Firing sequence of the SCRs of phase-*a*. (a) 30-Hz operation. (b) 15-Hz operation. (c) 12-Hz operation.

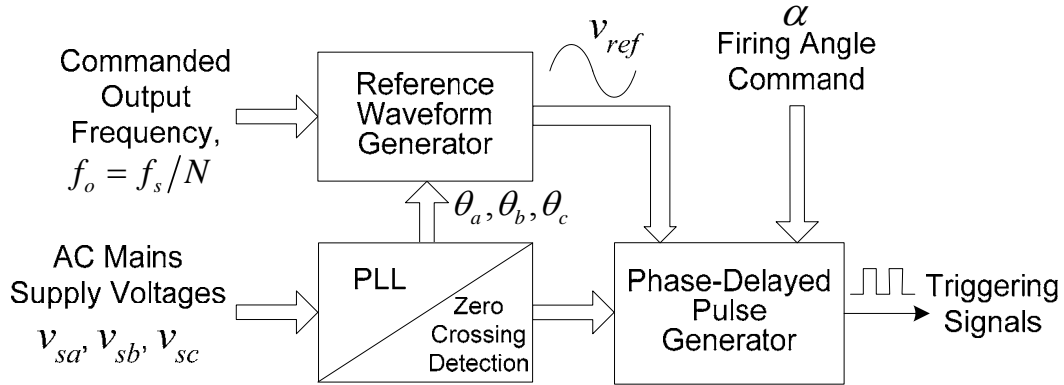


Figure 7.8: Block diagram of proposed control scheme for variable-speed operation.

To generate the proper sequencing of the triggering pulses for the SCRs, a phase-delayed pulse generator was conceived. The input requirements for this phase-delayed pulse generator, see Figure 7.8, are the three-phase reference waveforms for phases- $a$ ,  $b$ , and  $c$ , the angle,  $\alpha$ , and the zero-crossing time instants of all three phases of the supply voltages. The control logic (flow-chart) of the phase-delayed pulse generator for phase- $a$  of the present topology is illustrated in Figure 7.9. The same control logic is also applied to phase- $b$  and phase- $c$ . It first begins by sensing the phase- $a$  supply mains,  $v_{sa}$ , and applying the zero-crossing detection scheme to the measured signal. When a zero crossing of the voltage,  $v_{sa}$ , is detected, a phase-delayed angle counter will be initiated to begin counting. Once the phase-delayed angle counter has reached the value of the angle,  $\alpha$ , a single firing pulse is generated by either the positive pulse generator or the negative pulse generator depending upon the nature of the zero crossing. If the zero crossing occurs during the instant when the polarity of the voltage changes from negative to positive, the positive pulse generator will be selected, and vice versa. Once a train of pulses has been generated, the last and crucial step is to decide the proper instant of triggering the SCRs,  $S_{A1}^+$  and  $S_{A2}^+$ . This is carried out by monitoring the polarity of the reference waveform,  $v_{ref}$ , for phase- $a$ . If  $v_{ref} > 0$ , the firing pulse generated by the positive pulse generator is sent to the gate of  $S_{A1}^+$  for

the turn-on, while  $S_{A2}^+$  remains off. On the contrary, if  $v_{ref} < 0$ ,  $S_{A2}^+$  will be turned-on by the firing pulse generated by the negative pulse generator, and  $S_{A1}^+$  will be in its turn-off state. A simple graphical illustration for the case of the 15-Hz output waveform is shown in Figure 7.10. As may be observed in this figure, a train of pulses is generated by both the positive and negative pulse generators, after a phase-delay by an angle,  $\alpha$ , with respect to the zero crossings of the supply voltage. Depending upon the polarity of  $v_{ref}$  of phase- $a$ , the SCRs,  $S_{A1}^+$  and  $S_{A2}^+$ , are selectively triggered accordingly, to produce a 15-Hz output waveform. Meanwhile, the same control logic is also applicable for phase- $b$  and phase- $c$  of the SCRs shown in Figure 7.4 using  $v_{ref}$  of phase- $b$  and phase- $c$ , respectively. The only difference lies in the selection of either the positive-connection switches or the negative-connection switches, the decision of which is depending upon the commanded output frequency. According to the aforementioned criteria, the positive-connection switches are selected for  $N = 4, 7, 10, 13, 16, 19, 22, \dots, (3k+1)$ , whereas the negative-connection switches are selected for  $N = 2, 5, 8, 11, 14, 17, 20, \dots, (3k+2)$ , where,  $k = 0, 1, 2, 3, 4, 5, \dots$ , etc.

As illustrated in Figure 7.5 or Figure 7.7, the three-phase motor currents obtained using the present discrete-frequency control approach exhibit non-sinusoidal waveforms, which will entail some torque pulsations in the motor performance, as will be elaborated later-on in simulation and test results in the next chapter. Nevertheless, the average torque at the desired motor operating condition will still be maintained.

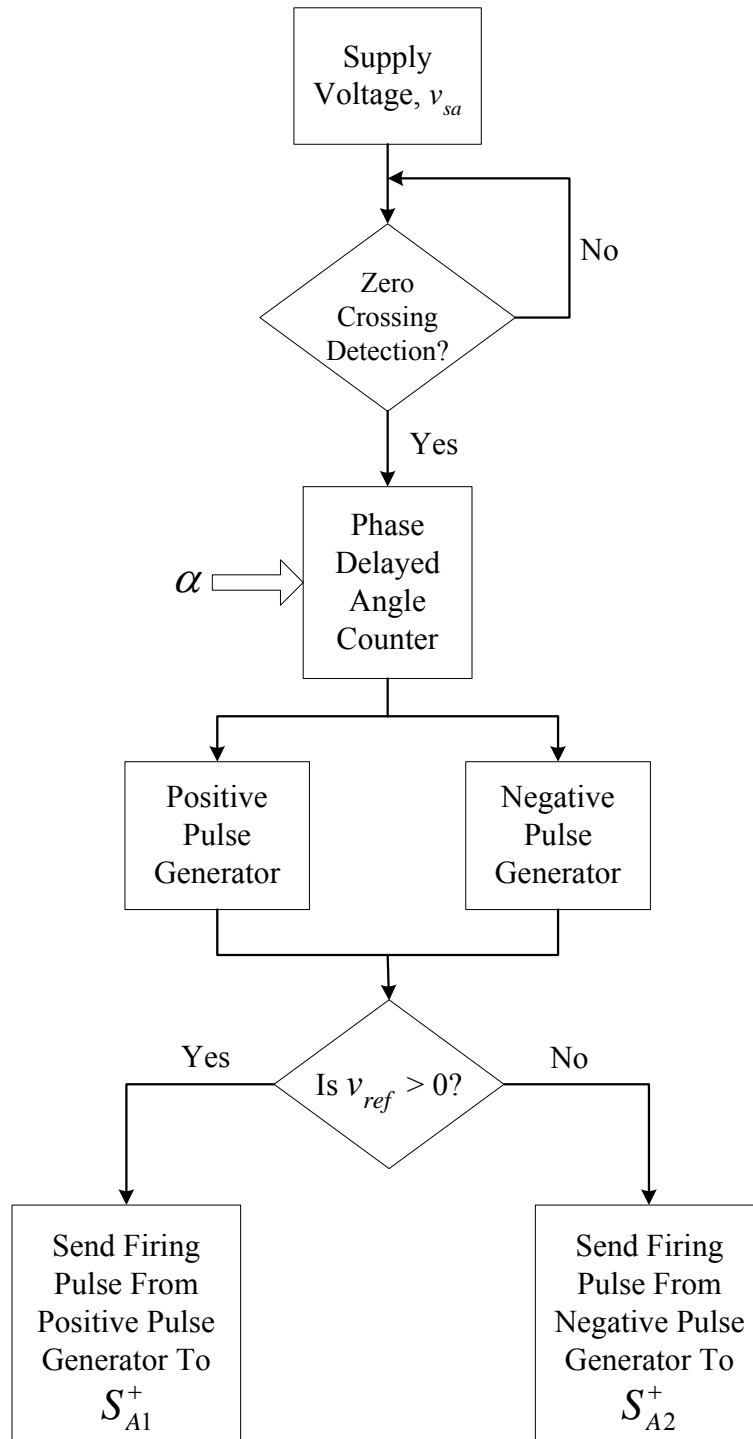


Figure 7.9: Control logic of phase-delayed pulse generator for each phase.

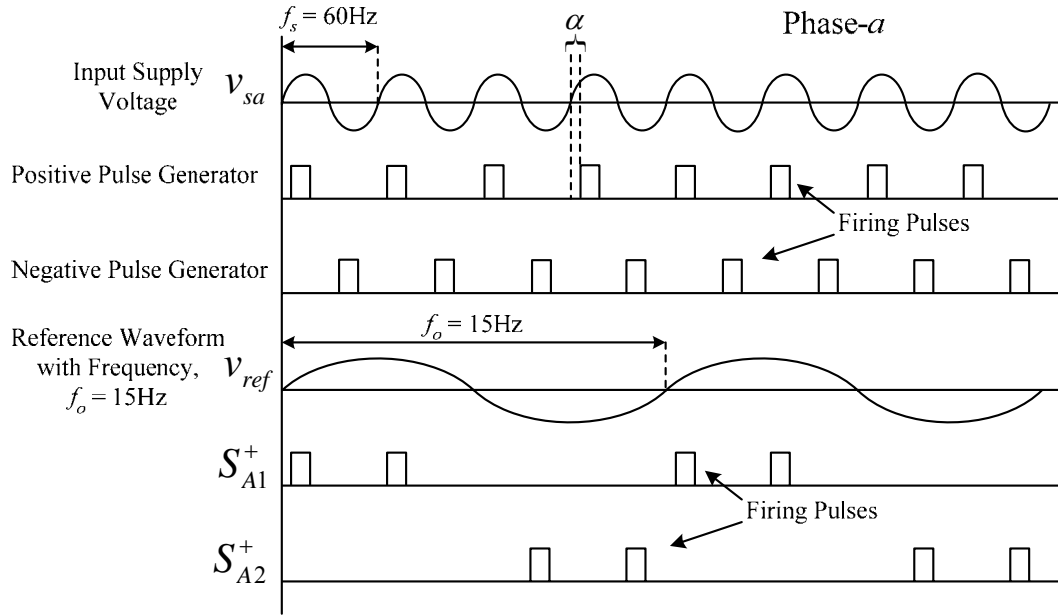


Figure 7.10: Graphical illustration of the control logic to achieve 15-Hz operation.

### 7.3 Summary

In summary, a fault tolerant strategy is presented herein as a potential solution for overcoming the negative impact of inverter switch fault on motor performance. The present approach requires minimum hardware modifications at a modest cost to the conventional off-the-shelf three-phase PWM drive, as compared to the existing topologies proposed by others. These modifications require only the addition of electronic components such as SCR switches and fast-acting fuses. Due to its circuit configuration and control principles, the present fault tolerant approach is suitable for “limp-home” low-speed motor applications such as in vehicle and propulsion systems. In addition, the present approach does not suffer from drawbacks such as the need for accessibility to a motor neutral, larger size dc link capacitors, or higher dc bus voltage. Another “upside” element of the proposed approach is its potential use for mitigating other drive-related faults that can potentially occur in the diode-rectifier bridge or the dc-link of the drive because of the fact that this approach bypasses the entire drive system, provided that such faults

can be safely isolated. Furthermore, the present topology can also function as a soft-starter during the post-fault operation in situations in which the motor has to be brought to a stop before starting-up again from standstill, as a result of the malfunction of the drive. The effect of soft-starting the motor reduces any high inrush currents and consequently high starting torque pulsations. The major downside of the present approach is the presence of pulsating torques due to the non-sinusoidal nature of the motor current waveforms. The simulation results on the motor performance using the proposed topology, as well as corresponding experimental results, are given in the upcoming chapter.

In light of the above, it is to be understood that within the scope of this work regarding mitigating inverter switch faults, the present technology may be applied to applications other than as specifically described herein. In such other practical applications, one may envision the present topology as a high-performance soft-starter and a moderate-performance drive. Such technology is well-suited for users who are unwilling to bear the burden of the high price of a typical PWM drive, and still hope to achieve with reduced requirements the performance of variable speed operation at a lower affordable cost.

# CHAPTER 8

---

---

## SIMULATION AND EXPERIMENTAL RESULTS OF INVERTER-MOTOR FAULT TOLERANT OPERATION

---

---

### 8.1 Introduction

In this chapter, the circuit simulation results of the inverter-motor system, as well as the corresponding experimental test results are given. Namely, the inverter-motor fault tolerant operations using the conceived and implemented quasi-cycloconverter based configuration are presented. The simulation work was carried out using a commercially available circuit simulation software package, namely *Matlab-Simulink* [91]. A prototype replica of the simulation model was built and tested in the laboratory for experimental verification/validation purposes. A 2-hp, 460-volt, 4-pole, 60-Hz, three-phase, case-study induction motor was used as the subject for both the simulation and experimental work. The dynamic behavior of the conceived and implemented quasi-cycloconverter topology during initial soft-starting to the final desired speed operation was also simulated and tested in the laboratory. This is in order to emulate the starting performance of an adjustable-speed PWM drive having constant volts-per-hertz control. Practical application

considerations and opportunities for practical use of the present conceived design are also discussed herein. This is in order to highlight the potentials of the present design as a possible fault-tolerant solution for drive-related faults, as well as the potential utilization of this type of design as a low-cost, moderate-performance drive with high reliability.

## 8.2 Simulation Performance

### 8.2.1 Circuit Simulation Model

The *Matlab-Simulink* simulation model of the power circuit structure of the induction motor-drive system is depicted in Figure 8.1. A three-phase back-to-back connected SCR bridge is connected in parallel with the drive system to provide fault tolerant / “limp-home” operation in the event of a fault occurring in the drive using the discrete-frequency control algorithm conceived here in this work. The machine parameters of the induction motor used here in the simulation were those corresponding to the characteristics of the 2-hp test motor used in the experimental setup (see Appendix A). This induction motor was simulated in the  $dq$  frame of reference. The complete simulation model parameters and conditions are listed in Table 8.1.

The system block diagram of the proposed discrete-frequency control algorithm is depicted in Figure 8.2. A predetermined firing angle,  $\alpha$ , along with the zero-crossing time instants of the three-phase utility voltages, are the necessary parameters for generating a train of triggering pulses for turning-on the SCRs of each of the phases. Thereafter, a reference waveform of each of the phases at the commanded output frequency is synthesized. Using the generated reference waveforms and the train of firing pulses, the SCR associated with each of the phases is triggered at the specific time instant. This is in order to produce a set of output voltages whose fundamental frequency corresponds to the commanded output frequency. The simulation work was carried out at a time step of  $10\mu\text{sec}$ . The results using the present control approach are presented next.

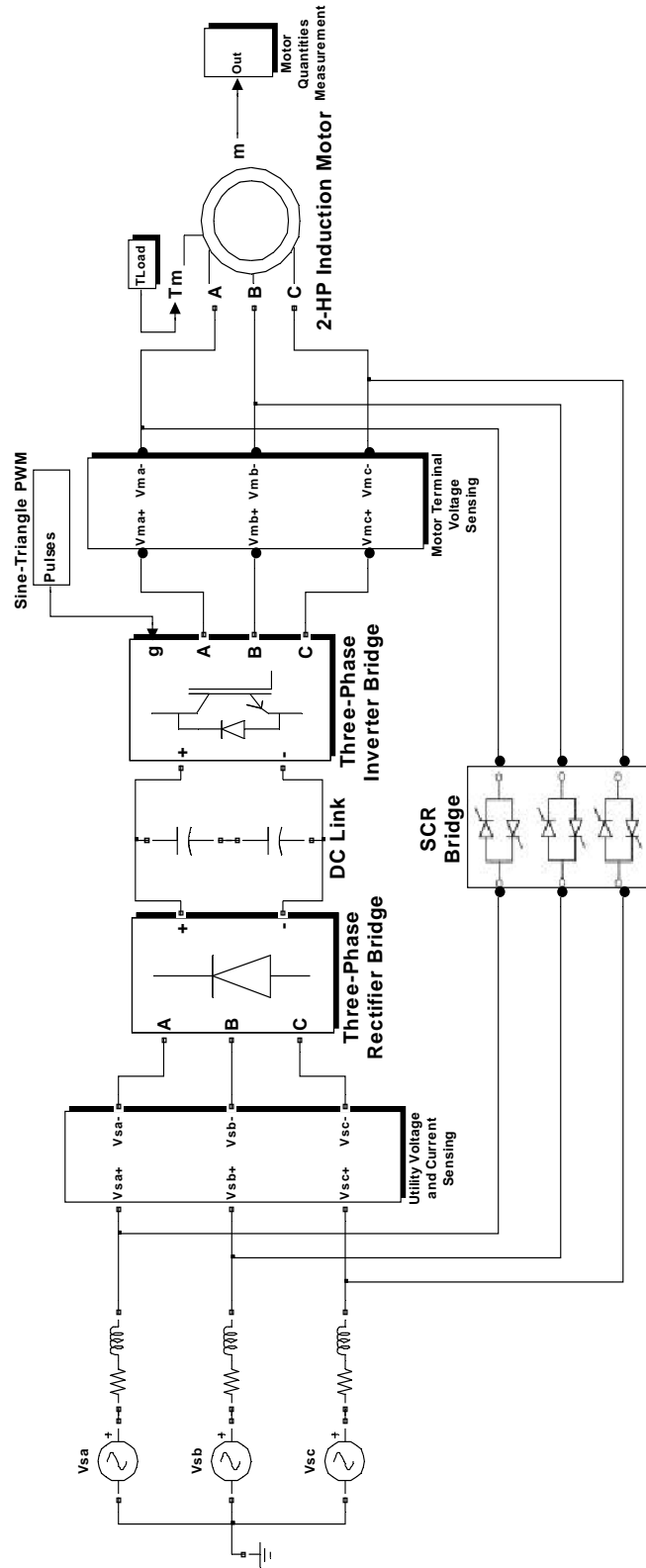


Figure 8.1: Schematic of induction motor-drive power structure with “limp-home” capability in *Matlab-Simulink* [91].

Table 8.1: Simulation conditions of induction motor-drive system.

<b>Utility</b>	
Utility Input Voltage (Line-To-Line)	460 Volts
Frequency	60 Hz
Line Resistance (4.8%)	0.7082 $\Omega$
Line Inductance (4.8%)	1.8786 mH
<b>DC Link (2 capacitors in series)</b>	
Capacitance Value	2000 $\mu$ F per capacitor
<b>Induction Motor</b>	
Rated Power	2 hp (1492 Watts)
Rated Voltage (Line-To-Line)	460 Volts (rms)
Rated Current	3.0 Amps (rms)
Rated Frequency	60 Hz
Rated Speed	1744 r/min
Rated Torque	8.169 Nm
Phase	3
Number of Poles	4
Stator Resistance, $R_s$	3.850 $\Omega$
Rotor Resistance, $R_r$	2.574 $\Omega$
Stator Leakage Inductance, $L_{ls}$	17.5594 mH
Rotor Leakage Inductance, $L_{lr}$	17.5594 mH
Magnetizing Inductance, $L_m$	0.372674 H
Moment of Inertia, $J$	0.028 kg.m <sup>2</sup>
<b>PWM Controller</b>	<b>Carrier-Based Sine-Triangle</b>
Modulation Index, $m_a$	0.9
Switching Frequency	5 kHz

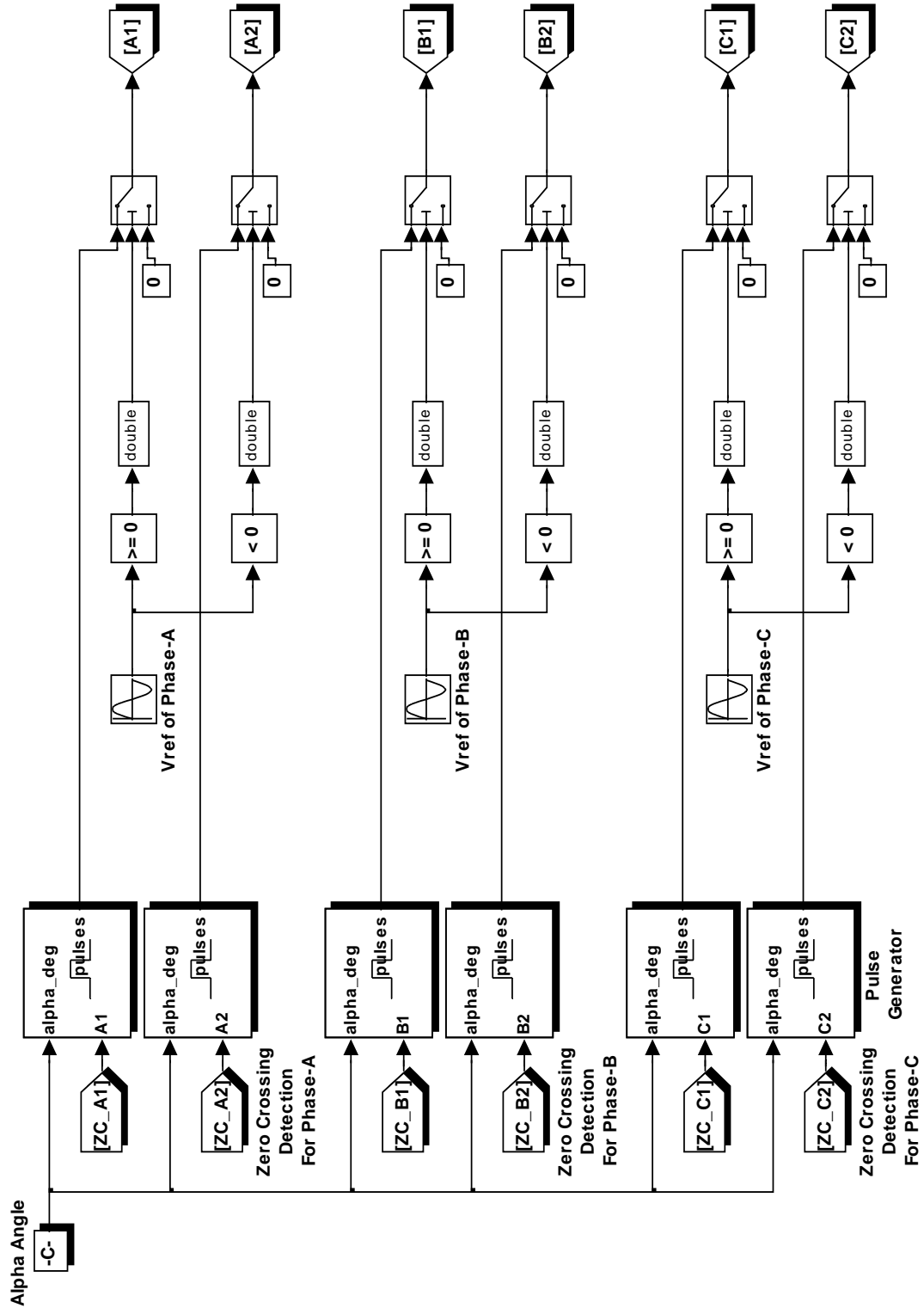


Figure 8.2: Block diagram of discrete-frequency control algorithm in *Matlab-Simulink* [91].

## 8.2.2 Simulation Results

### 8.2.2.1 The No-Load Case

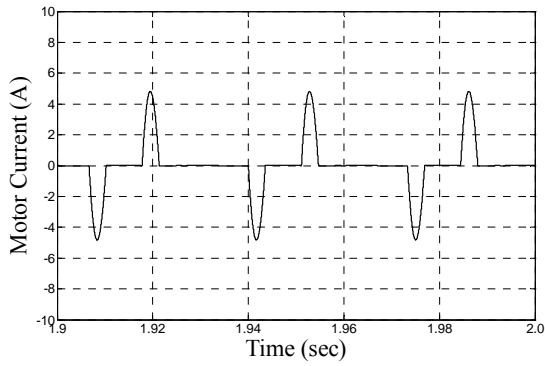
The simulation results of the motor performance using the present quasi-cycloconverter topology at different output frequencies under no-load condition are first presented here. This is in order to demonstrate the concept/theory of the conceived discrete-frequency control algorithm. The output frequencies of the test cases were commanded at  $f = 30\text{-Hz}$ ,  $15\text{-Hz}$ ,  $12\text{-Hz}$ ,  $8.57\text{-Hz}$ ,  $7.5\text{-Hz}$ , and  $6\text{-Hz}$ . The corresponding synchronous speeds of the case-study 2-hp, 4-pole induction motor at the commanded frequencies, accordingly, are: 900-r/min, 450-r/min, 360-r/min, 257-r/min, 225-r/min, and 180-r/min, respectively. The simulation waveforms of the motor phase currents, voltages, and speeds at the aforementioned frequencies are depicted in Figure 8.3 through Figure 8.8, respectively. As one may observe from these figures, the unique pattern of each motor phase current waveform of Figure 8.3(a) through Figure 8.8(a) at the specific frequency matches with the ideal current pattern as presented in Figure 7.5 of the previous chapter, in so far as the number of current pulses at each specific frequency are concerned. Observation of the voltage waveforms of Figure 8.3(b) through Figure 8.8(b) reveals the presence of low-frequency harmonic components, whose frequencies correspond to the commanded output frequencies. In addition, it is clearly evident from the speed profiles of Figure 8.3(c) through Figure 8.8(c) that the motor reaches the desired speed associated with the commanded output frequency. Hence, the simulation results presented herein under no-load condition clearly verify the soundness of the theory of the conceived discrete-frequency control algorithm being applied on the present quasi-cycloconverter power structure. Meanwhile, it should be highlighted that the smooth starting of the motor, as can be observed from the initial transient of the speed profiles, is due to the soft-starting capability that the present topology possesses. Such feature presents an “upside” (advantage) of the present topology. Details on this under motor loading condition will be elaborated on later. An interesting phenomenon can be observed in the speed profiles of Figure

8.5(c) through Figure 8.7(c) at the commanded frequencies of 12-Hz, 8.57-Hz, and 7.5-Hz, respectively, in which the motor overshoots the desired speed during soft-starting before the conceived control scheme is applied. Despite the overshoot, the motor reverts to its desired speed in a smooth manner upon the initiation of the discrete-frequency control mode at the time instant,  $t = 0.6 \text{ sec}$ . This clearly demonstrates the dynamic behavior of the present approach beginning from soft-starting mode until the discrete-frequency control mode is reached. This is namely in the event in which the motor requires starting-up from standstill. Hence, this very much resembles the starting behavior of a typical constant volts-per-hertz PWM drive.

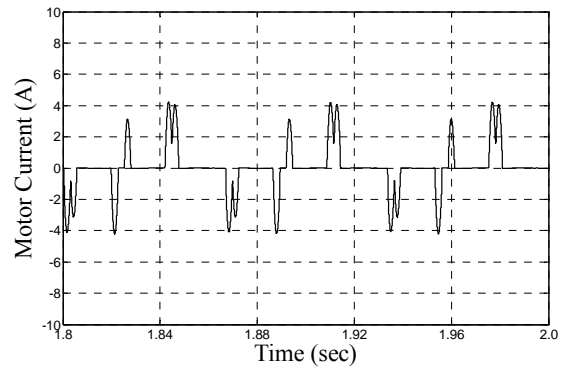
### 8.2.2.2 Limp-Home Operation of the Conceived Topology under Inverter Fault Case

Three simulation case studies were performed at full-load (8.169Nm) under different speed conditions, namely at 60-Hz, 30-Hz, and 15-Hz. An open-circuit inverter switch fault is assumed to occur at  $t = 1 \text{ sec}$ , followed by the “limp-home” operation at  $t = 1.3 \text{ sec}$ . The drive control is of the open-loop constant volts-per-hertz PWM type during the healthy inverter state.

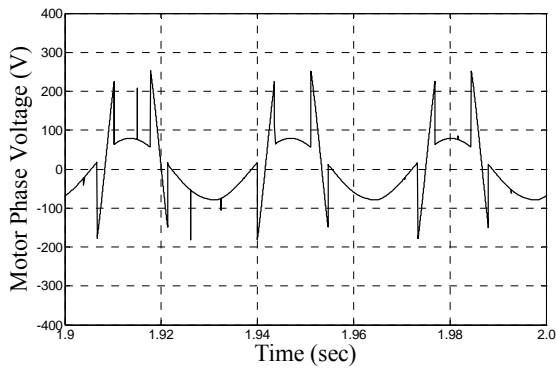
The first case study was simulated at rated 60-Hz supply frequency. The three-phase motor currents, developed torque, and motor speed during pre-fault and post-fault 60-Hz operating conditions under transistor open-circuit switch fault occurring at switch,  $S_1$ , are depicted in Figure 8.9(a), Figure 8.9(b), and Figure 8.9(c), respectively. The open-circuit switch fault was triggered at  $t = 1 \text{ sec}$  after the motor has reached steady-state condition. As previously discussed in Chapter 6, during the faulty period, the current in phase- $a$  is negative for half a cycle when the corresponding phase voltage is negative, and zero for the other half cycle when the corresponding phase voltage is positive, see the period from  $t = 1 \text{ sec}$  to  $t = 1.3 \text{ sec}$  in Figure 8.9(a). This is due to the malfunction of the top switch,  $S_1$ , which prevents any positive current flow into the motor terminal of phase- $a$ . Accordingly, this induces a dc (unidirectional) offset in the phase- $a$  current.



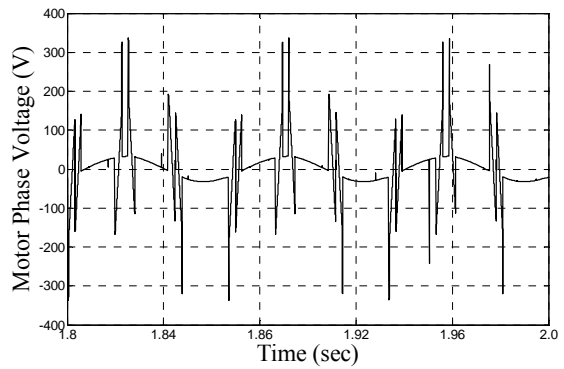
(a) Motor phase current.  
(rms value = 1.63 A)



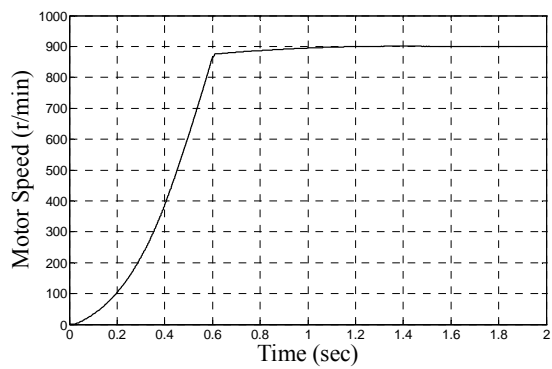
(a) Motor phase current.  
(rms value = 1.19 A)



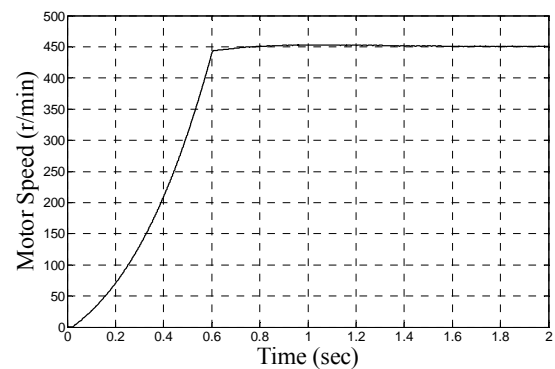
(b) Motor phase voltage.  
(rms value = 77.70 V)



(b) Motor phase voltage.  
(rms value = 41.27 V)



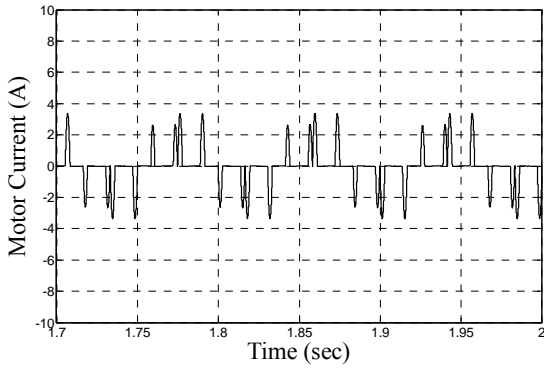
(c) Motor speed.



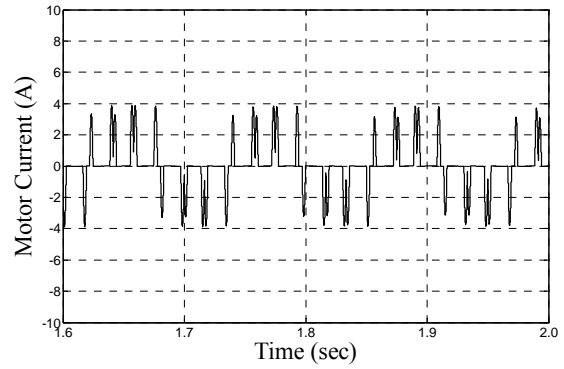
(c) Motor speed.

Figure 8.3: Simulation, 30-Hz operation.

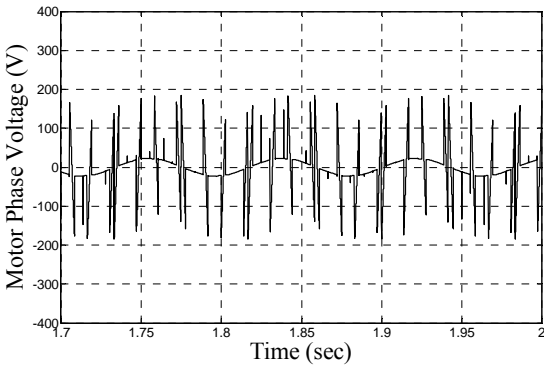
Figure 8.4: Simulation, 15-Hz operation.



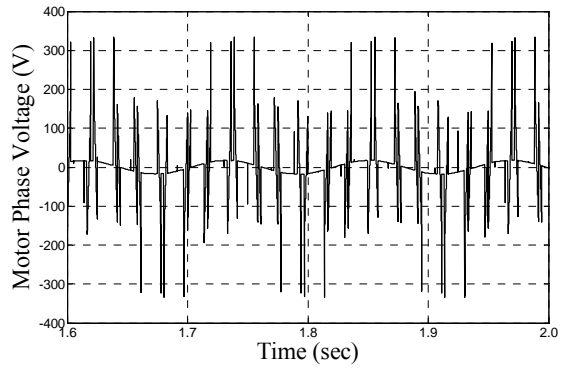
(a) Motor phase current.  
(rms value = 1.27 A)



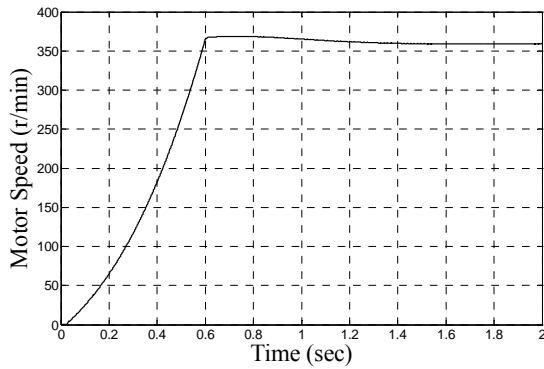
(a) Motor phase current.  
(rms value = 1.32 A)



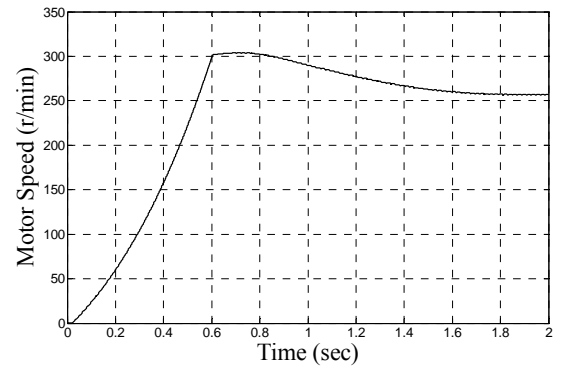
(b) Motor phase voltage.  
(rms value = 49.46 V)



(b) Motor phase voltage.  
(rms value = 46.14 V)



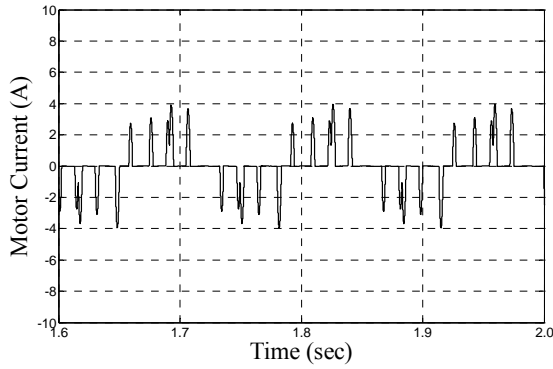
(c) Motor speed.



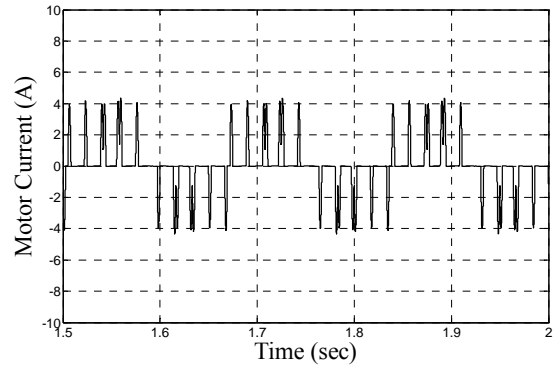
(c) Motor speed.

Figure 8.5: Simulation, 12-Hz operation.

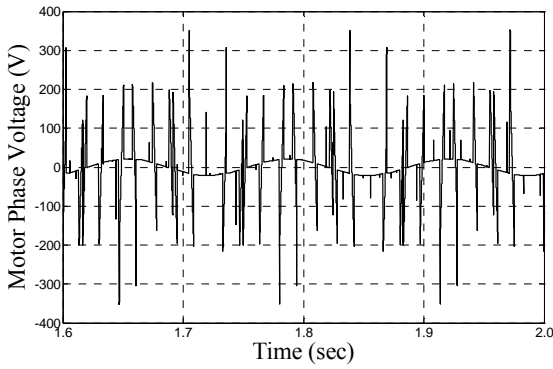
Figure 8.6: Simulation, 8.57-Hz operation.



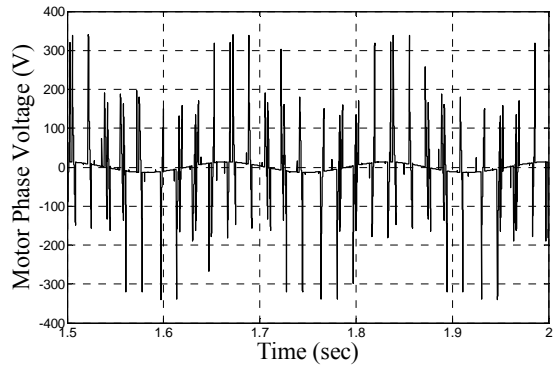
(a) Motor phase current.  
(rms value = 1.71 A)



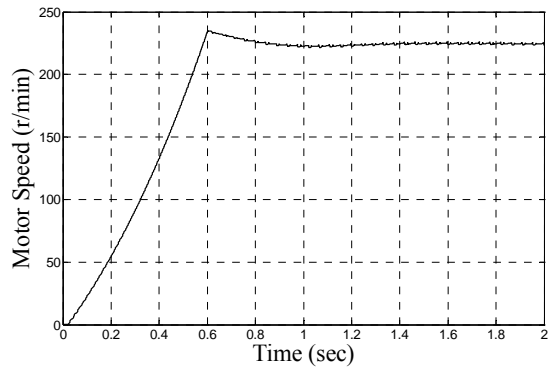
(a) Motor phase current.  
(rms value = 1.46 A)



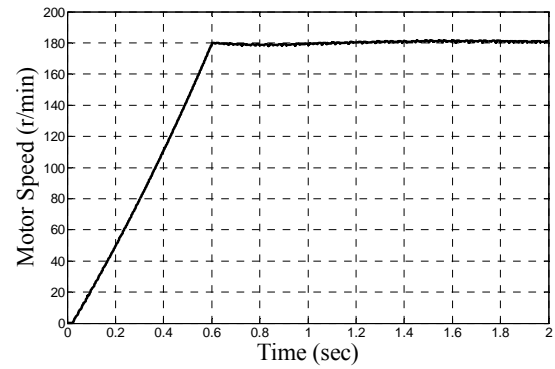
(b) Motor phase voltage.  
(rms value = 47.82 V)



(b) Motor phase voltage.  
(rms value = 47.79 V)



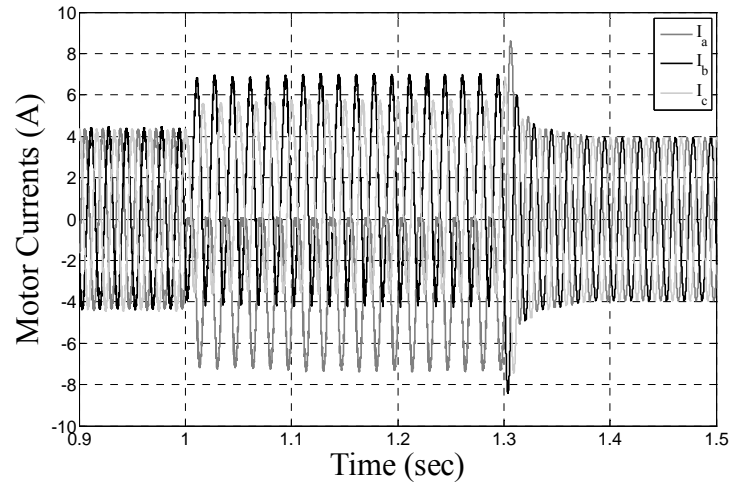
(c) Motor speed.



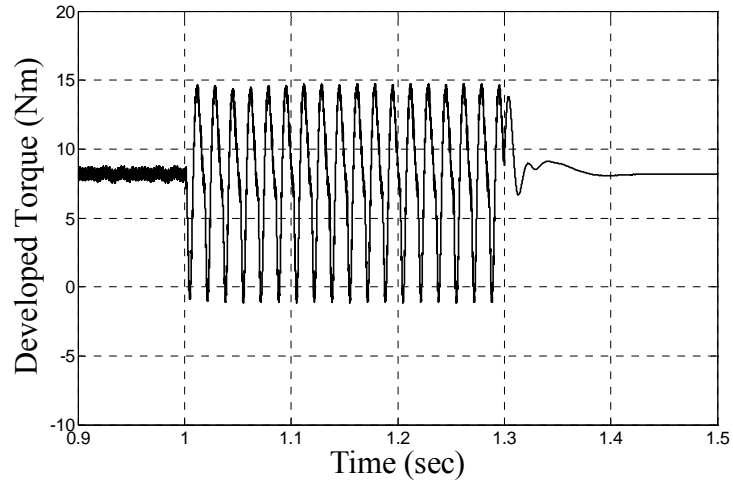
(c) Motor speed.

Figure 8.7: Simulation, 7.5-Hz operation.

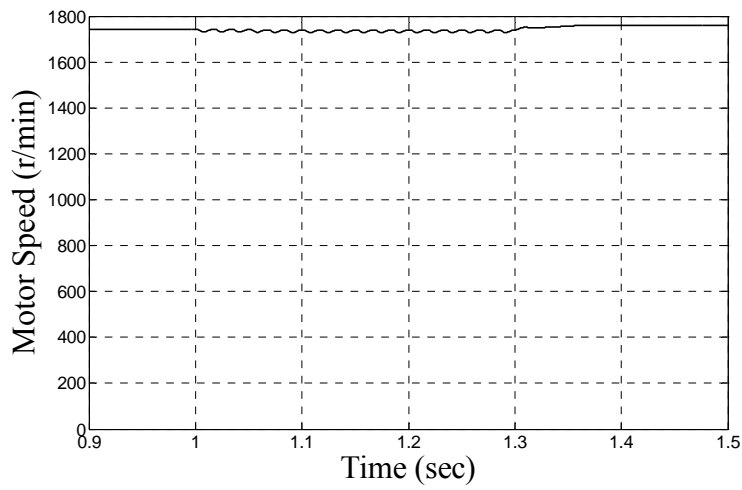
Figure 8.8: Simulation, 6-Hz operation.



(a)



(b)



(c)

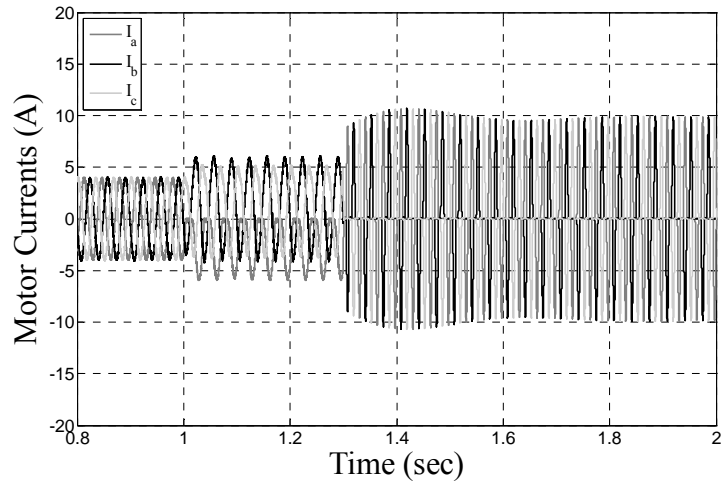
Figure 8.9: Simulation results of motor performance at 60-Hz operation during pre- and post-fault conditions. (a) Three-phase currents. (b) Developed torque. (c) Motor speed.

This dc (unidirectional) offset is divided between the paths of the remaining two healthy phases, given that the motor has an isolated (floating) neutral connection. The electromagnetic interaction between the stator current dc (unidirectional) component and the fundamental component of the rotor magnetic field generates a pulsating torque at the stator line current frequency, as illustrated from  $t = 1 \text{ sec}$  to  $t = 1.3 \text{ sec}$  in Figure 8.9(b), and the consequent corresponding speed ripples are shown in Figure 8.9(c). Moreover, the dc (unidirectional) component of the stator current generates unequal current stresses in the upper and lower transistor switches which may have thermal consequences in these transistors and may need further consideration. As one may observe from Figure 8.9(a), the phase currents revert to their healthy state when the SCRs are commanded to turn-on at  $t = 1.3 \text{ sec}$  to perform the bypass transfer in which the motor is now being energized directly from the supply mains. Also, one can notice that there were no significant interruptions during the point of bypass transfer in the motor phase currents, torque, and speed profiles, owing to the fact that the inverter PWM reference (modulation) waveforms are in synchronism with the supply mains through a PLL routine.

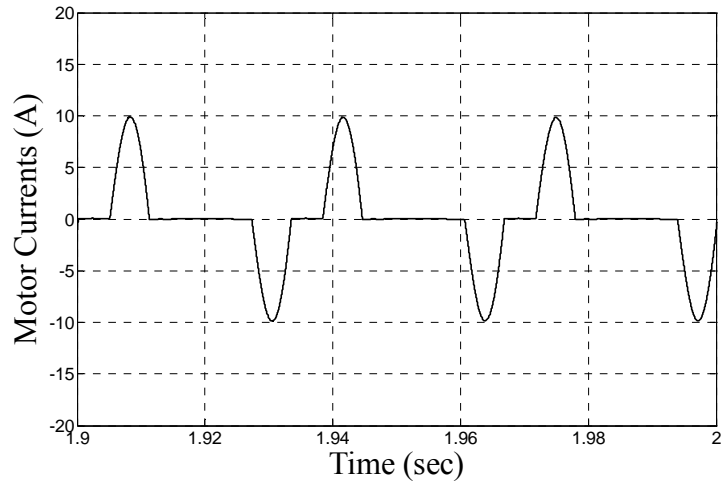
In order to demonstrate variable speed operations using the proposed discrete-frequency control technique, the simulations were carried out under rated-load condition (8.169 Nm) at two other frequencies, namely at 30-Hz and 15-Hz. The three-phase motor current waveforms during pre- and post-fault operating conditions for the 30-Hz control are shown in Figure 8.10(a), and the corresponding detail (zoom) of the steady-state “limp-home” post-fault current is shown in Figure 8.10(b). It may appear from Figure 8.10(a) that the post-fault currents have increased by more than twice their values of the healthy currents at rated-load condition. This is in fact not true when the total rms value of the post-fault current of Figure 8.10(b) is computed and given, along with the corresponding harmonic contents of the “limp-home” post-fault motor phase voltage and current, in Table 8.2. From the harmonic contents, the total rms value of the current was computed to be 4.261 Amps, which is about 1.42 times that of the rated case-study motor phase

current which is 3 Amps (rms). Despite the need for the increased currents to obtain the desired full-load torque, the amount of current increase is still less than that of the previous method proposed by other researchers [49]-[51], which is  $\sqrt{3}$  times that of the rated motor phase current. In fact, the increased current value by a factor of  $\sqrt{3}$  in the topology of [49]-[51] will result in a motor neutral current of 3 times that of the rated motor phase current. Also, no motor neutral connection is necessary for the presently conceived approach. Due to the non-sinusoidal nature of the “limp-home” post-fault currents, torque pulsations and speed ripples will arise, as can be seen from Figure 8.10(c) and Figure 8.10(d), respectively. Nevertheless, the torque pulsations are significantly reduced, as compared to the faulty case, upon introducing the control algorithm of the “limp-home” strategy. In addition, the motor is able to maintain the desired speed associated with the 30-Hz frequency during the “limp-home” operation.

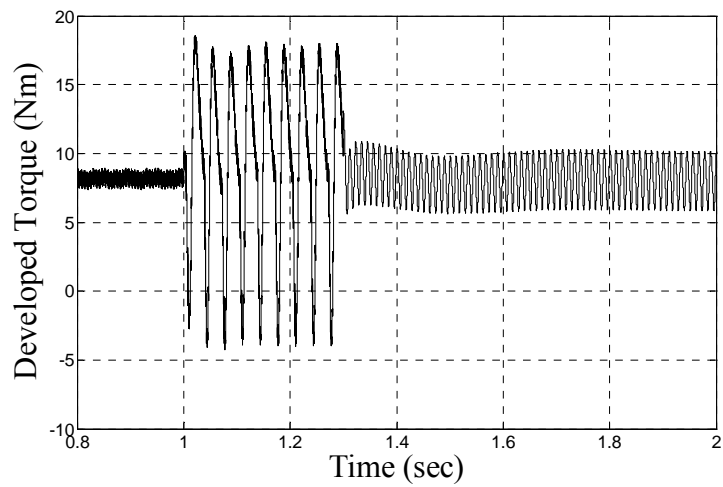
The same simulation was carried out for the case of 15-Hz frequency control at full-load motor condition. The results are depicted in Figure 8.11 for the motor phase currents, developed torque, and motor speed. Again, torque pulsations and speed ripples, as a result of the “limp-home” operation, are evident from Figure 8.11(c) and Figure 8.11(d), respectively. The harmonic contents of the motor phase voltage and current, along with their rms values, are given in Table 8.3. The total rms value of the motor phase current for the 15-Hz control operation was calculated to be 4.392 Amps, which is about 1.464 times that of the rated rms current value (3 Amps rms) at full-load condition. Again, this amount of increase in the motor phase current is still considerably less than the necessary increase (1.73 times) required by the previously reported method of [49]-[51] for full-load motor condition. Table 8.4 summarizes the torque pulsation in percent for both the cases of the 30-Hz and the 15-Hz operations, during pre- and post-fault full-load conditions. Due to the presence of torque and speed ripples, the present approach that may be acceptable for “limp-home” purposes, such as in vehicles and other propulsion applications, fans, cement mills, mine hoists, rolling mills and the like, is not suitable for applications such as paper mills or



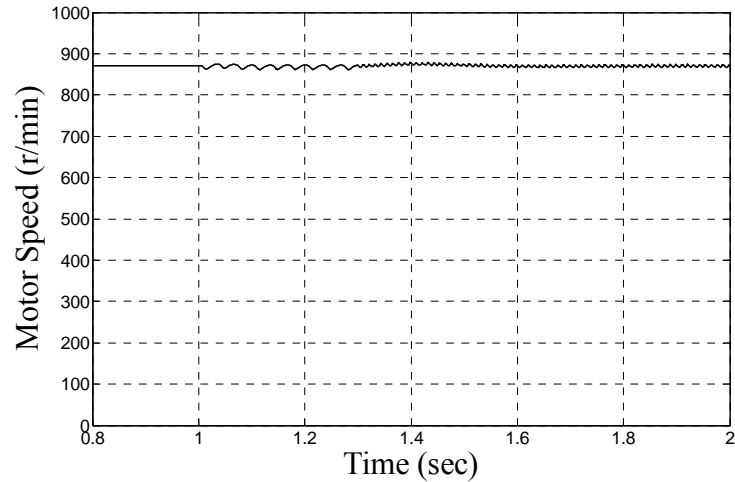
(a)



(b) rms value = 4.261 A



(c) Average torque = 8.169 Nm

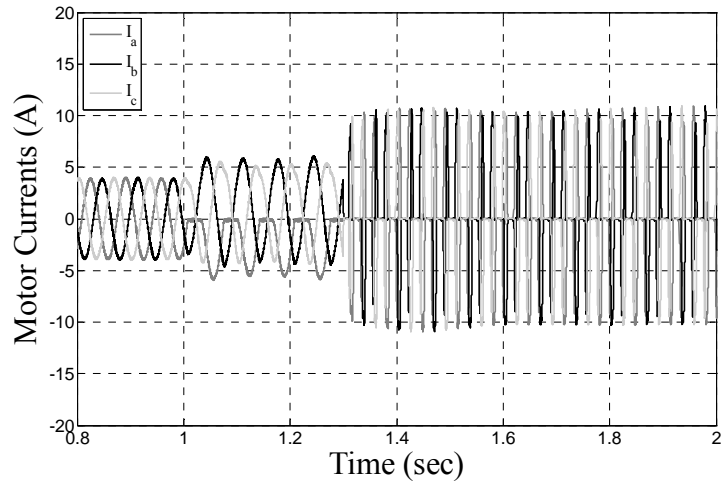


(d) Average speed = 871 r/min

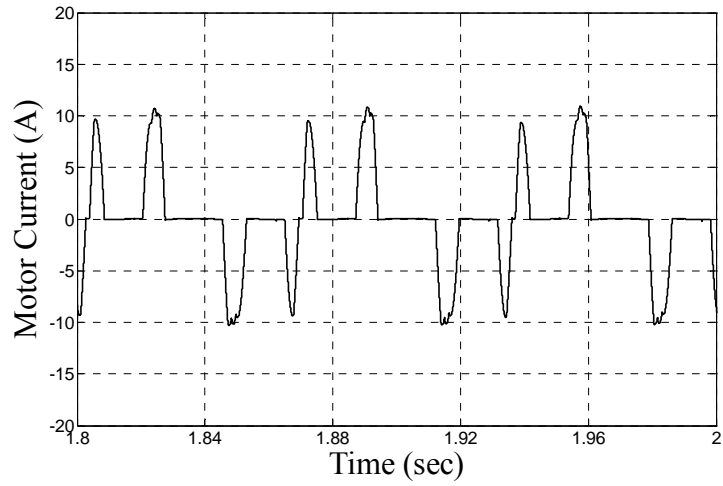
Figure 8.10: Simulation results of motor performance at 30-Hz operation during pre- and post-fault conditions at full-load. (a) Three-phase currents. (b) Steady-state “limp-home” post-fault current. (c) Developed torque. (d) Motor speed.

Table 8.2: Simulation results of harmonic contents of motor phase voltage and current during post-fault limp-home at 30-Hz operation under full-load (8.169 Nm) condition.

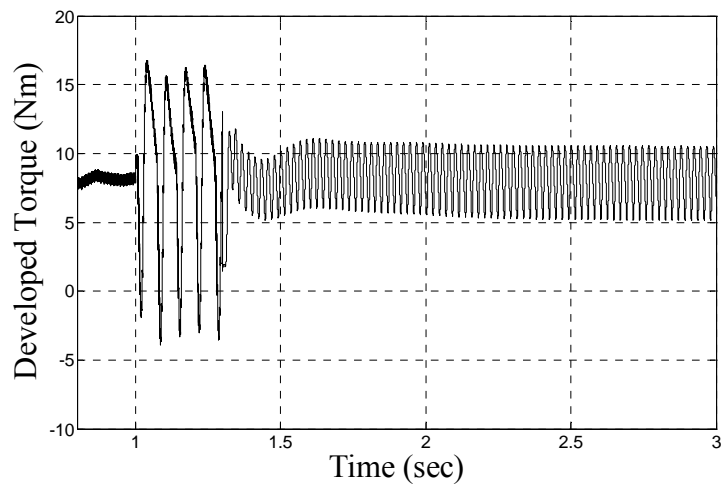
Harmonic Order	Harmonic Frequency (Hz)	Motor Phase Voltage (rms value - Volts)	Motor Phase Current (rms value - Amps)
1	30	156.80	2.780
2	60	35.24	2.514
4	120	43.75	1.633
5	150	37.02	1.127
7	210	12.55	0.275
8	240	1.67	0.031
10	300	14.13	0.217
11	330	13.58	0.190
13	390	3.02	0.036
14	420	3.64	0.040
16	480	9.35	0.090
17	510	7.66	0.069
19	570	1.08	0.009
20	600	4.63	0.036
Total RMS Value:		<b>173.19</b>	<b>4.261</b>



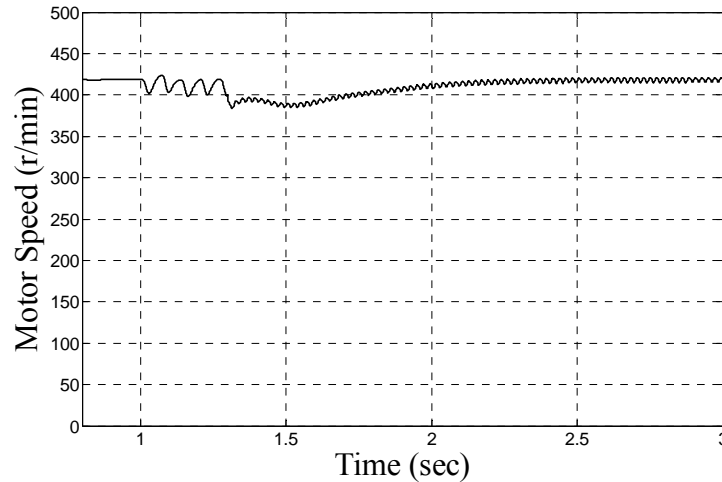
(a)



(b) rms value = 4.392 A



(c) Average torque = 8.169 Nm.



(d) Average speed = 419 r/min

Figure 8.11: Simulation results of motor performance at 15-Hz operation during pre- and post-fault conditions at full-load. (a) Three-phase currents. (b) Steady-state “limp-home” post-fault current. (c) Developed torque. (d) Motor speed.

Table 8.3: Simulation results of harmonic contents of motor phase voltage and current during post-fault limp-home at 15-Hz operation under full-load (8.169 Nm) condition.

Harmonic Order	Harmonic Frequency (Hz)	Motor Phase Voltage (rms value - Volts)	Motor Phase Current (rms value - Amps)
1	15	64.48	2.341
2	30	8.394	1.016
4	60	37.21	2.655
5	75	5.633	0.223
7	105	36.01	2.002
8	120	16.25	0.696
10	150	20.16	0.795
11	165	8.101	0.252
13	195	3.114	0.072
14	210	11.02	0.288
16	240	4.580	0.164
17	255	22.05	0.488
19	285	0.928	0.015
20	300	14.38	0.267
Total RMS Value:		<b>94.54</b>	<b>4.392</b>

Table 8.4: Simulation results of torque pulsations during pre- and post-fault “limp-home” conditions at full-load (8.169 Nm).

Commanded Output Frequency	Torque Ripple % of Average Torque		
	Pre-Fault	During Fault	Post-Fault Limp-Home
30-Hz	10.18 %	270.49 %	52.64 %
15-Hz	5.49 %	239.57 %	65.11 %

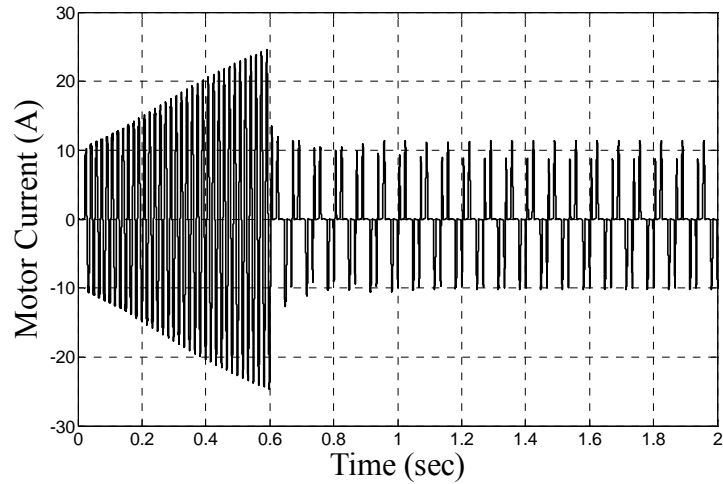
conveyor belt-driven types of applications where torque pulsation constitutes a major concern. All things considered, the present approach is still able to maintain the desired motor speed associated with the commanded output frequency during the post-fault “limp-home” operation.

### 8.2.2.3 Starting Performance of the Conceived Topology

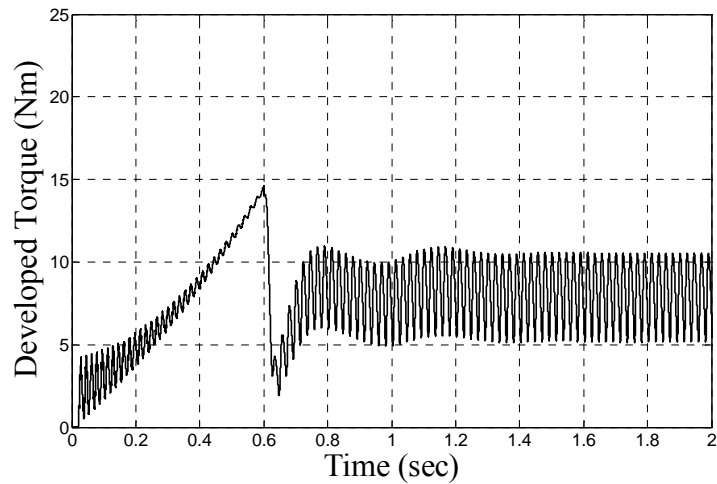
An “upside” of the present topology is its ability to start-up with reduced starting currents and minimum starting torque transients. With this feature, the present topology can function as a drive with starting behavior that is comparable to that of a typical constant volts-per-hertz PWM drive. This is carried out using the soft-starting algorithm that was presented in the earlier chapters. The notion is to soft-start the motor before using the discrete-frequency control scheme to control the motor to the desired speed that is associated with the commanded output frequency. The starting performance of the present topology is demonstrated here for the case of 15-Hz and 12-Hz operations under half-load (4.084 Nm) and full-load (8.169 Nm) conditions.

The starting performance of the motor phase currents, developed torque, and motor speed for the case of 15-Hz control under full-load (8.169 Nm) condition is shown in Figure 8.12(a) through Figure 8.12(c), respectively. As one can observe from Figure 8.12(a), the motor experiences reduced starting inrush currents during starting, which consequently result in reduced starting torque pulsations, see Figure 8.12(b), and reduced speed ripples, see Figure 8.12(c). At the time instant,  $t = 0.6 \text{ sec}$ , the discrete-frequency control scheme which is initiated at that

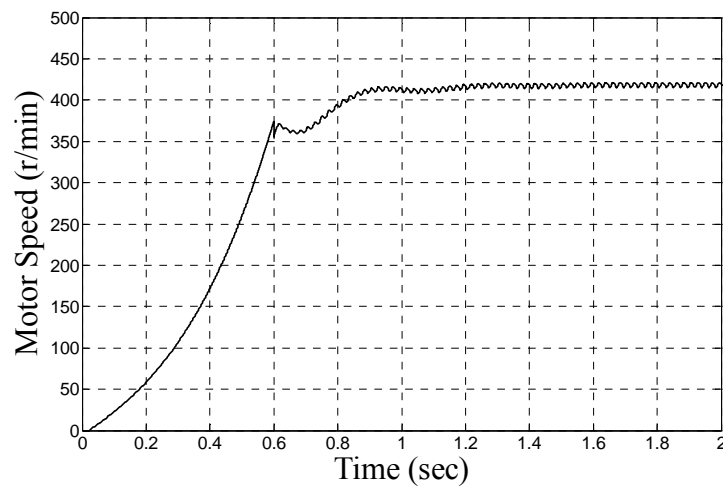
instant causes the motor to approach the desired speed at the commanded 15-Hz frequency. As can be seen from the torque and speed profiles, there is a slight transient before the motor reaches the desired speed. The same simulation was carried out at 15-Hz operation under half-load (4.084 Nm) condition. The results of the motor phase currents, developed torque, and motor speed are depicted in Figure 8.13(a) through Figure 8.13(c), respectively. Again, one can see a similar trend in the starting performance as compared to the full-load case, that is with reduced starting currents and torque transients. A simulation was carried out at a different output frequency of 12-Hz to demonstrate the starting behavior of the present conceived topology. The simulation results of which are illustrated in Figure 8.14 and Figure 8.15 for the case of full-load and half-load conditions, respectively. Conclusion similar to those mentioned above regarding the starting performance of the present motor-inverter topology can be reached for these results shown in Figure 8.14 and Figure 8.15. The steady-state motor performance, in terms of phase current rms value, torque ripple %, and speed ripple %, of the results presented in Figure 8.12 through Figure 8.15 are summarized in Table 8.5.



(a) rms value = 4.392 A

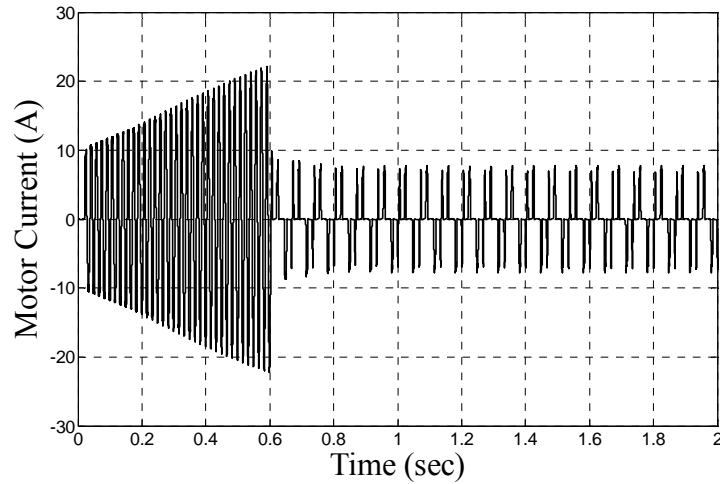


(b) Average torque = 8.169 Nm

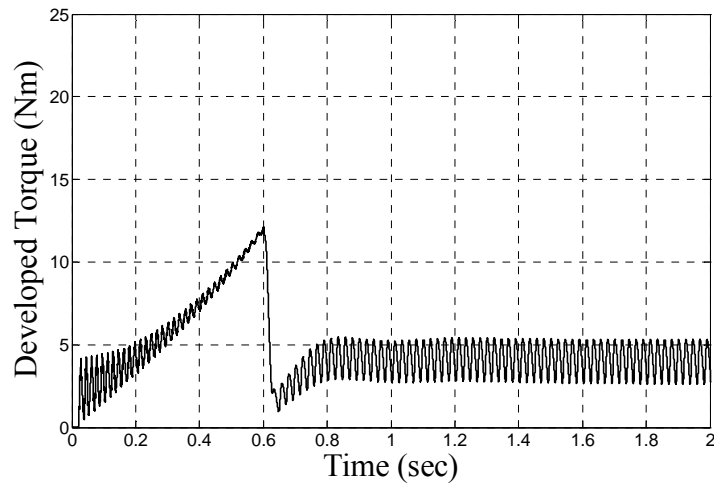


(c) Average speed = 418 r/min

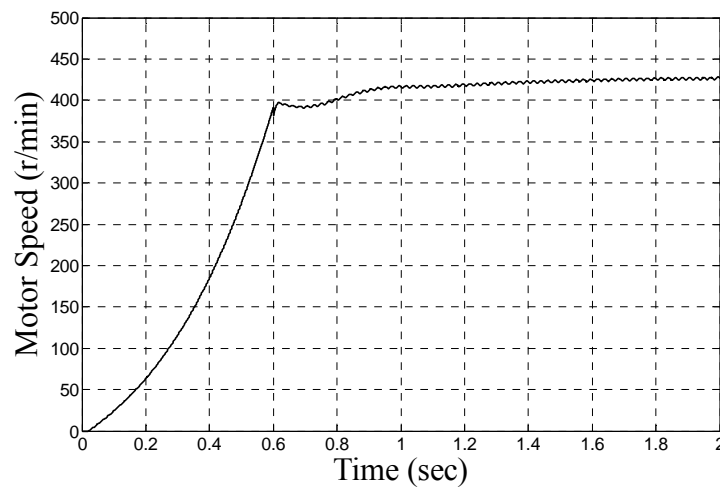
Figure 8.12: Simulation results of soft-starting performance of present topology for 15-Hz operation at full-load (8.169 Nm) condition. (a) Motor phase current. (b) Torque. (c) Speed.



(a) rms value = 3.237 A

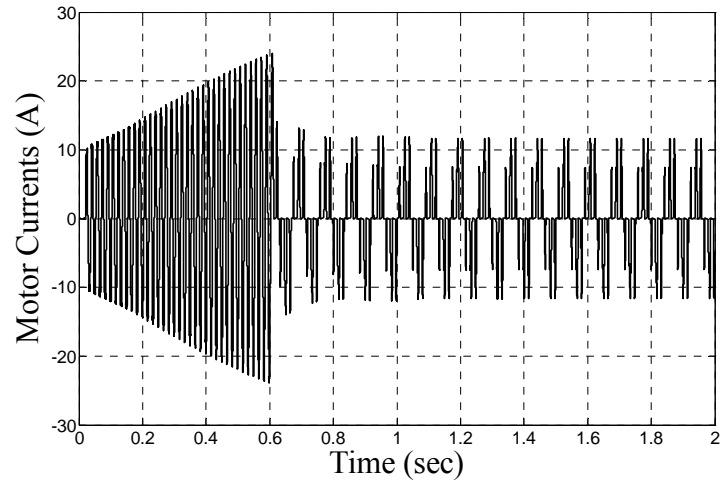


(b) Average torque = 4.084 Nm

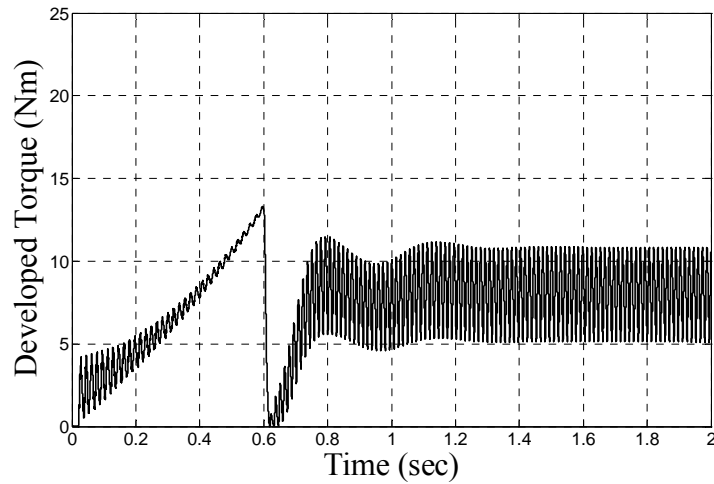


(c) Average speed = 426 r/min

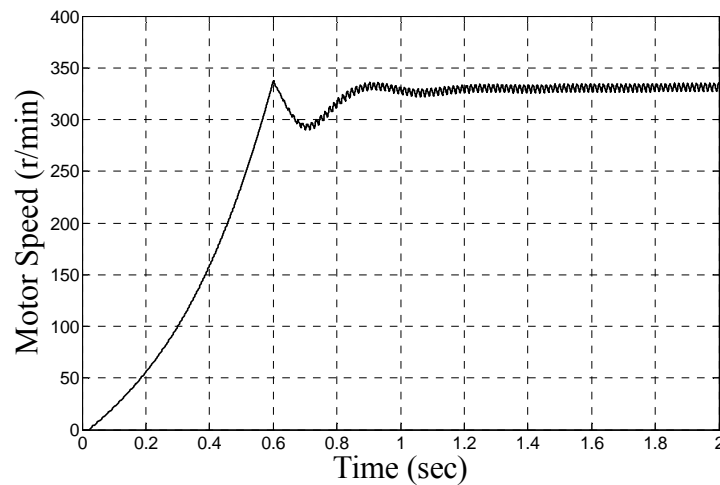
Figure 8.13: Simulation results of soft-starting performance of present topology for 15-Hz operation at half-load (4.084 Nm) condition. (a) Motor phase current. (b) Torque. (c) Speed.



(a) rms value = 4.504 A

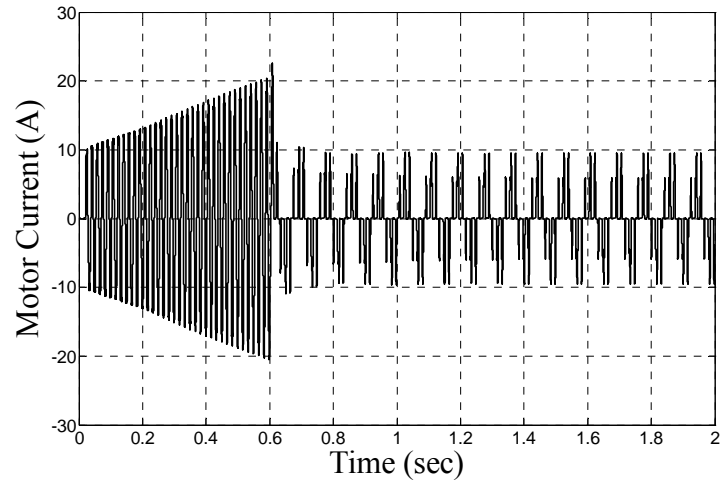


(b) Average torque = 8.169 Nm

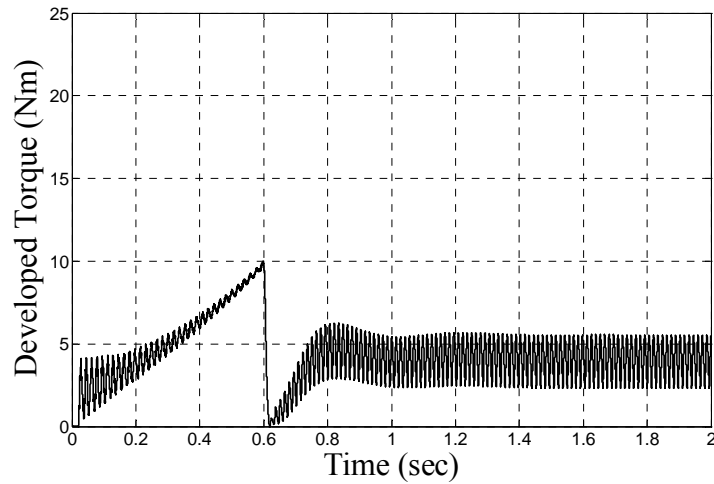


(c) Average speed = 331 r/min

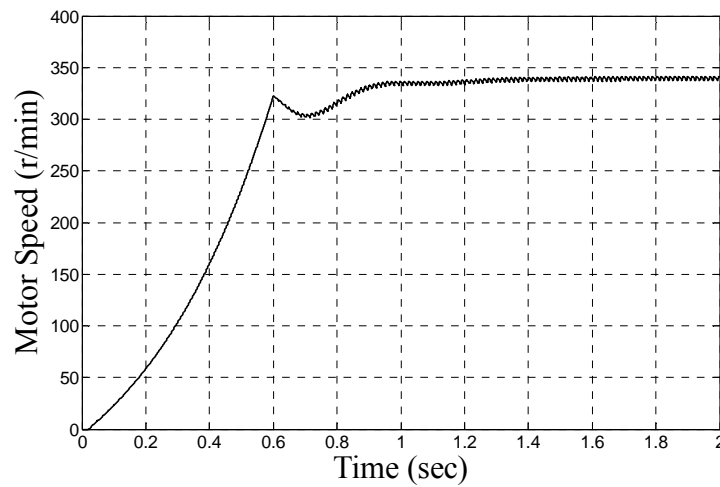
Figure 8.14: Simulation results of soft-starting performance of present topology for 12-Hz operation at full-load (8.169 Nm) condition. (a) Motor phase current. (b) Torque. (c) Speed.



(a) rms value = 3.339 A



(b) Average torque = 4.084 Nm



(c) Average speed = 340 r/min

Figure 8.15: Simulation results of soft-starting performance of present topology for 12-Hz operation at half-load (4.084 Nm) condition. (a) Motor phase current. (b) Torque. (c) Speed.

Table 8.5: Simulation results of steady-state motor performance under full-load and half-load conditions for 15-Hz and 12-Hz motor operations.

Commanded Output Frequency	Phase Current (rms - Amps)	Torque Ripple (% of Full-Load Torque)	Speed Ripple (% of Average Speed)
<b>Full-Load (8.169 Nm)</b>			
<b>15-Hz</b>	4.392 A	65.11 %	1.34 %
<b>12-Hz</b>	4.504 A	70.14 %	2.33 %
<b>Half-Load (4.084 Nm)</b>			
<b>15-Hz</b>	3.237 A	33.48 %	0.71 %
<b>12-Hz</b>	3.339 A	39.61 %	1.18 %

### 8.3 Experimental Validations

A hardware prototype of a PWM drive along with the conceived quasi-cycloconverter power topology was built and tested in the laboratory, as depicted here in the circuit schematic of Figure 8.16 and the photographs of Figure 8.17. The quasi-cycloconverter has the same power configuration as the soft starter prototype that was utilized in the earlier experimental work as reported in Chapter 5. For more details on the configurations and specifications of the quasi-cycloconverter and the PWM drive, Appendix A should be consulted. Since the soft starter power circuit topology consists of only three sets of back-to-back connected SCRs, two more sets of similar SCRs are required for the conceived quasi-cycloconverter to operate at more selectable frequencies/speeds, that is at  $f_o = f_s/N$ , where  $N = 2, 5, 8, 11, 14, 17, 20, 23, 26, 29, \dots, 3k+2, \dots, \text{etc}$ . Here,  $k = 0, 1, 2, 3, 4, \dots, \text{etc}$ . Therefore, instead of adding two more sets of SCR switches to the hardware prototype, two of the phases of the utility mains that are connected to the SCR bridge are manually interchanged whenever the need to test the prototype at the aforementioned commanded output frequency arises.

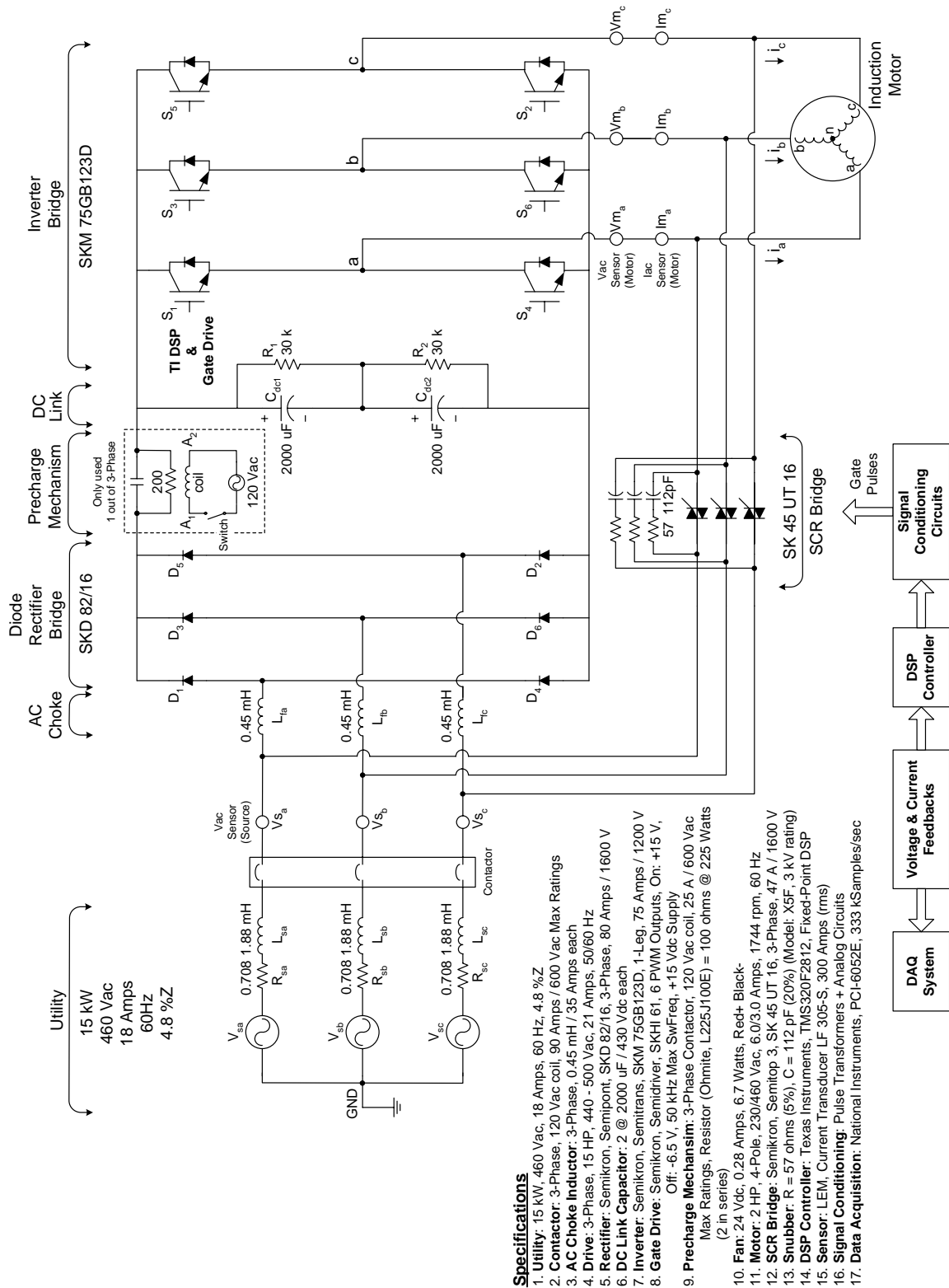
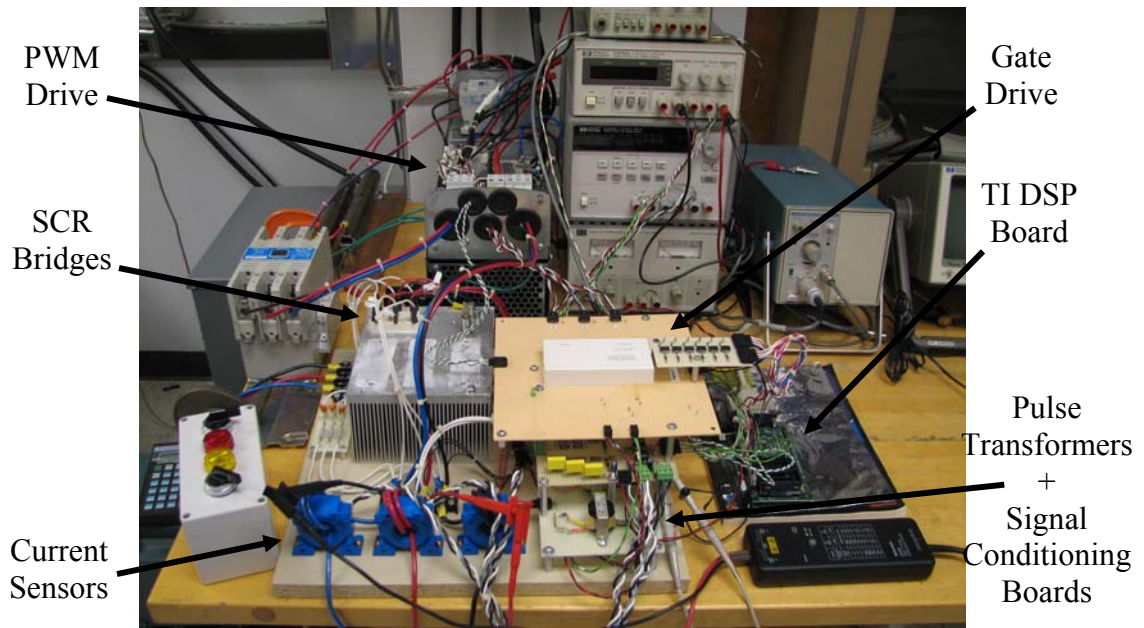
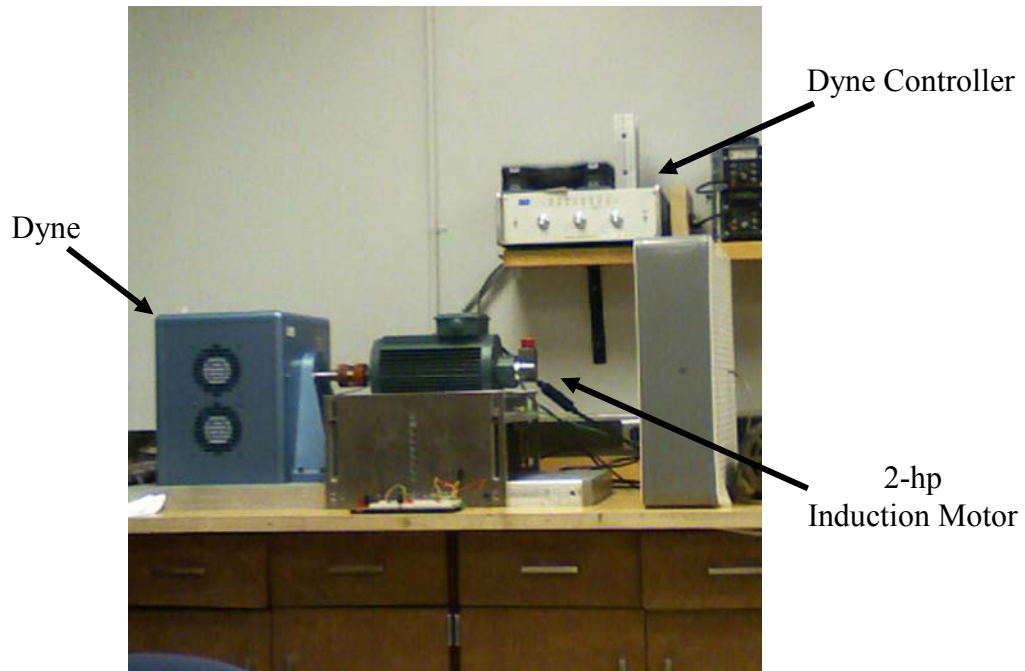


Figure 8.16: Schematic and specifications of induction motor-drive test setup system.



(a)



(b)

Figure 8.17: Test rigs. (a) PWM drive and quasi-cycloconverter power topology. (b) Induction motor and dynamometer.

### 8.3.1 The No-Load Case

Experimental results of steady-state motor performance at no-load condition obtained from using the conceived quasi-cycloconverter power circuit topology for the different cases of commanded output frequencies, that is at  $f = 30\text{-Hz}$ ,  $15\text{-Hz}$ ,  $12\text{-Hz}$ ,  $8.57\text{-Hz}$ ,  $7.5\text{-Hz}$ , and  $6\text{-Hz}$ , are presented first. These test results at the aforementioned frequencies are depicted in Figure 8.18 through Figure 8.23, respectively. As one may observe from these test figures, the measured current waveforms match reasonably well with the simulation current waveforms given in Figure 8.3(a) through Figure 8.8(a), in so far as the profiles are concerned. The same observation can be made for the measured waveforms of the motor phase voltages shown in Figure 8.18(b) through Figure 8.23(b), in comparison with the simulation phase voltage waveforms given in Figure 8.3(b) through Figure 8.8(b), for the different commanded output frequencies. Notice from the voltage waveforms the presence of a low-frequency harmonic component which corresponds to the commanded output frequency. Hence, the experimental results presented herein clearly verify the soundness of the theory of the conceived discrete-frequency control algorithm being applied using the conceived quasi-cycloconverter power circuit topology.

### 8.3.2 Limp-Home Operation of the Conceived Topology under Inverter Fault Case

The test results of the motor performance under inverter switch fault case are first presented. The measured three-phase current waveforms at  $15\text{-Hz}$  output frequency and  $25\%$  load condition ( $\sim 2\text{ Nm}$ ), in the event of a transistor open-circuit switch fault at  $S_I$ , are depicted in Figure 8.24. These current waveforms are in good agreement with the simulation waveforms, as depicted in Figure 6.14(b) of Chapter 6, in so far as the profiles are concerned. In order to further investigate the motor performance due to an open-circuit switch fault, the current space-vector locus, obtained by plotting the measured waveforms of  $i_d$  versus  $i_q$  current components, under different

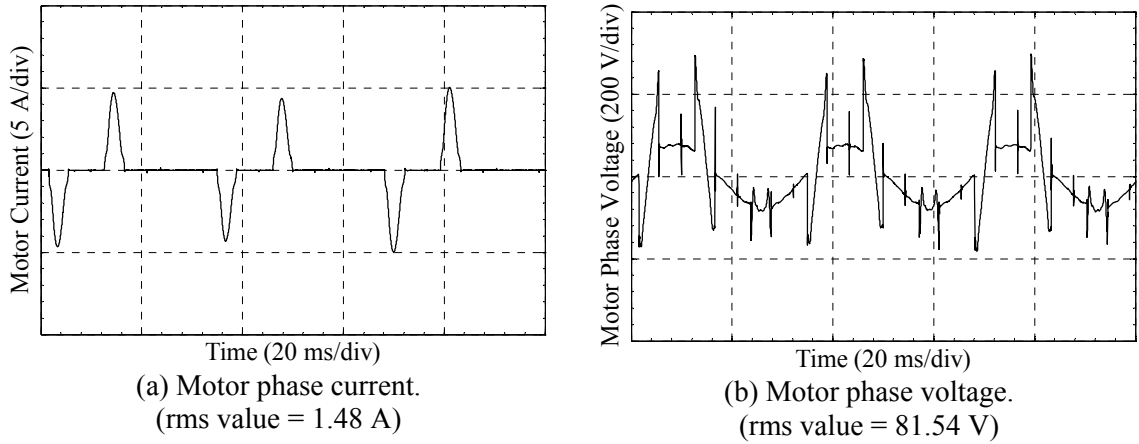


Figure 8.18: Experimental results, 30-Hz operation.

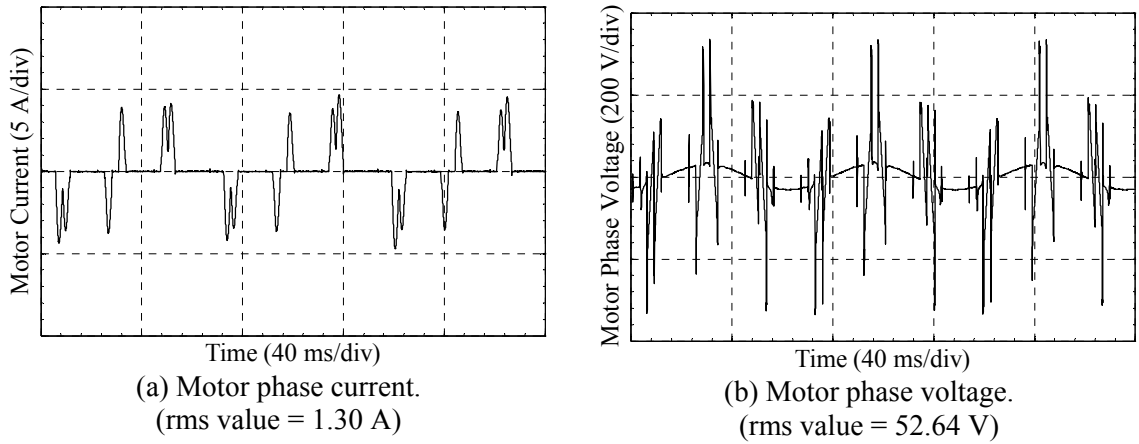


Figure 8.19: Experimental results, 15-Hz operation.

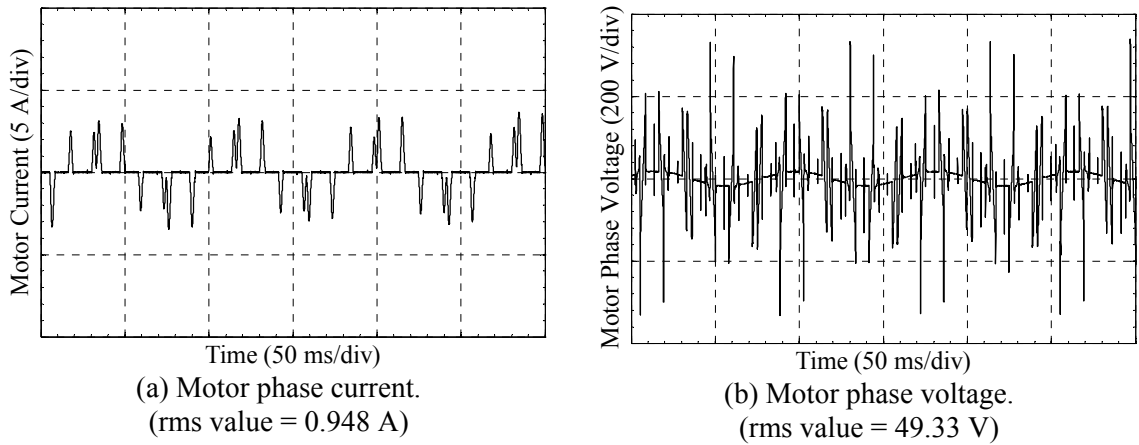


Figure 8.20: Experimental results, 12-Hz operation.

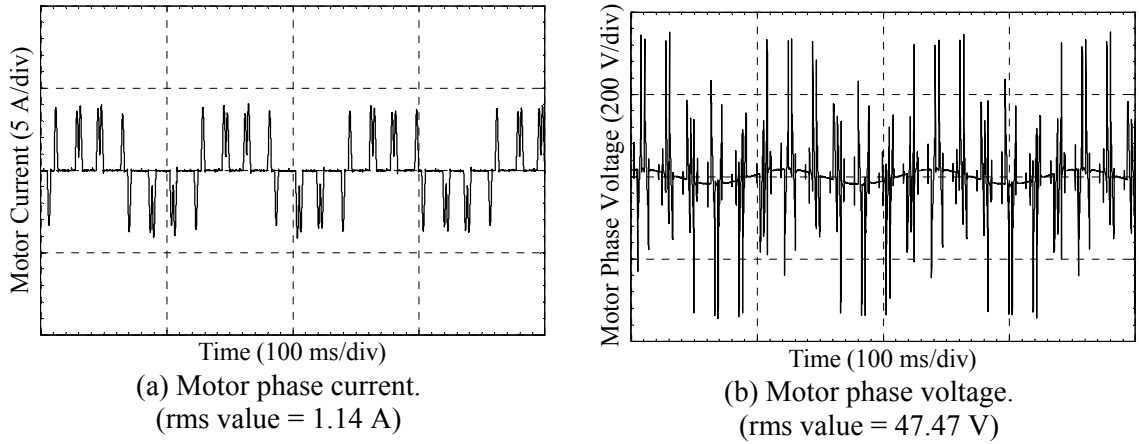


Figure 8.21: Experimental results, 8.57-Hz operation.

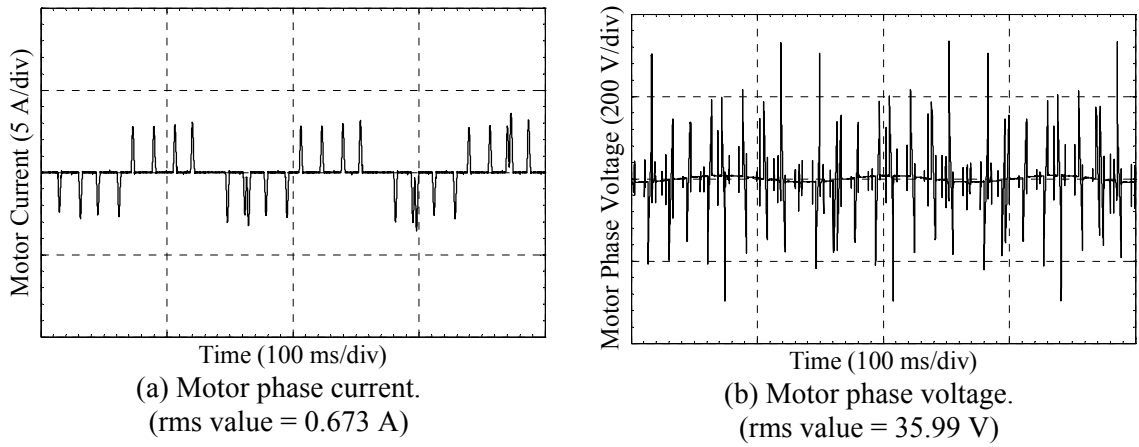


Figure 8.22: Experimental results, 7.5-Hz operation.

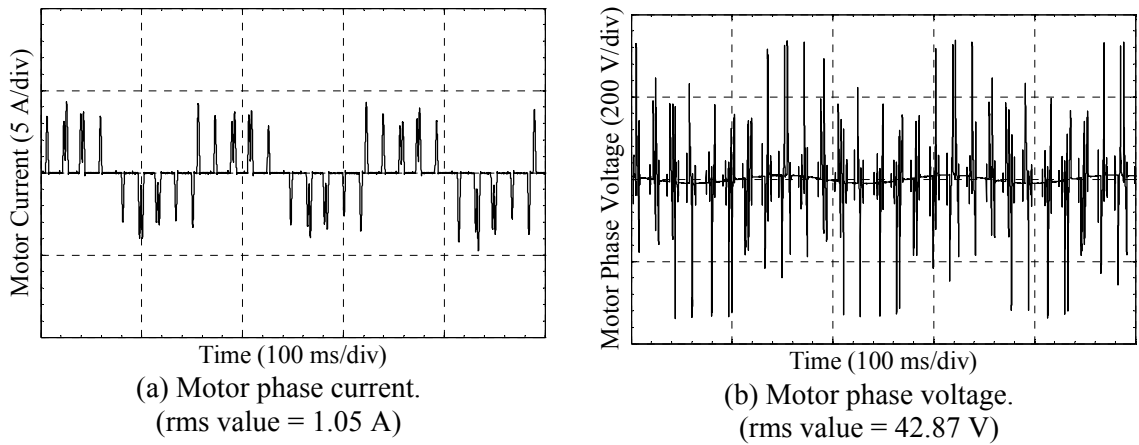


Figure 8.23: Experimental results, 6-Hz operation.

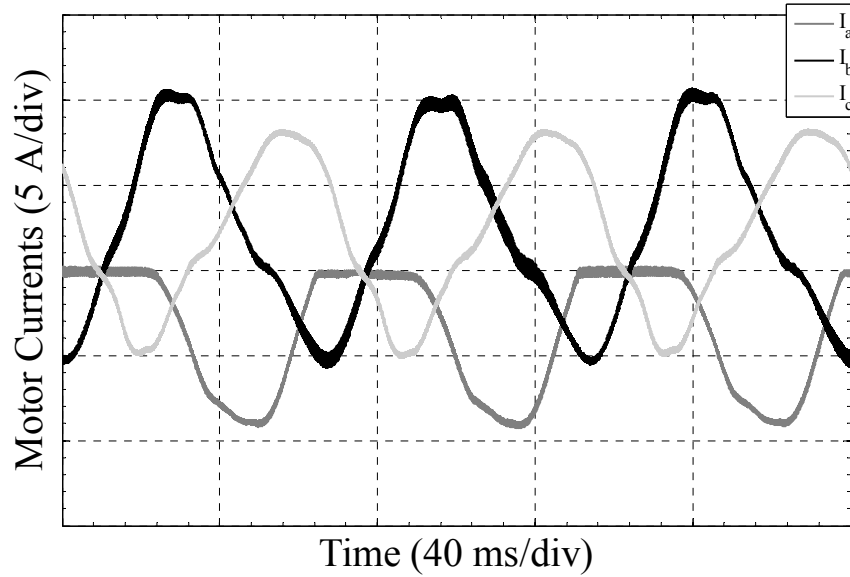
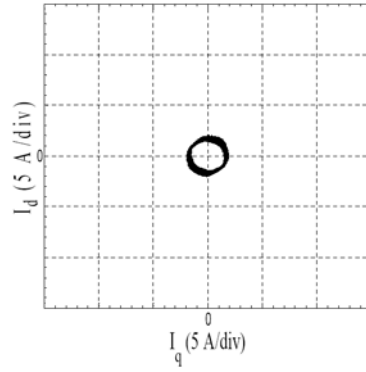


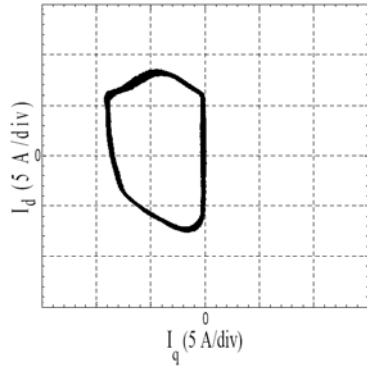
Figure 8.24: Measured three-phase motor current waveforms at 15-Hz output frequency, 25% load condition under an inverter open-circuit switch fault at  $S_l$ .

locations of the faulty transistor switch are plotted and shown here, along with the healthy case, under the condition of 15-Hz output frequency and 25% load, in Figure 8.25. Again, these current space-vector loci match reasonably well with those obtained from the simulation results, as given earlier in Figure 6.20 of Chapter 6.

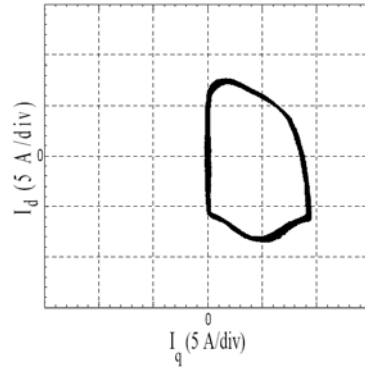
In order to experimentally validate / verify the “limp-home” motor performance using the conceived approach, the experimental work was carried out at 15-Hz output frequency under 25% load ( $\sim 2$  Nm) condition. The test was first run in the healthy PWM drive condition, and thereafter an open-circuit switch fault was deliberately introduced at switch,  $S_l$ . After one second from which the fault had occurred, the “limp-home” strategy was initiated. The test result of the three-phase motor current waveforms demonstrating pre-fault, during fault, and post-fault cases is depicted in Figure 8.26. As one may observe from Figure 8.26, the seamless transition from one case to another is in considerably good agreement with the simulation waveforms in profiles, given in Figure 8.11(a), for the case of 15-Hz output frequency. The differences in the rms current magnitudes of the simulation and test results during pre-fault and post-fault conditions are



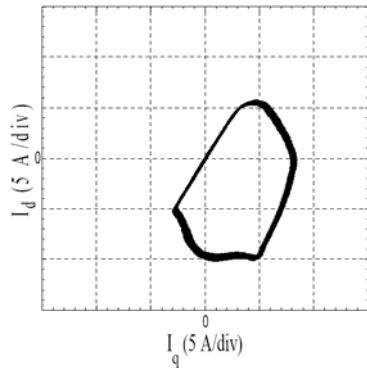
(a) Healthy.



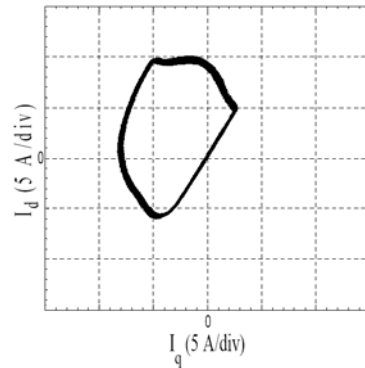
(b) Open-circuit fault at  $S_7$ .



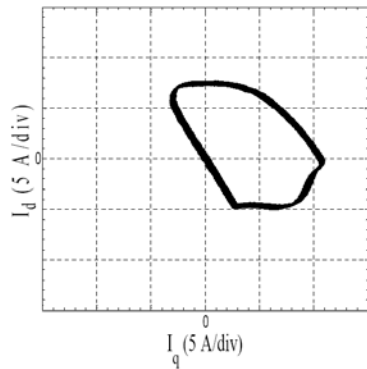
(c) Open-circuit fault at  $S_4$ .



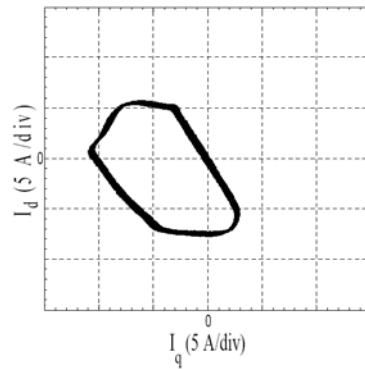
(d) Open-circuit fault at  $S_3$ .



(e) Open-circuit fault at  $S_6$ .



(f) Open-circuit fault at  $S_5$ .



(g) Open-circuit fault at  $S_2$ .

Figure 8.25: Experimental results of current space-vector locus at 15-Hz, 25% load condition.

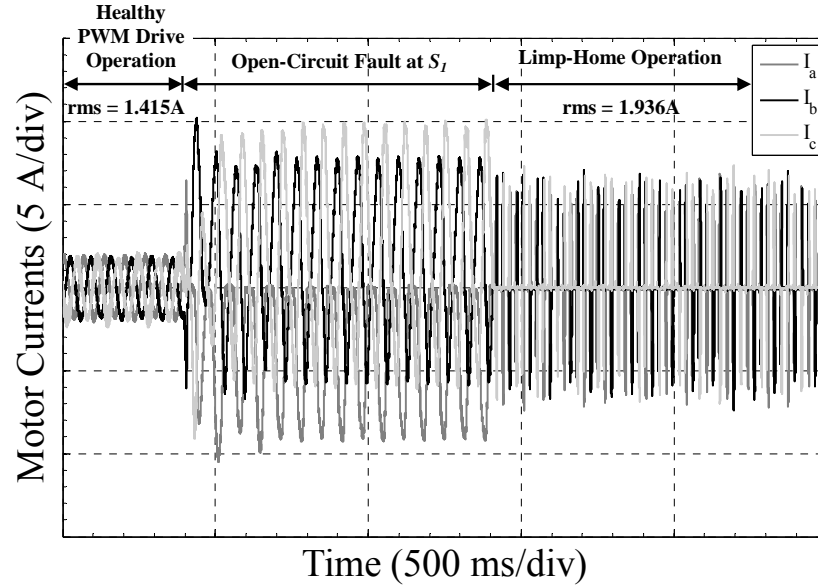


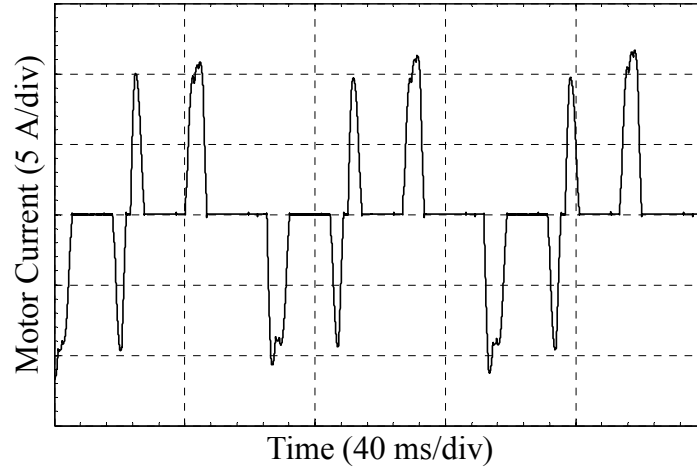
Figure 8.26: “Limp-home” motor performance of measured phase currents at 15-Hz, 25% load condition in the event of an inverter open-circuit switch fault at  $S_7$ .

due to the fact that the simulation was carried out under full-load condition, whereas the test was carried out at 25% load condition.

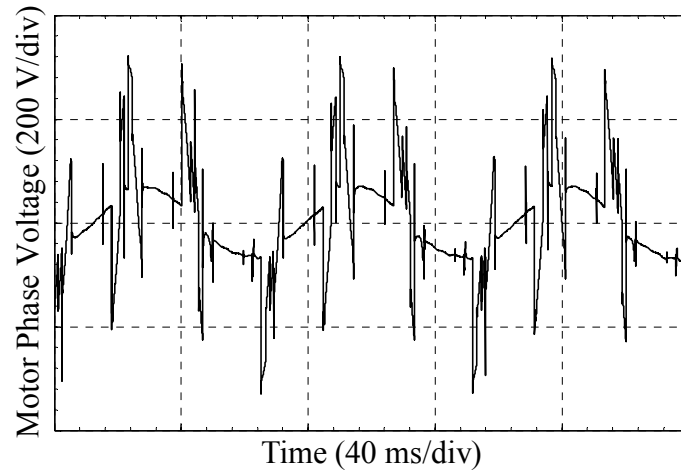
The test results of the *steady-state post-fault* motor performance using the conceived “limp-home” strategy under motor loading conditions at full-load and half-load for the case of 15-Hz ( $N = 4$ ) and 12-Hz ( $N = 5$ ) motor operations are presented next. For the case of 12-Hz motor operation, two phases of the supply mains are manually interchanged in the test setup in order to impress negative-sequence voltages at the input terminals of the SCR bridge. The purpose of this interchange is to ensure that the sequence of the fundamental components of the voltages received at the motor terminals from the output of the SCR bridge shall always possess a positive-sequence to produce the same forward rotation of the motor, as a result of using the present control scheme. The measured waveforms of the motor phase current, voltage, and developed torque for the full-load and half-load conditions are given here in Figure 8.27(a)-(c) and Figure 8.28(a)-(c), respectively. Notice that the developed (airgap) torque illustrated here was acquired implicitly from the measured motor terminal quantities (currents and voltages) using the expression in (5.2) given in Chapter 5 of this dissertation [95]. The measured current waveforms

of Figure 8.27(a) and Figure 8.28(a) have similar shapes to the steady-state portion of the simulation phase current waveforms given earlier in Figure 8.12(a) and Figure 8.13(a), which are repeated here in “zoom” form in Figure 8.29(a) and Figure 8.30(a), for the full-load and half-load cases, respectively. Due to the non-sinusoidal nature of the current waveforms, torque ripple contents are clearly evident from the developed (airgap) torque computed from the experimental readings of the motor terminal operating conditions, which are shown in Figure 8.27(c) and Figure 8.28(c) for the different load cases. The “zoom” forms of the corresponding simulation torque profiles, given earlier in Figure 8.12(b) and Figure 8.13(b), are repeated here in Figure 8.29(b) and Figure 8.30(b), respectively, for comparison purposes.

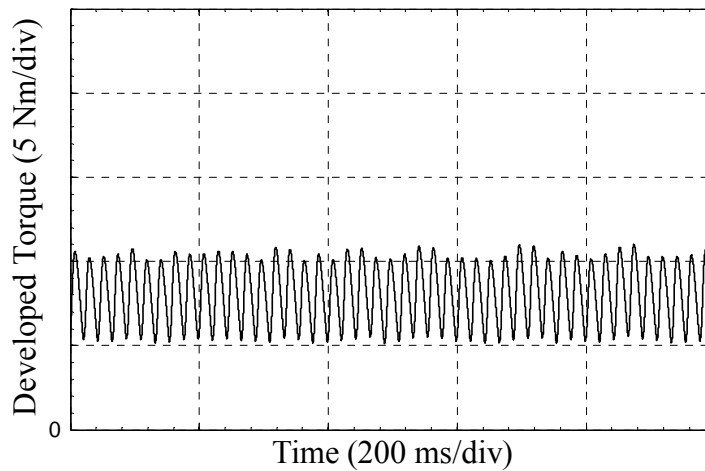
To further demonstrate the performance of the motor using the conceived topology and control strategy, the experimental work was carried out at the commanded output frequency of 12-Hz, the results of which are depicted in Figure 8.31 and Figure 8.32 under full-load and half-load conditions, respectively. Again, the test results match considerably well with the steady-state portions of the simulation waveforms of the motor phase currents and developed torques shown in Figure 8.14(a)-(b) and Figure 8.15(a)-(b), with their corresponding “zoom” forms given in Figure 8.33(a)-(b) and Figure 8.34(a)-(b), under full-load and half-load conditions, respectively. The motor performance in terms of torque ripple (%) and total rms current values for both the simulation and experimental results for the case of the 15-Hz and 12-Hz motor operations under full-load and half-load conditions are summarized in Table 8.6. It can be seen from this table that the simulation results are in fairly good agreement with the experimental test results. Even though the torque ripples are considerably higher at full-load condition, these torque ripples are reduced by about one-half under half-load condition. Furthermore, the motor rms phase currents are also reduced to near their rated value at half-load condition. Hence, this implies that the present approach is most suitable for light motor-load applications. Practical application considerations and opportunities for use of the present design will be further detailed in the forthcoming section.



(a) rms value = 4.297 A

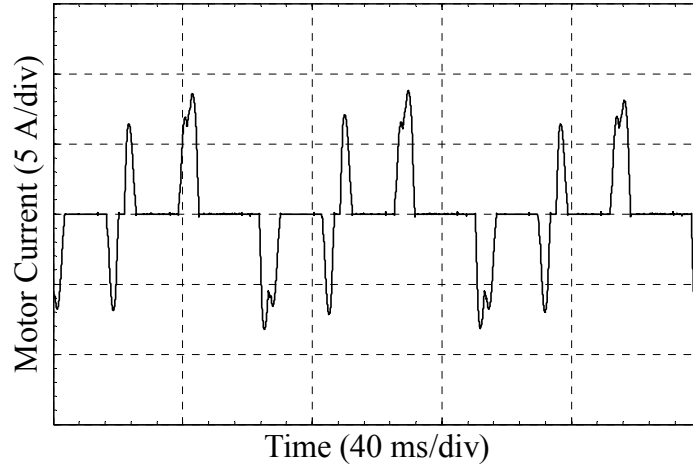


(b) rms value = 90.99 V

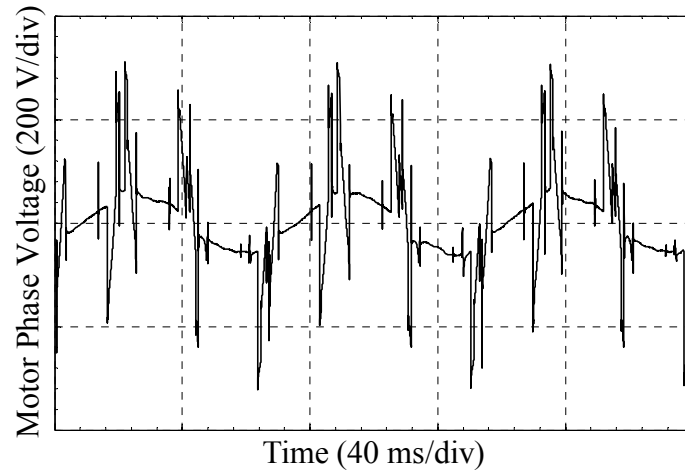


(c) Average torque = 8.099 Nm

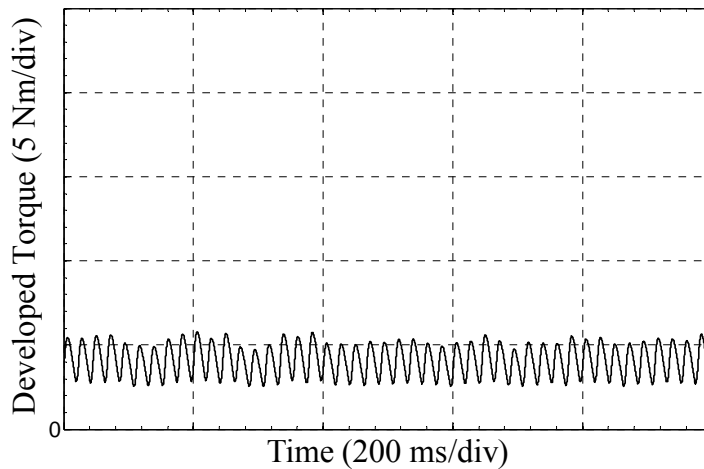
Figure 8.27: Experimental results of post-fault limp-home motor performance for 15-Hz operation at full-load condition. (a) Motor phase current. (b) Motor phase voltage. (c) Motor developed torque.



(a) rms value = 2.934 A

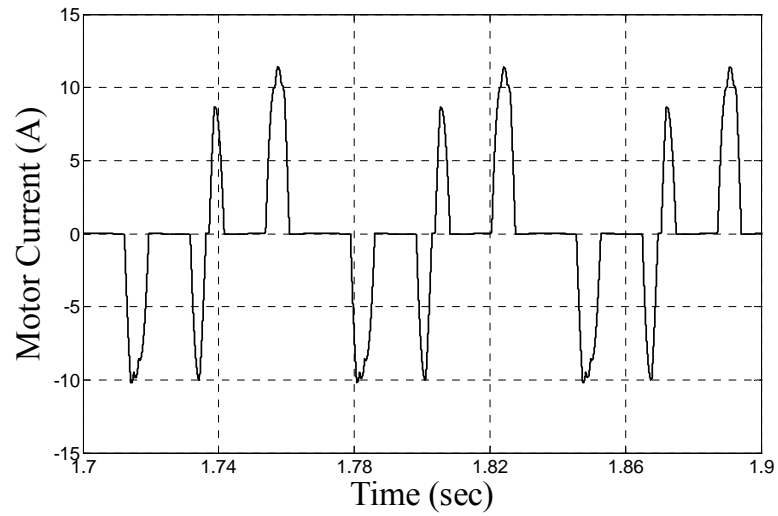


(b) rms value = 75.11 V

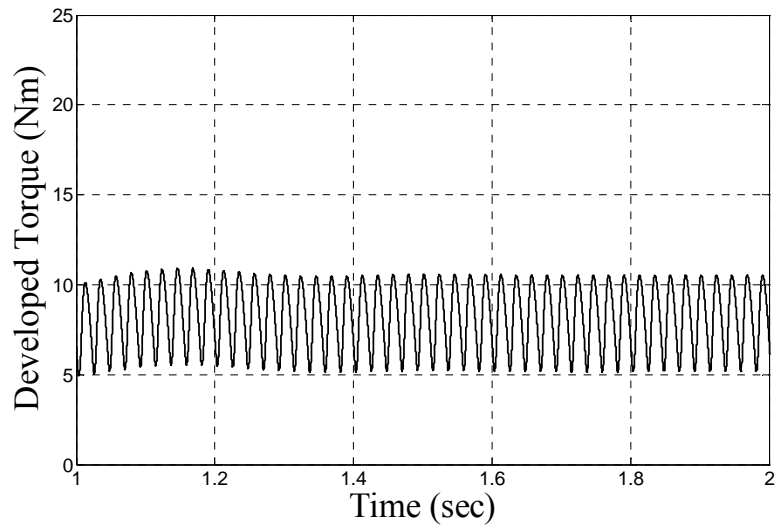


(c) Average torque = 4.101 Nm

Figure 8.28: Experimental results of post-fault limp-home motor performance for 15-Hz operation at half-load condition. (a) Motor phase current. (b) Motor phase voltage. (c) Motor developed torque.

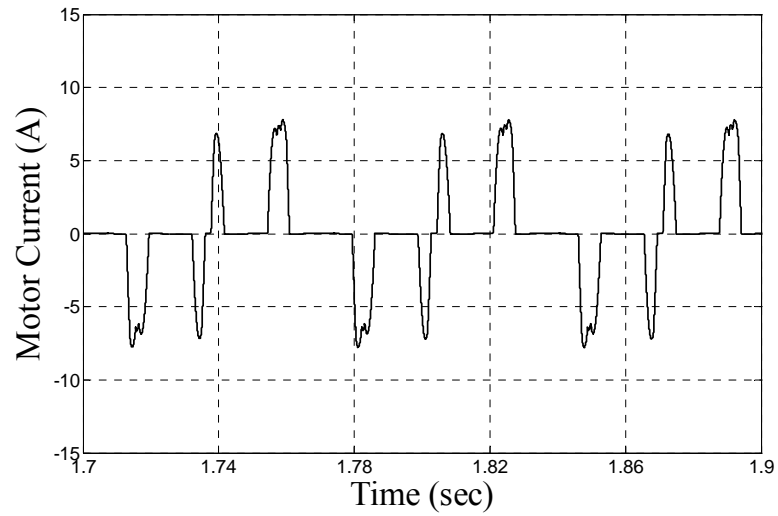


(a) rms value = 4.392 A

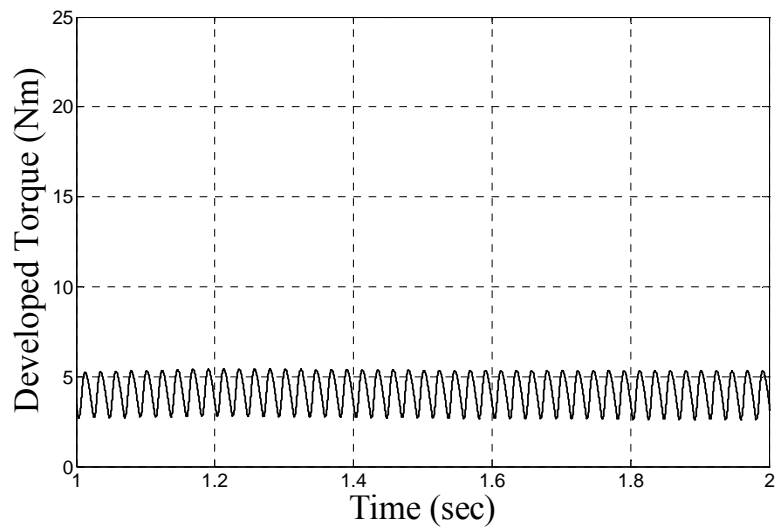


(b) Average torque = 8.169 Nm

Figure 8.29: Steady-state “zoom” form of the simulation results of Figure 8.12 for 15-Hz operation at full-load (8.169 Nm) condition. (a) Motor phase current. (b) Torque.

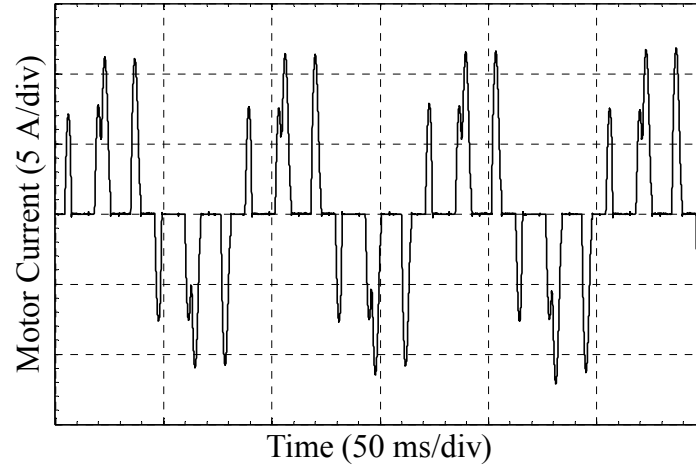


(a) rms value = 3.237 A

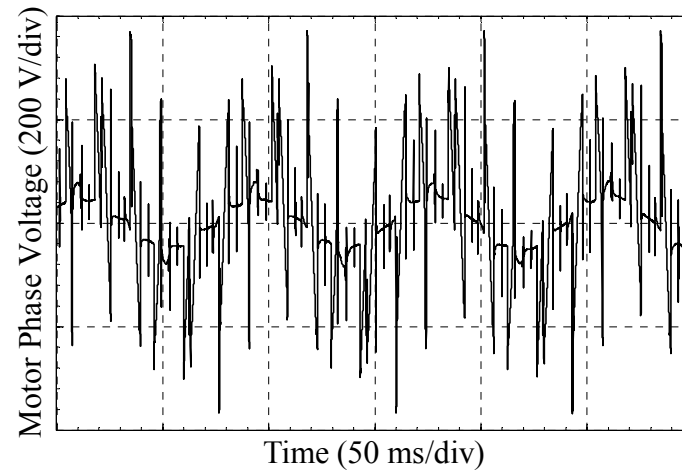


(b) Average torque = 4.084 Nm

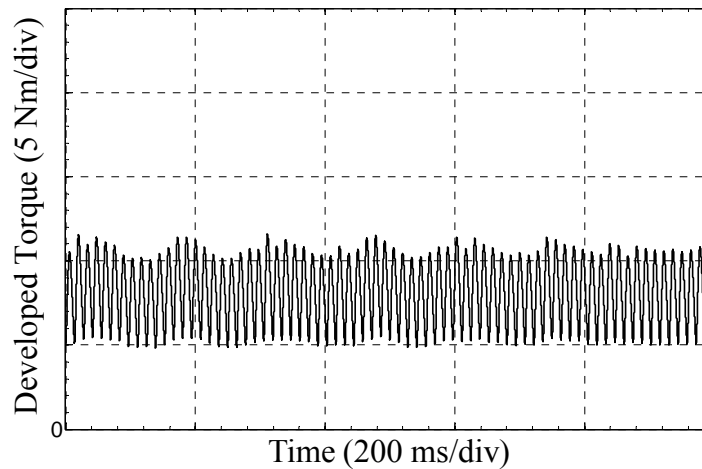
Figure 8.30: Steady-state “zoom” form of the simulation results of Figure 8.13 for 15-Hz operation at half-load (4.084 Nm) condition. (a) Motor phase current. (b) Torque.



(a) rms value = 4.317 A

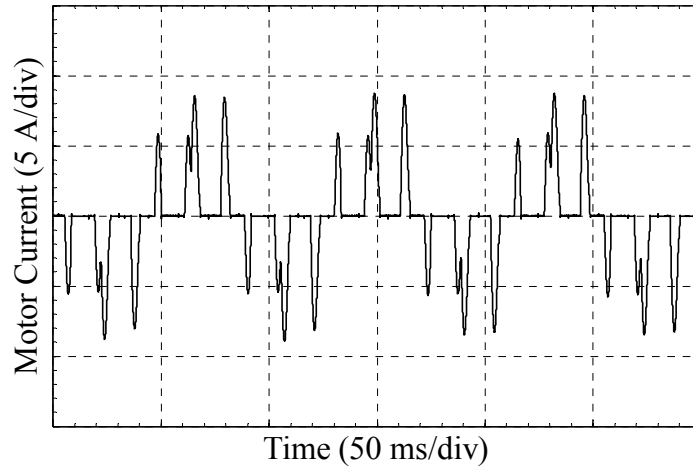


(b) rms value = 101.04 V

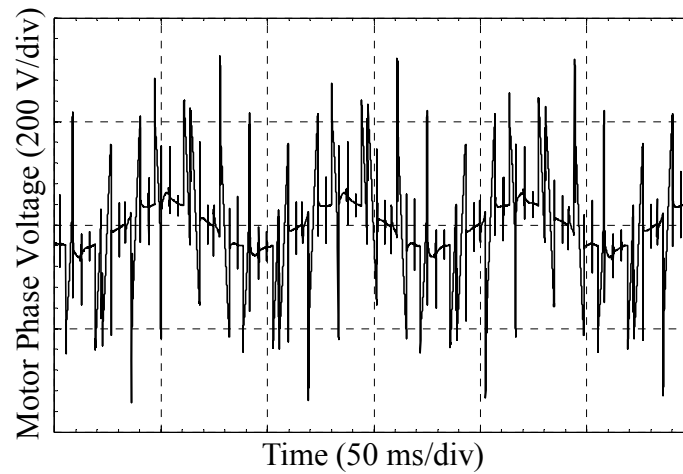


(c) Average torque = 8.211 Nm

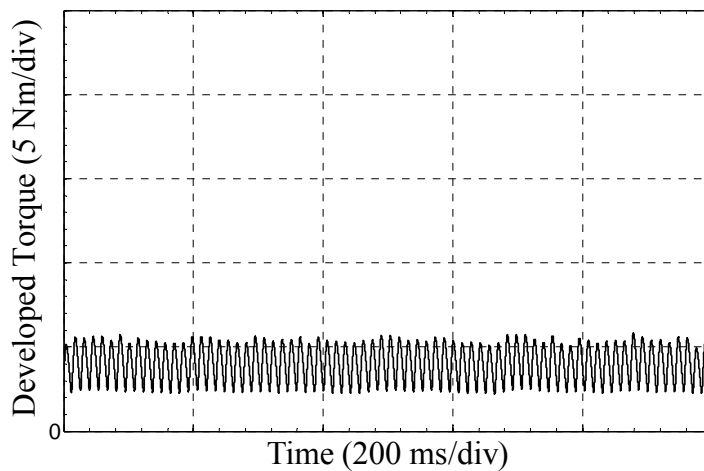
Figure 8.31: Experimental results of post-fault limp-home motor performance for 12-Hz operation at full-load condition. (a) Motor phase current. (b) Motor phase voltage. (c) Motor developed torque.



(a) rms value = 3.032 A

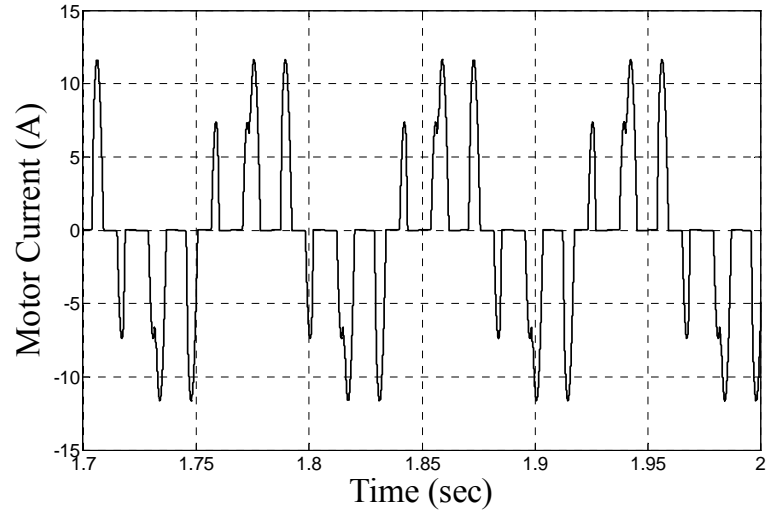


(b) rms value = 76.73 V

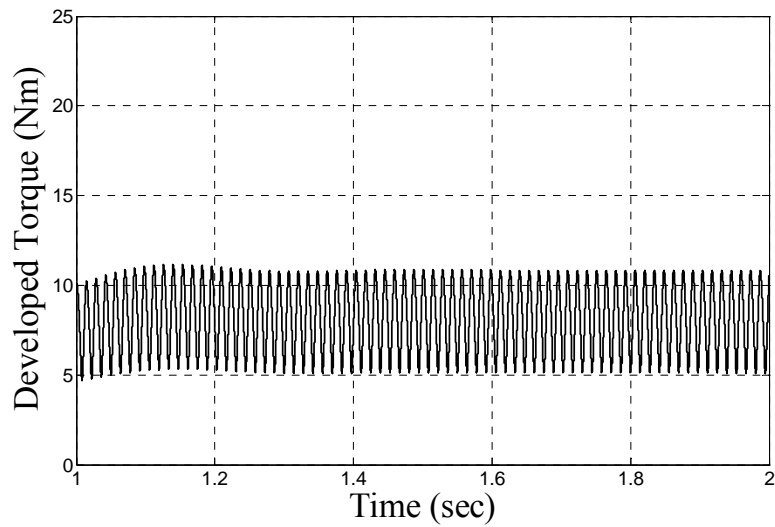


(c) Average torque = 4.054 Nm

Figure 8.32: Experimental results of post-fault limp-home motor performance for 12-Hz operation at half-load condition. (a) Motor phase current. (b) Motor phase voltage. (c) Motor developed torque.

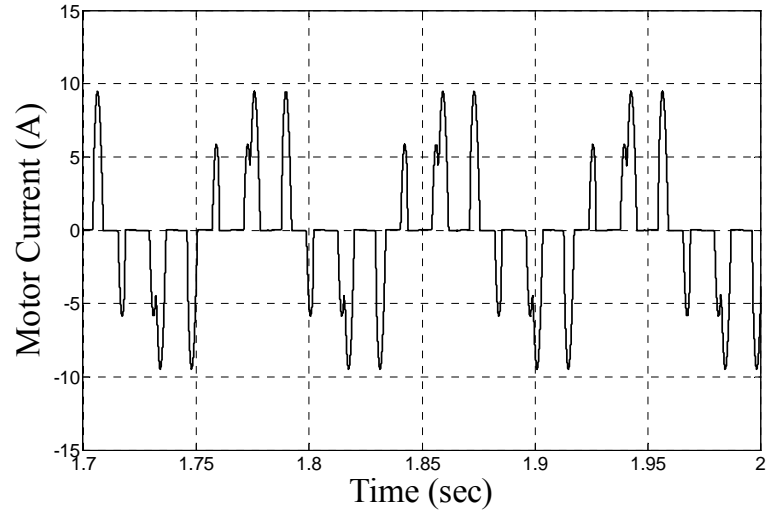


(a) rms value = 4.504 A

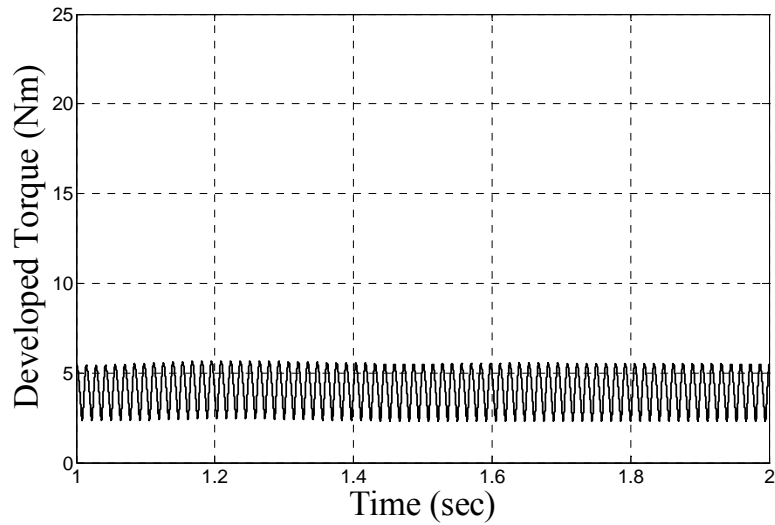


(b) Average torque = 8.169 Nm

Figure 8.33: Steady-state “zoom” form of the simulation results of Figure 8.14 for 12-Hz operation at full-load (8.169 Nm) condition. (a) Motor phase current. (b) Torque.



(a) rms value = 3.339 A



(b) Average torque = 4.084 Nm

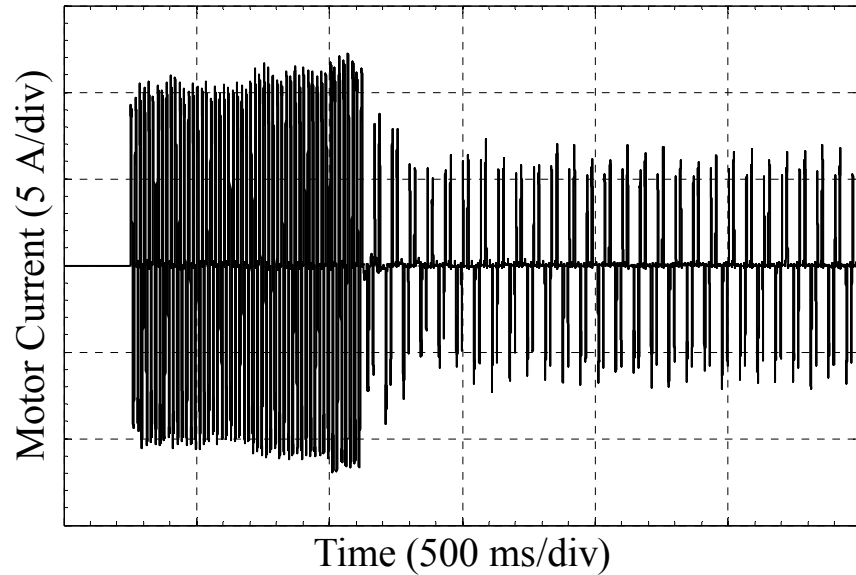
Figure 8.34: Steady-state “zoom” form of the simulation results of Figure 8.15 for 12-Hz operation at half-load (4.084 Nm) condition. (a) Motor phase current. (b) Torque.

Table 8.6: Comparisons between simulation and experimental results for the case of 15-Hz and 12-Hz motor operations.

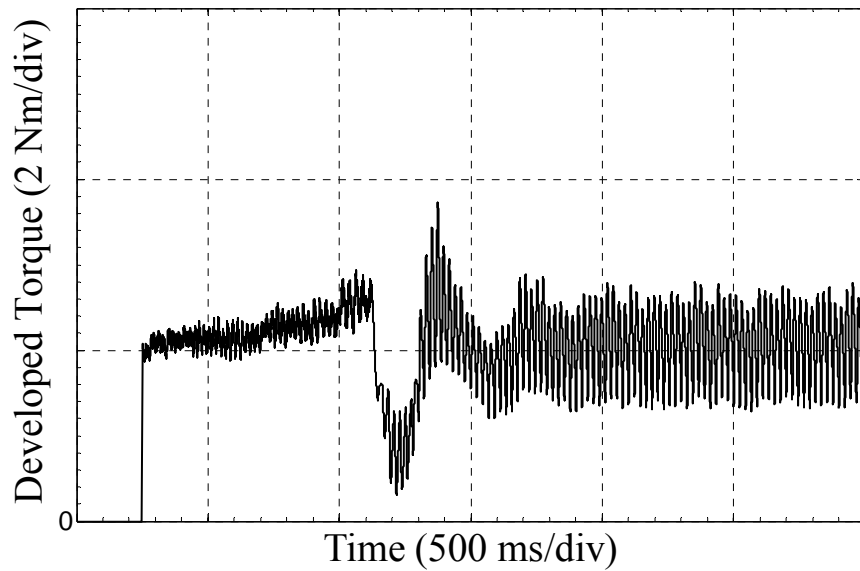
Commanded Output Frequency	Simulation		Experiment	
	Current (rms)	Torque Ripple	Current (rms)	Torque Ripple
	(Amps)	(% of Full-Load Torque)	(Amps)	(% of Full-Load Torque)
<b>Full-Load</b>				
<b>15-Hz</b>	4.392	65.11 %	4.297	64.49 %
<b>12-Hz</b>	4.504	70.14 %	4.317	73.11 %
<b>Half-Load</b>				
<b>15-Hz</b>	3.237	33.48 %	2.934	30.90 %
<b>12-Hz</b>	3.339	39.61 %	3.032	36.29 %

### 8.3.3 Starting Performance of the Conceived Topology

The starting performance of the motor from standstill when using the conceived topology was also verified / validated experimentally. The test results of the starting transient of the motor phase current and the motor developed torque are presented in Figure 8.35(a) and (b), respectively, for the case of 15-Hz operation at 25% load ( $\sim 2$  Nm) condition. The motor was first energized using the open-loop symmetrical-triggering soft-starting control, before being driven using the conceived discrete-frequency control scheme to achieve the desired speed that corresponds to the commanded output frequency. As one can observe from Figure 8.35(a), the motor experiences reduced starting inrush currents during starting, which consequently result in reduced starting torque pulsations, see Figure 8.35(b). Also, one can notice from the torque profile that there is a slight transient before the motor reaches the steady-state condition. It is evident from the experimental results that the conceived topology clearly demonstrates smooth starting performance, which in a sense emulates the starting behavior of a PWM drive which utilizes volts per hertz control.



(a)



(b)

Figure 8.35: Experimental results of soft-starting performance of present topology for 15-Hz operation at 25% load ( $\sim 2$  Nm) condition. (a) Motor phase current. (b) Motor developed torque.

## 8.4 Application Considerations and Opportunities

In many industrial applications, the average load factor of electric motors is estimated to be less than 60% [101], [103]. In other words, these electric motors only operate up to 60% of their rated conditions. In fact, in some industrial applications, the average load factor can be as low as 25% [103]. This means that the motor selected for any specific application is usually oversized. Meanwhile, there are numerous applications in which low-speed operations are required, such as vehicle and ship propulsion systems, cement mills, mine hoists, rolling mills and the like. Based on these low-speed applications and the fact that oversized motors are usually selected according to industrial standard, the present conceived approach is a good candidate for these types of low-speed applications at partial motor-loading conditions. This is due to the fact that the present approach, which is designed for low-speed operations, exhibits moderately low torque ripples/pulsations at partial motor-loading conditions which makes it a perfect fit for “limp-home” operations in such types of applications. Evidence supporting this claim is presented in the following analysis.

An investigation was performed to study the nature of the torque ripple/pulsation resulting from the conceived approach with regard to the motor frequency and the effect of the load torque level. The motor torque ripple in percentage representation of the full-load motor torque was obtained through simulation that was carried out under different output motor frequencies at different load levels, the results of which are depicted in Figure 8.36. Examination of Figure 8.36 clearly shows that the torque ripple is dramatically reduced with decreasing load level. In applications where a load factor of only 25% is required [103], the torque pulsation resulting from this study can be seen to be less than 25% of the full-load torque, which may be tolerable for “limp-home” operation for a certain period of time. One can also notice from the figure that the torque pulsation increases as the motor output frequency decreases. This is due to the fact that the

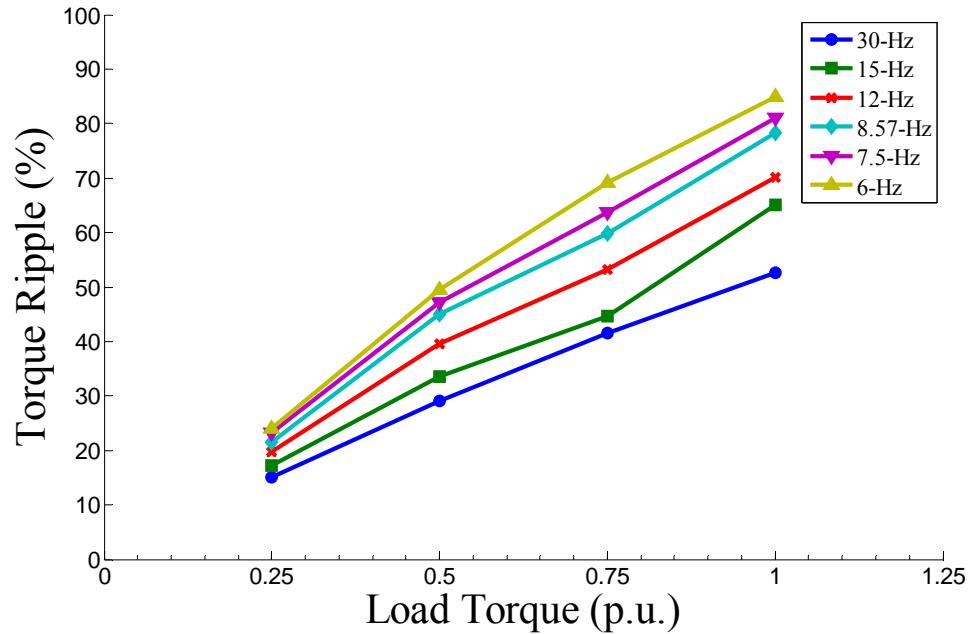


Figure 8.36: Simulation results of torque-ripple percentage of full-load torque at different load levels.

motor's moment of inertia, which behaves as a low-pass filter, filters out the higher-order torque harmonics. This reduction of higher-order torque harmonics is extremely evident when the motor is operating at a higher frequency. Similar study with regard to motor torque ripple/pulsation calculation was also carried out using the experimental test results that were presented earlier. The torque ripple/pulsation calculation from the test results, along with those from the corresponding simulation results acquired from Figure 8.36, for the cases of 30-Hz, 15-Hz, and 12-Hz motor operations are illustrated in Figure 8.37. It is evident that one can see a considerably good agreement between the computed torque ripple/pulsation in percentage between the experimental test and simulation data.

Meanwhile, the rms phase currents of the test and simulation results under the foregoing conditions were plotted in Figure 8.38 in per-unit representation of its rated value as a function of the load torque. From Figure 8.38, one can see a reasonable degree of agreement in the rms phase current values between the test and simulation results. Further examination of Figure 8.38 also

indicates that the rms phase currents of the motor are within or below its rated current value when the motor is operating at less than 50% of its rated condition. Therefore, thermal issues are not of a major concern when the motor is operating at low-load condition using the conceived approach. Hence, the curves presented in Figure 8.36 through Figure 8.38 support the earlier claim in which it is safe to operate the motor at low-load conditions using the present conceived torque-speed control approach with acceptable motor performance for reasonably limited periods of “limp-home” operating time.

It has been reported earlier in [104]-[107] that it is a well-known fact that induction machines could exhibit a region of instability when supplied by an adjustable-speed PWM drive. The range of unstable operating frequencies is typically between 10-Hz and 35-Hz for a 60-Hz rated frequency, and the size and range of this unstable region is dependent upon the variation of motor parameters under operating conditions, motor inertia, switching dead-time, PWM carrier frequency, rectifier-inverter link parameter variations, and the load [104]-[107]. This instability was observed during low-frequency motor-drive operation, and translates itself into undesirable oscillations in the motor phase currents, which leads to an oscillating torque. Therefore, it appears that the present conceived control approach could provide a better “limp-home” solution than previously reported methods proposed by other researchers [38]-[59], when low-speed operation constitutes the main concern. In addition, the present approach does not suffer from drawbacks such as the need for accessibility to a motor neutral, larger size dc link capacitors, or higher dc bus voltage. Another “upside” element of the conceived approach is its potential use for mitigating other drive-related faults that can potentially occur in the diode-rectifier bridge or the dc-link of the drive because of the fact that this approach bypasses the entire drive system, which is not possible with the previous methods given in [38]-[59]. Therefore, the conceived approach presents itself as a low-cost solution for prolonging the life of the motor-drive system in the event of a fault in the drive, allowing the motor to function under limited torque-speed control means.

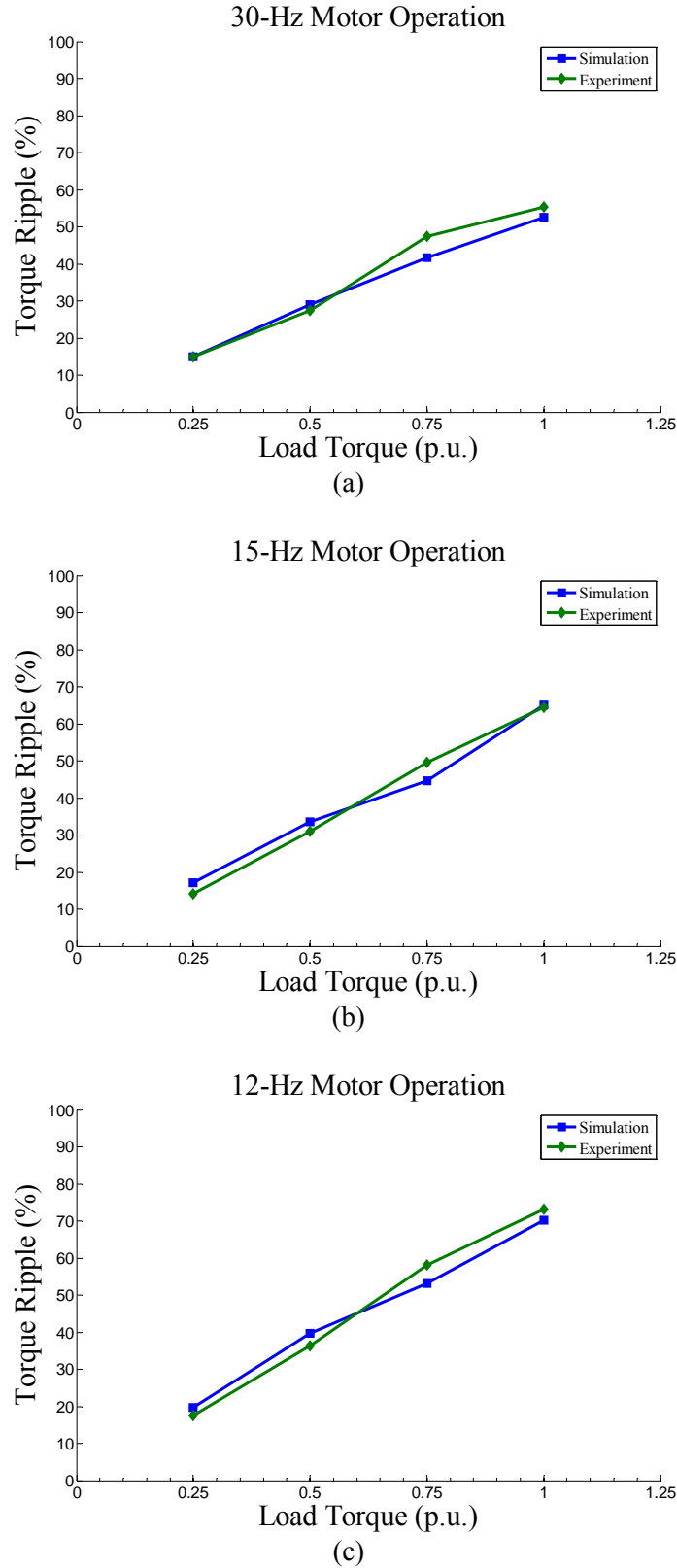


Figure 8.37: Torque-ripple percentage of full-load torque versus load torque at different output motor frequencies. (a) 30-Hz operation. (b) 15-Hz operation. (c) 12-Hz operation.

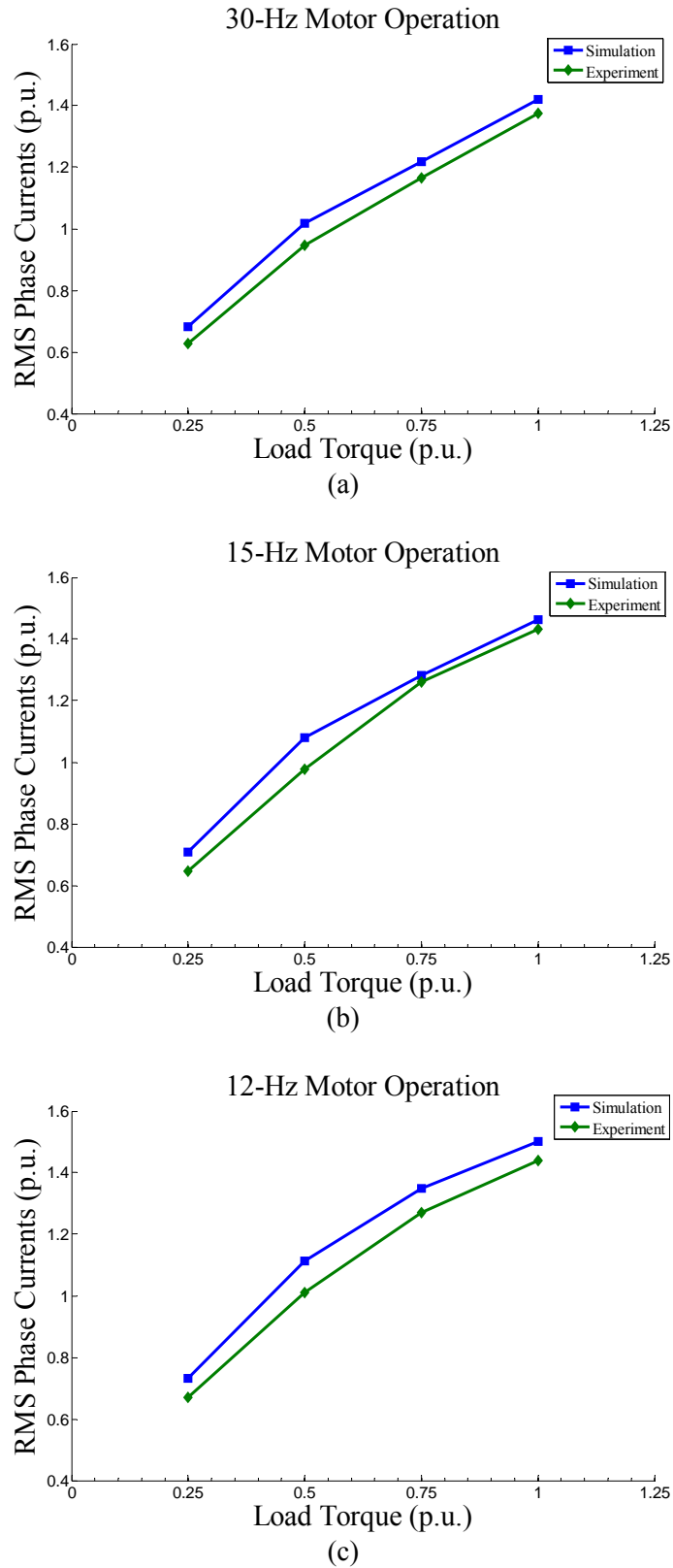


Figure 8.38: RMS value of motor phase currents versus load torque at different output motor frequencies. (a) 30-Hz operation. (b) 15-Hz operation. (c) 12-Hz operation.

## 8.5 Summary

In this chapter, the simulation and experimental test results of the conceived quasi-cycloconverter-based “limp-home” strategy under inverter switch faults have been presented. The presented simulation and test results have demonstrated the soundness and validity of the conceived approach for practical use. Practical application considerations and opportunities for use of the conceived design were also investigated. The results of the study suggest that the conceived approach is best suited for partial motor-loading operating conditions, which is normally the case for many practical industrial applications in which the motors are usually oversized. Accordingly, this investigator perceives that there is still a place in real practice for the present topology to “stand out” as a potential means of mitigating any drive-related faults, based on its low-cost requirements as well as other merits that were previously mentioned and discussed above.

## CHAPTER 9

---

---

# CONCLUSIONS, CONTRIBUTIONS, AND SUGGESTED FUTURE WORK

---

---

### 9.1 Summary and Conclusions

In this chapter, the summary of the accomplishments of this work and main contributions of this dissertation are reviewed. This is followed by recommendations and suggestions regarding possible directions of future research topics.

In Chapter 1, the background and motivation of this work have been described with emphasis on the importance of incorporating fault tolerant or “limp-home” capability for prolonging/extending the life of an ac motor-drive system. A literature survey of the previous research work performed by other investigators has been presented. Based on a simple functionality categorization of the “limp-home” strategies of three-phase ac motor-drive systems, some of the strategies have been briefly reviewed for some of the categories, with greater emphasis on strategies that have been applied on the standard three-phase, six-switch inverter type of adjustable-speed PWM drives. Such type of drives is the focal research element in this work. Through this survey, it has been shown that the existing “limp-home” methods have their own merits and drawbacks. The merits are the ability to maintain rated motor performance, while

the drawbacks are the essential system cost increase for maintaining continuous motor operation in the event of an inverter switch fault. Also, these methods are only applicable for mitigating inverter-type switch fault. To the knowledge of this investigator, no prior work has been done on both the investigation of the effect of SCR switch fault of soft starters on motor performance and the development of their corresponding remedial strategies during the occurrence of such fault. Hence, this opens a door to this investigator to pursue his research area in the development of low-cost fault-tolerant solutions for both the soft starters and adjustable-speed PWM drives. This chapter is then concluded with the main objectives and contributions that this work brings about, followed by the organization of this dissertation.

In Chapter 2, an analytical closed-form solution describing the transient performance of a motor-soft starter system under healthy and faulty conditions has been presented. The types of faults under study are the SCR open-circuit and short-circuit switch faults occurring only in one phase of the soft starter system. Analytical closed-form expressions for the non-sinusoidal phase voltages impressed upon the motor windings under both healthy and faulty soft starter operating conditions have been derived. According to these closed-form voltage expressions, the well-known T-equivalent circuit motor model was utilized to obtain the motor phase currents for the fundamental voltage term and each subsequent harmonic voltage term. Superposition was then applied to express the resulting motor phase currents in a Fourier series form. The closed-form analytical studies demonstrate that the short-circuit SCR fault produces undesired fault response on motor performance with unbalanced, high starting currents which accordingly result in high starting torque pulsations. On the contrary, it is shown here that the open-circuit SCR switch fault results in no starting torque from the motor. Hence it constitutes a total failure of motor starting. On the other hand, it does not expose the soft starter elements to the severity of motor current unbalances and the severity of motor torque pulsations. Evidently, the use of the conventional open-loop symmetrical-triggering control in a two-phase switching mode under faulty condition

contribute to detrimental impacts on motor performance which result in disruption of normal operation of the motor-load system during soft starting. With a better understanding of these fault impacts, a remedial strategy was then developed to minimize the negative effects resulting from such faults during normal soft starting operation.

In Chapter 3, the above mentioned remedial strategy consisting of a simple low-cost fault tolerant solution capable of mitigating SCR open-circuit and short-circuit switch faults for soft starters has been presented. Minimum hardware modifications are required for the existing commercially available soft starter in order for the fault tolerant operation to be possible. It should be emphasized that such essential modifications do not significantly increase the cost and size of the existing system. One of the essential changes involves adding a set of three-phase voltage transducers on the motor end of the soft starter for acquiring the motor terminal voltages needed for fault tolerant control purposes. The second hardware modification involves the replacement of the existing 3-pole synchronously-controlled modular bypass contactor with a set of individually-controlled 1-pole contactors for all three phases. These contactors are used for fault isolation purposes in such a way that the soft starter can switch into a two-phase switching mode in the event of an SCR switch fault occurring in any one of the phases. As for the conceived two-phase control approach, two types of feedback control loops were adopted and utilized concurrently. Namely, these are the voltage and current feedback loops, respectively. The voltage feedback control is responsible for the starting acceleration of the motor, while the current feedback loop is responsible for mitigating the unbalanced effects of the starting currents under thyristor switch fault condition. In fact, by adopting the proposed control technique, a low-cost soft starter with only two-phase switching mode can be developed and produced in the market for consumers at a lower cost with reasonably good performance, as compared to the existing three-phase soft starter products.

In addition, small-signal modeling of the motor-soft starter controller system was developed. More specifically, the open-loop and closed-loop transfer functions of the voltage and current control feedback loop systems were derived. The main thrust of this small-signal modeling approach was to design the PI regulators in the voltage and current loops so as to achieve the desired bandwidth to render a good dynamic and fast transient response. Upon designing the PI controllers, the entire system was simulated under large-signal conditions to evaluate the stability and response of the controllers.

In Chapter 4, the accuracy of the closed-form analytical results from Chapter 2 was verified versus the corresponding simulation results. It has been shown that the analytical results are in good correlation with the simulation results, which raises confidence in the fidelity and value of the analytical approach. Such efforts provide an alternative means of analyzing the transient performance of the motor in lieu of using the elaborate simulation approach. In the same chapter, the motor performance under three different control cases, namely, three-phase open-loop, two-phase open-loop, and the newly conceived method with two-phase closed-loop controls were simulated and compared. The newly conceived fault tolerant method with resilient control has demonstrated reduced starting inrush currents, and consequently reduced starting torque pulsations under SCR fault in one phase of the soft starter, as compared to the two-phase open-loop control case. These promising results demonstrate the feasibility of the conceived strategy for improving the reliability of an industrial-type three-phase soft starter system at a modest cost increase.

In Chapter 5, the measured results during the soft starting transients under healthy and short-circuit switch fault conditions were compared with the analytical and simulation results presented earlier in Chapters 2 and 4, respectively. The objective was to verify the accuracy of the analytical and detailed simulation work that was carried out earlier in Chapters 2 and 4, respectively. The resulting comparisons indicate good agreements between the test, simulation,

and analytical waveforms. In the same chapter, the motor performance obtained from both the experiment and simulation, under 3-phase open-loop, 2-phase open-loop, as well as the newly conceived 2-phase closed-loop controls were compared. Overall, the experimental test results match reasonably well with the simulation results. It is evident from both the test and simulation results given in this and earlier chapters that the present newly conceived fault tolerant soft starter has demonstrated its efficacy and practicability to be retrofitted into industrial-type three-phase soft starter systems.

In Chapter 6, the focus was redirected to analyzing the impact of various inverter faults, more specifically transistor/switch failures, on motor performance using a combination of detailed time-domain simulations and analytical derivations based on averaged switching function concepts. The two distinct types of inverter failure modes investigated herein are: (1) a transistor short-circuit switch fault, and (2) a transistor open-circuit switch fault. In the event of a short-circuit switch fault, the complementary switch of the same inverter leg has to be instantaneously turned-off upon the on-set of such a fault in order to avoid the catastrophic event of a dc link shoot-through situation. The resulting inverter circuit reconfiguration was accordingly investigated. It was found from the study that the short-circuit switch fault produces a severe fault impact on the motor performance. A dc (unidirectional) offset of high magnitude is imposed on the motor current of each phase, which results in a braking torque that causes the motor speed to drop sharply. In addition, huge torque pulsations are also generated as a result of such an event. Moreover, the presence of a high magnitude circulating dc (unidirectional) current in the motor windings will eventually lead to insulation failure if the motor is left unattended. As a consequence, such a fault will require immediate shut-down of the motor-drive system in order to prevent secondary failures.

On the other hand, it was demonstrated here that an open-circuit switch fault will still permit the operation of the motor-drive system, but at a much inferior performance due to the presence

of significant torque pulsations. It was found from this specific simulation case study that the peak-to-peak torque pulsations were computed to be about 190% of the post-fault average torque for the case-study 2-hp motor. This clearly indicates that the operation of the motor-drive system, after the fault occurrence, can only be extended for a short period of time. This is in order to avoid damages to the mechanical portions of the motor-drive system. Analytical studies were also presented in this work to determine the causes of these torque pulsations. In the opinion of this investigator, a detailed understanding of these fault impacts on machine performance is essential when one proceeds to the design stage of developing remedial strategies for such types of faults.

In Chapter 7, a fault-tolerant strategy for remedy of inverter faults based on a quasi-cycloconverter-based topology and control was presented as a potential solution. This strategy was conceived with the goal of overcoming the negative impact of inverter switch fault on motor performance, hence extending the life of a motor-drive system for a period of time before maintenance is called upon. The newly conceived approach requires minimum hardware modifications at a modest cost to the conventional off-the-shelf three-phase PWM drive, as compared to the existing topologies proposed by others. These modifications require only the addition of electronic components such as SCR switches and fast-acting fuses. Due to its circuit configuration and control principles, the present fault-tolerant approach is suitable for “limp-home” low-speed motor applications such as in vehicle and propulsion systems. In addition, the present approach does not suffer from drawbacks such as the need for accessibility to a motor neutral, larger size dc-link capacitors, or higher dc-bus voltages. Another “upside” element of the newly conceived approach is its potential use for mitigating other drive-related faults that can potentially occur in the diode-rectifier bridge or the dc-link of the drive because of the fact that this approach bypasses the entire drive system, provided that such faults can be safely isolated. Furthermore, the present topology can also function as a soft-starter during the post-fault operation in situations in which the motor has to be brought to a stop before starting-up again

from standstill, as a result of the malfunction of the drive. The effect of soft-starting the motor reduces any high inrush currents and consequently high starting torque pulsations. The major downside of the present approach is the presence of pulsating torques due to the non-sinusoidal nature of the resulting motor current waveforms. The simulation results of the motor performance using this newly conceived topology, as well as the corresponding experimental results are addressed next.

In Chapter 8, the simulation and experimental test results of the newly conceived quasi-cycloconverter-based “limp-home” strategy under inverter switch faults have been presented. The simulation and test results presented have demonstrated the soundness and validity of this conceived approach for practical use. Practical application considerations and opportunities for use of the newly conceived design were also investigated. The results of this study suggest that this conceived approach is best suited for partial motor-loading operating conditions, which is normally the case for many practical industrial applications in which the motors are usually oversized. The reason for choosing to operate under such conditions is the resulting reduced torque pulsations that the motor will experience when supplied by the newly conceived topology at light-load conditions. Accordingly, this investigator perceives that there is still a place in real practice for the present topology to “stand out” as a potential means of mitigating any drive-related faults, based on its low-cost requirements, as well as the fact that this approach is unencumbered by the drawbacks that other methods experience.

In light of the above, it is to be understood that within the scope of this work regarding mitigating inverter switch faults, the present technology may be applied to applications other than as specifically described herein. In such other practical applications, one may envision the present topology as a high-performance soft-starter and a moderate-performance drive. Such technology is well-suited for users who are unwilling to bear the burden of the high price of a typical PWM

drive, and still hope to achieve with reduced requirements the performance of variable speed operation at a lower affordable cost.

## 9.2 Contributions of this Work

The contributions made in this dissertation can be summarized as follows:

1. A closed-form analytical solution has been conceived to investigate the transient performance of induction motors during soft starting when experiencing thyristor/SCR switch faults. The two distinct types of failure modes under investigation in this work are: (1) short-circuit SCR fault, and (2) open-circuit SCR fault, which occur only in one phase of the soft starter.
2. A low-cost fault-tolerant approach capable of mitigating SCR open-circuit and short-circuit switch faults for soft starters has been conceived. The conceived approach can be easily retrofitted into the existing commercially-available soft starters with only minimum hardware modifications. Hence, this makes the conceived approach an attractive and feasible means as a potential fault-tolerant solution.
3. An investigation of the impact of inverter switch failure on machine performance was carried out using the averaged switching function modeling concept. Such an approach provides a constructive analytical understanding of the extent of these fault effects. Meanwhile, detailed time-domain simulation studies, in parallel with the analytical approach, were also employed to solidify the conclusive outcomes resulting from this study. The two distinct types of inverter transistor switch failure modes under investigation in this work are: (1) a transistor short-circuit switch fault, and (2) a transistor open-circuit switch fault.

4. A low-cost fault-tolerant strategy, based on a quasi-cycloconverter-based topology and control, as a potential solution for overcoming the negative impact of an inverter switch fault on motor performance was newly conceived. The newly conceived approach requires minimum hardware modifications at a modest cost to the conventional off-the-shelf three-phase PWM drive, as compared to the existing fault-tolerant topologies proposed by others. In fact, the present approach is also capable of mitigating other drive-related faults that can potentially occur in the diode-rectifier bridge or the dc-link of the drive because of the fact that this approach bypasses the entire drive system, provided that such faults can be safely isolated.

### 9.3 Future Investigations

Despite the progress made in this dissertation as well as in the earlier research work by others, fault tolerant operation is still a topic of ongoing investigation. Significant work remains to identify the most effective approaches at an affordable cost without jeopardizing the desirable motor performance. Hence, feasibility, performance, and cost issues are the deciding factors in the adoption of the various methods conceived thus far for real practical use. Accordingly, one of the possible topics for future research is the continuing effort to develop more advanced “limp-home” strategies for various types of faults that can potentially occur in the drive. This includes faults in the rectifier bridges, capacitor links, inverter bridges, sensors, control boards, or even the input and output terminals of a drive. Meanwhile, one should not neglect the type of fault that can occur at the motor side, such as the commonly occurring stator winding fault. Hence, another possible research area is the development of fault mitigation strategies for stator winding faults in a three-phase / poly-phase induction motor. The main challenge here is to devise a method that can reduce the induced current in the shorted loop, while still providing acceptable motor

performance. This can be achieved through either modifying the control algorithm or redesigning the winding layout of the machine to minimize the mutual flux couplings between each stator phase, thereby reducing the induced emf in the shorted loop.

As for the soft starter, one of the research areas that this investigator is very keen on developing further in the near future is to apply the newly conceived closed-loop control approach to the IGBT-based soft starter. Recently, IGBT-based soft starters have been introduced but no investigative effort has been spent on this type of topology. This investigator believes that IGBT-based soft starters will demonstrate a better performance than traditional SCR-based soft starters, especially in the case of heavy loads or high-inertia loads. Lastly, “limp-home” or “life-extending” operation of ac motor-drive systems is a very challenging issue which will continue to receive a lot of attention in the coming years.

---

---

## BIBLIOGRAPHY

---

---

- [1] T. Funaki, "High power electronics in Japan – backgrounds and applications," *IEEE Power Electronics Society Newsletter*, Vol. 18, No. 4, pp. 13-15, 2006.
- [2] H. Rehaoulia and M. Poloujadoff, "Transient behavior of the resultant airgap field during run-up of an induction motor," *IEEE Transactions on Energy Conversion*, Vol. EC-1, pp. 92-98, Dec. 1986.
- [3] A. H. Bonnett and G. C. Soukup, "Cause and analysis of stator and rotor failures in three-phase squirrel-cage induction motors," *IEEE Transactions on Industry Applications*, Vol. 28, pp. 921-937, Jul./Aug. 1992.
- [4] W. Shepherd and J. Stanway, "The polyphase induction motor control by firing angle adjustment of silicon controlled rectifiers," *IEEE International Convention Record*, pp. 135-154, 1964.
- [5] W. Shepherd, "On the analysis of the three-phase induction motor with voltage control by thyristor switching," *IEEE Transactions on Industry and General Applications*, Vol. IGA-4, pp. 304-311, May/Jun. 1968.
- [6] D. W. Novotny and A. F. Fath, "Analysis of induction machines controlled by series connected semiconductor switches," *IEEE Transactions on Power Apparatus and Systems*, Vol. PAS-87, pp. 597-605, Feb. 1968.
- [7] T. A. Lipo, "The analysis of induction motors with voltage control by symmetrically triggered thyristors," *IEEE Transactions on Power Apparatus and Systems*, Vol. PAS-9, No. 2, pp. 515-525, Mar./Apr. 1971.

- [8] W. McMurray, "A comparative study of symmetrical three-phase circuits for phase-controlled AC motor drives," *IEEE Transactions on Industry Applications*, Vol. IA-10, pp. 403-411, 1974.
- [9] S. Rahman, *Thyristor and diode controlled variable voltage drives for three-phase induction motors*, Ph.D. Thesis, University of Bradford, UK, 1975.
- [10] S. S. Murthy and G. J. Berg, "A new approach to dynamic modeling and transient analysis of SCR controlled induction motors," *IEEE Transactions on Power Apparatus and Systems*, Vol. PAS-101, pp. 219-229, Sept. 1982.
- [11] G. Nath and G. J. Berg, "Transient analysis of three-phase SCR controlled induction motors," *IEEE Transactions on Industry Applications*, Vol. IA-17, No. 2, pp. 133-142, Mar./Apr. 1981.
- [12] T. M. Rowan and T. A. Lipo, "A quantitative analysis of induction motor performance improvement by SCR voltage control," *IEEE Transactions on Industry Applications*, Vol. IA-19, No. 4, pp. 545-553, Jul./Aug. 1983.
- [13] L. X. Le and G. J. Berg, "Steady-state performance analysis of SCR controlled induction motors: A closed form solution," *IEEE Transactions on Power Apparatus and Systems*, Vol. PAS-103, pp. 601-611, Mar. 1984.
- [14] N. H. Malik, S. M. E. Haque, and W. Shepherd, "Analysis and performance of three-phase phase-controlled thyristor AC voltage controllers," *IEEE Transactions on Industrial Electronics*, Vol. IE-32, No. 3, pp. 192-9, Aug. 1985.
- [15] F. M. H. Khater and D. W. Novotny, "An equivalent circuit model for phase back voltage control of AC machines," *IEEE Transactions on Industry Applications*, Vol. IA-22, pp. 835-841, Sept./Oct. 1986.
- [16] S. A. Hamed and B. J. Chalmers, "Analysis of variable-voltage thyristor controlled induction motors," *IEE Proceedings of Electric Power Applications*, Vol. 137, No. 3, pp. 184-193, May 1990.
- [17] F. M. Bruce, R. J. Graefe, A. Lutz, and M. D. Panlener, "Reduced-voltage starting of squirrel-cage induction motors," *IEEE Transactions on Industry Applications*, Vol. IA-20, pp. 46-55, Jan./Feb. 1984.

- [18] J. Bowerfind and S. J. Campbell, "Application of solid-state AC motor starters in the pulp and paper industry," *IEEE Transactions on Industry Applications*, Vol. IA-22, pp. 109-114, Jan./Feb. 1986.
- [19] W. Deleroi, J. B. Woudstra, and A. A. Fahim, "Analysis and application of three-phase induction motor voltage controller with improved transient performance," *IEEE Transactions on Industry Applications*, Vol. 25, No. 2, pp. 280-286, Mar./Apr. 1989.
- [20] F. Blaabjerg, J. K. Pedersen, S. Rise, H. H. Hansen, and A. M. Trzynadlowski, "Can soft-starters help save energy?," *IEEE Industry Applications Magazine*, Vol. 3, No. 5, pp. 56-66, Sept./Oct. 1997.
- [21] V. V. Sastry, M. R. Prasad, and T. V. Sivakumar, "Optimal soft starting of voltage-controller-fed IM drive based on voltage across thyristor," *IEEE Transactions on Power Electronics*, Vol. 12, Issue 6, pp. 1041-1051, Nov. 1997.
- [22] W. J. Lukitsch, "Soft start vs AC drives – Understand the differences," *Conference Proceedings of IEEE Textile, Fiber and Film Industry*, pp. 1-5, May 1999.
- [23] D. Gritter, D. Wang, and T. G. Habetler, "Soft starter inside delta motor modeling and its control," *Conference Proceedings of Industry Applications Society Annual Meeting*, Vol. 2, pp. 1137-1141, Oct. 2000.
- [24] J. A. Kay, R. H. Paes, J. G. Seggewiss, and R. G. Ellis, "Methods for the control of large medium-voltage motors: application considerations and guidelines," *IEEE Transactions on Industry Applications*, Vol. 36, Issue 6, pp. 1688-1696, Nov./Dec. 2000.
- [25] R. F. McElveen, and M. K. Toney, "Starting high-inertia loads," *IEEE Transactions on Industry Applications*, Vol. 37, Issue 1, pp. 137-144, Jan./Feb. 2001.
- [26] G. Zenginobuz, I. Cadirci, M. Ermis, and C. Barlak, "Soft starting of large induction motors at constant current with minimized starting torque pulsations," *IEEE Transactions on Industry Applications*, Vol. 37, Issue 5, pp. 1334-1347, Sep./Oct. 2001.
- [27] G. Zenginobuz, I. Cadirci, M. Ermis, and C. Barlak, "Performance optimization of induction motors during voltage-controlled soft starting," *IEEE Transactions on Energy Conversion*, Vol. 19, No. 2, pp. 278-288, Jun. 2004.
- [28] A. Gastli and M. M. Ahmed, "ANN-based soft starting of voltage-controlled-fed IM drive system," *IEEE Transactions on Energy Conversion*, Vol. 20, Issue 3, pp. 497-503, Sep. 2005.

- [29] M. G. Solveson, B. Mirafzal, and N. A. O. Demerdash, "Soft-started induction motor modeling and heating issues for different starting profiles using a flux linkage ABC frame of reference," *IEEE Transactions on Industry Applications*, Vol. 42, No. 4, pp. 973-982, Jul./Aug. 2006.
- [30] K. Sundareswaran, and B. M. Jos, "Development and analysis of novel soft-starter/energy-saver topology for delta-connected induction motors," *IEE Proceedings in Electric Power Applications*, Vol. 152, Issue 4, pp. 922-932, Jul. 2005.
- [31] Cutler-Hammer/Eaton Corporation, *IT. S811 Soft Starter User Manual*, <http://www.eatonelectrical.com>.
- [32] Allen-Bradley/Rockwell Automation, *SMC-Flex™ Bulletin 150 User Manual*, <http://www.ab.com>.
- [33] Benschaw-Advanced Controls & Drives, *Redistart Solid State Starter Software Manual MX Control*, <http://www.benschaw.com>.
- [34] O. V. Thorsen and M. Dalva, "A survey of the reliability with an analysis of faults on variable frequency drives in industry," *European Conference on Power Electronics and Applications*, Sevilla, pp. 1033-1038, 1995.
- [35] Military Handbook 217F, *Reliability Prediction of Electronic Equipment*, Feb. 28, 1995.
- [36] B. A. Welchko, T. A. Lipo, T. M. Jahns, and S. E. Schulz, "Fault tolerant three-phase ac motor drive topologies: A comparison of features, cost, and limitations," *IEEE Transactions on Power Electronics*, Vol. 19, No. 4, pp. 1108-1116, Jul. 2004.
- [37] T. M. Jahns, "Improved reliability in solid-state ac drives by means of multiple independent phase-drive units," *IEEE Transactions on Industry Applications*, Vol. IA-16, No. 3, pp. 321-331, May/June. 1980.
- [38] R. Spée and A. K. Wallace, "Remedial strategies for brushless dc drive failures," *IEEE Transactions on Industry Applications*, Vol. 26, No. 2, pp. 259-266, Mar./Apr. 1990.
- [39] J. R. Fu and T. A. Lipo, "Disturbance-free operation of a multiphase current-regulated motor drive with an open phase," *IEEE Transactions on Industry Applications*, Vol. 30, No. 5, pp. 1267-1274, Sept./Oct. 1994.
- [40] S. Bolognani, M. Zordan, and M. Zigliotto, "Experimental fault-tolerant control of a PMSM drive," *IEEE Transactions on Industrial Electronics*, Vol. 47, No. 5, pp. 1134-1141, Oct. 2000.

- [41] N. Bianchi, S. Bolognani, M. Zigliotto, and M. Zordan, "Innovative remedial strategies for inverter faults in IPM synchronous motor drives," *IEEE Transactions on Energy Conversion*, Vol. 18, No. 2, pp. 306-314, Jun. 2003.
- [42] M. B. de R. Corrêa, C. B. Jacobina, E. R. C. da Silva, and A. M. N. Lima, "An induction motor drive system with improved fault tolerance," *IEEE Transactions on Industry Applications*, Vol. 37, No. 3, pp. 873-879, May/Jun. 2001.
- [43] C. B. Jacobina, R. L. de A. Ribeiro, A. M. N. Lima, and E. R. C. da Silva, "Fault-tolerant reversible AC motor drive system," *IEEE Transactions on Industry Applications*, Vol. 39, No. 4, pp. 1077-1084, Jul./Aug. 2003.
- [44] R. L. de A. Ribeiro, C. B. Jacobina, E. R. C. da Silva, and A. M. N. Lima, "Fault-tolerant voltage-fed PWM inverter ac motor drive systems," *IEEE Transactions on Industrial Electronics*, Vol. 51, No. 2, pp. 439-446, Apr. 2004.
- [45] T. Elch-Heb and J. P. Hautier, "Remedial strategies for inverter ac motor system at the occurrence of a transistor drive fault," *Conference Proceedings in EPE*, pp. 4-286 – 4-291, 1991.
- [46] D. Kastha and B. K. Bose, "Fault mode single-phase operation of a variable frequency induction motor drive and improvement of pulsating torque characteristics," *IEEE Transactions on Industrial Electronics*, Vol. 41, No. 4, pp. 426-433, Aug. 1994.
- [47] D. Kastha and B. K. Bose, "On-line search based pulsating torque compensation of a fault mode single-phase variable frequency induction motor drive," *IEEE Transactions on Industry Applications*, Vol. 31, No. 4, pp. 802-811, Jul./Aug. 1995.
- [48] D. Kastha and A. K. Majumdar, "An improved starting strategy for voltage-source inverter fed three phase induction motor drives under inverter fault conditions," *IEEE Transactions on Power Electronics*, Vol. 15, No. 4, pp. 726-732, Jul. 2000.
- [49] T. H. Liu, J. R. Fu, and T. A. Lipo, "A strategy for improving reliability of field-oriented controlled induction motor drives," *IEEE Transactions on Industry Applications*, Vol. 29, No. 5, pp. 910-918, Sept./Oct. 1993.
- [50] T. Elch-Heb and J. P. Hautier, "Remedial strategy for inverter-induction machine system faults using two-phase operation," *Conference Proceedings in European Conference on Power Electronics and Applications*, Vol. 5, pp. 151-156, Sep. 1993.

- [51] J. R. Fu and T. A. Lipo, "A strategy to isolate the switching device fault of a current regulated motor drive," *Conference Proceedings in IEEE Industry Applications Society Annual Meeting*, Vol. 2, pp. 1015-1020, Oct. 1993.
- [52] H. W. Van Der Broeck and J. D. Van Wyk, "A comparative investigation of a three-phase induction machine drive with a component minimized voltage-fed inverter under different control options," *IEEE Transactions on Industry Applications*, Vol. IA-20, No. 2, pp. 309-320, Mar./Apr. 1984.
- [53] G. A. Covic and G. L., "DC link imbalance compensation in four-switch inverter ac motor drives," *Electronics Letters*, Vol. 33, No. 13, pp. 1101-1102, Jun. 1997.
- [54] G. L. Peters, G. A. Covic, and J. T. Boys, "Eliminating output distortion in four-switch inverters with three-phase loads," *IEE Proceedings in Electric Power Applications*, Vol. 145, No. 4, pp. 326-332, Jul. 1998.
- [55] F. Blaabjerg, S. Freysson, H.-H. Hansen, and S. Hansen, "A new optimized space-vector modulation strategy for a component-minimized voltage source inverter," *IEEE Transactions on Power Electronics*, Vol. 12, No. 4, pp. 704-714, Jul. 1997.
- [56] F. Blaabjerg, D. O. Neacsu, and J. K. Pedersen, "Adaptive SVM to compensated dc-link voltage ripple for four-switch three-phase voltage-source inverters," *IEEE Transactions on Power Electronics*, Vol. 14, No. 4, pp. 743-752, Jul. 1999.
- [57] M. B. de R. Corrêa, C. B. Jacobina, E. R. C. da Silva, and A. M. N. Lima, "A general PWM strategy for four-switch three-phase inverters," *IEEE Transactions on Power Electronics*, Vol. 21, No. 6, pp. 1618-1627, Nov. 2006.
- [58] A. M. S. Mendes and A. J. M. Cardoso, "Fault-tolerant operating strategies applied to three-phase induction-motor drives," *IEEE Transactions on Industrial Electronics*, Vol. 53, No. 6, pp. 1807-1817, Dec. 2006.
- [59] A. M. S. Mendes, X. M. Lopez-Fernandez, and A. J. M. Cardoso, "Thermal behavior of a three-phase induction motor fed by a fault-tolerant voltage source inverter," *IEEE Transactions on Industry Applications*, Vol. 43, No. 3, pp. 724-730, May/June. 2007.
- [60] P. N. Enjeti and A. Rahman, "A new single-phase to three-phase converter with active input current shaping for low cost ac motor drives," *IEEE Transactions on Industry Applications*, Vol. 29, No. 4, pp. 806-813, Jul./Aug. 1993.

- [61] Chingchi Chen, D. M. Divan, D.M., and D. W. Novotny, "A hybrid inverter / cycloconverter-based variable-speed three-phase induction motor drive for single-phase inputs," *IEEE Transactions on Industry Applications*, Vol. 31, No.3, pp. 630-635, May/Jun. 1995.
- [62] Gi-Taek Kim and T. A. Lipo, T.A, "VSI-PWM rectifier/inverter system with a reduced switch count," *IEEE Transactions on Industry Applications*, Vol. 32, No. 6, pp. 1331-1337, Nov./Dec. 1996.
- [63] C. B. Jacobina, C.B.; M. B. d. R. Correa, E. R. C. da Silva, and A. M. N. Lima, "Induction motor drive system for low-power applications," *IEEE Transactions on Industry Applications*, Vol. 35, No. 1, pp. 52-61, Jan./Feb. 1999.
- [64] B. K. Lee, B. Fahimi, and M. Ehsani, "Overview of reduced parts converter topologies for AC motor drives," *Conference Proceedings in 32nd Annual Power Electronics Specialists Conference*, Vol. 4, pp. 2019-2024, 17-21 Jun. 2001.
- [65] B. A. Welchko, and T. A. Lipo, "A novel variable-frequency three-phase induction motor drive system using only three controlled switches," *IEEE Transactions on Industry Applications*, Vol. 37, No. 6, pp. 1739-1745, Nov./Dec. 2001.
- [66] C. B. Jacobina, M. B. d. R. Correa, A. M. N. Lima, and E. R. C. da Silva, "AC motor drive systems with a reduced-switch-count converter," *IEEE Transactions on Industry Applications*, Vol. 39, No. 5, pp. 1333-1342, Sep./Oct. 2003.
- [67] C. B. Jacobina, I. S. De Freitas, E. R. C. da Silva, A. M. N. Lima, and R. L. A. Ribeiro, "Reduced switch count dc-link ac-ac five-leg converter," *IEEE Transactions on Power Electronics*, Vol. 21, No. 5, pp. 1301-1310, Sep. 2006.
- [68] Dong-Choon Lee and Young-Sin Kim, "Control of single-phase-to-three-phase AC/DC/AC PWM converters for induction motor drives," *IEEE Transactions on Industrial Electronics*, Vol. 54, No. 2, pp. 797-804, Apr. 2007.
- [69] C. B. Jacobina, I. S. de Freitas, and A. M. N. Lima, "DC-link three-phase-to-three-phase four-leg converters," *IEEE Transactions on Industrial Electronics*, Vol. 54, No. 4, pp. 1953-1961, Aug. 2007.
- [70] C. B. Jacobina, E. C. dos Santos, E. R. C. da Silva, M. B. d. R. Correa, and A. M. N. Lima, and T. M. Oliveira, "Reduced switch count multiple three-phase ac machine drive

- Systems,” *IEEE Transactions on Power Electronics*, Vol. 23, No. 2, pp. 966-976, Mar. 2008.
- [71] S. Kwak and H. A. Toliyat, “Fault-tolerant topologies and switching function algorithms for three-phase matrix converter based ac motor drives against open and short phase failures,” *Conference Proceedings in IEEE International Electric Machines & Drives Conference*, Vol. 1, pp. 886-891, May 2007.
- [72] S. Kwak, H. A. Toliyat, “An approach to fault-tolerant three-phase matrix converter drives,” *IEEE Transaction on Energy Conversion*, Vol. 22, No. 4, pp. 855-863, Dec. 2007.
- [73] S. Kwak and H. A. Toliyat, “Remedial switching function approach to improve reliability for ac-ac converters,” *IEEE Transaction on Energy Conversion*, Vol. 22, No. 2, pp. 541-543, Jun. 2007.
- [74] S. Li and L. Xu, “Strategies of fault tolerant operation for three-level PWM inverters,” *IEEE Transactions on Power Electronics*, Vol. 21, No. 4, pp. 933-940, Jul. 2006.
- [75] S. Khomfoi and L. M. Tolbert, “Fault diagnosis and reconfiguration for multilevel inverter drive using AI-based techniques,” *IEEE Transactions on Industrial Electronics*, Vol. 54, No. 6, pp. 2954-2968, Dec. 2007.
- [76] K. S. Smith, L. Ran, and J. Penman, “Real-time detection of intermittent misfiring in a voltage-fed PWM inverter induction-motor drive,” *IEEE Transactions on Industry Applications*, Vol. 44, pp. 468-476, Jul./Aug. 1997.
- [77] R. Peugeot, S. Courtine, and J. P. Rognon, “Fault detection and isolation on a pwm inverter by knowledge-based model,” *IEEE Transactions on Industry Applications*, Vol. 34, pp. 1318-1326, Nov./Dec. 1998.
- [78] R. L. de A. Ribeiro, C. B. Jacobina, E. R. C. da Silva, and A. M. N. Lima, “Fault detection of open-switch damage in voltage-fed PWM motor drive systems,” *IEEE Transactions on Power Electronics*, Vol. 18, No. 2, pp. 587-593, Mar. 2003.
- [79] L. Zhang, I. B. Aris, and L. N. Hulley, “A knowledge-based system for on-line fault diagnosis of power inverter circuits for ac machines,” *European Power Electronics Conference*, pp. 3.334-3.339, 1995.
- [80] A. M. S. Mendes and A. J. Marques Cardoso, “Fault diagnosis in a rectifier-inverter system used in variable speed ac drives by the average current park’s vector approach,” *European Power Electronics Conference*, pp. 1-9, 1999.

- [81] K. Debebe, V. Rajagopalan, and T. S. Sankar, "Expert systems for fault diagnosis of VSI fed drives," *Proceedings of IEEE Conference on Industry Applications*, pp. 368-373, 1991.
- [82] P. J. Chrzan and R. Szczesny, "Fault diagnosis of voltage fed inverter for induction motor drive," *IEEE International Symposium in Industrial Electronics*, pp. 1011-1016, 1996.
- [83] D. Kastha and B. K. Bose, "Investigation of fault modes of voltage-fed inverter system for induction motor drive," *IEEE Transactions on Industry Applications*, Vol. 30, No. 4, pp. 1028- 038, Jul./Aug. 1994.
- [84] N. Mohan, T. M. Undeland, and W. P. Robbins, *Power Electronics -Converters, Applications, and Design*, John Wiley & Sons, Inc., 2<sup>nd</sup> Edition, 1995.
- [85] A. Lahyani, P. Venet, G. Grellet, and P.-J. Viverge, "Failure prediction of electrolytic capacitors during operation of a switchmode power supply," *IEEE Transactions on Power Electronics*, Vol. 13, No. 6, pp. 1199-1207, Nov. 1998.
- [86] B. A. Welchko, J. Wai, T. M. Jahns, and T. A. Lipo, "Magnet-flux-nulling control of interior PM machine drives for improved steady-state response to short-circuit faults," *IEEE Transactions on Industry Applications*, Vol. 42, No. 1, pp. 113-120, Jan./Feb. 2006.
- [87] P. C. Krause, O. Wasynczuk, and S. D. Sudhoff, *Analysis of Electric Machinery and Drive Systems*, John Wiley & Sons, Inc., 2<sup>nd</sup> Edition, 2002.
- [88] A. E. Fitzgerald, C. Kingsley, Jr, S. D. Umans, *Electric Machinery*, McGraw-Hill, 6<sup>th</sup> Edition, 2003.
- [89] P. Vas, *Vector Control of AC Machines*, Oxford University Press, 1990.
- [90] B. C. Kuo, *Automatic Control Systems*, Prentice-Hall, Inc., 5<sup>th</sup> Edition, 1987.
- [91] The MathWorks, Inc., *Matlab-Simulink*, version 7.1, <http://www.mathworks.com>.
- [92] Texas Instruments, *TMS320F281X*, C2000 Family, <http://www.ti.com>.
- [93] A. V. Oppenheim, R. W. Schaffer, and J. R. Buck, *Discrete-Time Signal Processing*, Prentice-Hall, Inc., 2<sup>nd</sup> Edition, 1999.
- [94] National Instruments, *Data Acquisition (DAQ) Hardware*, <http://www.ni.com>.
- [95] J. S. Hsu, "Monitoring of defects in induction motors through air-gap torque observation," *IEEE Transactions on Industry Applications*, Vol. 31, No. 5, pp. 1016-1021, Sept./Oct. 1995.

- [96] R. S. Chokhawala, J. Catt, and L. Kiraly, "A discussion on IGBT short-circuit behavior and fault protection schemes," *IEEE Transactions on Industry Applications*, Vol. 31, No. 2, pp. 256-263, Mar./Apr. 1995.
- [97] A. Bhalla, S. Shekhawat, J. Gladish, J. Yedinak, and G. Dolny, "IGBT behavior during desat detection and short circuit fault protection," *Conference Proceedings in 10th International Symposium on Power Semiconductor Devices and ICs*, ISPSD 98, pp. 245-248, Jun. 1998.
- [98] P. Wood, *Switching Power Converters*, Van Nostrand Reinhold Company, 1981.
- [99] B. R. Pelly, *Thyristor Phase-Controlled Converters and Cycloconverters – Operation, Control, and Performance*, Wiley-Interscience, John Wiley & Sons, Inc., 1971.
- [100] R. E. Best, *Phase-Locked Loops – Design, Simulation, and Applications*, McGraw-Hill, 4<sup>th</sup> Edition, 1999.
- [101] H. Stemmler, "High-power industrial drives," *Proceedings of the IEEE*, Vol. 82, No. 8, pp. 1266-1286, Aug. 1994.
- [102] J. O. Pontt, J. P. Rodriguez, J. C. Rebolledo, K. Tischler, and N. Becker, "Operation of High-Power Cycloconverter-Fed Gearless Drives Under Abnormal Conditions," *IEEE Transactions on Industry Applications*, Vol. 43, No. 3, pp. 814-820, May/June. 2007.
- [103] F. J. T. E. Ferreira, and A. T. de Almeida, "Novel multflux level, three-phase, squirrel-cage induction motor for efficiency and power factor maximization," *IEEE Transactions on Energy Conversion*, Vol. 23, No. 1, pp. 101-109, Mar. 2008.
- [104] R. H. Nelson, T. A. Lipo, and P. C. Krause, "Stability analysis of a symmetrical induction machine," *IEEE Transactions on Power Apparatus and Systems*, Vol. PAS-88, No. 11, pp. 1710-1717, Nov. 1969.
- [105] Y. Murai, I. Hosono, and Y. Tsunehiro, "On stability of PWM inverter fed induction motor," *IEEJ Transactions*, Vol. 105-B, No. 5, pp. 467-474, May 1985.
- [106] T. H. Chin, "Instability of variable frequency induction motor drives fed from voltage source inverters," *Conference Proceedings of the 1985 Annual Meeting on IEEE Industry Applications*, pp. 704-709, 1985.
- [107] R. Ueda, T. Sonoda, and S. Takata, "Experimental results and their simplified analysis on instability problems in PWM inverter induction motor drives," *IEEE Transactions on Industry Applications*, Vol. 25, No. 1, Part 1, pp. 86-95, Jan./Feb. 1989.

# APPENDIX A

---

---

## DESIGNS AND SPECIFICATIONS OF HARDWARE PROTOTYPE

---

---

### A.1 Introduction

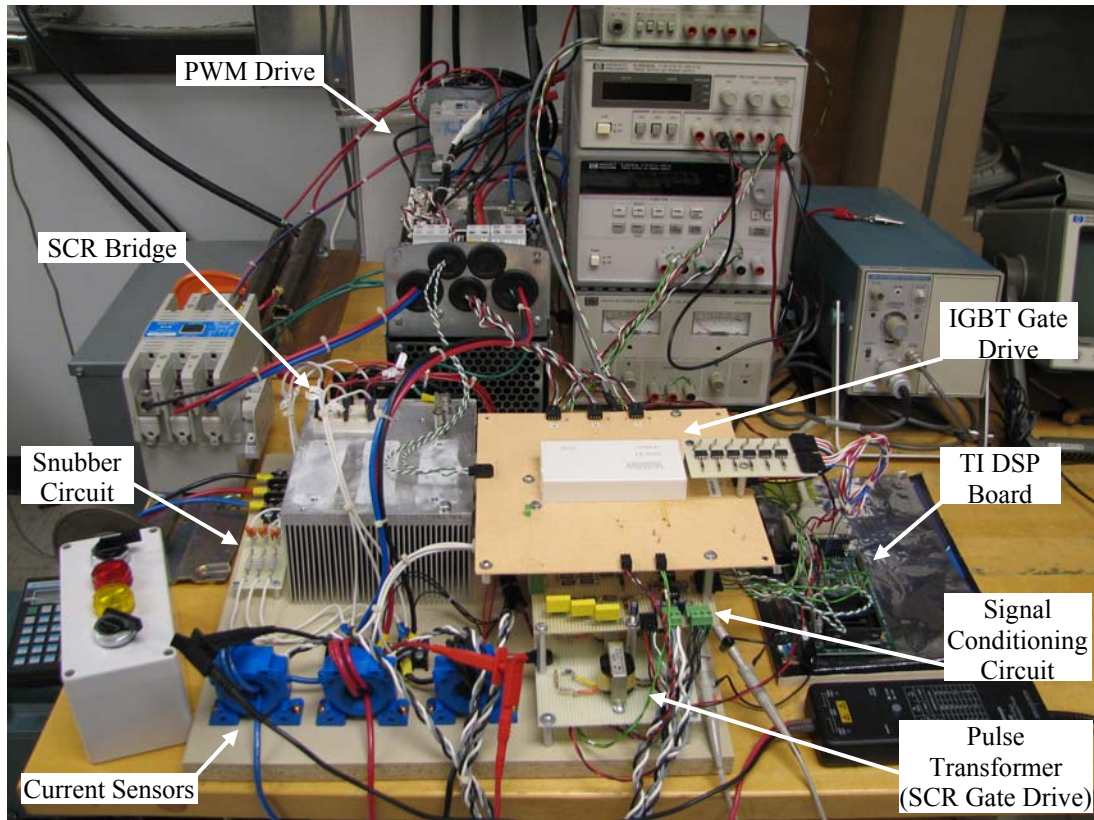
In this appendix, detailed designs and specifications of the hardware prototypes of both the fault-tolerant soft starter and the fault-tolerant adjustable-speed drive are set forth. These include a complete listing of the specifications of each of the hardware components utilized in the implementation of the test prototypes, as well as the design schematics and circuit wiring diagrams of the power topologies and their associated signal conditioning circuits and gate drives.

### A.2 System Descriptions

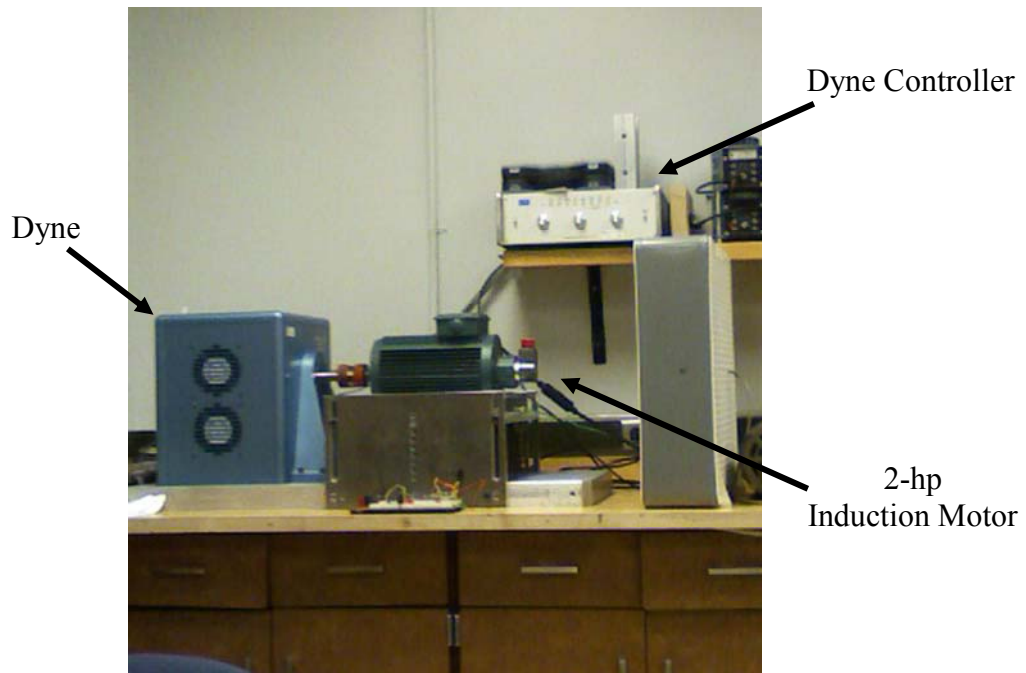
A digital photo of the overall system topology, including the PWM drive, the soft starter, the induction motor, and its mechanical load, is shown in Figure A.1. The corresponding circuit wiring schematics and the component/device specifications of the fault-tolerant soft starter and the fault-tolerant PWM drive are depicted in Figure A.2 and Figure A.3, respectively.

The experimental test setup consists of the following elements:

- Three-phase induction motor and the dynamometer (constant mechanical load), see Section A.2.1.
- Three-phase SCR bridge (for both the soft starter and the quasi-cycloconverter), see Section A.2.2.
- Six pulse-transformers to serve as gate drive for the SCR bridge, see Section A.2.2.
- Three-phase  $RC$  snubber circuit for the SCR bridge, see Section A.2.2.
- Three-phase PWM drive (with precharge mechanism), see Section A.2.3.
- IGBT gate drive for the PWM inverter bridge, see Section A.2.3.
- DSP controller board, see Section A.2.4.
- Voltage and current sensing devices and their signal conditioning circuits, see Section A.2.5.
- Data acquisition system, see Section A.2.6.



(a)



(b)

Figure A.1: Photos of the overall system. (a) Power electronic circuit. (b) Motor-load system.

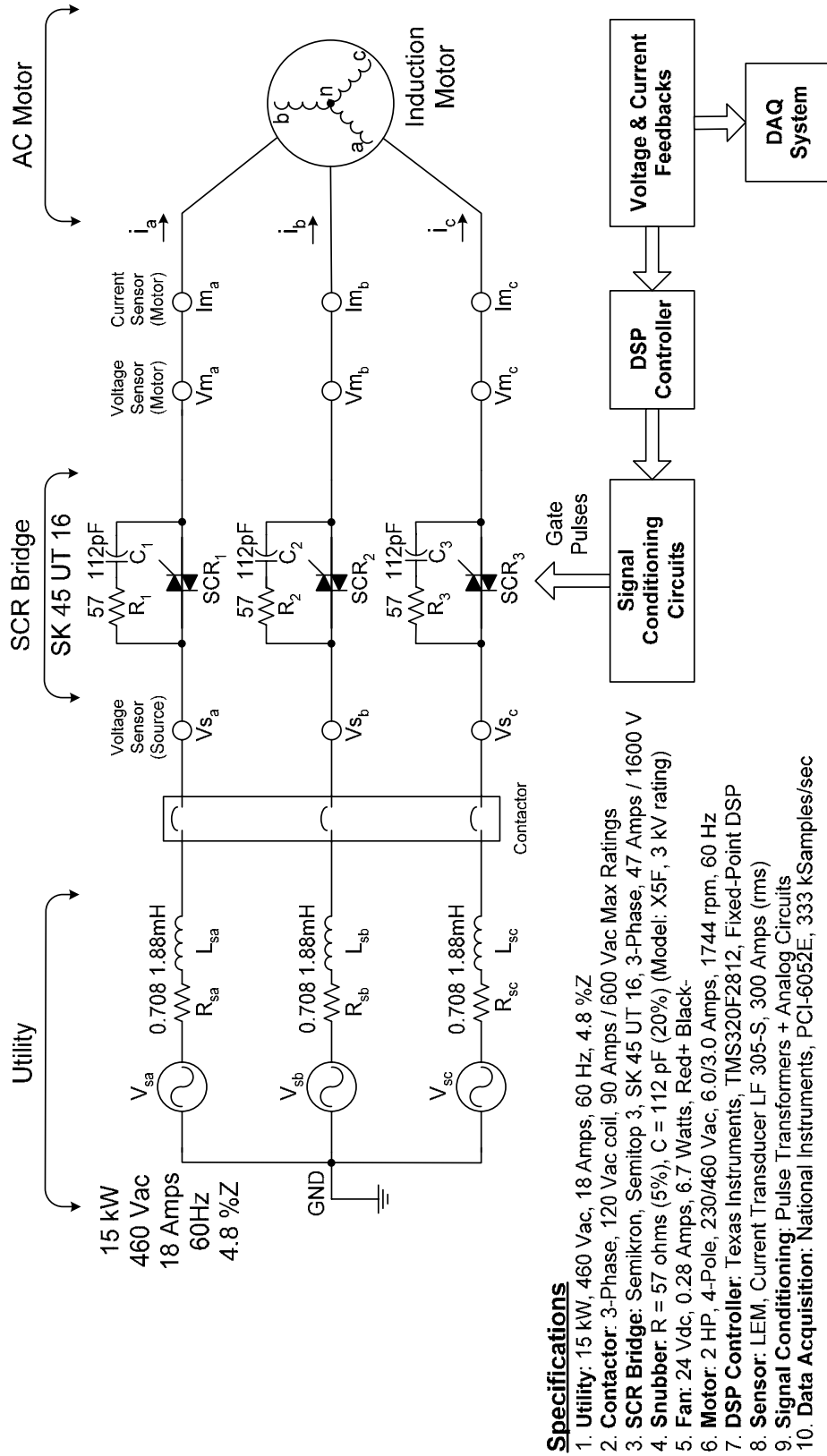


Figure A.2: Schematic and specifications of induction motor-soft starter test setup system.

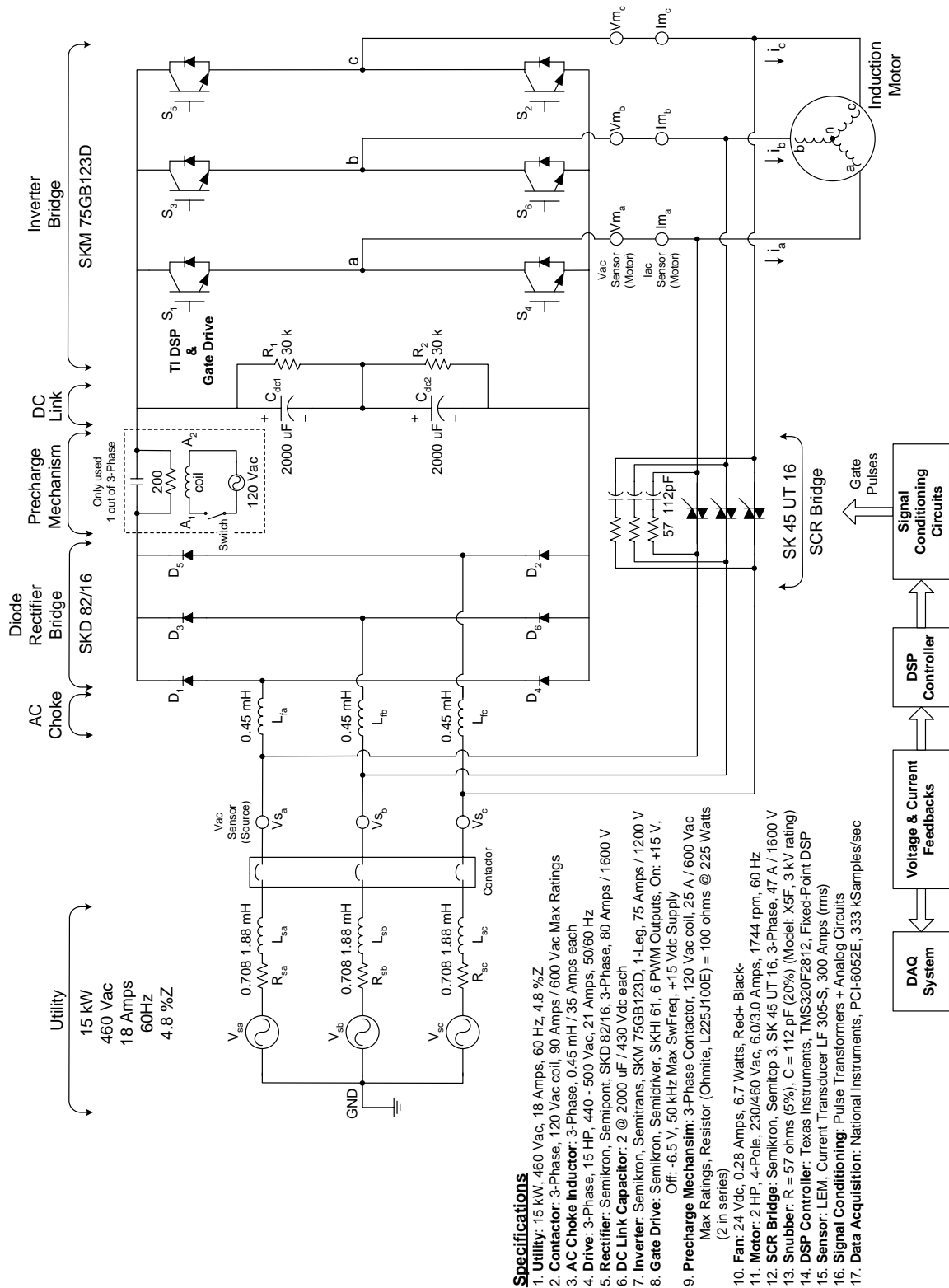


Figure A.3: Schematic and specifications of induction motor-drive test setup system.

### A.2.1 Motor Design Specifications and Datasheets

The design features of the case-study 2-hp induction motor are listed in Table A.1. The corresponding datasheets used for computing the motor T-equivalent circuit parameters are given in Figure A.4. The process of computing these T-equivalent motor parameters is described in detail in the steps given below.

According to the datasheet given in Figure A.4(a), the line-to-line measurement of the stator winding resistance for a high-voltage, series-connection winding type is given as  $7.7\Omega$ . Hence, the per-phase stator resistance can be computed as follows:  $R_s = 7.7/2 = 3.85\Omega$ .

With references to [88] as well as the class notes of EECE-123, the equivalent rotor resistance,  $R_r$ , and rotor leakage reactance,  $X_{lr}$ , referred to the stator side in the T-equivalent circuit are defined as follows:

$$\begin{aligned} R_r &= \frac{3V_{1a}^2 S_{\max}}{2\omega_{syn} T_{\max}} \\ X_{lr} &= \frac{R_r}{2S_{\max}} \end{aligned} \quad (\text{A.1})$$

where,  $V_{1a}$  represents the fundamental component of the motor phase voltage,  $T_{\max}$  represents the breakdown (pull-out) torque,  $S_{\max}$  represent the motor slip at  $T_{\max}$ , and  $\omega_{syn}$  represents the angular synchronous speed in mechanical radians per second. From the datasheet of Figure A.4(a), the above parameters of (A.1) are computed as follows:

$$\begin{aligned} V_{1a} &= 460/\sqrt{3} = 265.5811 \text{ Volt} \\ T_{\max} &= 522\% \text{ of Full-Load Torque} = \frac{522}{100} (5.99 \text{ lb.ft}) = 31.2678 \text{ lb.ft} \\ &= 42.393 \text{ Nm @ } 1450 \text{ r/min} \quad (\text{A.2}) \\ S_{\max} &= \frac{n_{syn} - n_{@T_{\max}}}{n_{syn}} = \frac{1800 - 1450}{1800} = 0.19444, \text{ and } \omega_{syn} = 188.50 \text{ m.rad/sec} \end{aligned}$$

By substituting the computed parameters of (A.2) into (A.1), the rotor resistance and rotor leakage reactance are found to be:  $R_r = 2.574\Omega$  and  $X_{lr} = 6.61988\Omega$ . Assuming the stator and rotor leakage reactance are identical, the corresponding stator and rotor leakage inductances are computed to be:  $L_{ls} = L_{lr} = X_{lr} \text{ (or } X_{ls}) / 377 = 17.5594 \text{ mH}$

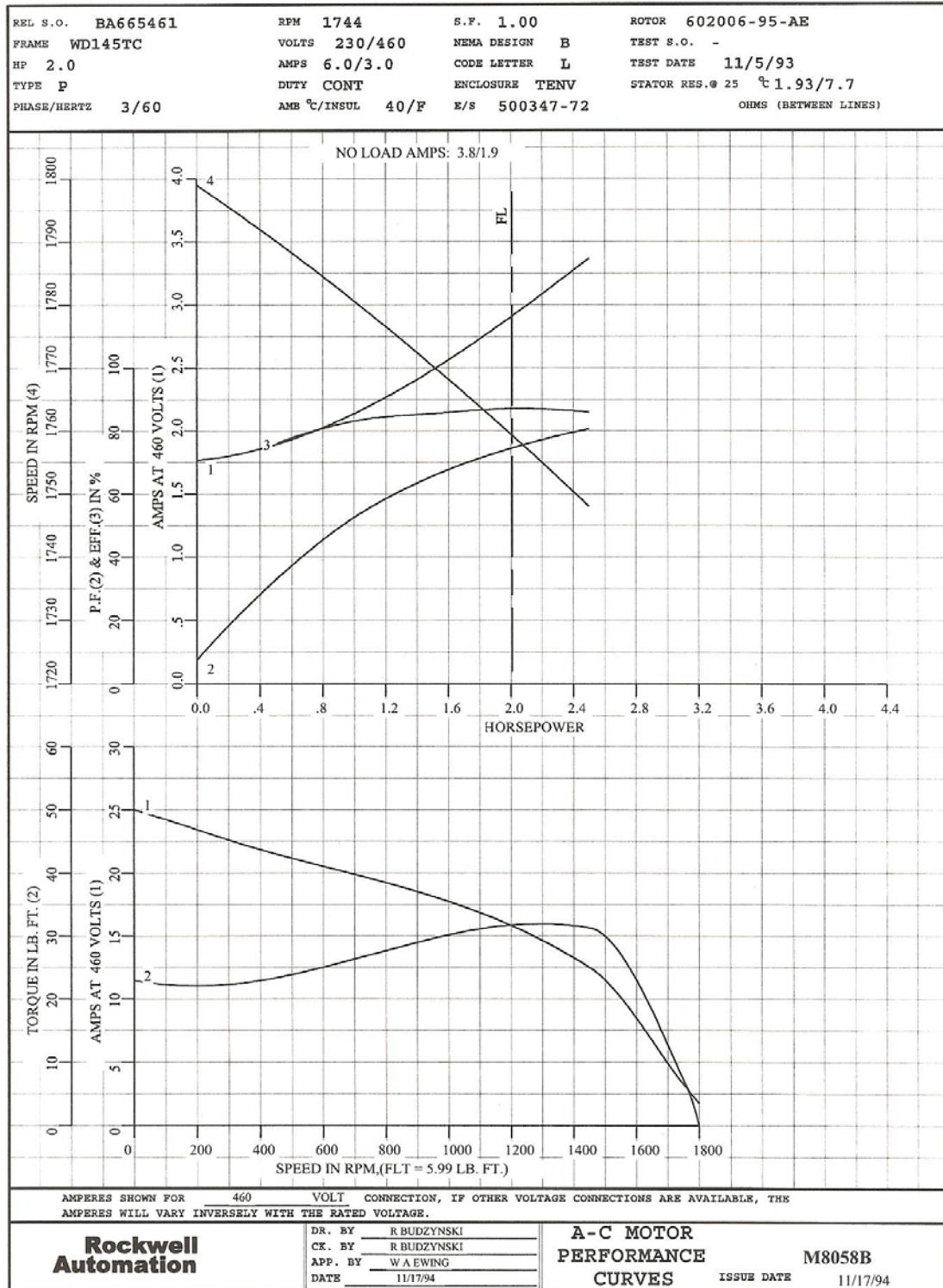
At no-load condition, see Figure A.4(a), the motor phase current,  $I$ , is given as 1.8 Amps, the motor phase voltage,  $V$ , is given as 265.58 Volt, and the power factor, PF, is given as 7.60%. In phasor representation with the motor phase voltage being the reference,  $\vec{V} = 265.58\angle 0^\circ$  Volt and  $\vec{I} = 1.8\angle -85.64^\circ$  Amps. As an approximation, one can assume  $R_r/s \rightarrow \infty$  at the no-load condition. Hence, one can compute the sum of the stator leakage reactance and the magnetizing reactance to be:  $X_{ls} + X_m = \text{imaginary}(\vec{V}/\vec{I}) = 147.118\Omega$ . Knowing the value of  $X_{ls}$  from above, the magnetizing inductance,  $L_m = X_m/377$ , is found to be:  $L_m = 0.372674 \text{ H}$ .

Table A.1: Design specifications of 2-hp induction motor.

Rated Power	2 hp (1492 Watts)
Rated Voltage (Line-Line)	460 Volts
Rated Current	3.0 Amps
Rated Frequency	60 Hz
Rated Speed	1744 r/min
Rated Torque	8.169 Nm
Phase	3
Number of Poles	4
Stator Resistance, $R_s$	3.850 $\Omega$
Rotor Resistance, $R_r$	2.574 $\Omega$
Stator Leakage Inductance, $L_{ls}$	17.5594 mH
Rotor Leakage Inductance, $L_{lr}$	17.5594 mH
Magnetizing Inductance, $L_m$	0.372674 H
Moment of Inertia, $J$	0.028 kg.m <sup>2</sup>
Load Coefficient, $k_L$ , where $T_L = k_L \omega_m^2$	$0.24493 \times 10^{-3} \text{ Nm}/(\text{m. rad/s})^2$

REL. S.O.	FRAME	HP	TYPE	PHASE/ HERTZ	RPM	VOLTS
BA665461	WD145TC	2.0	P	3/60	1744	230/460
AMPS	DUTY	AMB <sup>°C</sup> / INSUL.	S.F.	NEMA DESIGN	CODE LETTER	ENCL.
6.0/3.0	CONT	40/F	1.00	B	L	TENV
E/S	ROTOR	TEST S.O.	TEST DATE	STATOR RES.@25 <sup>°C</sup> OHMS (BETWEEN LINES)		
500347-72	602006-95-AE	-	11/5/93	1.93/7.7		
PERFORMANCE						
LOAD	HP	AMPERES	RPM	% POWER FACTOR	% EFFICIENCY	
NO LOAD	0	1.8	1799	7.60	0	
1/4	.51	1.9	1790	33.3	76.2	
2/4	1.02	2.1	1780	53.2	83.3	
3/4	1.52	2.5	1770	66.1	85.6	
4/4	2.01	2.9	1761	74.6	87.1	
5/4	2.50	3.4	1748	80.7	86.0	
SPEED TORQUE						
		RPM	TORQUE % FULL LOAD	TORQUE LB.-FT.	AMPERES	
LOCKED ROTOR		0	382	22.9	25.0	
PULL UP		250	369	22.1	23.0	
BREAKDOWN		1450	522	31.3	12.5	
FULL LOAD		1761	100	5.99	2.9	
AMPERES SHOWN FOR 460. VOLT CONNECTION. IF OTHER VOLTAGE CONNECTIONS ARE AVAILABLE, THE AMPERES WILL VARY INVERSELY WITH THE RATED VOLTAGE  REMARKS: NO LOAD AMPS: 3.8/1.9						
<b>Rockwell Automation</b>		DR. BY <u>  R BUDZYNSKI  </u> CK. BY <u>  R BUDZYNSKI  </u> APP. BY <u>  W A EWING  </u> DATE <u>  11/17/94  </u>		A-C MOTOR PERFORMANCE DATA M8058B ISSUE DATE 11/17/94		

(a)



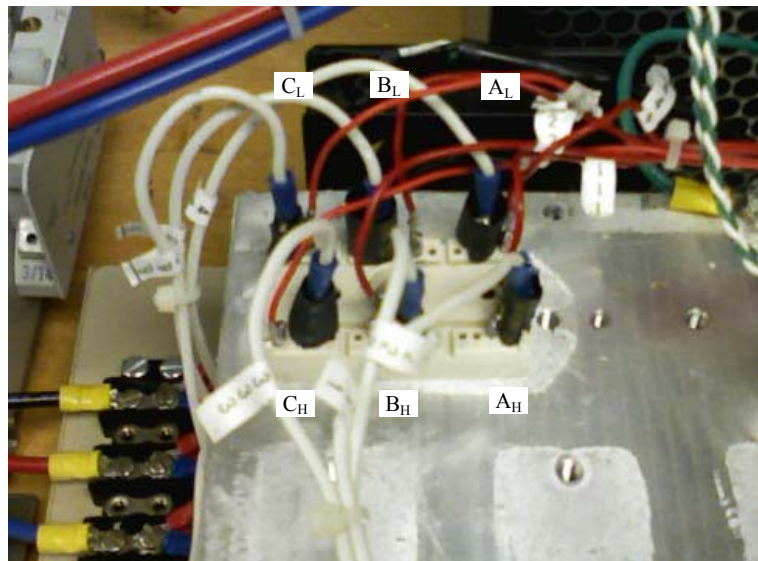
Printed on 2/29/00 11:05 @ rmm

(b)

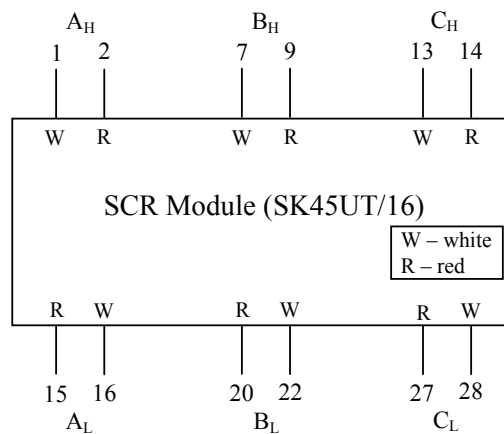
Figure A.4: Datasheets of 2-hp induction motor. (a) Performance data. (b) Performance curves.

### A.2.2 Soft Starter and Quasi-Cycloconverter Designs

A digital photo of the three-phase SCR bridge and its corresponding circuit diagram with wiring labels are depicted in Figure A.5. Its gate drive, which serves as the interface between the SCR bridge and the controller, is shown in Figure A.6. A set of pulse transformers is used to implement the gate drive function, whose purpose is to provide electrical galvanic isolations between the high and low power stages, as well as to provide sufficient currents to the gates of the SCRs to achieve the “turn-on” status. Meanwhile, a photo of the snubber circuit is also shown here in Figure A.7.



(a)



(b)

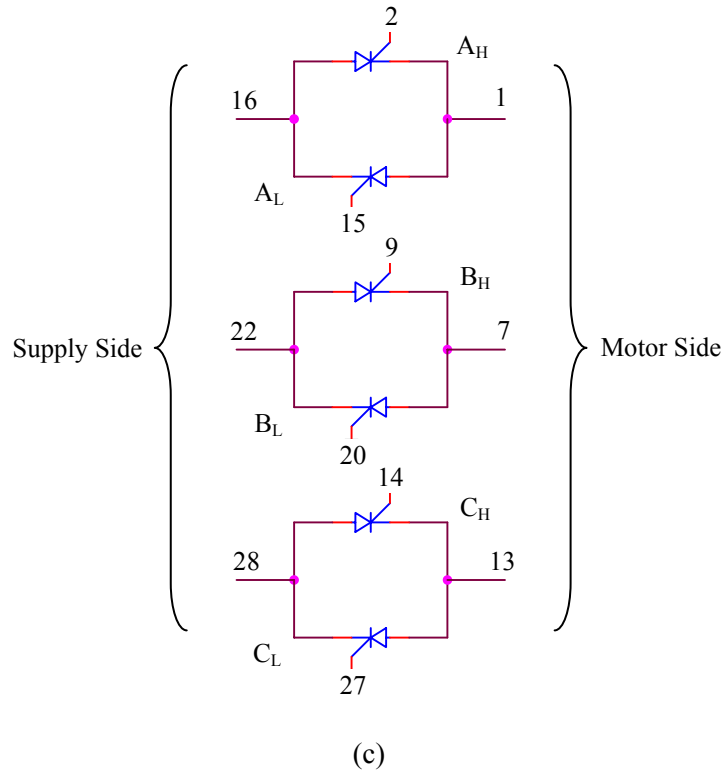
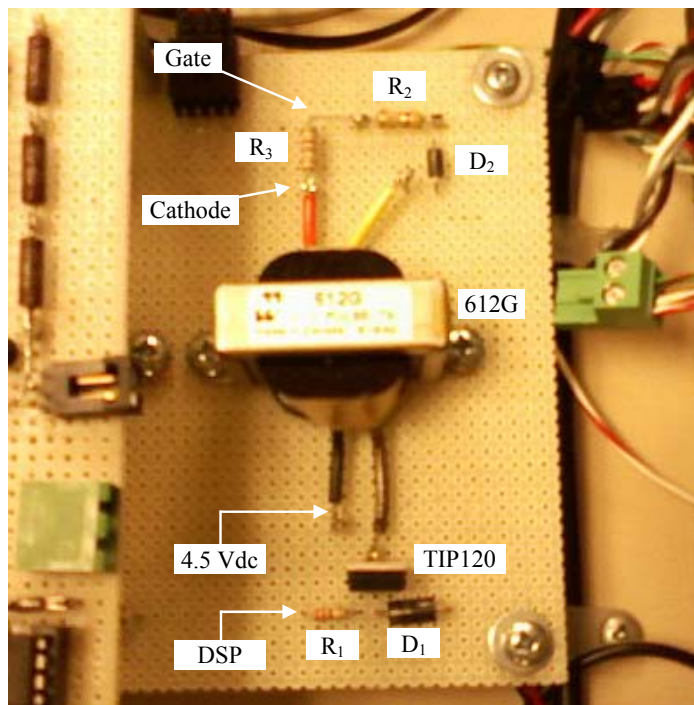
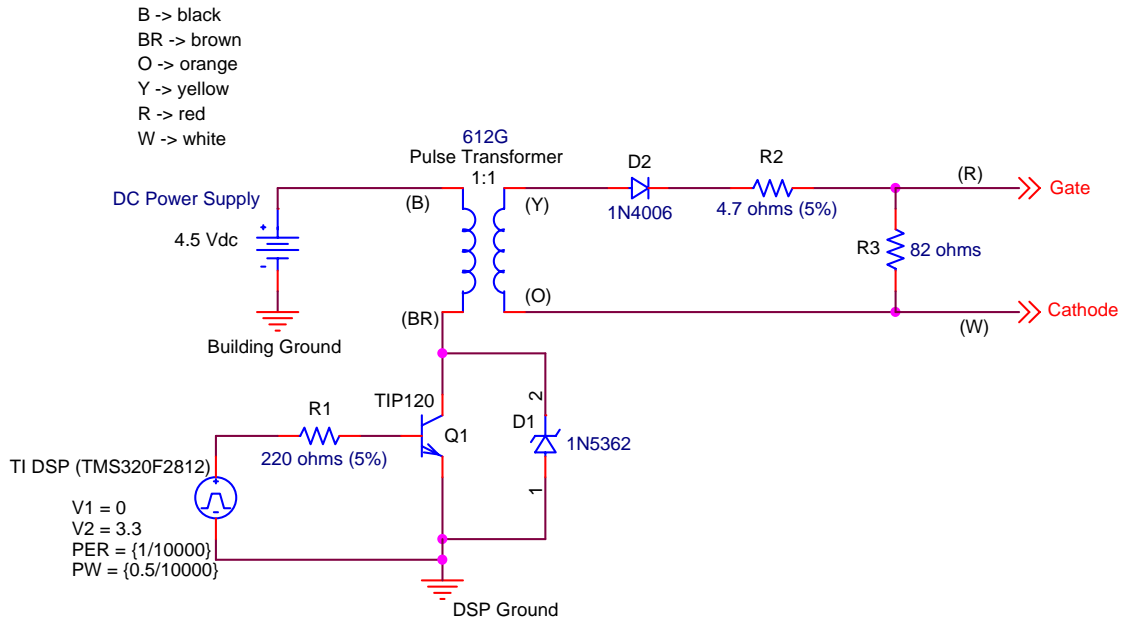


Figure A.5: Three-phase SCR bridge. (a) Digital photo. (b) A drawing of the SCR bridge with terminal labels. (c) Circuit diagram with wiring labels.



(a)



(b)

Figure A.6: Gate drive of the SCR bridge. (a) Digital Photo. (b) Circuit diagram.

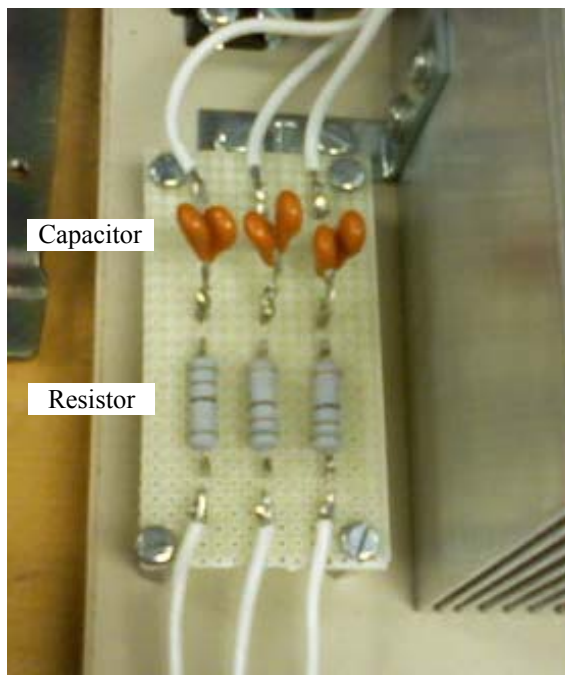


Figure A.7: Digital photo of the RC snubber circuits ( $R = 57\Omega$  and  $C = 112\text{pF}$ ).

### A.2.3 PWM Drive

A digital photo of the three-phase PWM drive and its “closed-up” view are shown in Figure A.8(a) and Figure A.8(b), respectively. A precharge device, which consists of a contactor and a 200 $\Omega$  power resistor, is used to precharge the dc-link capacitors during the initial start-up. Both the diode and inverter bridge are obtained from Semikron. In order to turn-on/off the IGBTs, a Semikron gate drive is utilized to provide the interface between the IGBTs and the controller. The block diagram and the connection schematics of the gate drive are depicted in Figure A.9. Since the input to the gate drive for turning-on is 5V and turning-off is 0V, and the fact that the DSP controller board only outputs PWM signal which goes from 0 to 3.3V, an opto-coupler is utilized. Its purpose is to convert the 0 – 3.3V of the PWM signals from the DSP board to 0 – 5V to the gate drive. The gate drive will then output the PWM signals to the IGBTs at -6.5V to +15V for turning-off and turning-on, respectively. The circuit diagram of the opto-coupler is depicted in Figure A.10.

### A.2.4 DSP Controller Board

A digital photo of the Texas Instruments (TI) DSP board is shown in Figure A.11, and its specifications are given in Table A.2.

Table A.2: Specifications of TI DSP board.

Generation	TMS320F2812
CPU	C28x, 32-bit, fixed-point
Frequency	150 MHz
PWM	16 channels
ADC	16 channels at 12-bit each
ADC Conversion Time	80 ns
IO Supply / Core Supply	3.3 V / 1.9 V
Flash	256 KB
Timers	3 32-bit General-Purpose Timers

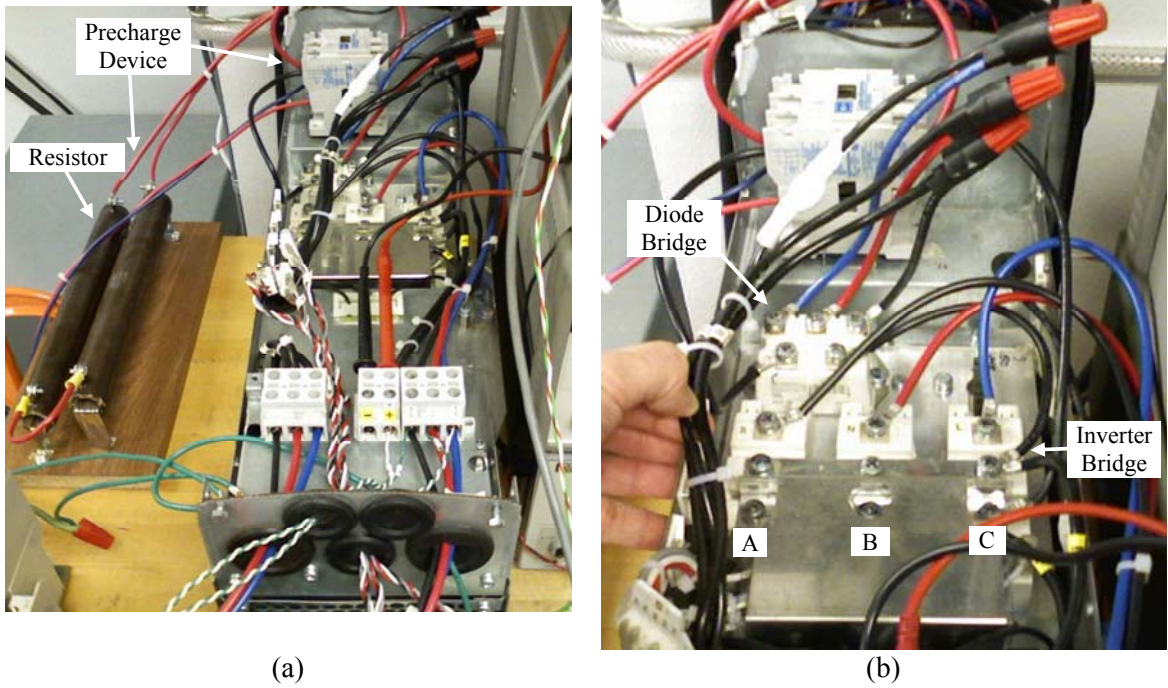
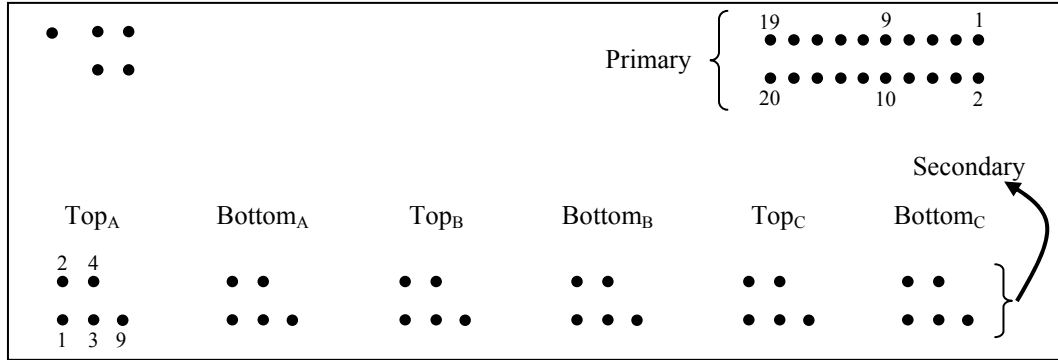
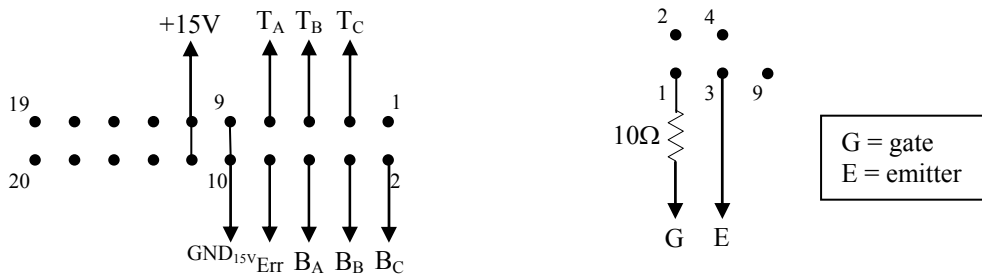


Figure A.8: Photos of the PWM drive. (a) Drive and precharge device. (b) Closed-up view.



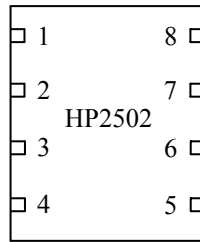
(a)



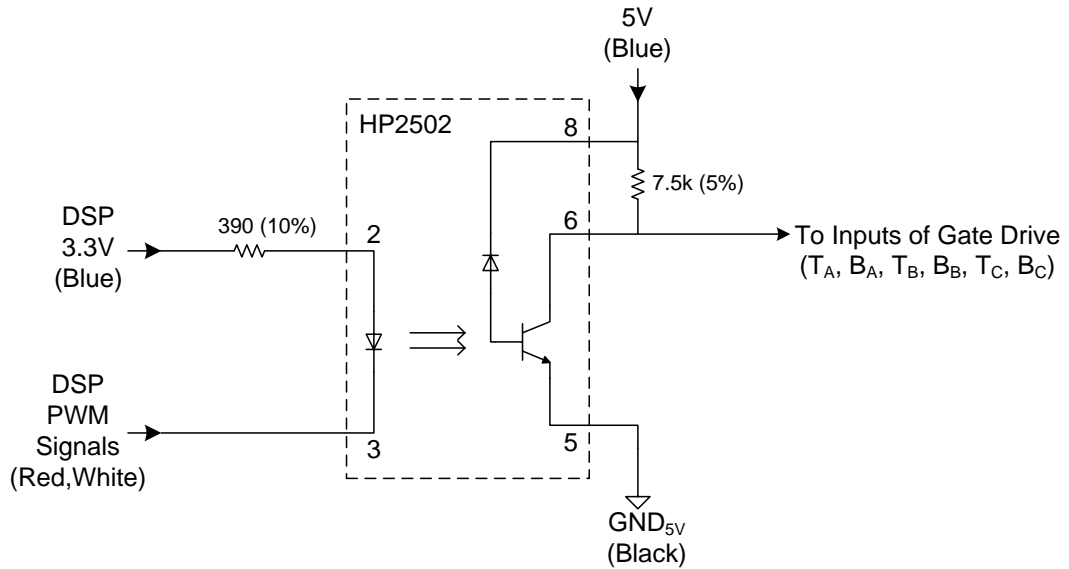
(b) Note: GND<sub>15V</sub> is not tied to DSP Ground.

(c)

Figure A.9: Gate drive of the inverter bridge. (a) A drawing of the gate drive. (b) Primary side connection diagram. (c) Secondary side connection diagram.



(a)



(b) **Note:**  $GND_{5V}$  is not tied to DSP Ground.

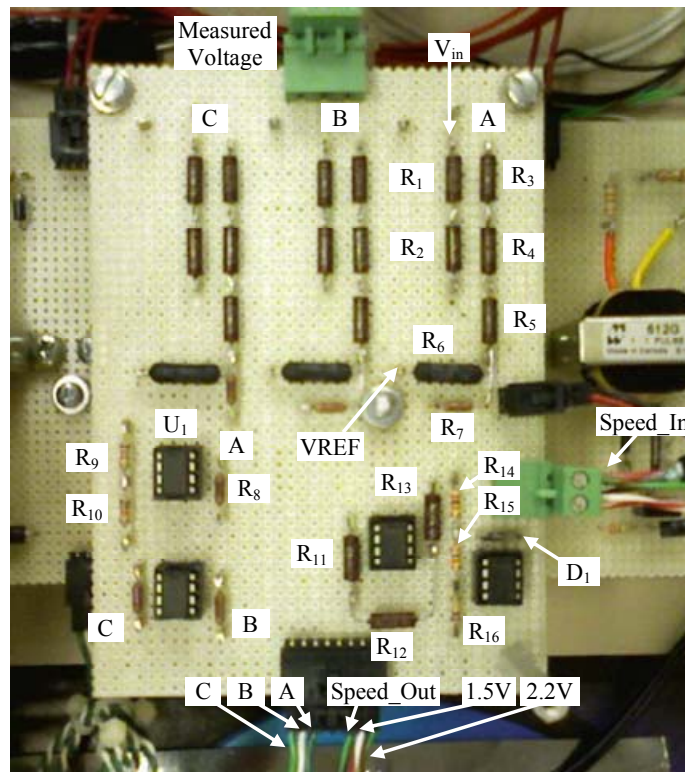
Figure A.10: Opto-coupler. (a) Block diagram. (b) Circuit diagram ( $GND_{5V}$  is tied to  $GND_{15V}$ ).



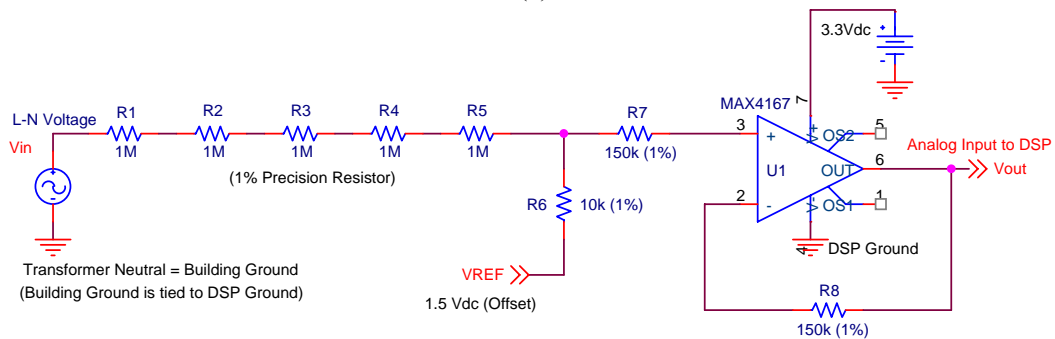
Figure A.11: DSP controller board.

### A.2.5 Signal Conditioning Circuits

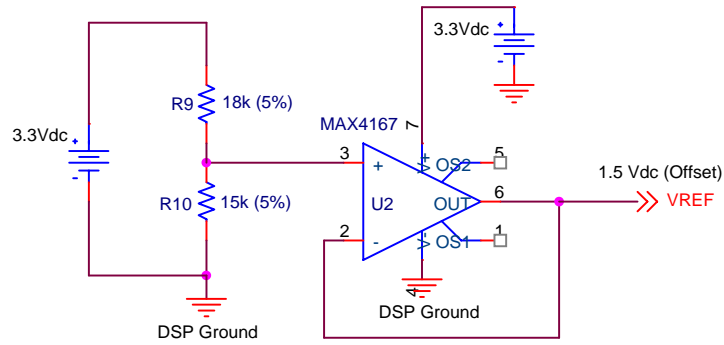
In this setup, there are two signal conditioning boards. The first board, which is depicted in Figure A.12(a), consists of a set of three-phase measurement circuits of the supply voltages (see Figure A.12(b) for per-phase circuit), a 1.5Volt dc-offset circuit (see Figure A.12(c)), an A/D calibration circuit (see Figure A.12(d)), and a speed sensing circuit (see Figure A.12(e)). Since the analog inputs of the DSP board only accept signals ranging from 0 to 3Volt, a 1.5Volt dc-offset circuit is used here to provide the necessary dc offset to the measured ac signals ( $\pm 1.5V$ ).



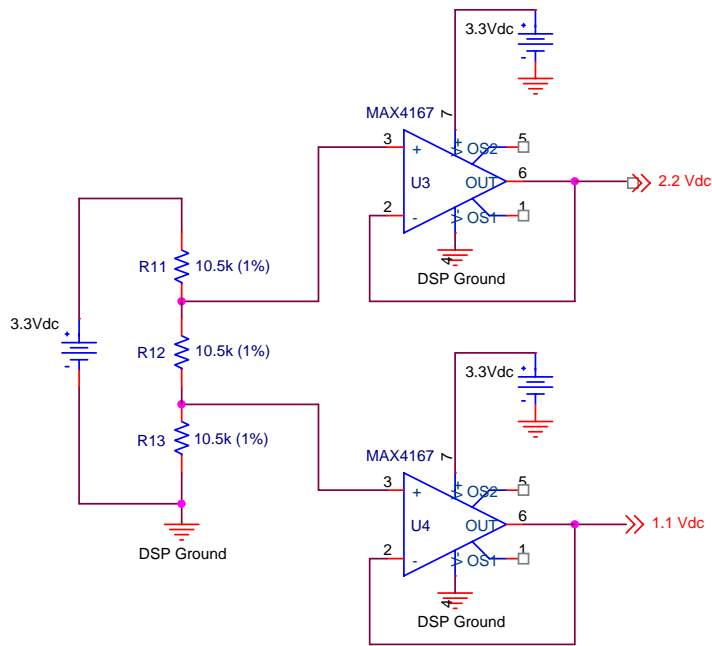
(a)



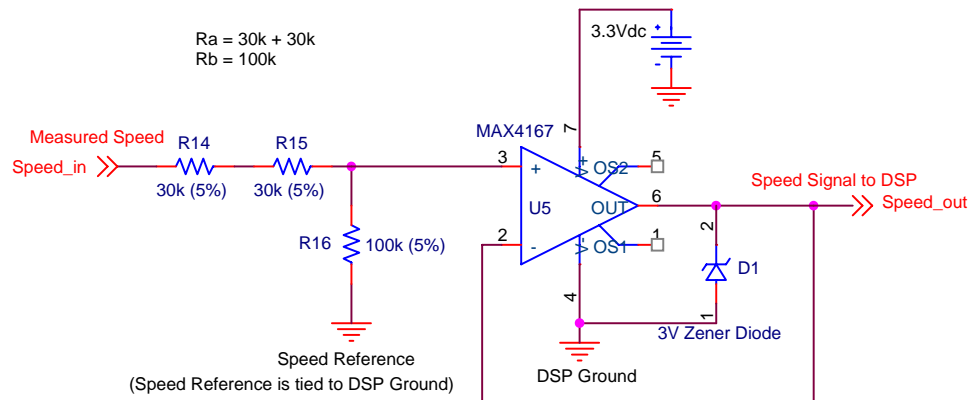
(b)



(c)



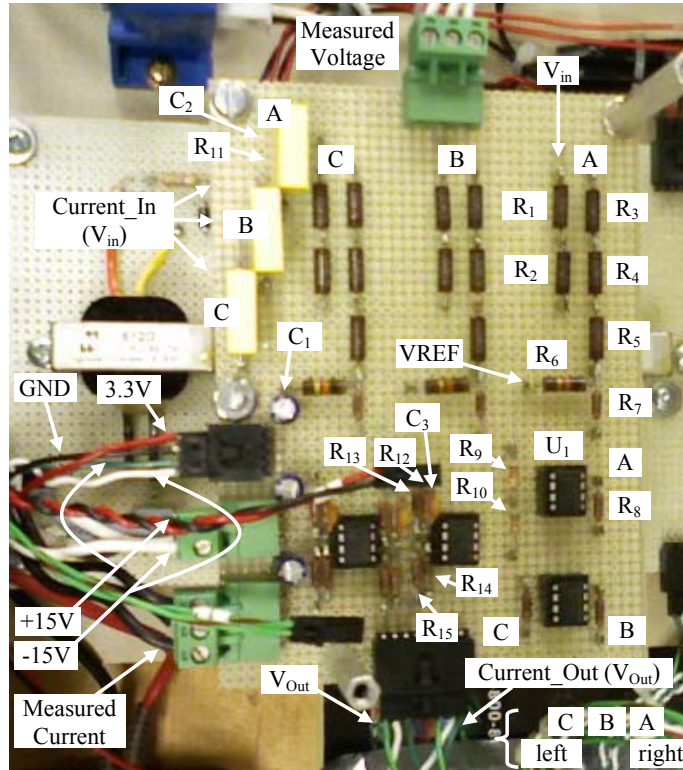
(d)



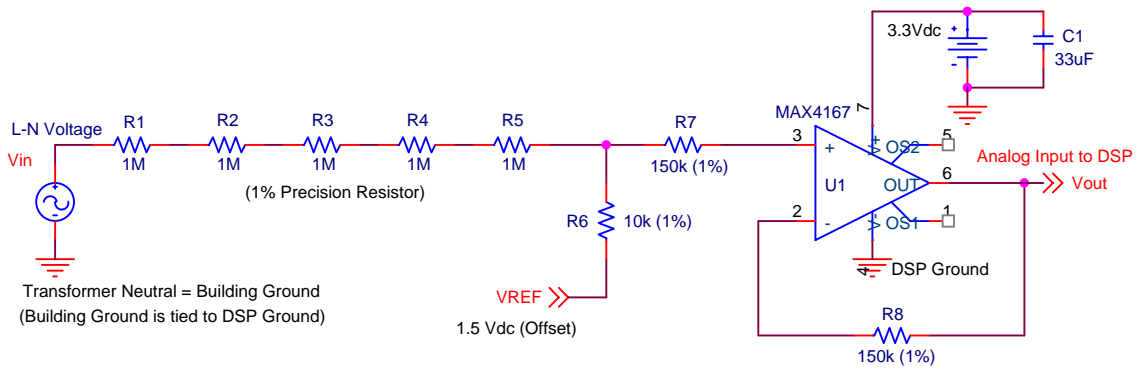
(e)

Figure A.12: Signal conditioning board #1. (a) Digital photo. (b) Voltage circuit. (c) 1.5Volt dc-offset circuit. (d) A/D calibration circuit. (e) Speed circuit.

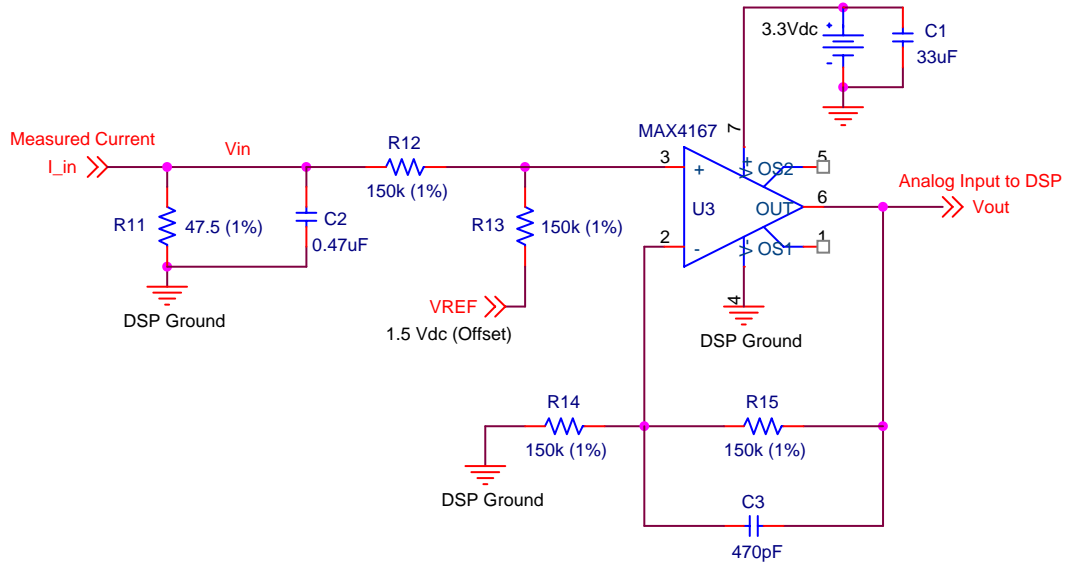
Meanwhile, the second signal conditioning board, which is shown here in Figure A.13(a), consists of a set of three-phase measurement circuits of the motor terminal voltages (see Figure A.13(b) for per-phase circuit), a set of three-phase signal conditioning circuits for the motor phase currents (see Figure A.13(c) for per-phase circuit), and a 1.5Volt dc-offset circuit (see Figure A.13(d)).



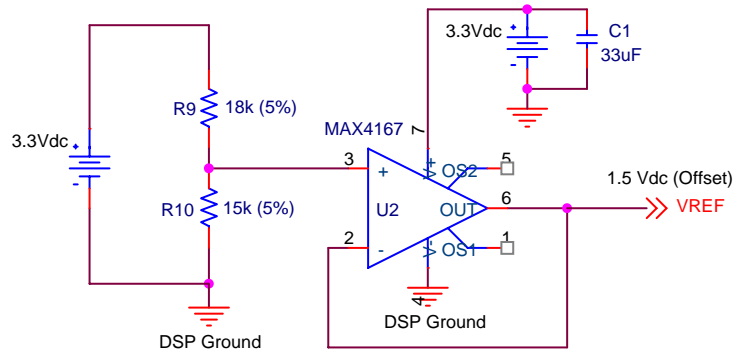
(a)



(b)



(c)



(d)

Figure A.13: Signal conditioning board #2. (a) Digital photo. (b) Voltage circuit. (c) Current circuit. (d) 1.5Volt dc-offset circuit.

### A.2.6 Data Acquisition System

The data acquisition (DAQ) system used in this work is a state-of-the-art technology hardware and software developed by National Instruments (NI). The high accuracy and precision of the NI-DAQ system makes it a very attractive and reliable data collection tool. The high sampling rate and high resolution of the DAQ system allow the user to obtain very precise and accurate data structures.

The DAQ system uses an E-Series technology (PCI-6052E) to deliver high performance, reliable data acquisition capabilities to meet a wide range of application requirements. It provides a sampling rate of 333 kSamples/sec and 16-bit resolution on 16 single-ended analog inputs. Depending on the type of hard disk of the computer, the NI PCI-6052E can stream to hard disk at rates up to 333 kSamples/sec. This DAQ board features analog and digital triggering capability, as well as two 24-bit, 20 MHz counter/timers, 8 digital Input/Output (I/O) lines, and two 16-bit analog outputs. Table A.3 summarizes the overall features of this DAQ system.

Table A.3: Features of NI DAQ system.

Family	PCI-6052E
Bus	PCI
Analog Input	16 Single-Ended
Resolution	16 Bits
Sampling Rates	333 kSamples/sec
Input Range	$\pm 0.05$ to $\pm 10$ Volts
Analog Output	2
Resolution	16 Bits
Output Rate	333 kSamples/sec
Output Range	$\pm 10$ Volts
Digital I/O	8
Counter / Timers	Two 24 Bit, 20 MHz
Triggers	Analog and Digital